# Development of a Synthetic External Stent to Prevent Vein Graft and Hemodialysis Access Site Failures

By

Timothy C. Boire

Dissertation

Submitted to the Faculty of the

Graduate School of Vanderbilt University

in partial fulfillment of the requirements

for the degree of

DOCTOR OF PHILOSOPHY

in

Biomedical Engineering

August 11, 2017

Nashville, Tennessee

Approved:

Craig L. Duvall, Ph.D.

Colleen M. Brophy, M.D.

Haoxiang Luo, Ph.D.

Brett C. Byram, Ph.D.

David Shaffer, M.D.

Robert L. Galloway, Ph.D.

*No bird soars too high, if he soars with his own wings.*

*~ William Blake*

To my grandparents:

Leo Boire (October 10, 1921 – November 7, 2002)

Carol Boire (December 23, 1921 –)

George H. Lovely (August 10, 1929 –)

Evelyn Lovely (October 21, 1929 - )

ACKNOWLEDGEMENTS

Wow, what a journey it has been! I'm incredibly grateful to all the people that I have met over these past six years that have helped mold me into the person that I am today. I would not be here without some really great friendships and mentorships.

I want to give a shout out to my former advisor, Dr. Hak-Joon Sung, for providing me the opportunity to come here in the first place and serve as my mentor for many years. It has been a blessing.

I am very thankful to my thesis chair, Dr. Craig Duvall, for stepping up big time when I really needed him. I am also very thankful for our friendship, and have been happy to see him be achieve a lot of success - it is well deserved.

I also would like to thank the rest of my committee members, Dr. Colleen Brophy and her mentorship through the years, Dr. Haoxiang Luo, Dr. Brett Byram, Dr. David Shaffer, and Dr. Robert Galloway for their continued guidance, mentorship, and collaboration. All of them have stepped up in very meaningful ways, and there is no way that I can repay them. In addition, I acknowledge my terrific collaborators Dr. Lauren Himmel, Dr. Kelli Boyd, Dr. Joyce Cheung-Flynn, Dr. Christy Guth, Dr. Shirin Masjedi, Brian O'Grady, Xin Zhang, and recent graduates William Kaplan and Jae Han Lee.

Moreover, it has been an honor to work in the trenches with fellow labmates Dr. Mukesh Gupta, Dr. Daniel Balikov, Dr. Xintong Wang, Dr. Young Wook Chun, Dr. Jung Bok Lee, Dr. Kellye Kirkbride, Dr. Charleson Bell, Dr. Eric Dailing, Dr. Brian Evans, Dr. Chris Nelson, Dr. Lucas Hofmeister, Dr. Sue Lee, Dr. Kelsey Mayo, Dr. Thomas Werfel, Dr. John Martin, Dr. Sammy Sarett, Dr. Sinead Miller, Byron Smith, Nicolo Garbin, Addisu Taddese, Piotr Slawinski, Ricky Rath, Kameron Kilchrist, Taylor Kavanaugh,

Meredith Jackson, Bryan Dollinger, Sean Bedingfield, Mary Dockery, and Stephanie Dudzinski.

I also want to thank the Vanderbilt University School of Engineering, Vanderbilt University Graduate School, the American Heart Association, the National Science Foundation, and the National Institutes of Health for financially supporting this work.

I would also like to thank all of my amazing friends here in Nashville that are just too many to name, Logan Rhea, Cole Jacobus, as well as life-long friends in Boston, Derek Engelking, and friends in California, New Hampshire, and all over. You know who you are.

Finally, I thank my family. To my parents, Dan and Judy, and my siblings Jeremy Jason, Nicole, and Nate, the greatest of people and the best family that I could ask for. You are all amazing.

TABLE OF CONTENTS

Page

LIST OF TABLES

# LIST OF EQUATIONS

LIST OF FIGURES

Figure Page

# CHAPTER 1: INTRODUCTION AND MOTIVATION

Dialysis is the primary lifeline for nearly half a million patients with end-stage renal disease (ESRD). Unfortunately, failure rates at dialysis access sites for arteriovenous fistulas (AVFs) and arteriovenous grafts (AVGs), the two preferred modes of hemodialysis, are very high at 40 - 60% within a year.[1-3] The main culprit of these failures is stenosis at the venous anastomosis caused by neointimal hyperplasia (NH), as well as negative vascular remodeling processes for AVF maturation failure. Therapeutic approaches attempting to improve access patency have achieved limited success, in part because they do not provide a sustained solution as vein walls continue to thicken beyond 12 weeks as they adapt to the arterial circulation.[4] Along these lines, several studies employing Dacron[5-9] or Nitinol[10, 11] external stents have exhibited some promise to reduce NH by promoting positive vascular remodeling processes and/or alleviating mechanical factors contributing to NH. Unfortunately, this has failed to translate to the clinic thus far.[12-14] For example, a 2007 Extent study had to be terminated because all 20 coronary artery bypass graft (CABG) patients treated with a Dacron/polytetrafluorethylene (PTFE) external stent experienced thrombosis within the first 6 months post-surgery.[14] The authors admitted that the failures may have been due to inappropriate material selection and/or device design which led to too rigid or soft of mechanical support, too tight or loose stent-to-vein spacing, and unforeseen complications such as kinking of the vein graft. Improper biomaterial selection and inadequate device design optimization therefore currently hinder clinical translation.

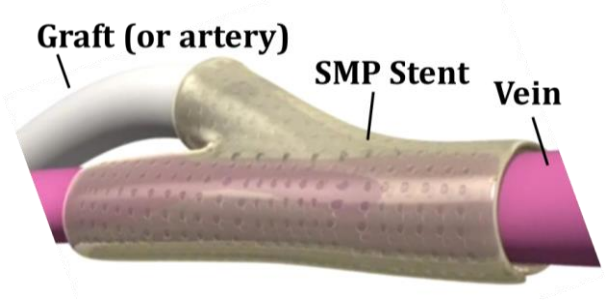


**Figure 1-1 SMP External Stent**
Animated geometric configuration of a shape memory polymer (SMP) external stent applied to the venous anastomosis of a hemodialysis patient utilizing a PTFE graft.

To address these shortcomings encountered with other external stent approaches, a novel class of poly(ε-caprolactone)-based shape memory polymers (SMPs) was developed[15] that possesses unique properties potentially beneficial for external stenting. These SMPs are biocompatible, slowly biodegradable, and mechanically-compliant in order to provide durable, flexible mechanical support. As a SMP with a melting temperature below body temperature, it allows for automatic custom-fitting to each patient's uniquely-shaped venous anastomosis. This potentially reduces NH arising from asymmetric wall thickening [5, 16-19] and improves ease-of-use for surgeons because it does not require sutures like other competitive products such as Vascular Therapies' collagen membrane that elutes sirolimus, Coll-R™.[20] Based on the material characteristics of these SMPs and an understanding of contemporary scientific literature on external stenting, it is *hypothesized* that a SMP external stent can mitigate NH and subsequent vein graft and hemodialysis access failures by promoting neoadventitial growth and providing compliant mechanical support to the venous anastomosis. While a significant amount of work remains to translate a SMP external stent approach to the clinic, these hypothesis are examined in part via the following specific aims:

Aim 1: *Synthesize and characterize a library of shape memory polymers (SMPs)*. Poly(ε-caprolactone) (PCL) is a biocompatible, slowly biodegradable polymer with favorable elasticity and toughness for vascular applications that can be chemically modified and crosslinked to form SMPs with excellent shape memory properties. However, PCL SMPs possess a melting temperature ($T_m$ > 50°C) that is too high for moldability at operating temperatures. It is anticipated that copolymerization with a novel monomer will produce a new class of PCL-based SMPs with $T_m$ ~37°C and desirable mechanical and shape memory properties for external stents.

Aim 2: *Rationally design an external stent prototype comprised of pores that promote neovascularization while minimizing fibrosis and inflammation*. SMP scaffolds comprised of different pore sizes and spacings will differ in the degree to which they elicit neovascularization, fibrogenesis, and inflammation. Candidate designs can be identified that stimulate new blood vessel formation while minimizing fibrogenesis and inflammation. Such responses are expected to promote constructive tissue remodeling, which can be further characterized by a transition from a pro-inflammatory M1 to an immunomodulatory, tissue remodeling M2 macrophage phenotype.[21] It is hypothesized that relative trends in responses to designs will translate to the arteriovenous environment in larger animals/humans and correlate with a mitigation in neointimal hyperplasia (NH) when applied as an external stent.

Other work in progress requiring further efforts includes developing an *ex vivo* anastomosis model that can be used to evaluate hemodynamic effects associated with NH from external stent treatments. As other works corroborate preliminary data showing that flow conditions may be necessary to observe external stent effects in an *ex vivo* environment,[22] it is desired to achieve artery-mimetic flow in an *ex vivo* model. Venous anastomoses can be constructed using vein segments leftover from heart bypass surgery and GORETEX tubing to more closely recapitulate the end-to-side anastomosis geometry encountered in hemodialysis access patients. Doppler ultrasound can be used to detect flow patterns within the anastomosis geometry and this information can be inputted into a computational fluid dynamic (CFD) model to quantify hemodynamic effects. Once established, various external stent designs can be evaluated in terms of their ability to reduce NH as well as hemodynamic factors associated with NH to determine promising design candidates.

Another avenue of exploration involves determining a therapeutic that can act synergistically with external stent effects to further mitigate NH and further improve vein graft and hemodialysis access site patency, albeit at the cost of adding years or even a decade to the commercialization process. Without foreknowledge of the precise mechanism of action of an SMP external stent treatment, it is unclear which therapeutic is optimal. One promising candidate is a peptide inhibitor targeted against Mitogen Activated Protein Kinase II (MK2i), as it has shown promise to reduce NH. [23, 24] However, serial ultrasound measurements in a murine inferior vena cava interposition model suggest that vein grafts progressively thicken

following an initial NH reduction after 7 days.[25] This indicates the need for more localized, sustained release of MK2i to the vein, especially considering that the half-life of MK2i is only 3 days and the majority of VSMC proliferation and migration occurs over the first 4 weeks.[4] Co-immobilization of heparin and MK2i to the surface of a polymer substrate provides a convenient means to localize and sustain release to the venous tissue.

# CHAPTER 2: BACKGROUND AND SIGNIFICANCE

## 2.1 The Clinical Problem of Vein Graft and Hemodialysis Access Failure

Vein graft and hemodialysis access failures impose significant morbidity and mortality risks for patients and place a particular financial burden on the Centers for Medicare & Medicaid Services (CMS) as the primary payer for treatments. Autologous saphenous vein grafts (SVGs) are connected to arteries to serve as conduits for bypassing arterial occlusions in approximately 250,000 annual coronary artery bypass grafting (CABG) and 80,000 peripheral artery bypass grafting (PABG) surgeries, respectively.[26-28] Despite intensive study and some advances in percutaneous techniques such as balloon angioplasty and intraluminal stenting, bypass grafting remains the gold standard for coronary artery disease (CAD) patients and for peripheral artery disease (PAD) patients with severe femoropopliteal lesions.[29] Peripheral artery bypass is also employed in more than 100,000 annual vascular access creation surgeries, where the access site created functions as a portal for hemodialysis in end-stage renal disease (ESRD) patients.[30] Hemodialysis serves as the primary lifeline for ESRD patients awaiting kidney transplantation. Typically in the arm, a vein-to-artery connection (i.e. arteriovenous fistula (AVF)) effectively creates an access site to the entire bloodstream, allowing a means to filter out toxins in the blood through an external dialyzer. Synthetic expanded polytetrafluoroethylene (ePTFE) arteriovenous grafts (AVGs) are also employed to create access sites in approximately 20% of cases.[30]

Although CABG is considered the gold standard for treating CAD patients with severe occlusions, 10 – 20% of SVGs fail within the first year after surgery, and up to 50% fail within 10 years.[31-35] Similarly, in the lower extremities of PAD patients, 30 – 50% fail

within 5 years.[36] The metric for vein graft or hemodialysis access failure is commonly defined as ≥ 70% occlusion of the grafted vessel that necessitates either revision via angioplasty, intraluminal stenting, or other surgical intervention, or replacement due to total graft/access loss.[37, 38] Primary patency is defined as the intervention-free interval following surgery, whereas secondary patency describes the total survival of the graft or access regardless of whether interventional procedures are required to maintain it.[37, 38] Graft failure can lead to disease progression, recurrent angina, myocardial infarction, and death.[30, 39-41] Failures are even more pronounced at hemodialysis access sites. Primary (i.e. intervention-free access survival) and secondary (i.e. access survival until abandonment)[37, 38] patency rates for fistulas are 60% and 71% at 12 months (i.e. 40% failure), and 51% and 64% at 24 months (i.e. 49% failure), respectively. Even worse, PTFE grafts exhibit primary and secondary patency rates of 58% and 76% at 6 months (i.e. 42% failure) and 33% and 55% at 18 months (i.e. 67% failure), respectively.[1-3] This affects the quality and length of life of patients, and also leads to disproportionate financial dispositions for CMS. For example, patients with graft failure are approximately $78,654 more expensive to treat per patient-year, which translates to $1.8 - 2.9 billion in direct costs primarily absorbed by Medicare for the hemodialysis graft population alone.[30]

## 2.2 Neointimal Hyperplasia

Neointimal hyperplasia (NH), a process in which the intimal layer of the vein wall thickens leading to stenosis and occlusion, is the primary culprit (>70%) for vein graft and hemodialysis access site failures.[26, 42] It is therefore an important process to understand for developing therapies that effectively prevent vein failures. Thrombosis (i.e. clotting) is a

typical cause of acute graft failures (within the first 30 days) whereas NH plays a dominant role in early vein failures (1 - 24 months) and contributes to atherosclerosis, the main cause of late-stage graft failures (2 years after surgery). NH is an excessive, pathological venous remodeling process in which myofibroblasts and vascular smooth muscle cells (VSMCs) migrate to the intimal layer and proliferate extensively, subsequently depositing extracellular matrix (ECM) proteins to form a "neointima".[43] Mitra et al. breaks down NH into five sequential events: 1) platelet activation, 2) inflammation and leukocyte recruitment, 3) coagulation, 4) VSMC migration and 5) proliferation (Figure 2-1).[44] Transdifferentiation of fibroblasts to myofibroblasts, and their subsequent migration and proliferation from the adventitia to the intima, are also involved in NH.[45, 46] Migration and proliferation of VSMCs and myofibroblasts and their deposition of ECM proteins culminates in stenosis of the graft/access that impedes blood flow, leads to disease progression, and increases the risk of adverse cardiac events, other complications, and death.

NH occurs as a result of intimal, medial, and adventitial damage to the vein graft before, during, and after surgery. In the case of CABG and PABG, significant endothelial and adventitial damage is also incurred from the vein harvesting process – as early as 4 hours after implantation, the endothelium is either denuded or attenuated with infiltrating inflammatory cells, other cells, and protein constituents present.[27, 47-49] Certain genetic factors, pre-existing NH, and medical conditions such as uremia in ESRD patients leave a patient predisposed to NH.[45, 50-53] During surgery, trauma from suturing damages all three layers of the vein wall.[51, 54] Injury and denuding of the protective endothelium exposes VSMCs directly to blood flow as well as pro-coagulatant and pro-inflammatory

constituents,[44] while damage to the adventitial vasa vasorum leads to hypoxia and subsequent NH development.[55-57] After surgery, exposure of the vein to an order of magnitude increase in pressure and flow in the arterial circulation causes abnormal distention of the vein, resulting in diameter mismatch between vein and artery, high tangential wall stresses, and low fluid shear stresses[58-61]. The vein walls thicken to normalize tangential shear stress regulated by the ratio of luminal radius to wall thickness.[62] Subsequent turbulent flow, especially around the distal (venous) anastomosis, damages the endothelium.[25, 50] In the case of hemodialysis patients, adventitial injury from repeated needling to perform dialysis and immune/inflammatory responses from PTFE implantation are thought to play a role in NH-mediated stenosis.[45, 51] Percutaneous techniques used to correct the ensuing obstructions in blood flow, namely balloon angioplasty and intraluminal stenting, have been shown to further damage the endothelium, adventitia, and perivascular tissue, thus promoting a proliferative and inflammatory response leading to recurrent stenosis.[63, 64] These procedures add pain and suffering to patients and are expensive, with balloon angioplasty alone adding more than $18,000 per patient-year for hemodialysis graft patients.[65] While placing an intraluminal stent has been shown to increase primary patency of AVGs from 23% to 46% over the first 6 months, 2 year patency remains very low at 9.5% compared to 4.5% for angioplasty alone.[66, 67] Poor clinical results such as those using the current standard-of-care, and the large expenses associated with their ineffective use, indicate the need for better therapies to prevent hemodialysis access and vein graft failure.

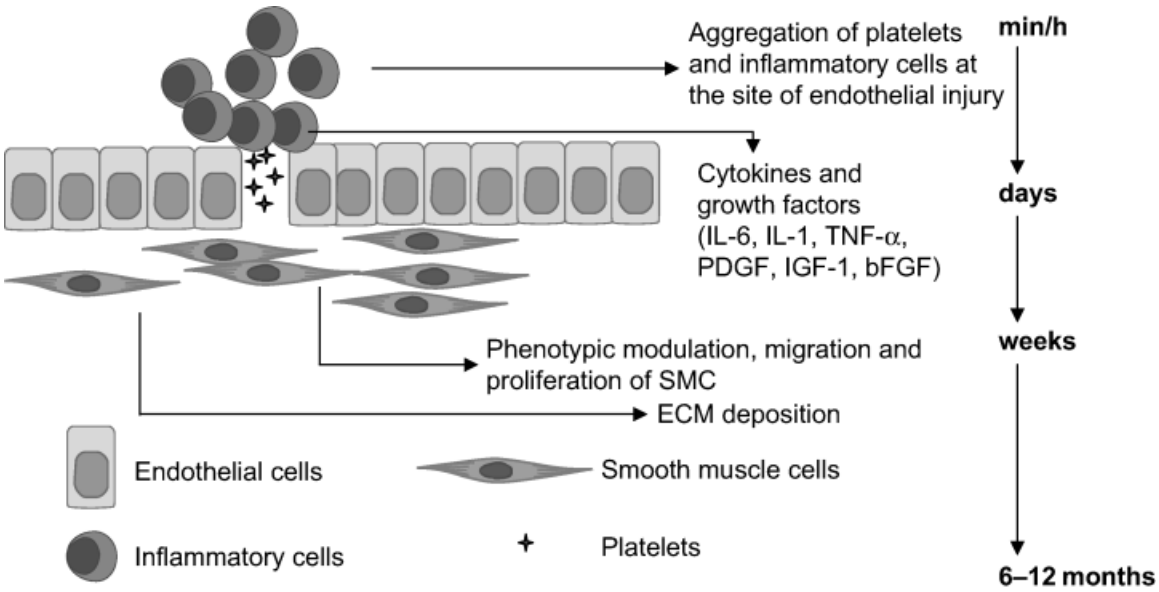


**Figure 2-1 Neointimal Hyperplasia**
Neointimal hyperplasia is triggered by injury at the time of surgery as well as from the high pressure and flow of the arterial environment. Endothelial injury exposes the VSMCs and subendothelial matrix containing tissue factor to the circulating blood, which activates platelets and causes their aggregation. Immune cells such as leukocytes and inflammatory cells are then recruited to the site, and a milieu of cytokines and growth factors are released from these cells. This causes a phenotypic switch in VSMCs that leads to their migration and proliferation into the intima along with myofibroblasts. An excessive amount of extracellular matrix milieu is also deposited into the intima from these migratory cells to form the neointima. Reproduced with permission.[44] Copyright 2006, Nature Publishing Group.

## 2.3 Use of Systemic Delivery of Therapeutics to Reduce Vein Failures

Current medical innovations used to sustain vein graft or hemodialysis access integrity have underperformed relative to desired long-term outcomes. Anti-platelet agents such as dipyridamole with aspirin inhibit thrombotic events and may improve early graft/access patency. In a study following angioplasty revision of SVGs in 343 CABG patients one year-post surgery, Chaser et al. revealed that dipyridamole plus aspirin treatments reduced SVG occlusions from 27% in the placebo to 16%.[32] In AVGs, this same treatment produced a modest, statistically significant improvement in one-year patency

compared to the placebo, from 23% to 28%.[68] However, Goldman et al. observed no effect on SVG patency 1 – 3 years post-CABG from these treatments,[69] and some studies have observed no benefit for SVGs of PABG patients.[70, 71] Some modest benefits of lipid-lowering agents (e.g. statins) on long-term SVG patency have been observed; a 1351 patient, 7.5 year Post CABG Trial revealed that moderate and aggressive administration of lipid-lowering drug lovastatin reduced revascularization procedures by 24% and 30%, respectively.[72] A 172 patient study demonstrated improved secondary patency of SVGs in PABG after 2 years with statin treatment (97% vs. 87% control),[73] but Pisoni et al. showed no improvement from statins in fistula or graft outcomes in a 601 hemodialysis patient study.[74] Antiplatelet agents and lipid-lowering drugs generally help and are part of the current CABG treatment paradigm,[75] but should not be considered "game-changers" on their own given the significant patency issues still reported with their administration.[58]

Cell cycle regulation is another possible approach to prevent NH. In a large, 1,404 patient study, an edifoligide oligonucleotide acting as a transcriptional cell cycle regulator of proliferation exhibited no patency benefit.[76, 77] This lack of efficacy despite drug functionality against a known NH target may suggest that sustained, localized release is required to make an impact. A one-time, localized application to the external surface of AVFs or AVGs with an aqueous solution containing vonapanitase (PRT-201®, Proteon Therapeutics), a recombinant human elastase that degrades elastin fibers to prevent NH, is one approach that has shown some promise to improve hemodialysis access patency and is currently in Phase III clinical trials.[78, 79] A plethora of other gene and drug delivery-based approaches have been investigated on the pre-clinical level and can be reviewed elsewhere.[80] In general, they aim to inhibit inflammatory, hypoxic, fibrotic, proliferative,

or migratory processes correlated with NH formation, or they promote vascularization to minimize hypoxia-induced effects. While positive effects have been observed in many of these animal models and in some clinical trials, the fact remains that there is no drug currently used on the market that effectively prevents vein graft or hemodialysis access failures on its own.

### 2.3.1 MK2i as a Pharmacological Agent

With its anti-fibrotic and anti-inflammatory properties (Figure 2-2), a mitogen-activated protein kinase (MAPK)-activated protein (MAPKAP) kinase 2 inhibitory peptide (MK2i) has shown promise as an agent to prevent intimal hyperplasia[23, 24]. MK2 phosphorylates transcription factors such as hnRNPA0 and tristetraprolin that interact with AU-rich regions of mRNA to control mRNA stability, particularly the stability of mRNA-encoding inflammatory cytokines. Inhibition of the phosphorylation of these transcription factors leads to degradation of the RNA that encodes these cytokines, thus reducing inflammation. MK2 also phosphorylates LIM kinase and HSP27, both of which have been implicated in stabilizing actin, the formation of actin stress fibers, and the development of the myofibroblast phenotype that leads to ECM production and fibrosis. MK2 is downstream of the TGFβ-p38 stress-activated protein kinase pathway, conferring specificity and limiting off-target toxicity. Thus, MK2 represents a unique target for the prevention of intimal hyperplasia. With this in mind, an inhibitor of MK2 (MK2i) was rationally designed and optimized based on the substrate (HSP27) binding site to the kinase[81] by collaborators at Purdue University. The peptide was rendered cell permeant by the covalent addition of an optimized protein transduction domain.[81]

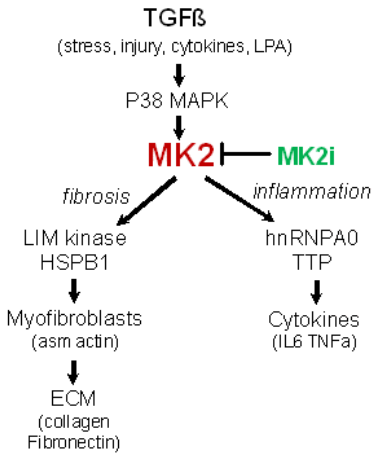


**Figure 2-2 MK2i inhibits MAPKAP Kinase II (MK2).**
MK2 is in the stress-activated protein kinase cascade. Stress, injury, TGFβ, cytokines and lysophosphatidic acid (LPA) activate p38 map kinase which in turn activates MK2. MK2 activates fibrotic pathways via LIM kinase and the small heat shock protein HSPB1 which lead to myofibroblast formation and the deposition of extracellular matrix (ECM). MK2 also activates hnRNPA0 and TTP, transcription factors which lead to cytokine production. Thus, MK2i inhibits both fibrosis and inflammation, two processes integral to the formation of the neointima.

Treatment of human saphenous veins (HSVs) with MK2i in an *ex vivo* organ culture model led to decreases in intimal thickening (Figure 2-3). In a murine inferior vena cava-to-aorta interposition model, a single 20 minute, 100 μM treatment of the vein graft prior to implantation decreased wall thickness by 72% at 28 days (Figure 2-4). Serial ultrasound evaluation of the grafts showed that while treatment with MK2i decreased intimal thickening, there remained progressive intimal thickening after the day 7 time point (Figure 2-5). This suggests a need for localized, sustained release of MK2i to more effectively minimize intimal hyperplasia.

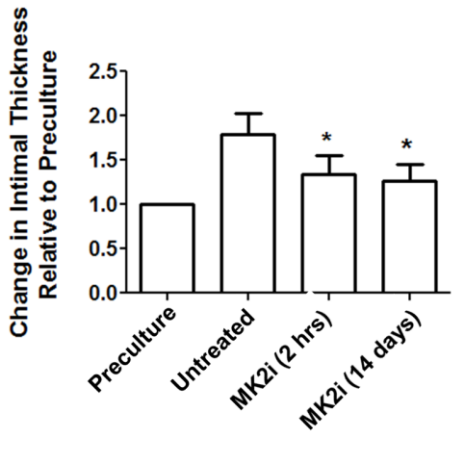


**Figure 2-3 Effect of MK2i on development of neointimal thickening in human saphenous vein**

Rings of human saphenous vein were cultured in RPMI medium supplemented with 30% fetal bovine serum for 14 days. The rings were either untreated (positive control) or treated with MK2i (50 µM) for either 2 hrs prior to organ culture or for 14 days with continuous treatment. After 14 days, rings were fixed in formalin, sectioned (5 µm) and stained using Verhoeff Van Gieson stain. Intimal thickening was measured morphometrically. * $p < 0.05$ compared to control, $n = 4 – 5$. Reproduced with permission.[25] Copyright 2012, Elsevier.

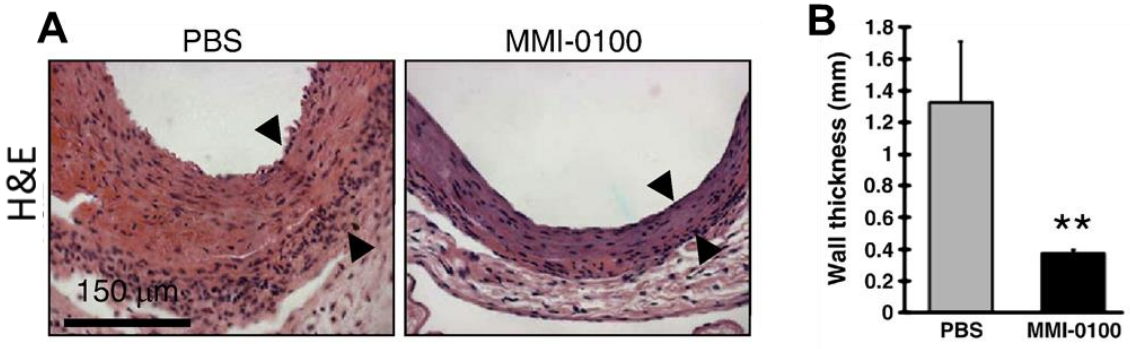


**Figure 2-4 Effect of MK2i on vein graft wall thickness in vivo.**

Vein grafts were either treated with 100 µM MK2i (i.e. MMI-0100) or saline (PBS) for 20 minutes prior to implantation in an inferior vena cava-to-aorta interposition model. A) Representative photomicrographs, with arrowheads indicating the internal elastic lamina separating medial and intimal layers. B) After 4 weeks, histological staining reveals a dramatic 72% decrease in wall thickness. ** $p < 0.05$, $n = 5 – 6$. Reproduced with permission.[25] Copyright 2012, Elsevier.

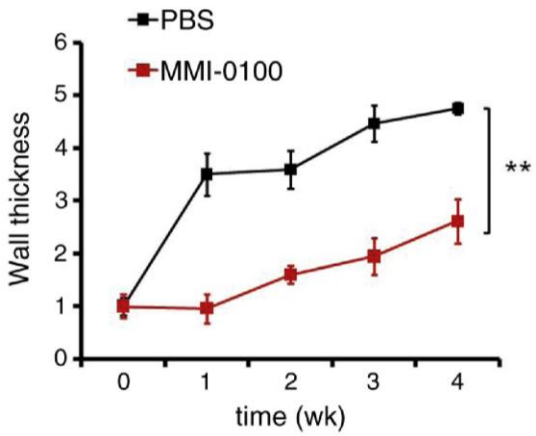


**Figure 2-5 Murine vein graft wall thickness over time.**
Ultrasound measurements of vein graft wall thickness over time compared to wall thickness at the time of implantation. **p < 0.0001 at 4 weeks. Reproduced with permission.[25] Copyright 2012, Elsevier.

## 2.4 External Stents

### 2.4.1 Seminal Studies of External Stenting

As vein graft disease is also defined by mechanical failures and drugs have not shown a great efficacy in preventing long-term failures, the biomedical community inquired if use of mechanical supports could reduce NH via external stents or sheaths comprised of a variety of materials. Parsonnet et al. became the first to apply external sheaths around vein grafts in 1963; their team observed that external sheaths comprised of knitted monofilament polypropylene fibers prevented over-distention of vein grafts and integrated into the host perivascular tissue in an end-to-end jugular vein-to-common carotid artery canine model.[82] The authors speculated that by preventing over-distention, the diameter of the vein could better match that of the artery and reduce turbulence that leads to thrombosis. Using the same canine model in 1978, Karayannacos et al. became the first to observe that an external mesh around a vein could reduce NH by preventing dilation of

the vein graft.[83] Given that the loose-fitting Dacron (poly(ethylene terephthalate)) meshes promoted a higher degree of neovasa vasorum and less intimal-medial thickness than a tightly woven Dacron sheath, the authors deduced that Dacron meshes reduced NH by promoting formation of neovasa vasorum that minimize ischemic conditions inducing VSMC proliferation. Going off of subsequent studies demonstrating the positive effect of constrictive meshes on jugular vein grafts to protect endothelium[84] and reduce cross-sectional wall area, VSMC volume, and matrix deposition compared to loose wraps,[85] Violaris et al. discovered that pig saphenous vein-to-carotid artery grafts constricted with a tight-fitting (4 mm diameter) PTFE graft had lower luminal cross-sectional area and greater NH, with only the media thinner.[86] This implied to the authors that restricting the ability of SVGs to distend may damage the adventitia and ultimately be disadvantageous. Following this result, Angelini et al. applied a nonrestrictive (6 mm diameter), highly porous Dacron stent helically wound with polypropylene in the same pig model.[5] Four weeks after implantation, the authors discovered that the lumen was larger, while the intima and media were almost four-fold thinner than the paired unstented control SVGs. Seeking to determine the ideal fit around the vein grafts, Angelini's team discovered in the same pig model[8] that the oversized (8 mm diameter) mesh performed better than the nonrestrictive (6 mm) mesh used earlier[5], and both of these sizes were superior to the mildly restrictive (5 mm) mesh in terms of both total wall thickness (in order of reducing diameter: 81%, 66% and 40% reduction compared to untreated control) and neointimal thickness (72%, 62% and 0% reduction for 8 mm, 6 mm, and 5 mm, respectively).[8]

Based on these findings, Mehta et al. applied the 8 mm Dacron mesh design to examine the underlying mechanism and long-term impact of external stent implantation in

pigs.[9] Compared to unstented controls, treated SVGs resulted in a significant reduction in intimal (93%) and medial (75%) thickness after 6 months (Figure 2-6). This correlated with decreases in cell proliferation in the intima and media of the stented grafts, as the proliferating cell nuclear antigen (PCNA) index of the unstented grafts were 18.7 and 3.9, respectively, compared to zero for both in the stented group (Figure 2-7A - B). PDGF, a potent mitogenic and chemotactic regulator of VSMCs,[87] was also significantly attenuated by 38 – 50% overall in the stented group at both 1 and 6 months (Figure 2-7C - F). Positive staining for endothelial cells by *Dolichos bifluorus* agglutinin (DBA) (Figure 2-8) and proliferating cells by PCNA (Figure 2-7A – B) in the adventitia of the stented group after 6 months indicates neovasa vasorum growth that is largely absent in the unstented grafts.

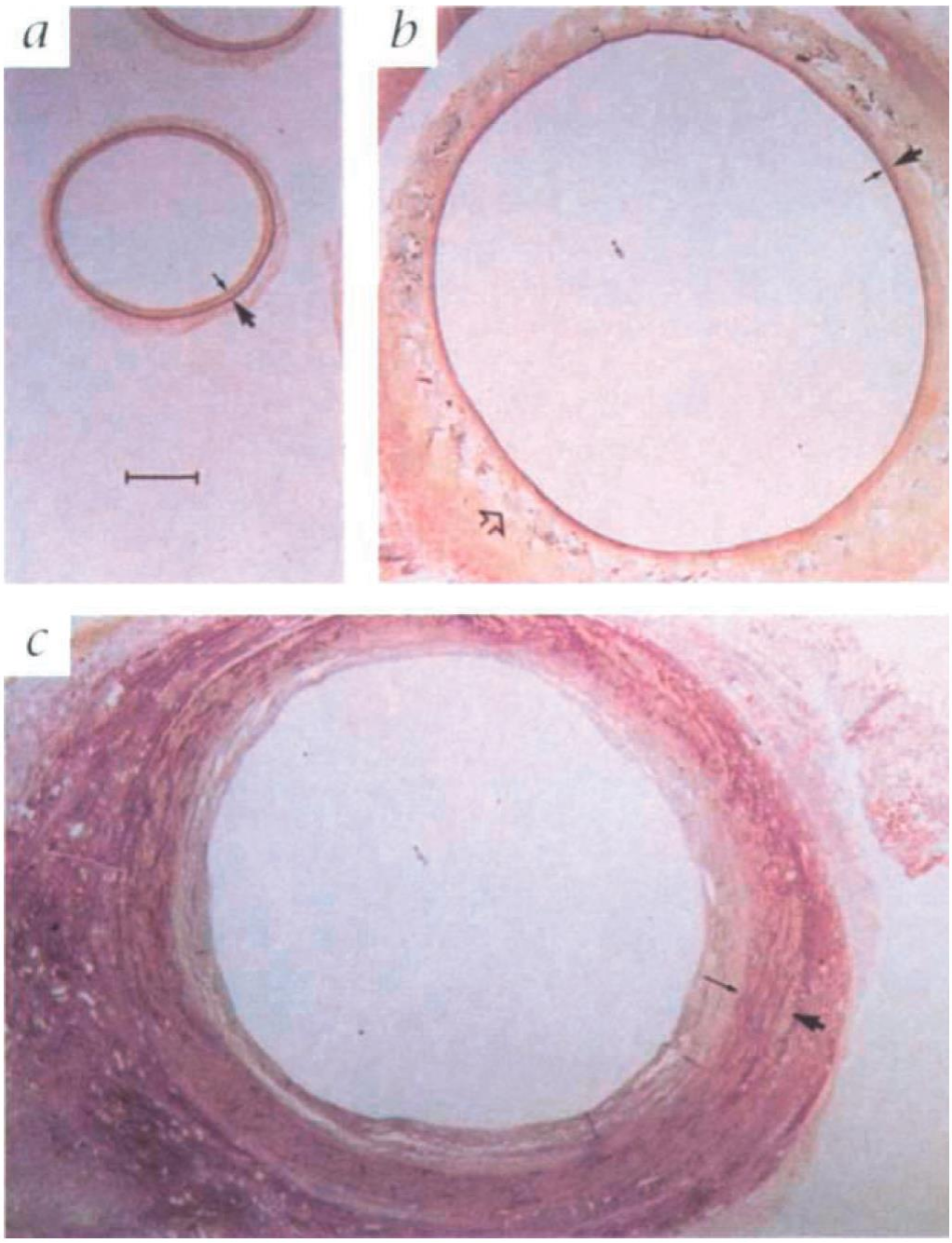


**Figure 2-6 Absence of intimal thickening from Dacron external stent treatment**
Histological sections from a) the ungrafted vein (negative control) compared to vein grafts 6 months after surgery that were either b) wrapped with an 8 mm Dacron external stent or c) unwrapped (positive control). Small arrows point out the internal elastic lamina defining the intimal-medial line, while the large arrow points out the external elastic lamina defining the boundary between medial and adventitial layers. Pronounced intimal and medial thickening in the untreated control is largely absent in the stented graft. Reproduced with permission. Copyright 1998, Nature Publishing Group.[9]

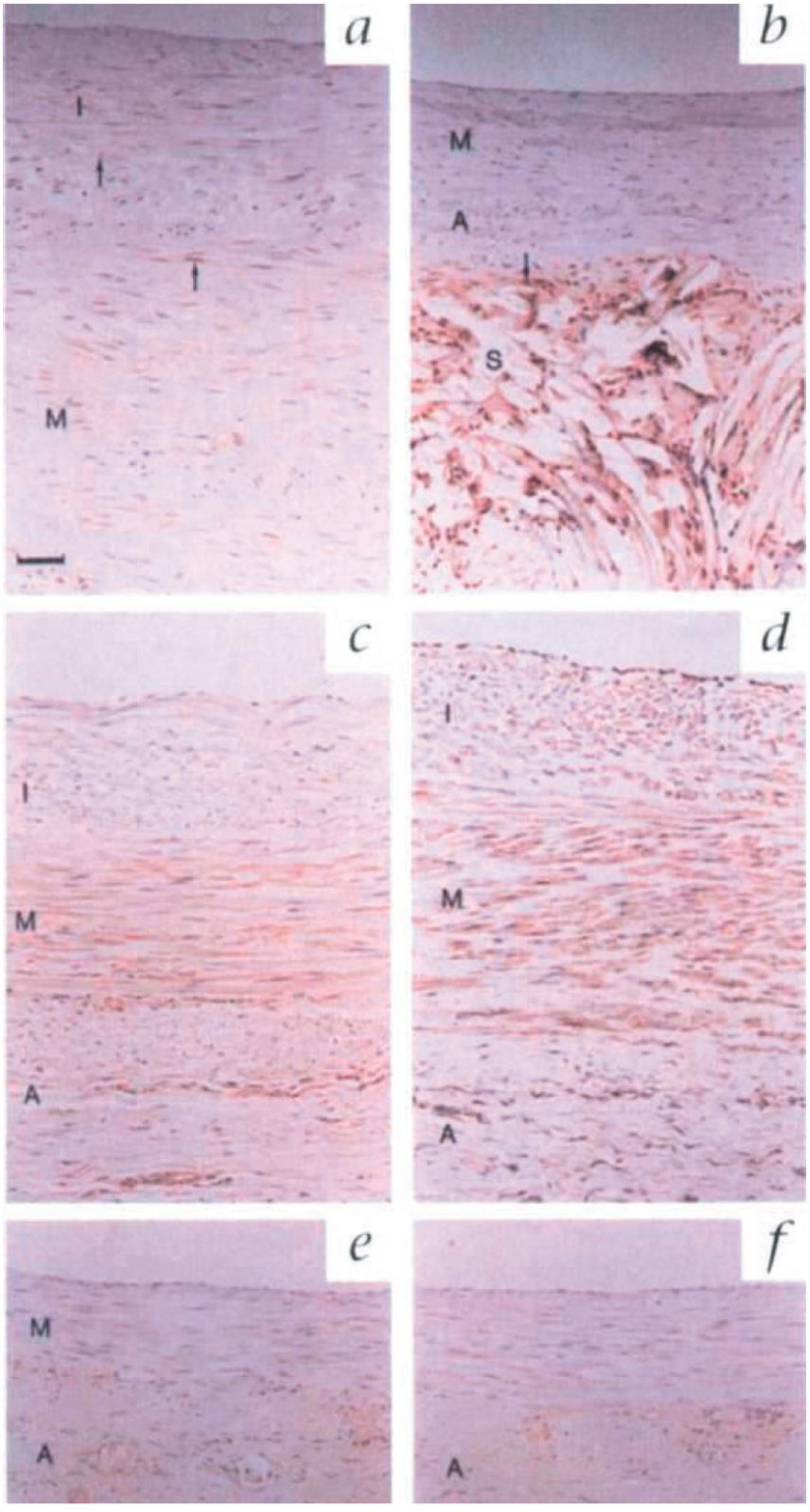


**Figure 2-7 Extensive adventitial proliferation from Dacron external stent treatment**
Immunohistochemical staining for proliferating cell nuclear antigen (PCNA) in a) an unstented and b) a stented graft after 6 months. Marked brown nuclear staining is present in the adventitia but not the media of stented grafts, indicating significant adventitial

proliferation forming the neoadventitia. Immunohistochemical staining for total PDGF protein (brown staining) in unstented grafts after c) 1 month and d) 6 months compared to stented grafts at e) 1 month and f) 6 months reveals increased PDGF staining in the untreated group, indicating extensive proliferation in the adventitia of stented grafts. Scale bars in a) and c) apply to the entire panel and represent 50 μm. Reproduced with permission. Copyright 1998, Nature Publishing Group.[9]

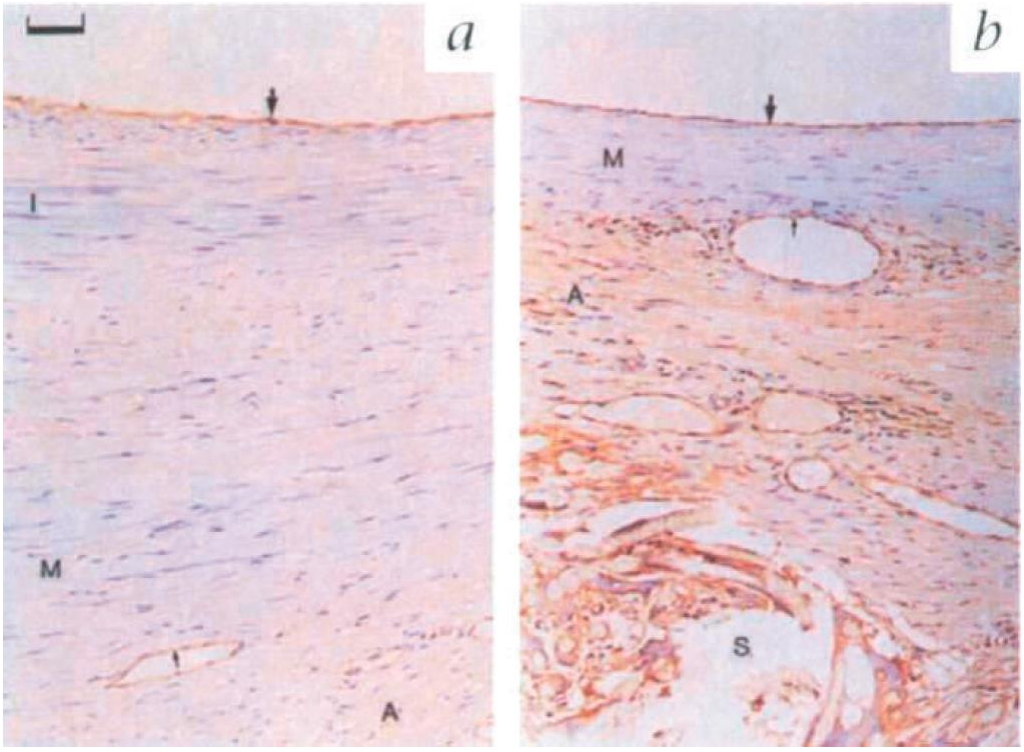


**Figure 2-8 Dacron external stent treatment induces adventitial vessel growth to form a neoadventitia**
*Dolichos bifluorus* agglutinin (DBA) staining demonstrating an intact luminal endothelium (large arrow) in both a) unstented and b) externally stented grafts after 6 months. Pronounced brown cytoplasmic staining in the adventitia of stented grafts indicates the presence of endothelial-lined vessel growth comprising a neoadventitia. Reproduced with permission. Copyright 1998, Nature Publishing Group.[9]

To understand the role of pore size on NH, the 8 mm macroporous Dacron mesh and an 8 mm microporous PTFE were implanted in the same pig model[7]. One month after surgery, pig SVGs treated with the macroporous stents exhibited a greater reduction in NH (Figure 2-9) that accompanied an increase in adventitial microvessel growth (Figure 2-10) and a decrease in PDGF expression and cell proliferation, suggesting the need for

macroporosity. Further mechanistic insights were gleaned in 2002 from a hypocholesterolemic pig model to better mimic vascular disease conditions.[6] After 3 months, mesh-mediated reductions in SVG NH correlated with significant reductions in graft cholesterol concentrations and atheroma markers, as well as vascular cell adhesion molecule 1 (VCAM-1) in the absence of atheroma precursor foam cells. This suggested that the macroporous Dacron stent can potentially inhibit both NH and atherosclerosis.

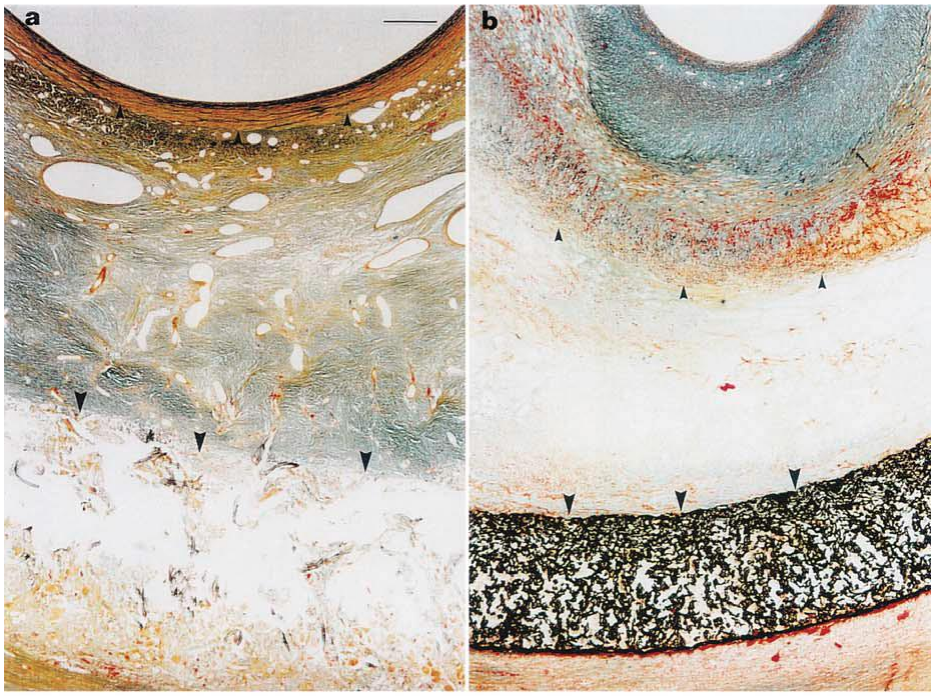


Fig. 1

**Figure 2-9 Dramatic morphometric differences in saphenous vein grafts treated with two different external stents**

Trichrome staining of porcine SVGs after one month wrapped with a) an 8 mm loos-fitting macroporous Dacron stent and b) an 8 mm loose-fitting microporous PTFE. The internal elastic lamina marked by small arrows and the external elastic lamina marked by large arrows clearly shows a large reduction in NH with the macroporous Dacron stents compared to the PTFE stent. The neointima in the PTFE-wrapped SVGs is highly collagenous, as indicated by the green-blue staining. Orange/brown staining represents VSMCs. There are large, abundant microvessels present in the Dacron-treated grafts, whereas the microvessels in b) are clearly absent, with no large microvessels outside the stent. Scale bare in a) applies to b) as well, and represents 50 mm. Reproduced with permission.[88] Copyright 2001, Elsevier.

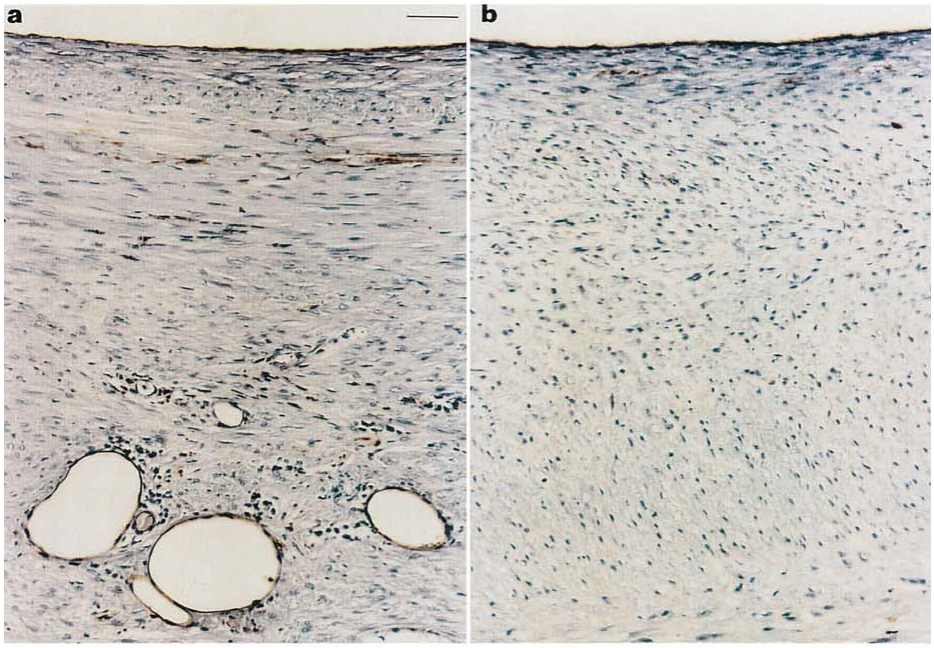


Fig. 2

**Figure 2-10 Macroporous Dacron external stent induces adventitial microvessel growth.**
Endothelial staining with lectin A demonstrates a marked increase in microvessels present in the adventitia of a) the macroporous Dacron stent, while b) this is absent in the microporous PTFE stent. Scale bare in a) applies to b) as well, and represents 50 mm. Reproduced with permission.[88] Copyright 2001, Elsevier.

### 2.4.2 Disappointing Clinical Trials with Dacron Meshes

Although these results are informative and promising, the first external Dacron stent clinical trial ended tragically, and a subsequent trial in 2011 using a different Dacron stent (ProVena®, B. Braun) (Figure 2-11) to reinforce varicose or ectatic vein grafts in PABG patients demonstrated no patency benefit 24 months after surgery (Table 2-1).[89] In the 2007 Extent study, an external Dacron stent reinforced with PTFE ribs spaced 1 cm apart (Extent®, Vascutek Inc.) (Figure 2-12) was implanted over the SVGs of 20 CABG patients, resulting in thrombosis for every patient within 6 months.[14] The authors were transparent that these failures could be the result of fatal miscalculations in the material selection or scaffold design that render inappropriate mechanical strength (e.g. too rigid or

too soft), stent-to-vein spacing (e.g. under or oversizing), or unforeseen complications (e.g. kinking of the graft). It is therefore prudent to consider and understand the function and tradeoffs of each component of the external stent design at the research stage in order to avoid making such costly mistakes in the clinic, beginning with the material selection. Alteration of external stent properties by material selection, mesh type (e.g. knitted, warp-knitted, woven, nonwoven, electrospun, ablated sheets)[90] or geometric design can be considered "passive" approaches to stent design, whereas incorporation of therapeutic agents and/or surface modifications can be described as "active" design approaches (Figure 2-13). By mastering passive design approaches, first-generation therapies can be created that effectively prevent vein graft or hemodialysis access failure with the possibility of lower regulatory hurdles relative to drug alone or drug-device combination products. The opportunity then exists to improve upon these initial methodologies with later generation products that incorporate active approaches.

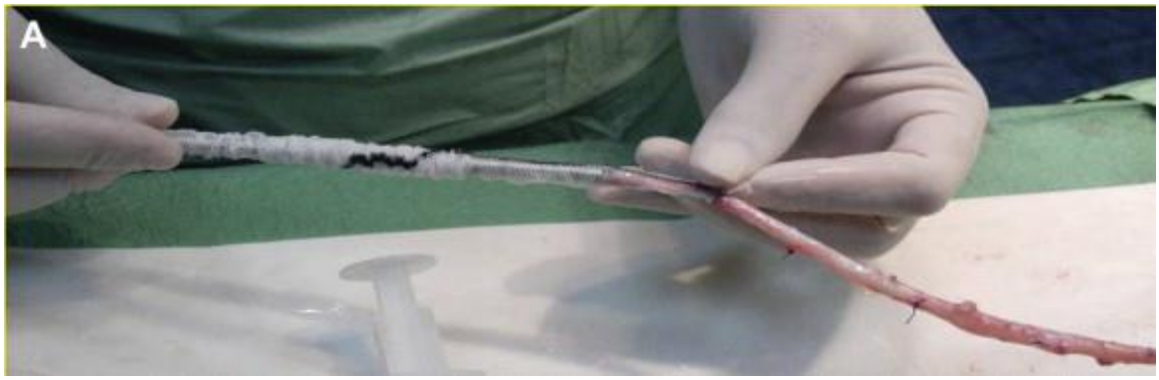


**Figure 2-11 Provena, a macroporous Dacron mesh**
Wrapping of the saphenous vein to bypass between superficial femoral to posterior tibial artery with ProVena®, a macroporous Dacron mesh. Reproduced with permission.[89] Copyright 2011, Elsevier.

**Figure 2-12 Extent, a macroporous Dacron sheath reinforced with PTFE ribs**
Extent®, a macroporous Dacron sheath reinforced with PTFE ribs. The flange permitted placement after completion of both anastomoses. Reproduced with permission.[14] Copyright 2007, Elsevier.

**Table 2-1 Recent Clinical Trials Utilizing External Supports and/or Localized Therapeutics**

| Technology | Intended use, Reference (Year) | Outcome |
|---|---|---|
| Dacron reinforced with PTFE ribs spaced 1 cm apart (Extent®, Vascutek Inc.) | Saphenous vein grafts of CABG patients, Murphy et al. (2007).[14] | Thrombosis observed in all 20 CABG patients within 6 months. |
| Dacron mesh with 750 μm pores (ProVena®, B. Braun) | Varicose or ectatic vein grafts utilized in peripheral bypass patients, Carella et al. (2011).[89] | Safety demonstrated in initial trial, but no patency benefit observed in 21 treated patients compared to untreated control group. |
| Nitinol mesh (eSVS Mesh®, Kips Bay Medical) | Saphenous vein grafts in CABG patients, Emery et al. (2015).[91] | Clinical trial terminated in September 2015 due to low patency rates |
| Braided Phynox mesh (Fluent®, Vascular Graft Solutions) | Saphenous vein grafts of CABG patients, Taggart et al. (2015).[92] | Reduced intimal hyperplasia, less ectasia, and more lumen uniformity observed after 1 year in 30 patient trial. |
| Nitinol mesh (VasQ®, Laminate Medical) | Arteriovenous fistula anastomoses, Chemla et al. (2016).[93] | Adequate safety with high maturation and patency rates observed after 6 months in 20 patient trial. |
| Replication-deficient adenoviral vector expressing a VEGF-D gene localized to the anastomosis with a collagen collar (Trinam®, Ark Therapeutics Group) | Arteriovenous graft (PTFE-vein) anastomoses of hemodialysis patients, Fuster et al. (2001).[94] | Phase III trial was terminated due to "strategic reasons" in November 2010. |
| Collagen gel loaded with allogenic endothelial cells (Vascugel®, Shire Pharmaceuticals) | Arteriovenous graft or fistula anastomoses of hemodialysis patients, Conte et al. (2009).[95] | No patency benefit demonstrated in two Phase II clinical trials, one of these studies was terminated in October 2014. No longer an active program at Shire. |
| Nonbiodegradable ethylene vinyl acetate wrap eluting paclitaxel (Vascular Wrap®, Angiotech Pharmaceuticals) | Arteriovenous graft (PTFE-vein) anastomoses in hemodialysis patients. Initially applied to PTFE-vein anastomoses of patients undergoing peripheral bypass surgeries, Mátyás et al. (2008).[96] | Phase III clinical trial terminated in April 2009 due to a higher infection rate in the treated group, with no demonstrated patency benefit. Initial trial in peripheral bypass patients showed lower amputation rates in treated group. |
| Sirolimus-eluting collagen membrane (Coll-R®, Vascular Therapies) | Arteriovenous graft or fistula anastomoses of hemodialysis patients, Paulson et al. (2008).[97] | Safety and technical feasibility demonstrated in Phase I/II trial. Currently recruiting patients for Phase III trial. |

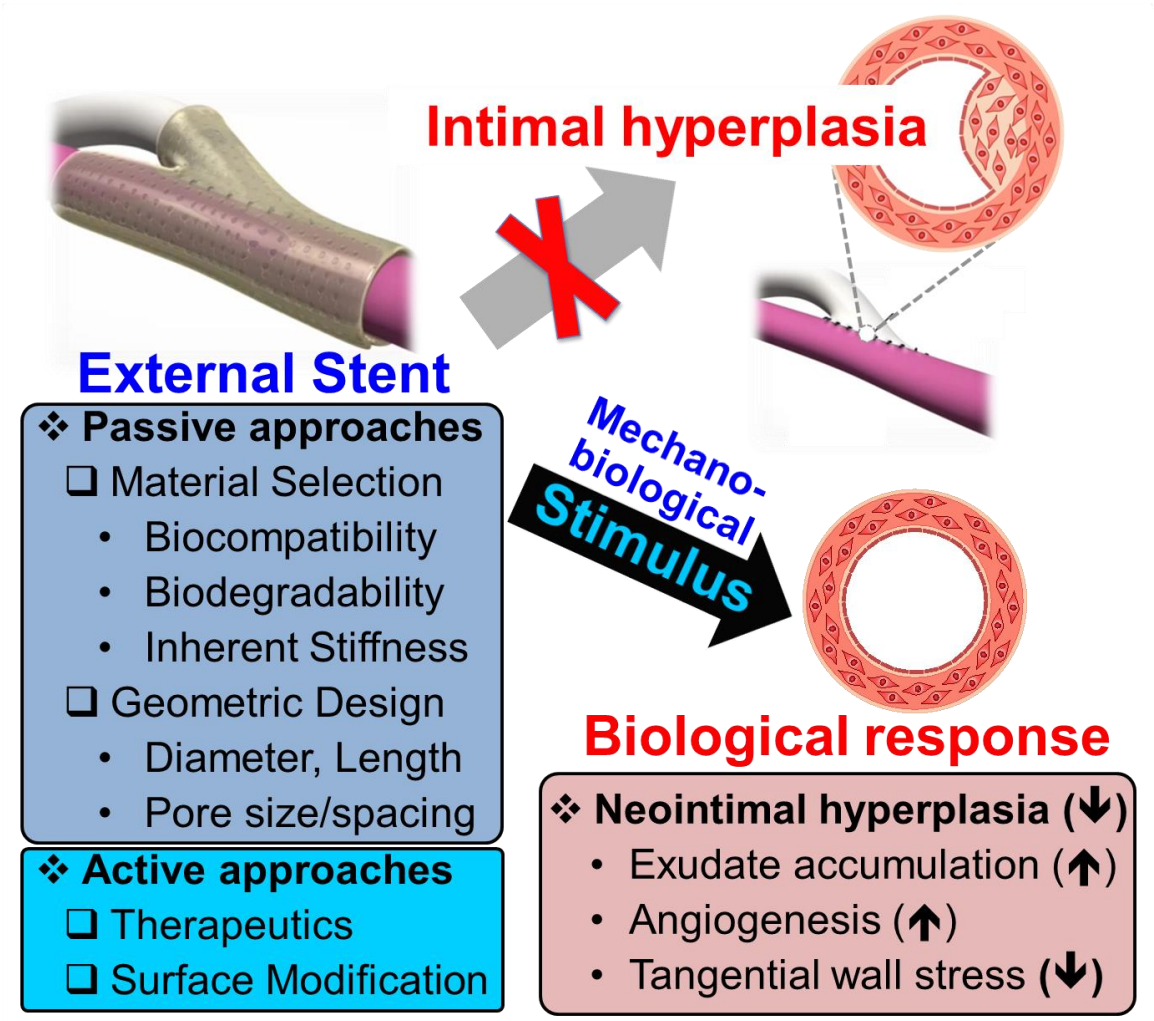


**Figure 2-13 Design consideration for external stents**
External stents have demonstrated an ability to reduce neointimal hyperplasia by promoting exudate accumulation in the interstitial space between the graft and stent, promoting adventitial angiogenesis, and reducing tangential wall stress. The external stent design should be carefully considered to maximize vein graft and hemodialysis access patency. Passive design approaches take into account material selection and device geometry. Active approaches incorporate therapeutics and/or modify the surface to change the bioactivity of the external stent. Reproduced with permission.[272] Copyright 2016, John Wiley & Sons.

## 2.5 Design Considerations for External Stenting

### 2.5.1 Passive Approaches – Material and Geometric Design Considerations

#### 2.5.1.1 Seminal Studies Shifting from Nondegradable to Biodegradable External Stents

The type of material selected will influence the biodegradability, biocompatibility, and mechanical properties of the device, among other considerations.[91-93] Like the other materials used as external sheaths at the turn of the 21st century such as Nitinol[10, 11, 94] and Phynox (a wrought Cobalt-Chromium-Nickel-Molybdenum-Iron Alloy)[95-98] metals or polymers such as polypropylene[82] or ePTFE,[85, 99-103] Dacron is nonbiodegradable. This is of concern because long-term implantation of nondegradable material carries a greater risk of infection, chronic inflammation, and/or compliance mismatches at different interfaces.[104-111] In contrast, hydrolytically degradable polyesters such as polyglactin (PGA) and poly(ε-caprolactone) (PCL), natural polymers (e.g. collagen or hyaluronic acid), or combinations thereof meet this criterion in addition to exhibiting good biocompatibility.[93] In 2004, Jeremy et al. and Vijayan et al. became the first researchers to employ a biodegradable material for external stenting of SVGs (Figure 2-14).[106, 107] In two separate studies, they demonstrated the ability of a PGA sheath to prevent neointimal and medial thickness in a bilateral saphenous vein-to-common carotid artery interposition graft model.[106, 107] Not only was there an effect in the one month following surgery when the PGA device was still intact,[106] but also well after its presumed 60 - 90 day degradation period[112, 113] at 6 months.[107] An abundance of inflammatory cells such as macrophages and giant cells, as well as endothelial cells, VSMCs, and microvessels in and around the material, were observed at both 1 and 6 months (Figure 2-15**,** Figure 2-16**,** Figure 2-17). These cells, particularly the macrophages and giant cells, accelerate degradation of the scaffold. The authors also postulated that the battery of chemokines and growth factors

released by these cells could help to attract VSMC migration towards the external stent instead of the intima while simultaneously spurring angiogenesis that prevents hypoxia (Figure 2-18). However, it stands to reason that a careful balance of this phenomena should be reached, as the authors concede that such an intense biological response as that seen at 6 months is partially fibrotic and can lead to encapsulation of the scaffold with fibrotic tissue[107] that could result in complications for a patient.[114, 115] A strong inflammatory response could also trigger NH and/or thicken the vessel enough that hypoxia-induced NH becomes an issue.[56, 57, 80]

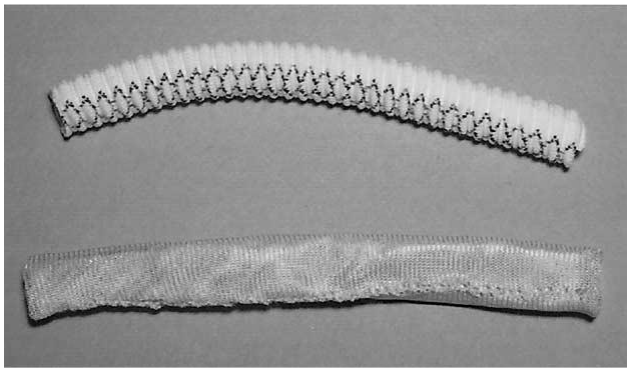

**Figure 2-14 Dacron and polyglactin external stents**
A Dacron external sheath (top) as compared to polyglactin sheath from Vascutek Ltd (bottom). Both are 8 mm in diameter. Reproduced with permission.[106] Copyright 2004, Elsevier.

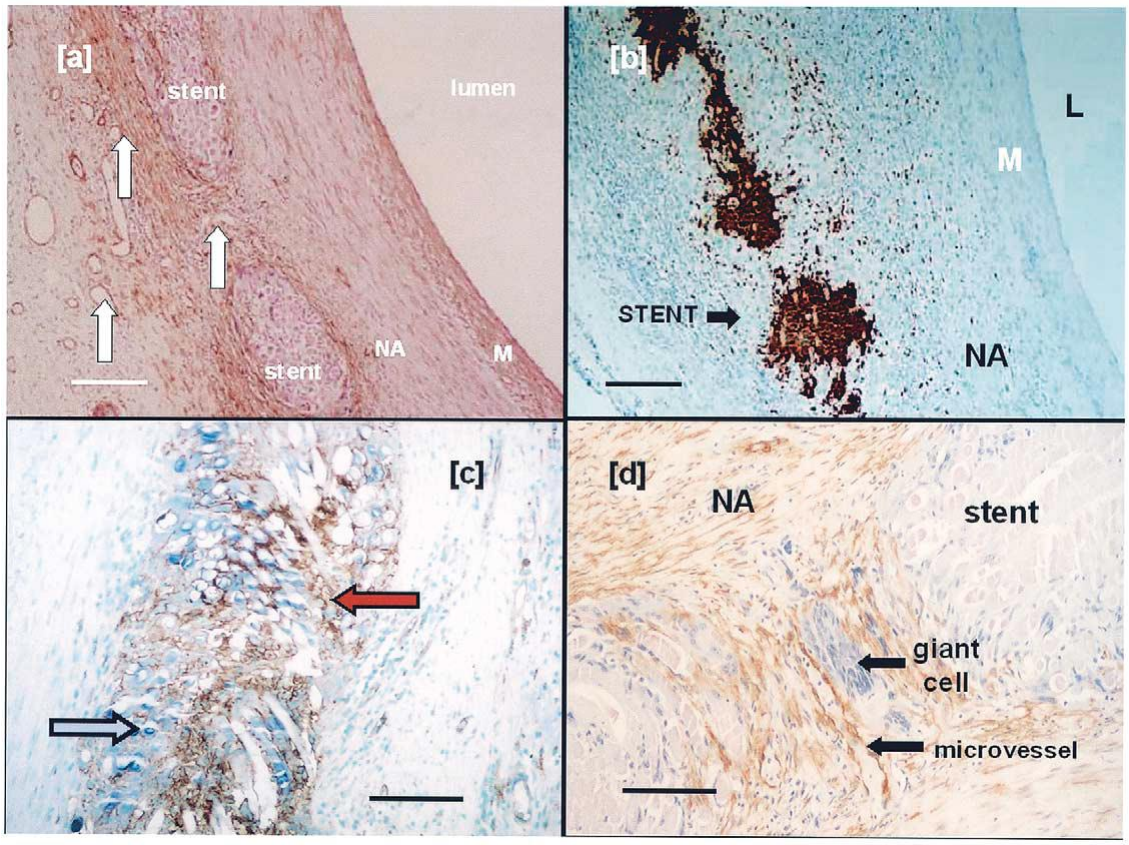


**Figure 2-15 Porcine vein graft responses to PGA external stent treatment**
Photomicrographs of pig SVGs fitted with an 8 mm PGA external stent after one month. In and around the PGA sheath, there is a high density of a) microvessels (white arrows), b) macrophages as revealed by immunostaining for MAC387, c) endothelial cells (blue arrow) and proliferating cells (PCNA positive, red arrow). Immunostaining for d) α-actin (brown) and giant cells (purple) reveals that VSMCs and giant cells have also accumulated in the interstitial space. In contrast, microvessels, macrophages, endothelial cells, and proliferating cells are largely absent in the media of the graft. Scale bar for 100 μm for a) and b), and 50 μm for c) and d). Reproduced with permission.[106] Copyright 2004, Elsevier.

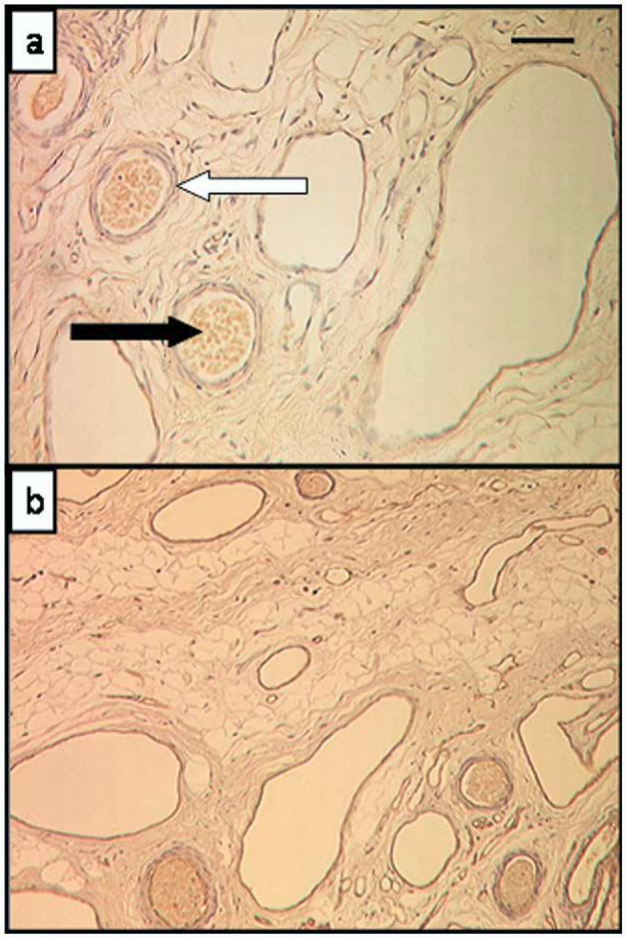


**Figure 2-16 Neoadventitial growth from PGA external stent treatment**
After one month treatment of pig SVGs with the PGA external stent, a notable neoadventitia has formed with endothelial cells lining microvessels and undergoing active angiogenesis. a) Lectin staining (brown) reveals a prominence of adventitial endothelial cells. The black arrow shows blood cells filling microvessels, while some VSMCs surround endothelial cells (white arrow). b) VEGF is also present, indicating active angiogenesis is taking place. Scale bar 50 μm. Reproduced with permission.[107] Copyright 2004, Elsevier.

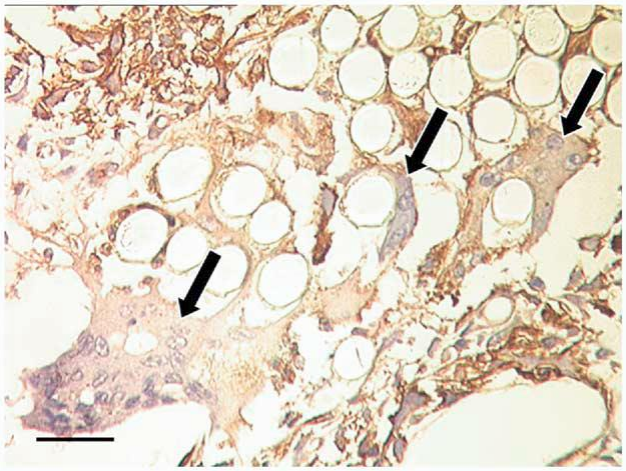

**Figure 2-17 Multilobed giant cells present within interstitial space from PGA external stent application**

A PGA external stent fitted around pig SVGs after one month demonstrates multilobed giant cells (arrows) with dark blue nuclei located within the interstitial space. Reproduced with permission.[107] Copyright 2004, Elsevier.

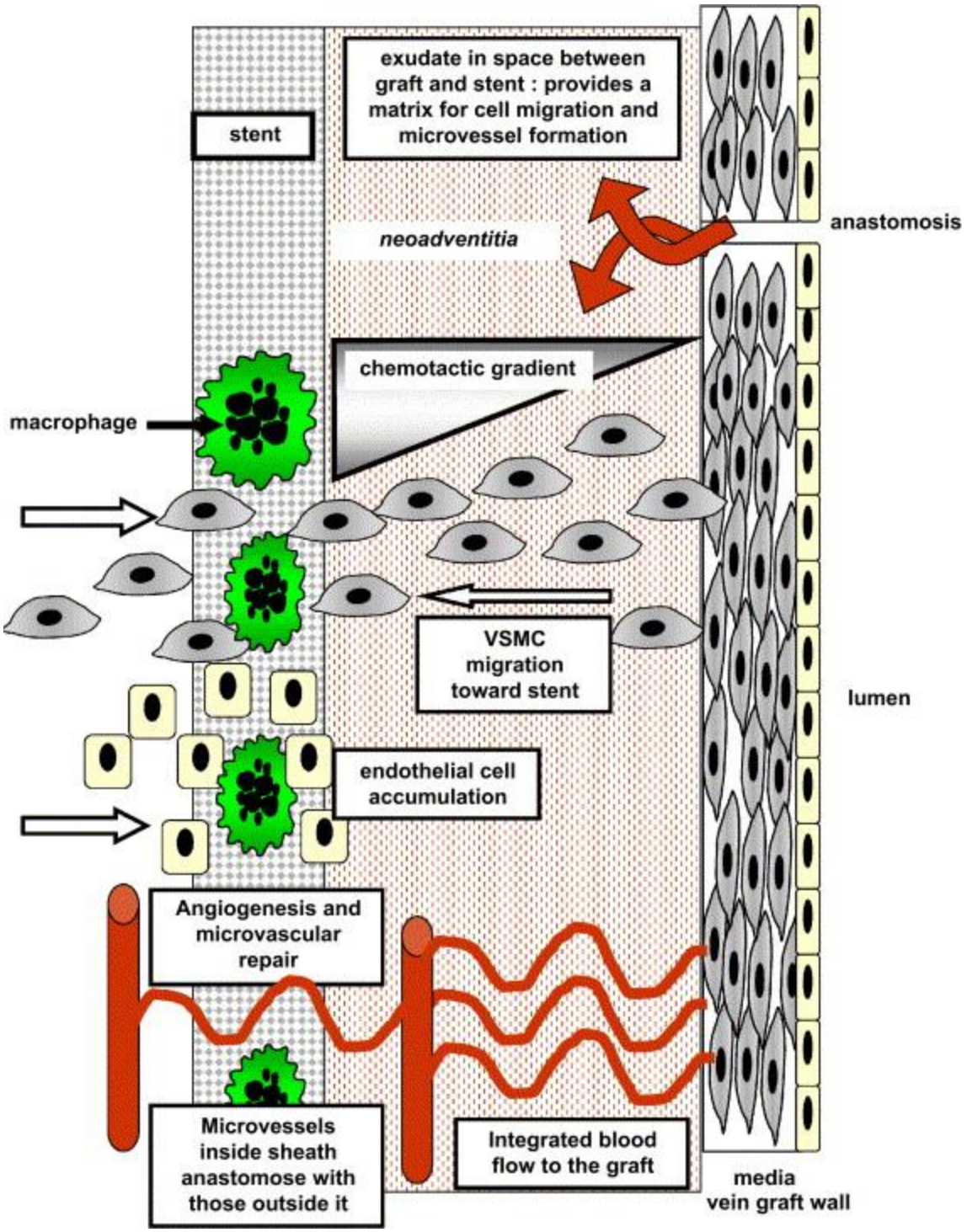


**Figure 2-18 Speculative mechanism of action of external stent treatment deduced by Jeremy et al.**

Schematic illustrating the main events stipulated to be responsible for the ability of external stents to reduce NH. First, an exudate forms in the interstitial space between the graft and sheath. The fibrin-rich exudate may trigger adventitial angiogenesis and promote cell migration. Second, macrophage and giant cell infiltration creates a chemotactic gradient, promoting VSMC migration from the media to the sheath. As endothelial cells are also

drawn to the external stent by chemotaxis, they can act as building blocks along with VSMCs to promote neovasa vasorum formation. The neovasa vasorum is then further promoted by the battery of angiogenic factors that are secreted by the infiltration macrophages and giant cells. Reproduced with permission.[116] Copyright 2007, Elsevier.

#### 2.5.1.2 Bodily Response to Implantation

Like any other implant, implantation of an external stent around the vein results in some degree of injury to the surrounding tissue that perturbs homeostasis and results in a complex wound healing response.[91] As alluded to earlier, the intensity and duration of this inflammatory response may play an important role in the function of the external stent and defines the biocompatibility of the device. Physicochemical and geometric properties of the external stent partially govern this response, which is characterized by the degree of acute inflammation, chronic inflammation, granulation tissue formation, foreign body reaction, and fibrosis.[91] The foreign body reaction, comprised of foreign body giant cells and granulation tissue (i.e. macrophages, fibroblasts, capillaries), is a critical step in the type of biological response elicited and is highly dependent upon the topology and surface chemistry of the implant. These properties mediate the type and quantity of proteins adsorbed on the surface of the substrate, which provide ligands for monocyte or macrophage attachment and may also signal the macrophage fusion process that generates foreign body giant cells.[91]

It is unclear what degree of inflammation and foreign body reaction is ideal for external stenting. However, it has been shown that complement and mast cells migrate onto NH-reducing macroporous polyester sheaths and deposit ECM proteins. Lymphocytes, neutrophils, giant cells, and T-cells were shown to be entrapped by these sheaths,[7] but not with the ineffective microporous ePTFE stents.[83, 117] In general, substrates with higher surface area-to-volume ratios such as porous materials exhibit higher ratios of macrophages

and foreign body giant cells, whereas smooth surfaces with low surface area-to-volume ratios exhibit a significant degree of fibrosis. From this perspective, porous substrates may be preferable to nonporous or less porous ones as fibrosis is intrinsically linked to NH,[115] but a balanced response is desired for a normal wound healing process to occur.[90] As meshes tend to be highly porous, comparative studies in the hernia repair environment have shown that the foreign body reaction is fairly uniform regardless of mesh type, but different raw materials affect the extent of the reaction.[90, 118] Studies comparing inflammatory responses between different materials are limited. In one such study, Dacron meshes exhibited the greatest foreign body reaction and chronic inflammatory response compared to ePTFE and polypropylene meshes in a mouse subcutaneous implantation model.[119] Meanwhile, ePTFE meshes were encapsulated with fibrotic tissue, exhibiting a significant amount of fibrosis at 12 weeks. Of the three materials compared, polypropylene exhibited the greatest biocompatibility, with less fibrosis and foreign body reaction. Coating polypropylene with a rapidly degrading material such as polyglactin increased inflammation after 40 days in a rat abdominal wall implantation model,[120] supporting the notion that degradation products elicit inflammatory responses. Of course, the nature of these degradation products and the rate by which the polymer is degraded will influence the type of inflammatory response observed. The nature of degradation products is determined by the material selected, whereas the rate of degradation is also influenced by the polymer's molecular weight, crystallinity, and porosity.[92, 121] In concert with studies that elucidate optimal inflammatory responses for external stenting, biocompatible, biodegradable materials can be devised that minimize NH and vein failures by promoting some degree of adventitial angiogenesis and meeting other axiomatic criterion.

#### 2.5.1.3 Choosing Biomaterials Based on Biodegradation Timescale

Fundamentally, implanted materials should not evoke a toxic or exacerbated inflammatory response and should have a degradation profile and mechanical properties that match the adaptive needs of the vein in the arterial circulation.[93] While the critical adaptive period of vein grafts is not exactly known and may vary depending on the patient, vein wall thickening has been shown to continue for over 12 weeks into arterial exposure in a rabbit jugular vein-to-carotid artery model.[4] Although further study may be required to verify whether wall kinetics in CABG, PABG, and ESRD patients precisely resemble this timeline, this suggests that a sheath should remain relatively intact for at least 3 months. PGA loses its strength when hydrolyzed over 1 – 2 months, as well as polydioxanone (PDX),[92] and therefore may not be ideal materials through the completion of vein remodeling around 3 months. Mechanical integrity is not an issue for nondegradable materials such as Dacron or metals but, as previously discussed, these types of implants carry a greater risk of infection, compliance mismatches, or other complications. Materials that degrade more slowly than PGA may provide a happy medium between biodegradability and mechanical integrity. For example, copolymers of PGA (85/15 poly(lactic-co-glycolic acid) (PLGA)) and PDX (50:50 poly(dioxanone-co-cyclohexanone) (PDS)) degrade over 5 – 6 months,[93, 122] which may be a sufficient amount of time to provide mechanical support. On the other hand, PCL degrades very slowly (2 – 3 years), and since some studies suggest degradation can act as a chemoattractant for external migration of VSMCs,[106, 107] it may be desirable to reduce the degradation time. This can be done with a 75/25 poly(ι-lactide-co-ε-caprolactone) (P(LA/CL) copolymer that has approximately 95% of its mass remaining 3 months after rat implantation.[123] The potential of these approaches for external stenting has not been extensively explored.[124-126]

Recently, Sato et al. examined 6 – 12 month patencies in 24 canine femoral vein-to-femoral artery interposition grafts reinforced with either a loose (8 mm) 75/25 poly(ι-lactide-co-ε-caprolactone) (P(LA/CL)) mesh, a nonabsorbable stent, or no stent (control).[126] The 6 - 12 month patencies for the P(LA/CL)-treated grafts (100%) were significantly better than both the nonabsorbable stent group (72.2%) and control groups (63.6%) despite the absorbable and nonabsorbable groups exhibiting equivalent NH reduction relative to control. The authors speculated that the more variable luminal perimeters and intimal-medial thicknesses for the nonabsorbable group may suggest that compliance mismatches played a role in the lower patency rates for this group. Follow-up studies examining potential flow disturbances will be needed to verify this claim.

#### 2.5.1.4 Type and Amount of Mechanical Support Provided by External Stents

Another important consideration for an external stent is the amount of mechanical support that it provides to the thin, compliant venous walls in the high pressure, high flow arterial environment. Preventing overdistention of the vein was hypothesized in early studies as one way to avert structural collapse by limiting turbulence caused by diameter mismatches between vein and artery.[82-85] Upon examination of several mechanical factors involved in wall thickening in canine autogenous vein grafts, Dobrin et al. observed that intimal and medial thickening associated most with low fluid shear stress and distention, respectively.[62] Likewise, Kohler et al. postulated that external supports preventing distention limit wall thickening because these hyperplastic responses are regulated in part by tangential wall stress - the ratio of luminal radius to wall thickness.[85] However, Violaris et al. showed in a pig SVG model that constrictive 4 mm PTFE external stents lowered the luminal cross-sectional area and increased NH despite medial thinning, which may

compromise blood flow through the graft.[86] Comparing pig SVG responses to 4, 6, and 8 mm Dacron sheaths, Izzat et al. demonstrated that loose-fitting Dacron meshes 8 mm in diameter exhibit the greatest attenuation of NH.[8] Since this time, numerous studies have adopted these findings to show the positive effects of loose-fitting external meshes to improve patencies and reduce NH.[6, 7, 9, 106, 107, 126] In these studies, the luminal area of stented grafts tended to increase to areas close to that of the carotid artery that it was replacing. Although some unstented grafts dilated while others did not relative to treated grafts, untreated grafts were consistently far thicker in terms of total wall thickness, with more NH and luminal encroachment. External stents did not suppress or restrict dilation, as the total cross-sectional areas (luminal + wall) were similar between untreated and treated grafts, but did promote interstitial adventitial growth between the graft and stent. Taken together, these observations imply that the adventitial growth promoted by external stenting may absorb some of the wall stresses experienced by the vein. The role of the neoadventitia in reducing wall tension may help explain why both constrictive metal meshes[10, 11, 94, 97, 98, 127-129] and loose-fitting polymeric approaches promoting adventitial angiogenesis can reduce NH. Metal based approaches have been shown to reduce wall tension, asymmetric wall thickening, and turbulence without promoting vascularization,[94, 97, 98, 127-132] but may ultimately suffer from fibrotic responses (Figure 2-19) and tissue buckling or kinking.[10] Although there is some promise with ongoing clinical trials utilizing a braided Phynox mesh (Fluent®, Vascular Graft Solutions)[97, 129] to support vein grafts in CABG and a Nitinol mesh to support fistulas for hemodialysis patients (VasQ®, Laminate Medical),[133] a recent clinical trial reinforcing vein grafts in CABG with a Nitinol mesh

(eSVS Mesh®, Kips Bay Medical) was terminated due to lower patency rates. It is possible that this also may have been due in part to tissue buckling or kinking.[134, 135]

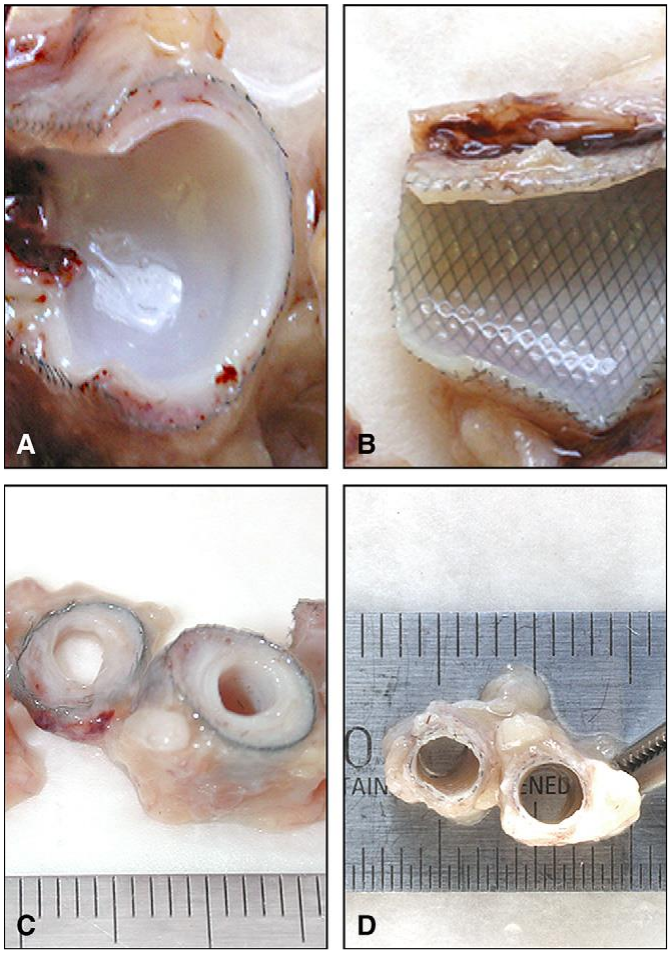


**Figure 2-19 Effects of a constrictive Nitinol mesh on baboon infrainguinal bypass grafts**
Macroscopic comparison of vein grafts 6-weeks after baboon infrainguinal bypass supported by 6.7 mm meshes (left, a and c) and more constrictive 3.3 mm meshes (right, b and d). Fibrosis and NH are rampant in the less constrictive meshes, while NH is suppressed from the 3.3 mm ones. Reproduced with permission.[10] Copyright 2008, Elsevier.

Superior biocompatibility, biodegradability, and flexibility warrant further studies that examine the mechanical impact of adventitial growth from polymeric external stenting, and how these variables might govern wall remodeling. Moreover, the diameter of the device is not the only factor involved in the type of mechanical support that is provided.

The inherent stiffness and biodegradability of the material, type of mesh (e.g. knitted, warp-knitted, woven, nonwoven, electrospun, ablated sheets),[90] thickness,[136, 137] and porosity[138-141] all factor into the mechanical support that it imparts. For example, reducing the thickness and increasing porosity limits stiffness and increases flexibility. Few studies to date have examined the influence of other variables besides device diameter on mechanical support and its ultimate effect on venous responses, hemodynamics, and graft patency.

#### 2.5.1.5 Role of Pore Parameters on the Effects of External Stenting

Pore size, porosity, and pore spacing (i.e. interconnectivity) clearly impact the mechanical properties of an external stent; greater void space from larger and more interconnected pores means less mechanical force applied to expanded venous tissue unless other properties are simultaneously altered such as mesh type and thickness. Pore parameters also affect the surface area-to-volume ratio and topology of the external stent, and play a large role in the extent of inflammatory reactions observed.[90, 140, 142] As previously discussed, the degree and duration of inflammation influences anti-neointimal angiogenic and chemoattractant responses.[116, 143] The positive effects observed from neoadventitial vascularization and accumulation of chemoattractants within the interstitial space between polymeric supports and venous tissue suggests that pore designs should be implemented that promote these characteristics to some degree. Few studies have directly examined the effect of an external stent's pore size on neoadventitial growth and NH, and analysis is made difficult by the fact that pore sizes of the meshes used are often unspecified. George et al. observed that external macroporous (presumably 750 μm diameter like ProVena®) Dacron sheaths helically wound with polypropylene significantly reduced NH

relative to microporous PTFE stents after one month in a porcine saphenous vein-to-carotid artery interposition graft model.[88] This reduction in NH was accompanied by an increase in adventitial microvessel growth and a decrease in PDGF expression and cell proliferation. However, the analysis from this study is complicated by the fact that two different materials, Dacron and PTFE, were used to compare effects of pore size. These materials bestow different mechanical and immunogenic properties. For example, Dacron exhibits a greater foreign body reaction and more chronic inflammation, while PTFE exhibits a significant amount of fibrosis.[90, 119] Future studies should isolate the effects of pore size by utilizing the same material.

It is difficult to determine what pore sizes are ideal for an external stent's ability to reduce NH and maintain patency without controlled studies isolating influences of the material and other parameters. It is generally accepted that pores and interconnections must be larger than 50 – 100 μm to promote blood vessel ingrowth, cell invasion, and enhanced biological responses without filling the pores with scar tissue.[90, 144, 145] In general, larger pores exhibit less scarring, inflammatory infiltrate, and connective tissue.[90, 146, 147] However, pore size requirements will differ depending on the material selected as well as the tissue environment where it is applied. For example, polypropylene requires pores larger than 1 mm while pores smaller than 650 μm are adequate for PVDF to obviate scarring between pores in abdominal wall hernias.[148] To enhance bone tissue formation by vascularization, pore sizes greater than 300 μm are recommended.[149, 150] Complicating matters further, when most studies vary one pore variable, another is changed. For example, no significant differences in vascularization or bone tissue ingrowth were detected over 8 weeks for PCL scaffolds (pore sizes of 350, 550, and 800 μm), but Roosa et al. admitted that simultaneous

changes in porosity between the groups may have influenced the results.[150] In light of these compounding factors, Bai et al. varied pore size while holding both interconnectivity and porosity constant.[145] In a rabbit model, β-tricalcium phosphate (TCP) cylinders with pores greater than 400 μm (i.e. 415, 557, and 632 μm) implanted into the fascia lumbodarsalis exhibited far more neovascularization than the 337 μm scaffolds.[145] More studies like this are needed with external supports in the venous environment to properly isolate variables and engineer supports that optimize mechanical, biological, and hemodynamic effects.

#### 2.5.1.6 Localization and Length of External Support

External stents should be designed that properly support veins and grafts in the areas most prone to failure, namely, directly around and adjacent to the distal (venous) anastomosis. Approximately 60% of stenoses in ePTFE hemodialysis grafts occur at or within 1 cm of the venous anastomosis, with another 4 – 29% at the proximal (arterial) anastomosis.[52] Venous injury from surgical trauma, compliance mismatches between the artery, vein, and/or graft,[111] and powerful, pulsatile arterial flow at the irregularly-shaped end-to-side geometry of the anastomoses gives rise to intense wall shear stress gradients and complex turbulent flow conditions (**Figure 16**).[151] This ultimately leads to significant NH at the shoulder and cushioning regions of the venous anastomosis, [152] which yields more drastic wall shear stress gradients and turbulent flow conditions that cause more NH in a vicious cycle.[153, 154] Few, if any, external stents today have been engineered to stop this vicious turbulence-induced NH cycle by effectively reducing compliance mismatches, tangential wall stresses, and asymmetric wall thickening. Trubel et al. demonstrated that sheep vein grafts wrapped with 8 mm Dacron meshes increased NH at the venous anastomosis with an approximately 2.5-fold increase in NH at this location compared to

unstented controls.[155] This indicated to the authors that these meshes should not be applied at the anastomosis, and may be the result of encompassing this region asymmetrically.[116] Similarly, it was advised after poor patency results in clinical trials[135, 156] that the constrictive Nitinol eSVS mesh not be applied to the anastomoses as it could restrict the blood flow through the graft.[12] A different Nitinol design, VasQ®, was devised by Laminate Medical to more easily fit around the venous anastomosis of hemodialysis fistula patients. Early clinical trials demonstrated adequate primary patency of 79% at 6 months for 20 patients[133] compared to historical levels of 60% at 12 months.[2] Although VasQ® still needs to go through significant clinical trials to become available in the US, it highlights how practical considerations related to surgery time, ease of use, and avoidance of injury from surgical implantation should be incorporated in designs to make wrapping around the critical venous anastomosis a more straightforward and beneficial process than in the past. The optimal geometry and length to achieve desirable biological and hemodynamic responses is still unclear and may vary depending on the material selected.

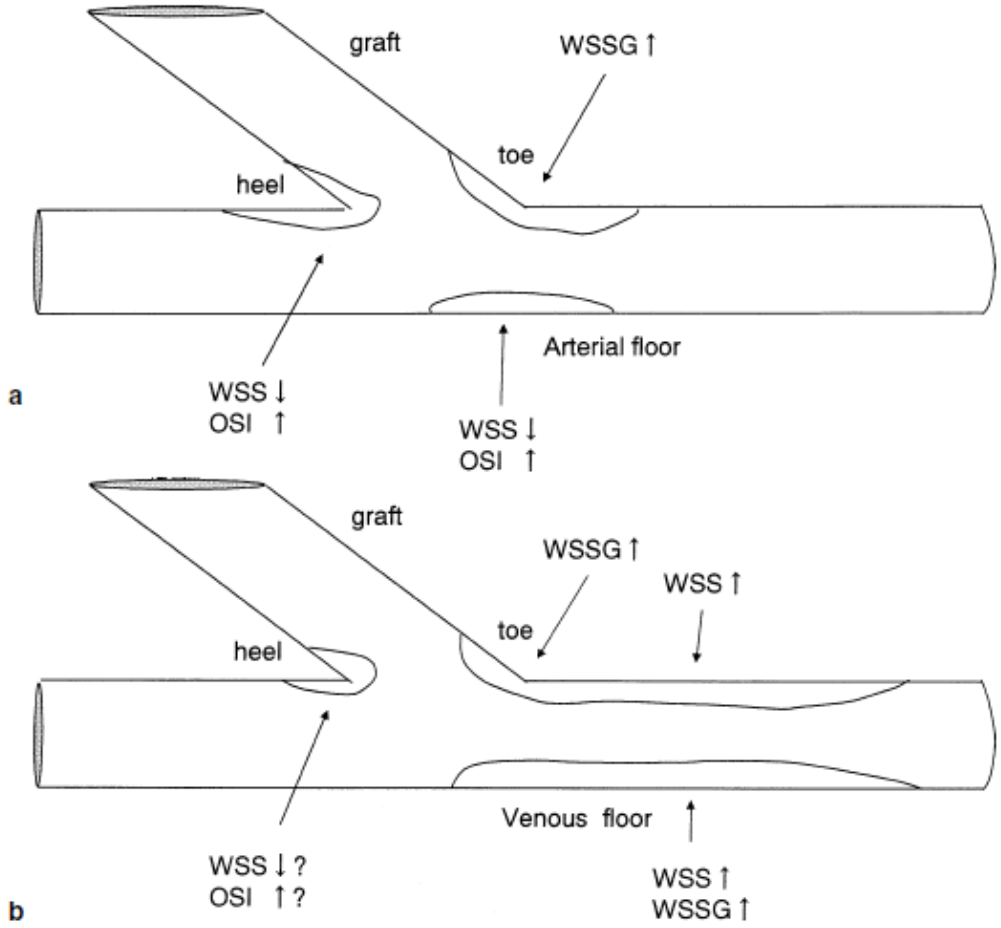


**Figure 2-20 Spatial distribution of neontimal hyperplasia in CABG vs AVGs**
The spatial distribution of NH a) in SVGs from CABG and b) in AVGs. WSS denotes wall shear stress, WSSG represents the WSS gradient, and OSI is the oscillatory shear index (i.e. the amount of turbulence). Reproduced with permission.[61] Copyright 2003, Springer.

### 2.5.2 Active Approaches – Applying Therapeutics to the Adventitia to Reduce Vein Failures

#### 2.5.2.1 Rationale for Localized, Sustained Delivery of Therapeutics

Incorporation of therapeutic agents into external supports can also be considered to improve vein graft and hemodialysis access patency. Localized, sustained release of a therapeutic with mechanisms that align with or are complimentary to the external stent can result in even greater positive outcomes. However, many of the current approaches employing therapeutics to-date have put more focus on the therapeutic itself without as

much consideration on the material choice and stent design. The main strategy behind this methodology is to create a therapeutic depot for longer lasting effects and administer higher localized concentrations of drugs to the outer adventitial layer while minimizing damage to the endothelium.[45]

#### 2.5.2.2 Clinical Trials for Therapeutic-Eluting External Supports

A handful of such approaches have reached clinical trials for improving hemodialysis access patency, but none have been successfully translated to-date. Two of them employed a collagen hydrogel that degrades within weeks, and therefore largely isolated the effects of the therapeutic without the added benefit of longer-term mechanical support. Both aimed to reduce NH by promoting angiogenesis, one by loading the gel with an adenoviral vector containing the VEGF-D gene (Trinam®, Ark Therapeutics Group)[157], and the other by loading the gel with allogenic endothelial cells (Vascugel®, Shire Pharmaceuticals).[158] Trinam® completed a Phase IIb clinical trial but its Phase III trial was terminated for "strategic reasons",[157] while Vascugel® completed two clinical trials without showing significant patency benefit, terminated a Phase II study, and is no longer a publically-active program at Shire.[158] A third approach loaded a nonbiodegradable ethylene vinyl acetate wrap with paclitaxel (Vascular Wrap®, Angiotech Pharmaceuticals),[159] but the Phase III clinical trial was terminated due to higher infection rates in the paclitaxel-treated group. Currently, a sirolimus-eluting collagen membrane (Coll-R®, Vascular Therapies) is recruiting patients for Phase III clinical trials after completing a first-in-man study demonstrating safety and technical feasibility.[160] Although Coll-R® is biodegradable, it may still bestow infection risks as the immunosuppressant

activity of sirolimus has been shown to increase superficial wound infections and other complications following kidney transplantation.[161, 162] Furthermore, the collagen matrix is unlikely to provide much in the way of beneficial mechanical support as it degrades rapidly. For these reasons, alternative therapeutics such as those mentioned on page 10 may ultimately be a better option than sirolimus, and other polymeric delivery platforms may be preferable to collagen.

#### 2.5.2.3 Improving Localization and Release Duration of Therapeutics

To maximize NH reduction and simultaneously minimize the risk of adverse complications, external supports should be engineered that sustain effective yet non-toxic drug concentrations localized within the vein walls without affecting the surrounding tissue. Several techniques have been investigated that aim to achieve these objectives by creating multi-layered systems, microneedles, altering the crosslinking density, copolymerizing, or combinations thereof.[163-173] For example, biodegradable, elastomeric poly(1,8-octanediolcitrate) copolymer membranes eluting vitamin A derivative all-trans retinoic acid (aTRA) exhibited a reduction in NH and restenosis in a rat carotid artery balloon injury model.[173] In another approach, Sanders et al. created a tunable platform to release drugs unidirectionally towards the adventitia. [166] It involved the creation and iteration of a multi-layer system consisting of a non-porous polymer layer ± a porous polymer layer ± a hyaluronic acid (HA) hydrogel layer loaded with the model drug sunitinib. The groups without the hydrogel had the drug loaded in the non-porous or porous layers instead of the hydrogel, and both PCL and PLGA were examined. The non-porous PCL layer sustained release 4-fold longer than the porous PCL construct (22 days vs. 5 days), while non-porous PLGA delayed release 3-fold (9 days vs. 3 days). It was demonstrated in an external jugular

vein porcine model that the non-porous PLGA bilayer evades drug loss, as significantly more drug was detected in the wrapped vein segment versus the adjacent extravascular muscle; at 1 week, 1048 ng $g^{-1}$ were detected in the vein segment versus none in the extravascular tissue, while at 4 weeks, the amounts were 1742 and 52 ng $g^{-1}$, respectively. Unidirectional approaches such as this more effectively localize and sustain release of therapeutics, but the effect of a nonporous layer on NH and angiogenesis was not examined.

#### 2.5.2.4 Comparing Material- and Therapeutic-Based Effects

Material-based effects on graft/access patency should be thoroughly examined and understood before incorporating a therapeutic. While such combinatorial approaches are lacking, some recent approaches have compared material-independent effects to material-drug combined effects.[165, 170, 172] Skalsky et al. loaded 70/30 P(LA/CL) with the immunosuppressant sirolimus and compared graft responses at 3 - 6 weeks in a rabbit jugular vein-to-common carotid artery model.[172] The group observed a significant reduction in intimal, medial, and intimal-medial thickening with both the mesh only and sirolimus-eluting mesh groups. Both groups exhibited a 73% reduction in intimal thickening after 3 weeks compared to the untreated graft. Levels of intimal thickening were the same compared to the untreated graft after 6 weeks for the sirolimus-eluting mesh, while that of mesh alone was 59% reduced at this timepoint. Medial thickness was relatively unchanged for the stent-alone group compared to the unstented graft, while the sirolimus-eluting mesh's medial thickness was reduced 65% and 20% at 3 and 6 weeks, respectively. Therefore, the sirolimus-eluting mesh reduced the total wall thickness in comparison to mesh alone by 60% and 13% at 3 and 6 weeks. It stands to reason that through more optimization of stent design and a better understanding of its NH-reducing

mechanism, a drug better tailored to the external stent's effects could be identified to maximize long-term patency.

## 2.6 Conclusions

Neointimal hyperplasia is the primary culprit for vein graft failure and hemodialysis access dysfunction. While several promising innovations have been devised, there is still no therapeutic approach currently available to patients to robustly prevent NH. External stents offer a particularly promising therapeutic avenue, as regulatory constraints may be lower for some of these devices, and it also offers the opportunity to combine a synergistic therapeutic payload. In order to translate these approaches to the clinic, a better understanding of NH that is specific to the material selected should be devised. Copolymers and modular iteration of design parameters can ultimately optimize external stent solutions. The effect of material chemistry, biodegradation timeline, mechanical properties, and geometry of the device and pores should all be carefully considered and tested for future devices. In combining biomedical engineering, clinical, and molecular biology insights, better solutions finding success in the clinic can be devised.

# CHAPTER 3: AIM 1- CREATION OF SMP LIBRARY

## 3.1 Introduction

Shape memory polymers (SMPs) contain chemical and/or physical crosslinks that afford the ability to be programmed and fixed into a temporary shape until provoked by a specific external stimulus to recover their original, permanent shape [174]. A diverse array of SMPs have been developed that recover their permanent shape in response to light [175], magnetic fields [176], electricity [177], moisture [178], or pH [179] for a variety of industrial, aeronautical, and biomedical applications and can be reviewed elsewhere [174, 180, 181]. In contrast to their shape memory alloy counterparts, SMPs can be created with diverse, multi-functional chemistries to enable drastic yet highly-controllable shape responses to various stimuli.[182-185] SMPs that are thermo-responsive remain the most convenient and widely studied, drawing extensive interest in the biomedical field in part because of the high predictability and consistency of the body temperature stimulus.[174, 186-188] The capability of thermo-responsive SMPs to recover their permanent shape near body temperature after programming into a distinct temporary shape provides an opportunity to develop the next generation of minimally-invasive medical devices [174, 186-188]. For example, their temporary shape can be programmed to fit through a small-bore incision for catheter insertion at room temperature and, when heated at or near body temperature, the polymeric device recovers its original functional shape, such as a stent mesh for intraluminal expansion [188-190], an expandable foam to fill an aneurysm [191-193], a tubular graft to bypass bloodflow in the advent of minimally invasive bypass grafting procedures [194], or a corkscrew shape to remove endovascular blood clots [195-197].

To be used in such vascular applications, materials should exhibit mechanical strengths that accomplish intended functions and minimize adverse compliance mismatch-induced host responses [108, 110, 198, 199], be biodegradable to prevent infectious complications [105, 200-202], and demonstrate switch-like shape recovery near body temperature [202, 203] with favorable biocompatibility [204-206]. SMPs triggered by melting temperature ($T_m$) may be more appropriate for many biomedical applications because they tend to exhibit sharper phase transitions and higher, more switch-like shape recovery than SMPs that respond to glass transition temperature ($T_g$) [202, 207]. Moreover, covalently-crosslinked SMP networks are often preferable to physically-crosslinked ones because they tend to undergo less creep and irreversible deformation during programming steps [174, 208], exhibiting superior shape memory properties and thermal stability [209]. However, current approaches to synthesize $T_m$-triggered SMP thermosets require an additional methacrylate functionalization step or multistep monomer synthesis.[203, 210, 211]

In this study, a new class of $T_m$-responsive SMPs with pendant, photocrosslinkable allyl groups, x%poly(ε-caprolactone)-co-y%(α-allyl carboxylate ε-caprolactone) (x%PCL-y%ACPCL), are created in a robust, facile manner with readily tunable material properties. While $T_g$-triggered SMPs have been created via thiol-ene crosslinking between monomers containing thiol and allyl groups [212] or via pendant crosslinking of acrylate groups [213], this is the first study to create SMPs by photocrosslinking pendant allyl groups. The x%PCL-y%ACPCL copolymerization format offers a convenient, combinatorial approach to fine-tune material properties of SMPs. The pendant allyl carboxylate-based crosslinkers enable pendant conjugation to growth factors, therapeutics, and extracellular matrix-derivatives via thiol-ene click chemistry [214, 215] or photocrosslinking of modified peptides [216] to control

cell and tissue responses. Allyl composition (y%) can be used to simultaneously control both the spacing of netpoints and crystallinity, offering an efficient means to tune thermomechanical, shape memory, and biological functions. Further tweaking of material properties and functions can be attained by altering other physicochemical properties such as molecular weight and gel content. Therefore, the new copolymerization format provides a unique, finely-tunable platform for studying structure-function relationships in order to better control biological responses and meet application requirements [217].

PCL notably has many desirable properties for vascular applications including biocompatibility/bioresorbability, slow biodegradability (2 – 3 years *in vivo*), and mechanical compliance [121], but its $T_m$ (> 50 ºC) is too high for physiological applications. Previous efforts to lower its $T_m$ near 37 ºC and achieve either dual- or triple-shape memory functions involve incorporation or complexation of rigid and/or soft components, blending, branching, and molecular weight alteration [203, 210, 211, 218-223]. In this study, the $T_m$ is tuned near body temperature primarily through subtle alteration in the molar composition of x%PCL-y%ACPCL. This new pendant-crosslinking system with photocrosslinkable ally-based crosslinkers offers the advantages of facile fabrication, robust tunability of material properties, and further functionalization with bioactive molecules. Molecular weight and gel content can also be controlled in this copolymerization format to fine-tune properties such as mechanical compliance and extensibility to more closely match that of the native artery, in turn reducing thrombotic and restenotic risks [121, 187, 199, 224]. These SMPs exhibit exceptional shape memory properties with high elastic recovery and switch-like shape responses near 37 ºC. In addition, these SMPs are compatible with vascular endothelial cells (ECs), as indicated by high levels of cell viability (≥ 85% after 91 hours relative to

tissue culture polystyrene (TCPS)) and healthy cell morphologies. These material features (e.g. high elastic recovery, ease of manufacturing and programming, low cost, vascular compatibility, tunable material properties, mechanical compliance, and biodegradability) are advantageous towards minimally invasive deployment of bulky, complex implantable devices for various biomedical applications [186-188], such as the aforementioned intraluminal stents, bypass grafts, or clot removal devices.

## 3.2 Methods

### 3.2.1 Materials

Lithium diisopropyl amine (LDA), allyl chloroformate, anhydrous tetrahydrofuran (THF), diethylzinc solution (15 wt% in toluene), dichloromethane (DCM), ethyl acetate, hexanes, poly(vinyl alcohol) (PVA), and ethanol were used as purchased from Sigma-Aldrich (St. Louis, MO). ε-caprolactone (CL) was dried with calcium hydride and vacuum distilled. To purify the synthesized α-allyl carboxylate ε-caprolactone (ACCL), Silica Gel Premium Rf (Sorbent Technologies, Norcross, GA) was first loaded into a glass column and wetted with 100% hexanes. Poly(methyl methacrylate) (PMMA) standards (Agilent Technologies, Inc., Santa Clara, CA) were used as purchased. SYLGARD® 184 Silicone Elastomer Kit (Dow Corning, Inc., Midland, MI) was used to prepare polydimethylsiloxane (PDMS) molds for preparing SMP shapes. MesoEndo Endothelial Cell Growth Media (Cell Applications, Inc., San Diego, CA) was used as purchased with passage 5-cultured human umbilical vein endothelial cell (HUVEC) and human coronary artery endothelial cell (hCAEC) lines (Cell Applications, Inc., San Diego, CA). Resazurin sodium salt (Sigma-Aldrich) was further diluted from prepared sterile 5 mM stock aliquots. Ethidium Homodimer-1 and Alexa Fluor® 488 Phalloidin were used as purchased (Molecular

Probes, Eugene, OR). For animal experiments, 5-0 Prolene sutures (Ethicon, Somerville, NJ) and optimal cutting temperature compound (OCT, Sakura Finetek USA, Inc., Torrance, CA) were used as purchased.

### 3.2.2 Synthesis of ACCL monomer

Analogous to other works [225-227], distilled CL (13.9 mL, 125 mmol) was added dropwise to a 250 mL round-bottom flask containing LDA (125 mL of 2 M in THF/n-heptane/ethylbenzene, 250 mmol) in anhydrous THF (200 mL) at -78 °C. After 1 hour, the temperature was raised to -30 °C and allyl chloroformate (13.3 mL, 125 mmol) was added dropwise. Thirty minutes later, the temperature was raised to 0 °C and quenched with saturated $NH_4Cl$ (30 mL). The crude ACCL was diluted in $H_2O$ (100 mL), extracted with ethyl acetate (300 mL x 3), dried with $Na_2SO_4$, filtered, evaporated, and purified by column chromatography using Silica Gel Premium Rf (Sorbent Technologies) with 10% ethyl acetate in hexanes to yield the novel monomeric compound (58% yield, 14.3 g, 72 mmol).

### 3.2.3 Synthesis of x%PCL-y%ACPCL copolymers

Analogous to other works [225, 228], varying molar ratios of dried ACCL and CL (100 mmol total) were introduced to a pre-dried test tube containing 1,6-hexanediol (0.5 mmol). The polymerization mixture was degassed with two freeze-purge-thaw cycles, submerged in a 140 °C oil bath, and catalyzed with dropwise addition of $Zn(Et)_2$ (1 mmol, 15 wt% in toluene) for 1 hour. The solution was precipitated in cold diethyl ether and dried under vacuum to yield the novel polymeric compound.

### 3.2.4 Fabrication of crosslinked x%PCL-y%ACPCL and 100%PCL-dimethacrylate SMP Films

Films of uniform thickness (~0.3 mm) were produced from a DCM solution (10 wt% polymer, 1 wt% 2,2-dimethoxy-2-phenylacetophenone) via a thin film applicator (Precision Gage & Tool, Co., Dayton, OH) and 365 nm irradiation (4.89 J $cm^{-2}$, 18.1 mW $cm^{-2}$, 4 min) with a Novacure 2100 Spot Curing System (Exfo Photonic Solutions, Inc., Mississauga, Ontario, Canada). Films were then solvent casted and vacuum dried.

### 3.2.5 Characterization of monomer, polymers, and crosslinked SMP films

To characterize molar compositions of compounds, $^{1}$H-NMR was performed on 5 wt% solutions in $CDCl_3$ with a 300 MHz spectrometer (Bruker Instruments, Inc., Billerica, MA). Molecular weight properties were determined by gel permeation chromatography against PMMA standards using a Phenogel 10E3A column (Phenomenex Inc., Torrance, CA) in THF. Polydispersity (PDI) was determined by the $M_w$ / $M_n$ ratio.

**Equation 3-1:**

$$X_G = m_{extracted}/m_{initial} \times 100\%$$

Thermal properties were determined by subjecting samples (n = 3 – 4) to two cycles from -80 $^{o}$C to 150 $^{o}$C on a Q1000 differential scanning calorimeter (DSC) (TA Instruments, Inc., New Castle, DE). $T_m$, crystallization temperature ($T_c$), $T_g$, enthalpy of fusion ($\Delta H_m$), and enthalpy of crystallization ($\Delta H_c$) are reported from the second cycle. Percent crystallinity, $X_C$, is calculated as:

**Equation 3-2:**

$$X_C = \Delta H_m/\Delta H_m^o \times 100\%$$

where $\Delta H_m^o$ = 139.5 J/g, the enthalpy of fusion for 100% crystalline PCL [229].

To determine mechanical and shape memory properties of the SMP films, rectangular strips (~8 mm x ~2.2 mm x ~0.3 mm) were loaded (n = 3 – 4) into a tensile clamp affixed within a dynamic mechanical analyzer (TA Instruments Q2000). Similar to Guo et al. [230], tensile mechanical properties were determined isothermally at 37 $^{o}$C with a stress ramp of 0.1 MPa min$^{-1}$. The modulus at 37 $^{o}$C, $E_{tn}$(37 $^{o}$C), was determined by measuring the slope in the initial linear region of the stress vs. strain curve.

Shape memory properties were determined in controlled force mode by stress-controlled thermomechanical cycling in which shape programming is controlled by stress and strain recovery is recorded under stress-free conditions [230-232]. SMP films were (1) heated to $T_m$ + 15 $^{o}$C, equilibrated for 10 minutes to achieve the original permanent shape, $\varepsilon_p(0)$, and programmed into an elongated shape by subjecting to tensile stress (0.004 MPa min$^{-1}$ to 0.039 MPa), (2) cooled (2 $^{o}$C min$^{-1}$ to 0 $^{o}$C) and equilibrated isothermally for 10 minutes at 0 $^{o}$C to yield the maximum strain, $\varepsilon_1$(N), and (3) relieved of stress (0.004 MPa min$^{-1}$ to 0 MPa) to yield the temporary shape, $\varepsilon_u$(N). (4) Heating (2 $^{o}$C min$^{-1}$) above $T_m$ yielded the permanent shape, $\varepsilon_p$(N), after a final 10 minute isothermal equilibration step at $T_m$ + 15 $^{o}$C. Shape recovery, $R_r$(N), describes how well shape is recovered ($\varepsilon_p$(N)) in comparison to the beginning of the N$^{th}$ cycle ($\varepsilon_p$(N-1)) after deforming to maximum strain $\varepsilon_1$(N). Shape fixity, $R_f$(N), defines the ability to maintain programmed shape $\varepsilon_1$(N) after unloading of stress to yield the temporary shape $\varepsilon_u$(N).

**Equation 3-3:**

$$\mathrm{R_r(N)} = \frac{\varepsilon_1(\mathrm{N}) - \varepsilon_\mathrm{p}(\mathrm{N})}{\varepsilon_1(\mathrm{N}) - \varepsilon_\mathrm{p}(\mathrm{N}-1)} \times 100\%$$

**Equation 3-4:**

$$R_f(N) = \frac{\varepsilon_u(N)}{\varepsilon_1(N)} \times 100\%$$

### 3.2.6 Shape programming

Closed-end polymer tubes (~1.0 – 2.0 cm length, ~0.90 mm in I.D., ~1.0 - 1.6 mm O.D.) were prepared by dipping a polyvinyl alcohol (PVA)-coated 0.90 mm O.D. glass capillary in the polymer film preparatory solution and UV-crosslinking as above. Capillaries containing the tubes were dried and immersed in deionized $H_2O$ and 100% ethanol before manually pulling the tubes off the capillaries. The tubes were washed with $H_2O$, dried, and the open side of the tube was closed by dipping it in polymer solution and UV crosslinking. A guitar shape comprised of 96%PCL-04%ACPCL was prepared by first laser etching (Epilog Laser, Golden, CO) a 2 mm PDMS mold containing a CAD-designed guitar, then pouring the 94%PCL-06%ACPCL polymer solution into the mold and UV crosslinking (365 nm, 26.1 J $cm^{-2}$, 290 mW $cm^{-2}$) on a 48 $^{o}$C hotplate.

### 3.2.7 Analysis of structure-function relationships

A 13 × 10 matrix was constructed containing the mean values of each variable to be compared (13 variables) for each of the 10 polymer films. Matrix values were standardized to their z-score for more apt comparison between variables, and a covariance matrix was computed and plotted using MATLAB (MathWorks Inc., Natick, MA). To highlight structure-function relationships and minimize redundancy, only a portion of this matrix is presented.

### 3.2.8 HUVEC viability

To prevent cell attachment on TCPS underneath test films, wells were coated with 1% agarose solution. Agarose-coated wells were dried, washed with 100% ethanol, UV sterilized, and washed with MesoEndo Endothelial Cell Growth Media. Ethanol-leached, media-soaked polymer disks (~31 $mm^2$, ~50 µm thick) were then placed on the agarose-coated wells, and Passage 5 HUVECs (470 cells $mm^{-2}$) were seeded directly on the film surfaces, TCPS (positive control), and 1% agarose (negative control) (n = 4). After 1.5 hours, 150 µL of media was added. Viability was assessed at 9, 35, and 91 hour time points via the resazurin assay [233]. Briefly, resazurin was added to each well to achieve a 5 µM concentration in MesoEndo, incubated for 4 hours at 37 $^oC$, and 560/590 nm excitation/emission of the supernatant was read on an Infinite® M1000 Pro plate reader (Tecan Group Ltd, San Jose, CA). Viable cell number was calculated based on a standard curve of fluorescence intensity from HUVECs on TCPS, and % cell viability was normalized to TCPS controls. All samples were tested in biological quadruplicates.

### 3.2.9 HCAEC viability and morphology

Cell viability was assessed for Passage 5 hCAECs seeded on TCPS (380 cells $mm^{-2}$) and subsequently co-incubated with ethanol-leached, media soaked films (n = 4). The resazurin assay was utilized in the same manner as that described above at 24 and 80 hours.

Cell morphology was evaluated by seeding the Passage 5 hCAECs directly onto polymer disks (n = 4). After 3 days on the polymer disks or TCPS controls, cells were fixed with 4% paraformaldehyde (15 minutes), permeabilized with 0.5% Triton X-100 (10 min), and blocked with 10% bovine serum albumin (30 min). Cells were then incubated with 2 µM Ethidium Homodimer-1 (10 min) and 50 µM Alexa Fluor® 488 Phalloidin (20 min).

Cells on polymer surfaces were imaged on a LSM 510 META Inverted Confocal Microscope (Carl Zeiss, LLC, Thormwood, NY), while TCPS controls were imaged with a Nikon Eclipse Ti inverted fluorescence microscope (Nikon Instruments Inc. Melville, NY). Images were post-processed and analyzed using ImageJ software (NIH, Bethesda, MD).

### 3.2.10 Statistical Analysis

All data are reported as mean ± standard deviation (n = 3 - 4). In comparisons between individual groups, an unpaired, two-tailed Student's t-test was used and $p < 0.05$ was considered statistically significant.

## 3.3 Results and discussion

### 3.3.1 Synthesis and characterization of x%PCL-y%ACPCL copolymers

To prepare this new class of SMP library, a novel α-allyl carboxylate ε-caprolactone (ACCL) monomer was first synthesized in a single reaction by lithium diisopropyl amine-mediated carbanion formation at the α-carbon of ε-caprolactone (CL) and subsequent addition of allyl chloroformate (Figure 3-1A) [225, 227]. $^1$H-NMR confirmed formation of the desired ACCL product, as indicated by characteristic allyl (5.92 (***G**$_i$*) , 5.31 (***H**$_{ii}$*) and 4.63 (***F**$_{ii}$*) ppm) and CL peaks (Figure 3-1C) [225, 226, 228, 234]. Ring-opening (co)polymerization (ROP) of ACCL with CL using a diethylzinc catalyst and 1,6-hexanediol initiator generated a library of novel *x%*PCL-*y%*ACPCL (*x* and *y*: molar ratio) copolymers with y = 4.16 – 14.5% as determined by the ratio of allylic CH protons (***G**$_i$*, δ = 5.92 ppm) to $CH_2$ protons at the ε-carbon of PCL and ACPCL units (***ε**$_{ii}$*, δ = 4.15 ppm) (Figure 3-1B and D, **Table 3-1**) [225, 226, 228, 234]. As a control, 100%PCL [**Table 3-1**, $M_n$ = 11300 Da, PDI = 1.54] was

similarly synthesized by ROP of CL using stannous octoate and terminally-functionalized via reaction with 2-isocyanatoethyl methacrylate to yield 100%PCL-dimethacrylate [100%PCL-DMA, **Table 3-1**, $M_n$ = 11628 Da, PDI = 1.41] with a terminal hydroxyl-to-methacrylate conversion ($D_M$) of 90.5% (Figure A-1 Synthesis of 100%PCL-DMA, Equation A-1:) [208, 235]. Allylic compositions attained were lower than the ACCL:CL feed ratios due to lower reactivity of the ACCL monomer (**Table 3-1**, Figure 3-1E) [225, 228]. Molecular weight [**Table 3-1**, $M_n$ = 12 – 19 kDa, polydispersity index (PDI) = 1.78 – 2.50] was controlled by the 1,6-hexanediol initiator: total monomer ratio but was also influenced by the feed ratio of the less reactive ACCL monomer.[225, 228] The higher PDIs and lower yields (22.6 – 56.6%) attained for these copolymers may be due to transesterification reactions involving both the polyester backbone and pendant allyl carboxylates.[211, 225, 228] There is a clear inverse relationship between several thermal properties and allyl composition, as the amorphous ACPCL disrupts PCL crystallinity, lowering the $T_m$ and percent crystallinity ($X_c$) (**Table 3-1**).

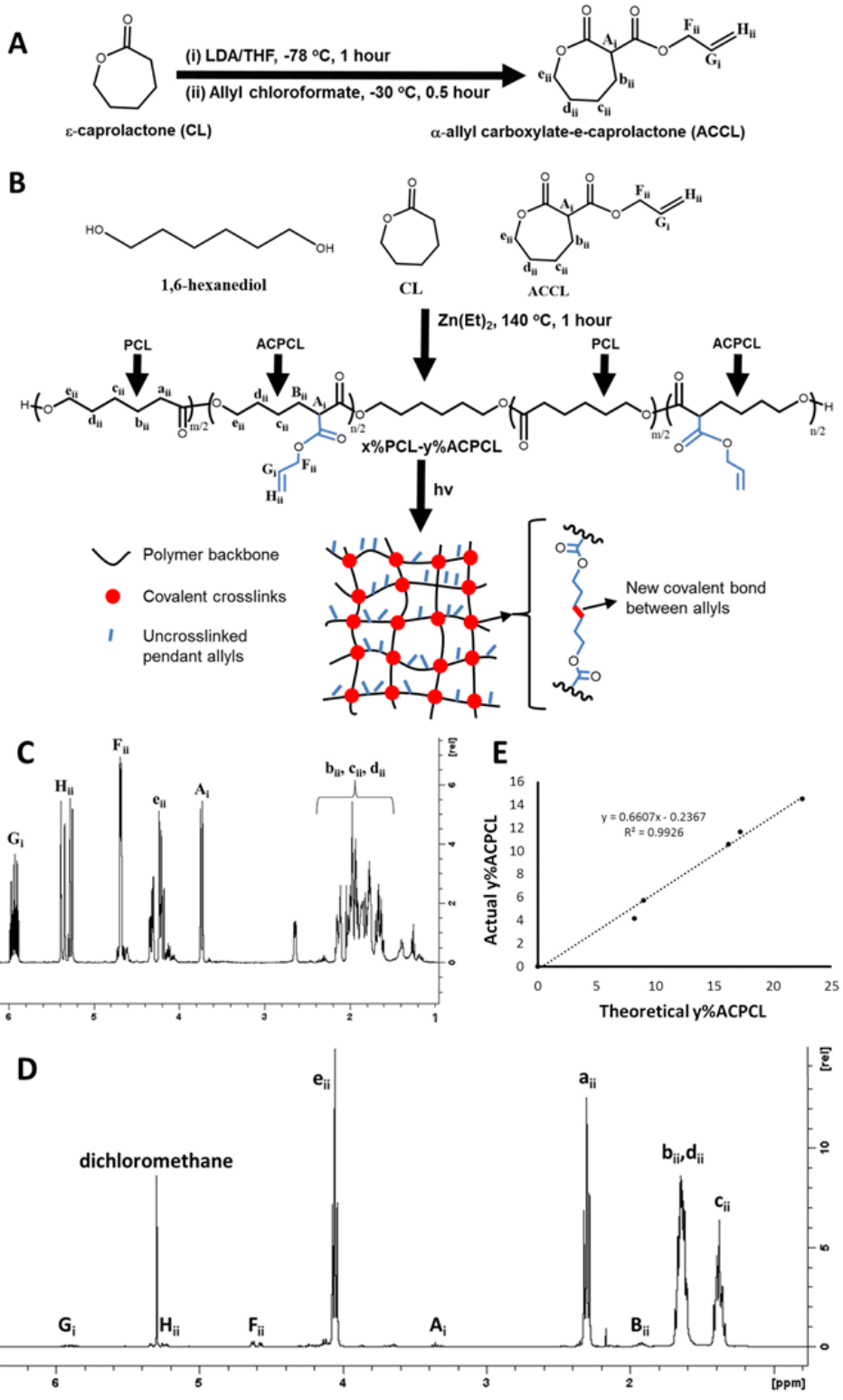


**Figure 3-1 Synthesis of PCL-ACPCL shape memory polymers**
(A) Synthetic scheme for ACCL and (B) x%PCL-y%ACPCL SMP networks. (C) $^{1}$H-NMR of ACCL (400 MHz, $CDCl_3$, 25 °C, TMS): δ = 5.92 (m, 1H;, -C**H**=$CH_2$ (***G*$_i$**)), 5.31 (m, 2H;

-CH=C**H**$_2$ (***H**$_{ii}$*)), 4.63 (m, 2H; -CH=C**H**$_2$O (***F**$_{ii}$*)), 4.20 (m, 2H; -OC**H**$_2$ (***e**$_{ii}$*)), 3.73 (d, $^3$J(H,H) = 10.7 Hz, 1H; -C**H**CH$_2$CH$_2$ (***A**$_i$*)), 2.40 – 1.50 (m, 6H; -C**H**$_2$ (***b**$_{ii}$,**c**$_{ii}$,**d**$_{ii}$*)). (D) $^1$H-NMR of 96%PCL-04%ACPCL (400 MHz, $CDCl_3$, 25 °C, TMS): δ = 5.92 (m, 1H;, -C**H**=CH$_2$ (***G**$_i$*)), 5.31 (m, 2H; -CH=C**H**$_2$ (***H**$_{ii}$*)), 4.63 (m, 2H; -CH=C**H**$_2$O (***F**$_{ii}$*)), 4.15 (m, 2H; -OC**H**$_2$ (***e**$_{ii}$*)), 3.35 (m, 1H; -C**H**-CH$_2$ (***A**$_i$*)), 2.33 (t, $^3$J(H,H) = 7.5 Hz, 2H; -C**H**$_2$ (***a**$_{ii}$*)), 1.96 (m, 2H; -C**H**$_2$ (***B**$_{ii}$*)), 1.62 (m, 4H; -C**H**$_2$ (***b**$_{ii}$,**d**$_{ii}$*)), 1.39 ppm (m, 2H; -C**H**$_2$ (***c**$_{ii}$*)). (E) Influence of ACCL:CL feed ratio on x%PCL-y%ACPCL molar composition. Reproduced with permission.[15] Copyright 2015, Elsevier.

**Table 3-1 Characterization of x%PCL-y%ACPCL copolymers**.

| Copolymer | Theoretical y (%) | Actual y (%) | Yield (%) | Initiator: Monomer | $M_n$ (Da) | $M_w$ (Da) | PDI | $T_m$ (°C) | $X_C$ (%) |
|---|---|---|---|---|---|---|---|---|---|
| 100%PCL | 0.00 | 0.00 | 86.2 | 1:100 | 11300 | 17368 | 1.54 | 53.0 □ 0.2 | 56.6 □ 1.5 |
| 100%PCL-DMA | 0.00 | 0.00 | N/A | N/A | 11628 | 16417 | 1.41 | 50.7 □ 0.5 | 45.8 □ 1.9 |
| 96%PCL-04%ACPCL | 8.24 | 4.16 | 44.8 | 1:200 | 15060 | 26870 | 1.78 | 45.9 □ 0.3 | 41.6 □ 1.2 |
| 94%PCL-06%ACPCL | 9.03 | 5.74 | 38.3 | 1:200 | 16546 | 39050 | 2.36 | 47.1 □ 0.1 | 36.1 □ 0.5 |
| 89%PCL-11%ACPCL | 16.2 | 10.6 | 39.8 | 1:200 | 13627 | 34049 | 2.50 | 39.1 □ 0.3 | 30.4 □ 0.7 |
| 88%PCL-12%ACPCL | 17.2 | 11.7 | 22.6 | 1:315 | 19087 | 36430 | 1.91 | 41.6 □ 0.2 | 31.1 □ 0.7 |
| 85%PCL-15%ACPCL | 22.5 | 14.5 | 56.6 | 1:200 | 12095 | 28931 | 2.39 | 32.5 □ 0.4 | 24.4 □ 0.9 |

Reproduced with permission.[15] Copyright 2015, Elsevier

### 3.3.2 Fabrication and characterization of crosslinked x%PCL-y%ACPCL SMP networks

A subset of x%PCL-y%ACPCL copolymers and the 100%PCL-DMA control were photocrosslinked to create the shape memory effect and evaluated in terms of gel content, thermal, mechanical, and shape memory properties. It was desired to produce SMPs with $T_m$'s both slightly above and below 37 °C as surgical preferences for the onset of shape recovery depend on the particular application [188, 236, 237]. In order to be used for various vascular applications (e.g. endovascular stents, bypass grafts), it was also desired that the SMP library exhibits tunable mechanical properties, with sufficient compliance and extensibility. Moreover, complete and repeatable shape recovery with an on-off "switch-like" response to small temperature changes is sought after in order to tightly control shape

memory behavior and preserve implant integrity and function following shape programming and recovery.

Gel content, which relates to the percent crosslinking of the material, is independent of composition (Figure 3-5, subset) and was an average of 57.3 ± 7.2% for the x%PCL-y%ACPCL films after photocrosslinking (365 nm, 4.89 J $cm^{-2}$, 18.1 mW $cm^{-2}$), well above the 10% [238] or 30% [239] threshold for achieving the shape memory effect in other SMP networks (Table 3-2). Higher gel content films can be achieved for each composition by increasing the UV dosage, but are not included here because they exhibit hindered shape memory functions due to low crystallinity. Crosslinking of the materials resulted in a $T_m$ reduction from 45.9 – 32.5 ºC to 43.4 – 29.7 ºC for y = 4.16 – 14.5% copolymer films (**Table 3-1** and Table 3-2) due to the restricted mobility of the crosslinked polymer chains. [203, 211, 230] This reduced chain mobility also disrupts the alignment of chains after melting, as indicated by a reduction in the percent crystallinity ($X_C$) after crosslinking [211]. There is a clear dependence of all thermal properties (except for $T_g$) on molar composition for the crosslinked polymers (Table 3-2, Figure 3-2 and Figure 3-5), as amorphous ACPCL disrupts the crystallinity of PCL and simultaneously lowers the $T_m$, $X_C$, crystallization temperature ($T_c$), and enthalpy of crystallization ($\Delta H_c$). Copolymers with > 15%ACPCL follow the same trend, but were not considered for this paper because their low crystallinity inhibits their shape memory utility. The $X_C$ generated is similar to branched PCL crosslinked films [203], indicating that switch-like shape recovery behavior is feasible with these SMPs. Crosslinking produced a library of SMPs with ideal switching temperatures (i.e. $T_m$'s near 37 ºC) and sufficient $X_C$ for complete shape recovery and switch-like behavior in physiological applications.

**Table 3-2 Gel content and thermal properties of crosslinked x%PCL-y%ACPCL SMP films.**

| Composition | $X_G$ (%) | $T_m$ (°C) | $\Delta H_m$ (J g$^{-1}$) | $X_C$ (%) | $T_c$ (°C) | $\Delta H_c$ (J g$^{-1}$) | $T_g$ (°C) |
|---|---|---|---|---|---|---|---|
| 100%PCL-DMA | 72.0 ± 17 | 48.1 ± 0.4 | 48.2 ± 0.5 | 34.6 ± 0.4 | 19.5 ± 1.0 | 48.6 ± 0.38 | -54.2 ± 3.0 |
| 96%PCL-04%ACPCL | 63.0 ± 8.6 | 43.4 ± 1.2 | 44.6 ± 3.2 | 32.0 ± 2.3 | 15.8 ± 0.89 | 43.2 ± 6.1 | -56.9 ± 0.10 |
| 94%PCL-06%ACPCL | 60.3 ± 21 | 37.9 ± 0.9 | 39.1 ± 5.3 | 28.0 ± 3.8 | 2.44 ± 0.54 | 38.7 ± 4.8 | -58.8 ± 4.9 |
| 89%PCL-11%ACPCL | 49.0 ± 6.2 | 37.9 ± 0.7 | 38.7 ± 1.6 | 27.7 ± 1.2 | -2.10 ± 0.74 | 36.5 ± 0.82 | -57.1 ± 1.5 |
| 88%PCL-12%ACPCL | 64.1 ± 3.1 | 33.4 ± 1.2 | 33.7 ± 1.1 | 24.2 ± 0.8 | -8.73 ± 0.20 | 31.4 ± 2.2 | -58.7 ± 2.2 |
| 85%PCL-15%ACPCL | 50.3 ± 0.64 | 29.7 ± 0.2 | 28.3 ± 2.7 | 20.3 ± 1.9 | -13.9 ± 0.84 | 17.2 ± 0.87 | -57.5 ± 1.1 |

Reproduced with permission.[15] Copyright 2015, Elsevier.

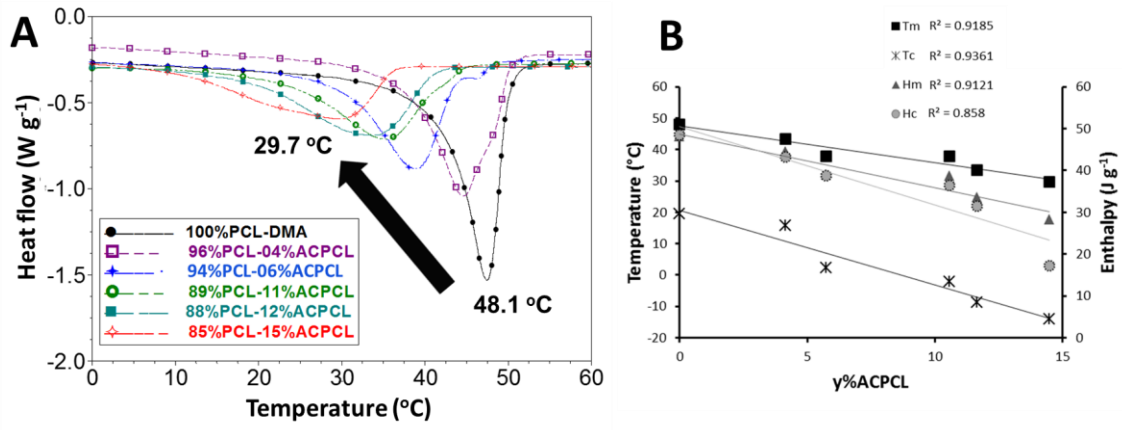


**Figure 3-2 Thermal properties of crosslinked SMP networks**
(A) DSC overlay and (B) correlation between y%ACPCL and thermal properties for crosslinked x%PCL-y%ACPCL SMP networks. Reproduced with permission.[15] Copyright 2015, Elsevier.

Mechanical properties of the SMP test films were assessed isothermally at 37 °C to determine suitability for vascular applications. The elasticity was of the same order of magnitude or one lower than the 100%PCL-DMA control [Table 3-3, for y = 4.16 – 14.5%: tensile modulus at 37 °C ($E_{tn}$(37°C)) = 70.8 - 2.48 MPa], which may be considered desirable compliance for vascular applications considering that this is only marginally less compliant than arteries [121, 187, 199, 203, 224]. By comparison, healthy human coronary arteries exhibit an average physiological elastic modulus of 1.48 MPa [240]. The higher y%ACPCL crosslinked

copolymer films displayed an order of magnitude lower $E_{tn}$(37°C) that more closely matches that of native arteries and is primarily the result of these materials partially or fully melting at 37 °C [203]. Stress-to-break, $\sigma_{max}$, exhibits a similar trend as $X_C$, decreasing from 3.15 to 0.46 MPa as y% increased from 4.16 to 14.5%. All materials exhibit good ductility at 37 °C, with >100% strain-to-break, $\varepsilon_{max}$, for every test film but 85%PCL-15%ACPCL ($\varepsilon_{max}$ = 71.5 ± 40.6%), which may be adversely affected by its low crystallinity (Table 3-3). These experiments demonstrate that the library of crosslinked SMPs has appropriate extensibility and compliance for vascular applications.

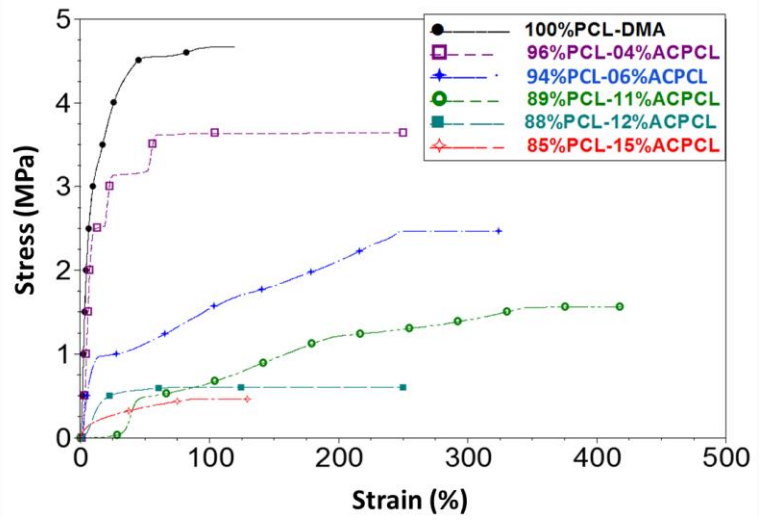


**Figure 3-3 Mechanical properties of crosslinked SMP films**
Stress vs. strain curves for crosslinked x%PCL-y%ACPCL SMP networks at 37 °C. Reproduced with permission.[15] Copyright 2015, Elsevier.

**Table 3-3: Mechanical and shape memory properties of crosslinked SMP films.**

| Composition | $E_{tn}$(37°C) (MPa) | $\varepsilon_{max}$ (%) | $\sigma_{max}$ (MPa) | $R_r$(1) (%) | $R_r$(N) (%) | $R_f$(N) (%) |
|---|---|---|---|---|---|---|
| 100%PCL-DMA | 66.7 ± 41.6 | 90.2 ± 110 | 3.86 ± 2.2 | 99.7 ± 0.12 | 99.5 ± 1.4 | 98.3 ± 1.5 |
| 96%PCL-04%ACPCL | 70.8 ± 37.4 | 126 ± 115 | 3.15 ± 0.39 | 99.2 ± 0.81[a)] | 99.4 ± 1.3[a)] | 94.2 ± 1.2[a)] |
| 94%PCL-06%ACPCL | 3.05 ± 2.64 | 253 ± 19.4 | 2.36 ± 0.87 | 93.7 ± 0.87 | 98.5 ± 0.57 | 98.7 ± 0.27 |
| 89%PCL-11%ACPCL | 5.44 ± 1.10 | 300 ± 127 | 1.43 ± 0.31 | 97.7± 0.62 | 99.7 ± 0.74 | 99.8 ± 0.16 |
| 88%PCL-12%ACPCL | 3.64 ± 1.10 | 109 ± 110 | 1.14 ± 0.59 | 99.3 ± 9.9 | 99.0 ± 6.2 | 98.6 ± 0.75 |
| 85%PCL-15%ACPCL | 2.48 ± 1.11 | 71.5 ± 40.6 | 0.463 ± 0.4 | 60.1 ± 0.64 | 86.9 ± 4.7 | 99.6 ± 0.23 |

[a] A 96%PCL-04%ACPCL test film with $X_G$ = 36.7 ± 8.6% had $R_r$(1) = 99.9 ± 0.2, $R_r$(N) = 99.8 ± 0.4%, and $R_f$(N) = 99.8 ± 0.1%. Reproduced with permission.[15] Copyright 2015, Elsevier.

Next, their shape memory properties were evaluated by stress-controlled thermomechanical cycling in which shape programming is controlled by stress and strain recovery is recorded under stress-free conditions (Figure 3-4A – C).[230-232] Some of the SMP films, most notably 96%PCL-04%ACPCL, exhibit shape changes when heated above their $T_m$ for the first time during the equilibration step at $T_m$ + ~15 ºC before any stress is applied (i.e. ~39% negative strain at 60 ºC in Figure 3-4A). Similar to crosslinked semi-crystalline SMPs utilized in heat-shrink tubing applications,[174, 241-243] this indicates that the film fabrication process (i.e. UV irradiating the SMPs below their $T_m$) can effectively fix the films in an ambient temporary shape. Heating beyond their $T_m$ for the first time triggers recovery of an entropically-favored permanent shape, $\varepsilon_p(0)$, that may differ from the temporary shape formed during the crosslinking event at room temperature. SMPs should therefore be photocrosslinked above their $T_m$ in the future to avoid any possible unanticipated alterations in the permanent shape. Smaller stresses than those in Figure 3-3 are required to achieve comparable levels of strain because the programming step is carried out at temperatures higher than 37 ºC ($T_m$ + ~15ºC). Shape fixity ($R_f$) represents the ability of materials to be programmed and fixed into a temporary shape (e.g. thread-like shape) and was > 98% for select films of every composition (Table 3-3). This indicates that even less crystalline materials have strong enough interactions between polymer chains [174], at least at freezing temperatures, to properly immobilize and fix a temporary shape. Shape recovery after the first cycle, $R_r(N)$, which indicates the quantitative ability of materials to recover their permanent shape (e.g. tubular shape), was > 98% for test films of every composition except for 85%PCL-15%ACPCL ($R_r(N)$ = 86.9 ± 4.7%) (Table 3-3). The

lower $R_r$, $X_C$, and ductility of crosslinked 85%PCL-15%ACPCL films indicate that the lower crystallinity and energy associated with the melting transition of materials with ≥ 15%ACPCL hinders their shape memory utility. The highly repeatable nature of shape programming and recovery for these SMPs with < 15%ACPCL is illustrated in three consecutive thermomechanical cycles with 96%PCL-04%ACPCL and 89%PCL-11%ACPCL along with the 100%PCL-DMA control (Figure 3-4A – C). This indicates their promising utility in biomedical applications involving deployment and recovery from minimally-invasive surgical devices such as catheters or laparoscopes.[174, 186-188] Shape memory demonstrations further affirm this potential capability to be programmed into and recover complex shapes in biomedical applications (Figure 3-4D – L, Video S1), including a thread-to-tube transition for possible minimally-invasive catheter/laparoscope deployment in endovascular stenting, bypass grafting, or clot removal at 37 $^{o}$C. Shape recovery occurs rapidly (within seconds) and fully once the SMPs are exposed to a temperature at or beyond their midpoint $T_m$ (Video S1). All copolymers, especially those with < 15% ACPCL, possess exceptional, tightly-controllable shape memory capabilities.

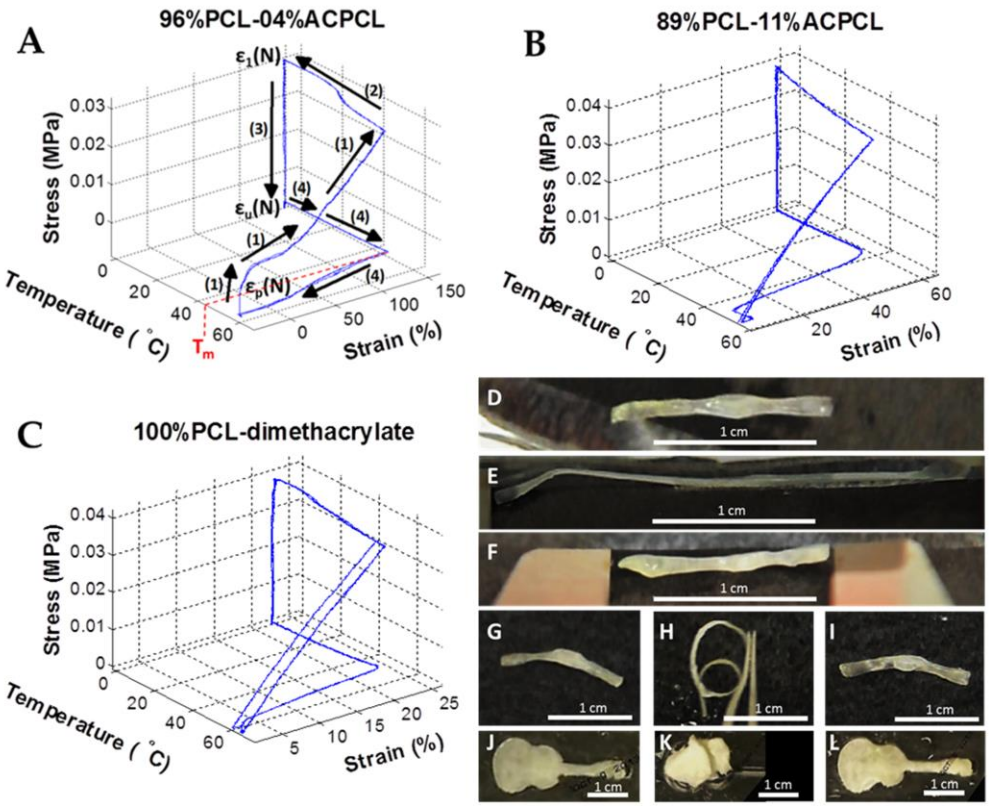


**Figure 3-4 Shape memory properties of crosslinked PCL-ACPCL films**
(A-C) Stress-controlled thermomechanical cycling of crosslinked x%PCL-y%ACPCL and 100%PCL-DMA SMP networks. (D-L) Shape memory demonstrations**. (**D, G) 88%PCL-12%ACPCL tubular permanent shape is (E, H) deformed into a thread by heating at 50 $^{o}$C, applying strain, and fixing in an ice bath. (F, I) Heating at 37 $^{o}$C results in recovery of the original, permanent tube shape. (J) 96%PCL-04%ACPCL guitar shape is (K) heated to 50 $^{o}$C, strained, contorted, and fixed at 4 $^{o}$C before (L) ultimate recovery of the complex guitar shape at 48 $^{o}$C. Reproduced with permission.[15] Copyright 2015, Elsevier.

### 3.3.3 Elucidation of structure-function relationships

To better elucidate correlations of material properties ($T_m$, $\Delta H_m$, $T_c$, $E_{tn}(37^oC)$, $\sigma_{max}$, $\varepsilon_{max}$, $R_r(N)$, $R_f(N)$) with physicochemical properties (y%ACPCL, $M_n$, $M_w$, PDI, $X_G$), a standardized covariance matrix was constructed from mean property values of an expanded polymer library (Figure 3-5). Covariances (covs) closest to the absolute value of 1 indicate the strongest correlations between variables, with positive and negative values indicating direct and inverse relations, respectively. While it should be cautioned that the low number of polymer test groups (n = 10), inherent variance in data, interdependent relationships,

and experimental parameters used to derive mechanical and shape memory properties (e.g. stress or strain rate, fixation and deformation temperature) can skew these correlations, some basic and useful conclusions can be drawn from this analysis. Thermal properties ($T_m$, $\Delta H_m$, $T_c$, $\Delta H_c$), $E_{tn}(37^oC)$, and $\sigma_{max}$ correlate most strongly with y%ACPCL (cov = -0.80 – -0.94), indicating the dominant role of molar composition in modulating thermal properties. The effect of molar composition on many material properties can be explained by the fact that altering allyl content simultaneously changes both the crystallinity and spacing of netpoints of the crosslinked networks. $R_r(N)$ was also most impacted by molar composition (cov = -0.60), although it is conceivable that programming parameters (e.g. fixation and deformation temperature, stress or strain rate) could be adjusted to improve $R_r(N)$ for higher y%ACPCL copolymers [244-246]. Also of note, $M_n$ only correlates strongly with $\varepsilon_{max}$ (cov = 0.78), indicating that increasing $M_n$ may be able to improve the extensibility of these SMPs if that is deemed a rate-limiting factor in implant performance. Along the same lines, it may be possible to increase $R_f(N)$ (cov = -0.54) and $\Delta H_m$ (cov = -0.46) by adjusting $X_G$. While a low number of polymer test groups, variability in the data, interdependencies, and the potential influence of experimental parameters convolute this analysis, it appears that the majority of material properties are most affected by molar composition. Furthermore, it appears that many material properties can be tweaked via modulation of other physicochemical properties to comprise PCL-ACPCL SMPs with optimal thermal, mechanical, and shape memory properties for a particular application. Firmer conclusions can be derived from these correlations if the polymer library is further expanded, thereby minimizing variance in the data and interdependent effects.

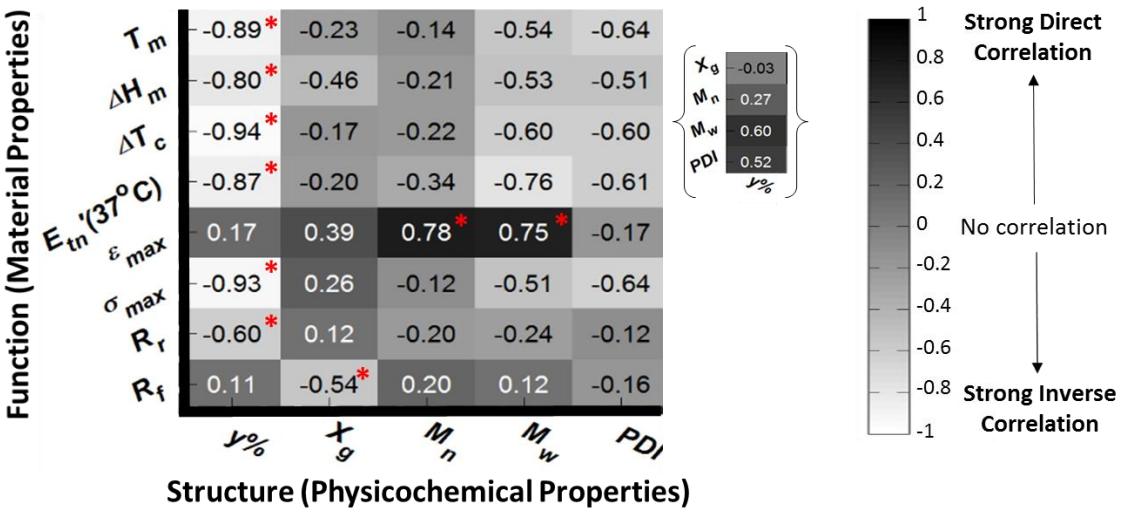


**Figure 3-5 Evaluation of structure-function relationships**
Standardized covariance matrix reveals structure-function relationships for the crosslinked SMP library. * does not indicate statistical significance, but rather the strongest Structural/Physicochemical Property correlation(s) with each Functional/Material Property. Molar composition (y%) has the strongest influence on the majority of material properties. The inset showing the correlation of y% with the other physicochemical properties provides context (i.e. interdependence information) for the structure-function relationships generated from the SMP library. Reproduced with permission.[15] Copyright 2015, Elsevier.

### 3.3.4 Cell viability studies

To assess biocompatibility of the films *in vitro*, HUVECs were seeded on washed polymer films and their viability was measured and normalized to TCPS over the course of four days using the resazurin assay (Figure 3-6A) [233]. The 85%PCL-15%ACPCL copolymer was not considered for this test due to its lower ductility and shape memory utility. 100%PCL (Sigma-Aldrich, $M_n$ = 70 – 90 kDa) is an appropriate control film as the base polymer of x%PCL-y%ACPCL films and is well known to be biocompatible [205, 247]. Nine hours post-seeding, there was no statistically significant difference in HUVEC viability on test SMP films (60.0 – 65.2% relative to TCPS) compared to 100%PCL (59.4 ± 4.9%), affirming that cell seeding was equivalent across the films. At later timepoints,

HUVEC viability on all copolymer films (102.9 – 106.7% for 35 hours and 85.0 – 103.0% for 91 hours) was comparable to that on the TCPS control (100%) and greater than that on 100%PCL (66.0 ± 14.4% and 64.1 ± 32.0%, respectively). hCAECs seeded on TCPS and immediately co-incubated with polymer films exhibited a viability of > 79% at 24 hours and > 85% at 80 hours relative to TCPS, with no statistically significant differences observed between test substrates (n = 4) (Figure A-2). In a separate experiment, hCAECs seeded directly on films demonstrate a trademark cobblestone morphology indicative of their excellent viability on all films three days post-seeding (Figure 3-6B - F)[248]. These experiments therefore demonstrate that the SMPs are compatible with vascular ECs.

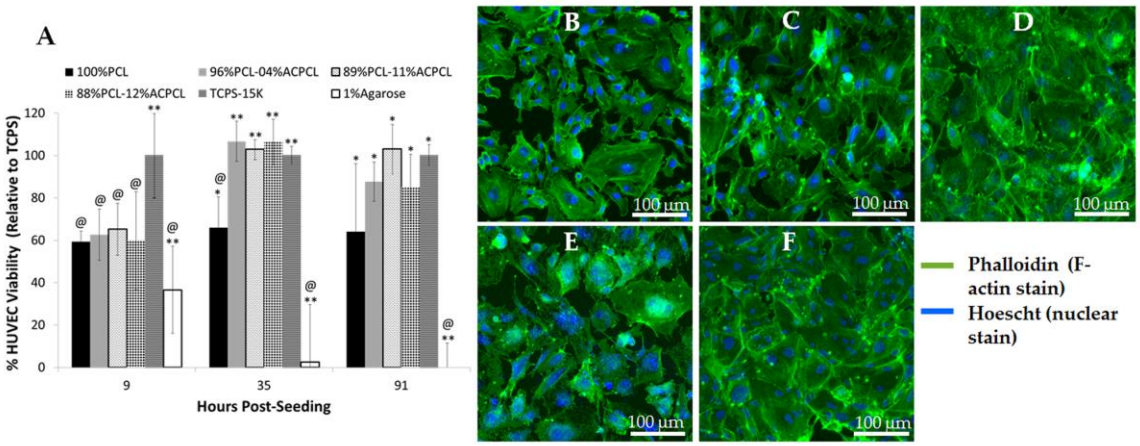


**Figure 3-6 Evaluation of cell viability**
(A) Viability of HUVECs seeded directly on polymer surfaces at specified timepoints, where @ = significantly different from TCPS, * = significantly different from 1% agarose, and ** = significantly different from 100%PCL as well as 1% agarose (if located above the 1% agarose bar, the only significant difference is to 100%PCL) (n = 4, $p < 0.05$). Confocal microscopy images of human coronary artery endothelial cells (hCAECs) 3 days post-seeding on (B) TCPS, (C) 100%PCL, (D) 96%PCL-04%ACPCL, (E) 89%PCL-11%ACPCL, and (F) 88%PCL-12%ACPCL exhibit trademark cobblestone morphology (Green: F-actin, Blue: Nuclei). Reproduced with permission.[15] Copyright 2015, Elsevier.

## 3.4 Conclusions

In conclusion, x%PCL-y%ACPCL crosslinked networks are the first SMPs with crosslinked pendant allyl groups, providing a robust, facile pendent crosslinking method to control material properties for biomedical applications. As allyl composition controls both the crystallinity and spacing of netpoints, subtle changes in molar composition result in drastic alterations in thermomechanical properties. Molecular weight and gel content can also be adjusted in this copolymerization format to fine-tune material properties. Such a convenient approach can be readily adapted to other promising polymer systems, and bioactive compounds can be incorporated into the crosslinked SMP networks to provide additional functionality. The SMPs possess excellent shape memory properties ($R_f$ and $R_r$ > 98% for most test films) and a suitable range of melting temperatures (43.4 – 29.7 $^oC$) for physiological applications. Films are compliant and ductile with appropriate elastic moduli (70.8 – 2.48 MPa) for vascular applications. Moreover, these SMPs are compatible with vascular endothelial cells (ECs), as indicated *in vitro* by high levels of cell viability (≥ 85% after 91 hours relative to TCPS) and healthy cell morphologies.

Switch-like shape responses near body temperature, tunable mechanical properties, hydrolytic degradability and vascular compatibility of x%PCL-y%ACPCL copolymers indicate a promising material for constructing stents, vascular grafts, and other medical devices. However, further studies are required before any of this translational potential can be realized. While preliminary short-term results suggest vascular compatibility, a long-term examination of *in vivo* biocompatibility and biodegradability with relevant controls and endpoints is required to adequately ensure the absence of strong host inflammatory reactions to x%PCL-y%ACPCL copolymers and its degradation products.[206] Hemocompatibility tests to assess thrombotic risks from these materials are mandatory.

Scalable fabrication techniques, packaging and storage requirements, and other additional testing requirements specific to the type of device desired would also need to be determined. For example, stents comprised of an x%PCL-y%ACPCL copolymer would also require a rational determination of device surface area and surface roughness and evaluation of radial expansion forces, pressure test ratings, fatigue, hysteresis, and radio opacity.[189, 202, 237, 249]

Another critical element that needs to be addressed for the ultimate utilization of these x%PCL-y%ACPCL copolymers in minimally-invasive applications is the demonstration of their deployment and recovery from minimally-invasive devices.[250] Depending on whether immediate or delayed onset of actuation is desired in the minimally-invasive surgical procedure and the mechanical requirements of the particular application, the physicochemical properties (i.e. molar composition, molecular weight, and gel content) of the material can be adjusted such that the implant recovers its original device-specific shape at body temperature or slightly above it via very mild resistive heating. In the latter scenario, safe and consistent supplemental heating requirements and methods would need to be determined that achieve sufficient, reliable shape recovery. Direct heating or more nuanced localized heating techniques involving ultrasound,[251] magnetic fields,[176, 252] electrical currents, [177, 253] or photothermal activation[254-258] have all been utilized towards this end. However, these latter three modes may require incorporation of magnetic nanoparticles (e.g. iron oxide), conductive materials (e.g. carbon nanotubes), or light absorbers (e.g. graphene, gold nanorods, metal complexes, carbon nanotubes, or organic dyes) [182] to produce enough heat for full shape recovery.

The readily-tunable, combinatorial nature of this SMP library provides a unique platform to elucidate unknown structure-function relationships to advance biomaterial and SMP fabrication techniques and optimize material properties for a particular application. A rationale optimization approach would involve 1) first defining the ideal outcome from administering the device (e.g. maximized radial expansion and endothelialization with minimal platelet adhesion to achieve long-term patency with no thrombotic events from stent implantation), 2) hypothesizing the ideal material characteristics to achieve these functional goals (e.g. stiffer material with enhanced surface roughness), and 3) carrying out all tests required for the specific application. 4) Examination of other studies, modeling approaches such as finite element analysis depicting the characteristic equations that determine the functional or material properties, and covariance or principle component analysis could aid in determining the physicochemical properties (e.g. molar composition, molecular weight, crosslinking density, surface roughness, surface area) that generate the desired material or functional properties. If necessary or desired, the existing x%PCL-y%ACPCL copolymer library can be iteratively expanded upon to more precisely elucidate these relationships. Future studies can examine the adaptability of this unique material design involving pendant allyl crosslinkers to other polymer systems, as well as the effects of incorporating bioactive molecules. This may be desired to achieve material and functional properties that cannot be achieved within this x%PCL-y%ACPCL copolymer library for other biomedical, aeronautical, or industrial applications.

# CHAPTER 4: AIM 2 – DESIGN OF POROUS EXTERNAL STENT

## 4.1 Introduction

The material characteristics of these SMPs - switch-like shape memory function, ductility, mechanical compliance, biodegradability and endothelial cell biocompatibility - render them potentially useful for a number of biomedical and industrial applications. A sampling of possible applications are provided by Lendlein et al.,[188] which includes uses in minimally invasive vascular and surgical applications. Based on our collaborative expertise, understanding of scientific literature, and recognition of unmet clinical needs for coronary (CABG) and peripheral bypass grafting patients (PABG) patients, it was determined to seek application of this material in the form of an external stent to improve patency of coronary and peripheral bypass grafts. Upon interviewing more than one hundred physicians and healthcare professionals through the NSF I-Corps program, a specific focus is placed on hemodialysis access patients requiring grafts due to the more acute clinical need and shorter clinical trials required for regulatory clearance. Neointimal hyperplasia is the primary culprit (>70%)[26, 42] of failures for both vein grafts and hemodialysis access sites. Another problem frequently encountered with arteriovenous fistulas (28 – 53%) is a lack of maturation or dilation to the extent that the site fails to ever be fit to support the high flow rates (>~500 mL/min) required for dialysis.[259-262]

As discussed in Chapter 2 and in Boire et al.,[263] several studies have demonstrated the promise of external stents to reduce neointimal thickening via promotion of neovascularization in the adventitia as well as through mechanical support. However, limited clinical success of these approaches has been achieved thus far, which may be due to inappropriate material selection (e.g. nondegradable, too stiff) and geometric design (e.g.

pore size and spacing, diameter, length). The overarching goals of this aim are to 1) synthesize and fabricate shape memory polymers in a manner conducive to scale up by a contract manufacturer, and 2) identify promising external stent designs in terms of their ability to promote neovascularization while minimizing inflammation and fibrosis. Immune and inflammatory responses as well as mechanical properties are also evaluated for the candidate designs. It is anticipated that SMP scaffolds comprised of different pore sizes and spacings will differ in the degree to which they elicit neovascularization, fibrogenesis, and inflammation. Candidate designs can be identified through this work that stimulate neovascularization while minimizing fibrogenesis and inflammation. Such responses are expected to promote constructive tissue remodeling, which can be further characterized by a transition from a pro-inflammatory M1 to an immunomodulatory, tissue remodeling M2 macrophage phenotype.[21] It is hypothesized that relative trends in responses to designs will translate to the arteriovenous environment in larger animals/humans and correlate with a mitigation in neointimal hyperplasia (NH) when applied as an external stent.

Pore parameters affect the surface area-to-volume ratio and topology, and play a large role in the extent and type of inflammatory reactions observed.[90, 140, 142] However, few studies have directly examined the effect of external stent pore size on neoadventitial growth and NH. George et al. observed that external macroporous (presumably 750 μm like ProVena) Dacron sheaths helically wound with polypropylene significantly reduced NH relative to microporous PTFE stents after one month in a porcine saphenous vein-to-carotid artery interposition graft model.[7] This reduction in NH was accompanied by an increase in adventitial microvessel growth (i.e. neovascularization) and a decrease in PDGF

expression and cell proliferation. Neovascularization and associated accumulation of chemoattractants (e.g. lymphocytes, neutrophils, T cells) in the interstitial space between external stent and venous tissue was observed to be inversely correlated with NH in other external stent studies.[5, 9] Although macrophage phenotypes were not characterized in these studies, this may indicate a transition to an immunomodulatory M2 phenotype. Macrophage phenotype transitions from M1 to M2 at early time points (7 – 14 days) have been shown to be predictive of more positive outcomes (i.e. constructive tissue remodeling) at later time points (e.g. 35 days)[264] and will be characterized in this study. Excessive fibrosis is undesirable as it can lead to fibrotic encapsulation[265] and has the potential to promote transdifferentiation of fibroblasts to myofibroblasts and exacerbate NH, at least to the intimal layer.[114, 115] While accumulation of chemoattractants within the interstitial space correlated with NH reduction,[5, 9] excessive inflammatory responses could also result in fibroblast transdifferentiation and lead to significant vessel wall thickening with associated hypoxia-induced NH.[56, 57, 80]

It is difficult to determine what pore sizes are ideal for an external stent's ability to reduce NH and maintain patency without controlled studies isolating influences of the material and other parameters. It is generally accepted that pores and interconnections must be larger than 50 – 100 μm to promote blood vessel ingrowth, cell invasion, and enhanced biological responses without filling the pores with scar tissue.[90, 144, 145] In general, larger pores exhibit less scarring, inflammatory infiltrate, and connective tissue.[90, 146, 147] However, pore size requirements will differ depending on the biomaterial selected and tissue applied to. For example, polypropylene requires pores larger than 1 mm while pores smaller than 650 μm are adequate for PVDF to obviate scarring between pores in

abdominal wall hernias.[148] To enhance bone tissue formation by vascularization, pore sizes greater than 300 μm are recommended.[149, 150] While no significant differences in vascularization or bone tissue ingrowth were detected over 8 weeks for PCL scaffolds (pore sizes of 350, 550, and 800 μm), Roosa et al. admitted that simultaneous changes in porosity and spacing between the groups may have influenced the results.[150] In light of these confounding factors, Bai et al. varied pore size while holding both interconnectivity and porosity constant.[145] In a rabbit model, β-tricalcium phosphate (TCP) cylinders with pores > 400 μm (i.e. 415, 557, and 632 μm) implanted into the fascia lumbodarsalis exhibited far more neovascularization than the 337 μm scaffolds.[145] Based on this information, it is hypothesized that pore sizes should be > 300 μm with spacings > 100 μm.

## 4.2 Methods

### 4.2.1 Synthesis of x%PCL-y%ACPCL copolymers

To significantly shorten and simplify the synthesis of PCL-ACPCL in order to make it amenable to scale up for a contract manufacturer, 10 kDa PCL was directly modified with LDA and allyl chloroformate instead of synthesizing α-allyl carboxylate ε-caprolactone (ACCL) monomer, purifying by column chromatography, and copolymerizing with ε-caprolactone as before. A set of reactions were conducted in which the molar ratio of LDA:CL and allyl chloroformate:CL (A:CL) were varied. Moles of CL were calculated by the following, with moles of PCL determined assuming its molecular weight is exactly 10 kDa:

**Equation 4-1:**

$$mol\ CL = \frac{mol\ PCL\ \times 10{,}000 \frac{g}{mol} PCL}{114.14 \frac{g}{mol}\ PCL}$$

Standardized conditions were established from this set of reactions. To modify 1.0 gram of 10 kDa PCL, a 4 w/v% solution of PCL in THF was added dropwise to a round-bottom flask equipped with a stir bar that contained LDA (3.6 mL of 2 M in THF/n-heptane/ethylbenzene) and 25 mL of additional THF at – 72 $^{o}$C. After transferring all of the PCL solution and maintaining the temperature at – 72 $^{o}$C for 45 more minutes, allyl chloroformate (0.80 mL) was added. The reaction vessel was then allowed to equilibrate to -30 $^{o}$C, where the temperature was maintained for 30 minutes before quenching the reaction with saturated ammonium chloride solution (6.8 mL at 0.28 g/mL). Contents were then transferred to a separatory funnel for extraction with ethyl acetate and deionized water (1:1:0.15 reaction contents: ethyl acetate: water). The organic layer was collected and solvent removed by rotary evaporation before precipitating in cold diethyl ether and vacuum drying. Yields were consistently > 90%.

### 4.2.2 Characterization of x%PCL-y%ACPCL copolymers

To calculate molar compositions of x%PCL-y%ACPCL copolymers, $^{1}$H-NMR spectra of 5 wt/v% polymer solutions in $CDCl_3$ on a 400 MHz spectrometer (Bruker Instruments, Inc., Billerica, Massachusetts) were used to determine the ratio of allylic (5.92 ($\boldsymbol{G_i}$), 5.31 ($\boldsymbol{H_{ii}}$) and 4.63 ($\boldsymbol{F_{ii}}$) ppm) (5.92, 5.31, and 4.63 ppm) to CL (4.20 ppm) proton peaks. Molecular weight properties were determined by dissolving polymer samples at a concentration of 10 mg/mL in DMF mobile phase containing 0.1% LiBr and running gel permeation chromatography (Agilent Technologies, Santa Clara, California) through three serial TSKGel Alpha columns (Tosoh Biosciences, Tokyo, Japan) at 60 $^{o}$C. Using empirically determined dn/dc values determined from refractometer measurements of

polymer dilutions, absolute molecular weight was calculated from GPC using inline Agilent refractive index and a Wyatt miniDAWN TREOS light scattering detectors (Wyatt Technology Corp. Goleta, California).

Thermal properties were measured on a Q1000 differential scanning calorimeter (DSC) (TA Instruments, Inc., New Castle, DE). $T_m$, crystallization temperature ($T_c$), $T_g$, enthalpy of fusion ($\Delta H_m$), and enthalpy of crystallization ($\Delta H_c$) are reported from the second cycle. Percent crystallinity, $X_C$, is calculated as:

**Equation 4-2:**

$X_C = \Delta H_m / \Delta H_m^o \times 100\%$, where $\Delta H_m^o$ = 139.5 J/g, the enthalpy of fusion for 100% crystalline PCL.[229].

### 4.2.3 Fabrication of crosslinked PCL-ACPCL meshes

A chloroform solution (30 wt/vol% polymer, 1 wt/v% 2,2-dimethoxy-2-phenylacetophenone) was prepared, poured onto a flat glass sheet or dish (810 $mm^2$/mL solution) and crosslinked under UV light using a Novacure 2100 Spot Curing System (Exfo Photonic Solutions, Inc., Mississauga, Ontario, Canada). Films were then solvent casted and vacuum dried.

To induce pores, 8 x 4 mm spherical pore arrays spaced evenly apart were drawn in CAD designs and cut using a Laser Engraver (KERN Laser Systems, Wadena, Minnesota) at a power of 1.5 W, speed of 0.08 in/sec, and frequency of 500 Hz. Films were then thoroughly washed in ethanol.

### 4.2.4 Pore characterization

Pore size and spacing were characterized by scanning electron microscopy (SEM). Samples were mounted onto aluminum studs covered by carbon adhesive, coated with gold and palladium, and imaged on a Quanta 250 Environmental SEM (Thermo Fisher Scientific, Waltham, Massachusetts). Pore diameter and spacing were determined by calculating the mean ± SD from individual measurements on ImageJ software (NIH, Bethesda, MD). Porosity was calculated as the ratio of void area: total area by assuming that pore diameter does not vary as a function of height and assuming that pores are exactly equidistant from one another:

**Equation 4-3:**

$$Porosity\ (\%) = \frac{2\pi\ (\frac{Diameter_{pore}}{2})^2}{\sqrt{3}(Diameter_{pore} + Spacing_{pore})^2}$$

### 4.2.5 Mechanical and shape memory characterization of PCL-ACPCL mesh designs

To determine mechanical and shape memory properties of the SMP films, pore designs (~12 mm x ~6 mm x ~0.4 mm) and nonporous controls (~12 mm x ~2 mm x ~0.4 mm) were loaded on the tensile clamp of a dynamic mechanical analyzer (TA Instruments Q2000). Similar to other works,[15, 230] tensile mechanical properties were determined isothermally at 37 $^{o}$C using a stress ramp of 0.1 MPa min$^{-1}$. The initial slope of the stress vs. strain curve was used to determine the modulus at 37 $^{o}$C, $E_{tn}$(37 $^{o}$C). Shape memory properties were determined in the same manner as Boire et al (Equation 3-3 and Equation 3-4).

### 4.2.6 Fabrication of PCL-ACPCL external stents

A viscous polymer solution (60 wt/vol%, 1% DMPA in chloroform) was prepared in a glass vial and sequentially dipped and exposed to UV light in an automated fashion utilizing a Mitsubishi RV-65DL (Mitsubishi Electric Corporation, Tokyo, Japan).

To cut pores into the stents, stainless steel mandrels were mounted onto a 3D printed holder attached to a rotary motor. The mandrel was centered under the laser to cut one line of pores on the y-shape cylinder at a time. The rotary motor was then rotated using command functions and another cut was made. This was repeated until pores covered the entire surface of the main cylinder.

### 4.2.7 Cell viability

To test cell viability of the polymers, polymer disks washed three times each with acetone, 100% ethanol, and fully supplemented DMEM under mixing were transferred to black clear-bottom 96 well plates. Human dermal fibroblast cells transfected with red fluorescent protein (HDF-RFPs) were seeded at a density of 6300 cells/cm$^2$ onto either TCPS or polymer film substrates (PCL-ACPCL and PCL positive control). After seeding, cells were supplemented with either fresh DMEM media or media leached from a 24 hour incubation with polymer films. In another test group, polymer disks were transferred into wells 30 minutes after supplementing with fresh media. At 24, 48, 96, and 168 hour timepoints, an equal volume of Cell Titer Glo solution was added to the media of each well and plates were imaged on an IVIS Lumina III imaging system (Caliper Life Sciences, Hopkinton, Massachusetts) to detect luminescence. The total number of viable cells in each

well was calculated by a standard curve of total flux (p/s) generated by TCPS controls, and %viability was calculated normalized to TCPS controls of the same seeding density.

### 4.2.8 Animal model

All animal experiments were approved by the Vanderbilt Institutional Animal Care and Use Committee (IACUC) in accordance with the NIH Guide for the Care and Use of Laboratory Animals. An initial pilot study was conducted in which a single midline incision was made on the back of 4 wild type A/J male mice for implantation of 6 different candidate PCL-ACPCL scaffold designs in the subcutaneous pocket. Scaffolds were washed with ethanol and gas sterilized prior to implantation. The 6 different designs, denoted 1A, 2A, 3A, 1B, 2B, 3B, were 4 mm x 4 mm porous arrays, sized approximately 6 mm x 6 mm x 0.4 mm in total size, with different sizes of spacing and pore diameter (Figure 4-9 and Table 4-5 Pore parameter characterization for individual and grouped designs). Mean ± standard deviation were computed for group variables (A, B, 1, 2, 3) by combining individual measurements from each design. The mice were euthenized at 14 days and the scaffolds and surrounding tissue were excised, fixed in 10% phosphate buffered formalin, sectioned 4 – 5 μm and stained with hematoxylin & eosin (H&E) by ASCP-certified biotechnicians for subsequent histological analysis by a board-certified veterinary pathologist.

Based on these results, a follow up study was conducted in which 21 mice were implanted with six 6 mm x 8 mm scaffolds: 4 candidate PCL-ACPCL porous scaffold designs (~0.4 mm thickness), a nonporous PCL-ACPCL control (~0.4 mm thickness), and a piece of Standard Wall GORETEX tubing (0.64 mm thickness). Placement of each

scaffold was randomized in terms of location. To ensure separation and minimize movement of each scaffold within the subcutaneous pocket, a separate small incision was made for each mouse. Mice were sacrificed after 4 (N = 5), 14 (N = 8), and 28 days (N = 8). Tissue embedding within and directly surrounding the samples was either flash frozen in liquid nitrogen for proteomics analysis, fixed in 2.5% glutaraldehyde with 0.1M sodium cacodylate buffer for scanning electron microscopy (SEM) imaging of scaffold-tissue interfaces, or fixed in 10% phosphate buffered formalin for immunhistochemical analysis.

### 4.2.9 Scanning electron microscopy of scaffold-tissue interfaces

After storing the glutaraldehyde-fixed samples at 4 $^{o}$C for 24 hours, samples were post-fixed with 1% osmium. Graded ethanol dehydration was then applied before critical point drying of the tissue. Once dried, samples were mounted on sticky carbon adhesive on aluminum stubs and coated with gold and palladium. Coated studs were imaged on a Quanta 250 Environmental SEM. Images were post-processed and analyzed using ImageJ software (NIH, Bethesda, MD).

### 4.2.10 Histological Analysis

All tissue samples fixed in 10% phosphate buffered formalin were processed, sectioned, and stained in Vanderbilt University's Translational Pathology Shared Resource (TPSR) by ASCP-certified biotechnicians. Samples were oriented sideways for paraffin embedding such that sections comprised a "sandwich" of polymer scaffolds surrounded by tissue on either side. Thin sections (4 - 5 μm) were cut at the polymer-tissue interface and

first stained with hematoxylin and eosin (H&E). Histological analysis was performed by a board-certified veterinary pathologist blinded to experimental conditions. Each sample was assigned semi-quantitative scores to assess the degree of neovascularization, inflammation, and fibrogenesis utilizing an established scoring criterion adapted from elsewhere.[140, 266] A composite score was calculated for samples of each design by summing the scores for each of these three categories.

**Table 4-1 Histological scoring criterion**

| Score | 0 | 1 | 2 | 3 |
|---|---|---|---|---|
| Neovascularization | No blood vessels present | Vessels only at periphery | Vessels Present within interstices but not bridging | Vessels bridge implant in at least one focus |
| Fibrogenesis | Connective tissue bridges implant in multiple foci | Connective tissue bridges implant focally | Fibrosis at periphery beginning to invest interstices | Peripheral fibrosis only |
| Inflammation | Marked: Inflammation consists of a thick, circumferential cuff of neutrophils, multinucleated giant cells, histiocytes, lymphocytes, and plasma cells | Moderate: Inflammation consists of moderate, multifocal/segmented aggregation of multinucleated giant cells, histiocytes, lymphocytes, and plasma cells with fewer neutrophils | Mild: Inflammation consists of mild, multifocal/segmental aggregates of multinucleated giant cells, histiocytes, lymphocytes, and plasma cells with fewer neuthrophils; >50% of implant's circumference is affected | Minimal: Inflammation consists of mild, multifocal aggregates of multinucleated giant cells, histiocytes, lymphocytes, and plasma cells with infrequent neutrophils; <50% of implant's circumference is affected. |

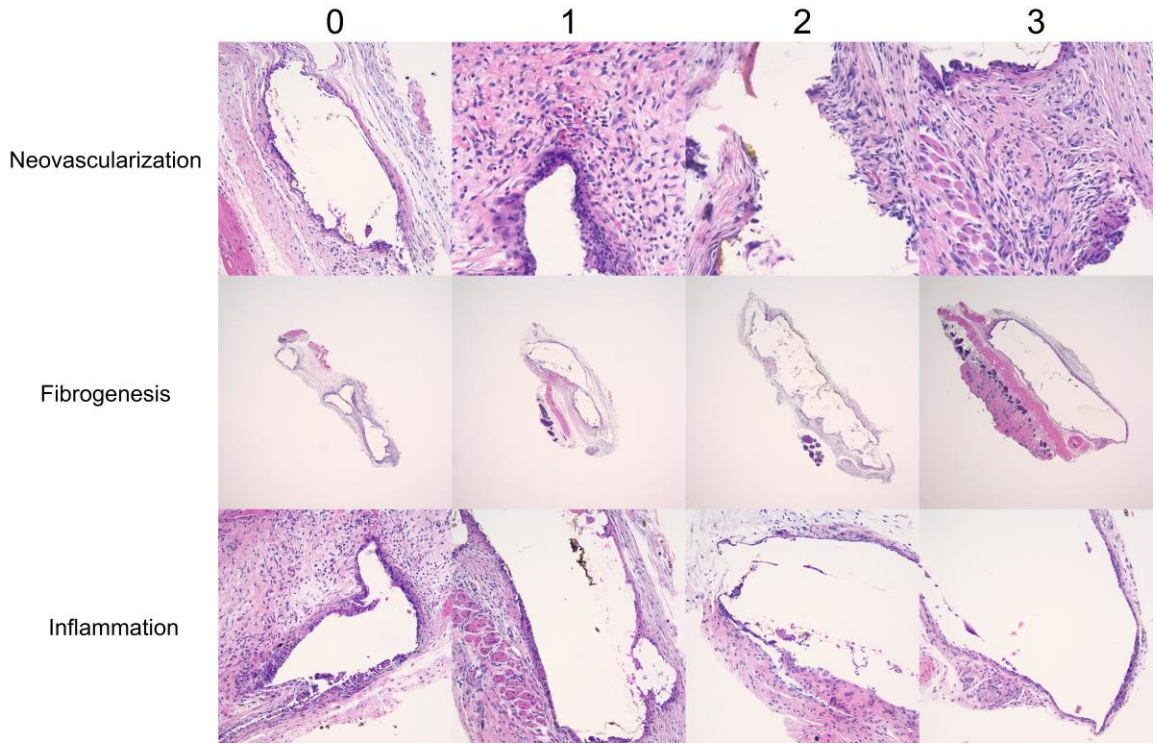


**Figure 4-1 Illustration of Histological Scoring**
Sample histological sections of the polymer-tissue interface illustrate tissue responses that correspond to a given score from 0 to 3. (Top) From left to right, sections depict a low to a high amount of neovascularization at 400x magnification. (Middle) From left to right, fibrogenesis is less apparent. (Bottom) From left to right, inflammation is milder and less marked.

### 4.2.11 Immunohistochemistry

Paraffin-embedded tissue blocks intentionally oriented to expose the polymer-tissue interface of explants were sectioned at 4-5μm and stained by ASCP-certified histotechnicians at Vanderbilt's TPSR for immunohistochemical labeling. Primary antibodies were subjected to quality control and validation processes using control tissue blocks established in TPSR. IHC was performed in a fully automated system on Leica Bond-Max autostainers (Leica Biosystems, Wetzlar, Germany). To quantify neovascularization, slides were first stained against CD31 and counterstained with DAB

(page 186 for details) before digitally imaging and scanning with an Aperio Versa 200 automated scanning microscope connected to a Leica SCN400 scanner (Leica Microsystems, Wetzlar, Germany). Using the Digital Image Hub, a web-based digital slide-viewing tool provided by the Digital Histology Shared Resource (DHSR) at Vanderbilt University, slides were imaged and quantified for neovascularization via modification of a pre-established, colorimetric-based DAB Microvessel Detection algorithm. The algorithm was optimized and regions of interest (ROIs) were drawn with the aid of a board-certified veterinary pathologist experienced in digital pathology. Algorithm specifications and ROIs were established to maximize specificity for the formation of new blood vessels contained within the tissue reaction site in close proximity (within a few hundred microns) of the polymer surface. Positive background staining of non-vascularized tissue, the polymer surface, and highly-organized, preexisting vessels were excluded from detection as much as possible. Specifications of the algorithm enables exclusion of vessels that are insignificantly small (< 60 pixel) or too large in size (> 5000 pixel) or aspect ratio (>1000) to be considered representative of a newly formed blood vessel. Further details of the algorithm are provided in the Appendix (Table C-2). The algorithm computed total number of vessels, total and average vessel area, average perimeter, and microvessel density.

To characterize macrophage phenotypes of tissue responses, primary antibodies against F4/80 (pan macrophage marker), CD206 (M2 macrophage marker), and iNOS (M1 macrophage marker) were used (See Table for a full list of antibodies). Stained slides were digitized using a Pannoramic 250 scanner. A board-certified veterinary pathologist experienced in digital pathology performed tissue image analysis in Aperio ImageScope using the Positive Pixel Count v9 algorithm. All slides were interpreted blinded to

experimental conditions. For each antibody, the algorithm was optimized in positive control tissues (primarily mouse spleen, lung, and skin) before applying to the polymer-tissue specimens; tuning mock-ups of each macrophage stain to the polymer-tissue interface are provided (Figure 4-2). For each tissue section, ROIs ranging from 1-12 total per specimen were defined prior to analysis. Depending on chronicity of the tissue response, the 50-150 μm surrounding an implant was selected for analysis, specifically excluding any undesired positively labeled structures or artifacts such as hair shafts or nonspecific DAB staining of the polymer material. Parameters reported for each specimen represent measures of positivity, which approximates the expression of a given protein within a tissue section. The output of positivity was defined for a given ROI as:

**Equation 4-4:**

$$\%\ Positivity = \frac{Total\ \#\ of\ moderately\ or\ strongly\ positive\ pixels}{Total\ \#\ of\ pixels} \times 100\%$$

Depending on the signal to noise ratio of the stain, weakly positive pixels were also included as positive in some of the samples. Similar to Brown et al.,[264] macrophage phenotype was further characterized by the ratio of M2 (CD206+) to M1 (iNOS+) cells:

**Equation 4-5:**

$$M2{:}M1 = \frac{\#\ of\ M2\ cells}{\#\ of\ M1\ cells}$$

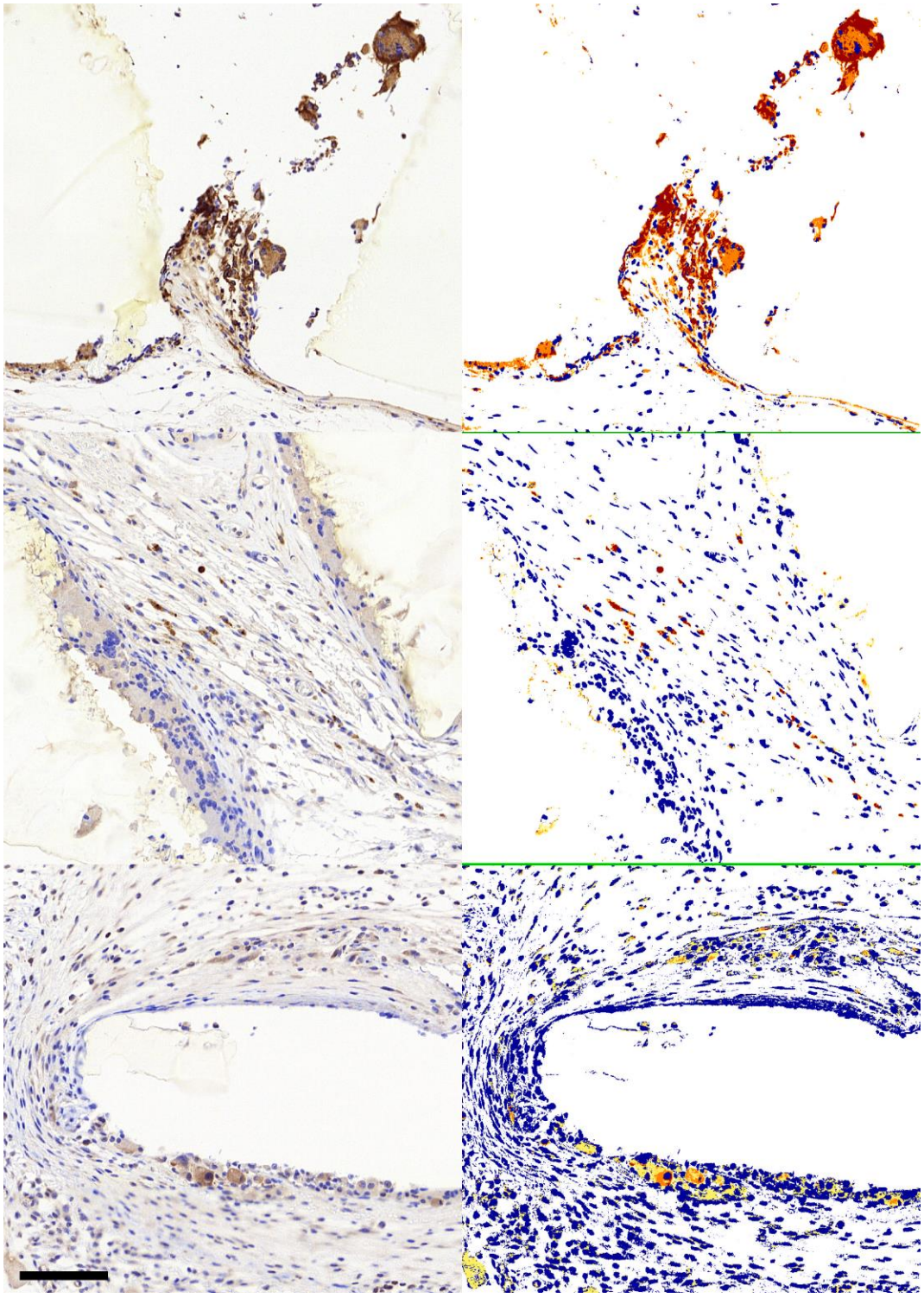

**Figure 4-2 Macrophage Phenotype Characterization**
Histological sections of polymer-scaffold interfaces used to optimize colorimetric-based quantitative algorithms to characterize macrophage phenotypes. Tissues were stained for total macrophage count by F4/80 (top), M2 macrophage phenotype by CD206 (middle), and M1 macrophage phenotype by iNOS (bottom). The three sections on the left side correspond to DAB staining results of three different histological sections, while the three

images on the right correspond to quantitative readouts of these sections using the established colorimetric detection algorithm. In the images on the right, intensity of DAB staining is depicted as a heat map, wherein blue pixels represent negative staining, yellow pixels represent weak positive staining, orange pixels represent moderate positive staining, and red pixels represent strong positive staining.

In addition to the CD31 and macrophage stains, polymer-tissue specimens were also stained for several different MMPs (MMP-3, 9, 12, 13, and 14) to further characterize the wound healing response. Slides were digitally scanned utilizing a Leica SCN400 (Leica Microsystems, Wetzlar, Germany) and quantified in terms of percent positive area utilizing color intensity-based algorithms of DAB counterstains. Masson's trichrome stain was also applied to visualize the prevalence and localization of collagen deposition as it relates to fibrogenesis induced by the scaffolds.

#### 4.2.12 Proteomics analysis

Sections of the tissue-scaffold explants were immediately placed in a cryovial and submerged for approximately 1 minute to flash freeze the tissue. Samples were then kept on dry ice for a short period of time before transferring to a -80 $^{o}$C freezer. Tissue samples were then thawed, immediately cut finely with a sterile surgical blade, and submerged in an NP-40 lysis buffer cocktail (10 mL of 50 mM Tris, 150 mM NaCl, pH 7.8 with 1% NP-40 added to protease inhibitor cocktail P2714-10TL from Sigma) under sonication for 2 – 3 minutes. The turbid solution was spun down at 2000 g for 2 minutes and the supernatant was transferred to a separate vial for storage at -80 $^{o}$C. Protein concentrations of the lysed tissue samples were determined by BCA assay.

Protein homogenates (50ug) were precipitated with ice-cold acetone overnight at -20°C. The samples were centrifuged at 14,000 *g* at 4°C for 30minutes, and the precipitated

protein pellets were washed with cold acetone, dried, and reconstituted in 500mM Tris with 50% Trifluoroethanol (TFE). Protein lysates were reduced with TCEP and available cysteine residues were alkylated with Iodoacetamide. Next, lysates were diluted 10-fold with Tris to obtain a final concentration of 10% TFE, and proteins were digested with sequencing-grade trypsin at 37C overnight.

Following digestion, protein digests were diluted 9-fold with 0.1% formic acid and each sample was analyzed by LC-coupled tandem mass spectrometry (LC-MS/MS). An analytical column (360 µm O.D. x 100 µm I.D.) was packed with 24cm of C18 reverse phase material (Jupiter, 3um beads, Phenomenex) directly into a laser-pulled emitter tip. Peptides aliquots (1.2ug of digested protein) were loaded on the capillary reverse phase analytical using a Dionex Ultimate 3000 nanoLC and autosampler and were introduced via nano-electrospray into a Q Exactive Plus mass spectrometer (Thermo Scientific, San Jose, CA). Each sample was analyzed using a 2-hour LC gradient. The Q Exactive Plus was operated in data-dependent mode, and the instrument method consisted of an MS1 scan following by up to 20 HCD MS/MS scans. Normalized collision energy was set to 27, dynamic exclusion was set to 30 s, and peptide match and isotope exclusion were enabled.

Comparisons of relative peptide and protein amounts were performed using MaxQuant-LFQ software (https://www.ncbi.nlm.nih.gov/pmc/articles/PMC4159666/). It utilizes full-scan peptide intensity determination and normalization both within and across samples. Missing values were imputed and cross group significance estimated via t-test with benjamini-hochberg correction for multiple testing.

#### 4.2.13 Statistical Analysis

Multiple group comparisons from histological scores were done using the nonparametric Kruskal-Wallis ANOVA test to detect likely differences in data distribution followed by Dunn's multiple comparison test corrected for multiple comparisons using statistical hypothesis testing. For non-ordinal data, normality was confirmed by the Shapiro-Wilk normality test and a two-way ANOVA was applied to determine whether there were sources of Type I error before doing Tukey's post-hoc tests corrected for multiple comparisons. In all cases, $p < 0.05$ is considered statistically significant. Mean ± standard deviation is reported, unless otherwise noted.

## 4.3 Results

### 4.3.1 Synthesis and characterization of PCL-ACPCL copolymers

A previous SMP library comprised of x%PCL-y%ACPCL copolymers (y = 0 – 15%) demonstrated promising material properties for biomedical applications such as switch-like shape recovery at body temperature, good shape fixity, mechanical compliance, and in vitro biocompatibility.[15] However, their synthesis required time-consuming purification of a novel monomer, ACCL. In order to avoid time-consuming purification and reduce the number of synthetic steps to make it more conducive to scale-up by a contract manufacturer for industrial and biomedical applications, x%PCL-y%ACPCL compositions were made from direct modification of PCL via LDA-induced carbanion formation and subsequent addition of allyl chloroformate at low temperatures (Figure 4-3A). A set of reactions were conducted to determine the conditions necessary to synthesize copolymers with melting temperatures and shape memory properties just below body temperature. The degree of modification, represented by y%ACPCL, was determined

by the ratio of allylic to caprolactone proton peaks as before (Figure 4-3B) and depended in large part on the mol:mol ratio of LDA:CL, with moles of CL determined from Equation 4-1:. Increasing the LDA:CL ratio from 0.2:1 to 1.2:1 results in a linear increase in y%ACPCL from 0.62% ± 0.11 to 26.4% ± 9.6 ($R^2$ = 0.99, Figure 4-4). The degree of modification continues to increase past a 2:1 LDA:CL ratio before saturating at y = 45 – 50%, as evidenced by 2.5:1 and 7.7:1 reactions yielding y = 45.0 and 47.3%, respectively. A small series of 8 test reactions were also run at fixed LDA:CL ratios to examine the effect of allyl choroformate addition (i.e. the A:CL ratio) on allyloxycarbonyl substitution (Figure B-1). The reaction does not appear to be nearly as sensitive to the amount of allyl chloroformate added. When LDA:CL was held constant at 0.99 ± 0.05 and A:CL was varied from 0.76 to 1.37 in four different reactions, allyloxycarbonyl substitution remained consistent at y = 15.3% ± 2.3. This implicates the LDA-induced carbanion formation step of the reaction as rate-limiting. Obviously, some amount of allyl chloroformate addition is too low and would affect the degree of allyloxycarbonyl substitution. In one pair of reactions, a 9-fold decrease in A:CL from 1.2 to 0.14 while keeping the LDA:CL ratio constant at 0.43 ± 0.02 reduced y from 5.3% to 1.7%, although it is unclear whether this change is significant. An excess amount of allyl chloroformate at an approximate A:CL ratio of 1:1 was used for all subsequent reactions to more definitively ensure complete reaction of allyloxycarbonyl groups with carbanion intermediates. A moderate increase in molecular weight properties was also observed when y%ACPCL surpasses 20%. This was encountered in previous studies and may be the result of the susceptibility of both PCL's polyester backbone and pendant allyl carboxylates to undergo transesterification reactions.[211, 225, 228, 267]

Also consistent with the previous x%PCL-y%ACPCL copolymer library, increasing allyl content (y%) resulted in a decrease in thermal properties such as melting temperature ($T_m$), enthalpy of fusion ($\Delta H_m$), crystallization temperature ($T_c$), and enthalpy of crystallization ($\Delta H_c$) (Figure 4-6). This shift, however, required a higher amount of allyloxycarbonyl substitution than the previous copolymerization reaction to reach a $T_m$ close to body temperature for the uncrosslinked polymers. Increasing y% from 0% to 20.8 ± 0.52% reduced $T_m$ from 53.0 ± 0.52 $^oC$ to just 45.3 ± 2.2 $^oC$, which compares to a y = 4 – 6% to achieve the same reduction with the previous copolymerization reaction. Further increasing y%ACPCL via an increase in the LDA:CL ratio resulted in y = 29.0% and 33.5 ± 1.5% copolymers with melting temperature of 38.2 ± 0.45 $^oC$ and 35.8 ± 2.7 $^oC$. This apparent disruption of PCL crystallinity also predictably coincided with a decrease in % crystallinity ($X_C$) and crystallization properties ($T_c$, $\Delta H_c$). As expected, crosslinking the polymers under UV light to form covalent bonds between the allyl groups of polymer chains further disrupted PCL crystallization and in turn further reduced $T_m$, $\Delta H_m$, $T_c$, $\Delta H_c$ (Figure 4-6C and D). In crosslinked form, increasing y from 4.1 ± 1.8% to 20.8 ± 0.52%, 29.0%, and 33.5 ± 1.5% decreased the melting temperature from 50.4 ± 2.2 $^oC$ to 39.1 ± 1.1 $^oC$, 34.4 ± 0.51 $^oC$ and 31.0 ± 2.7 $^oC$, respectively. Similar trends were observed for other properties.

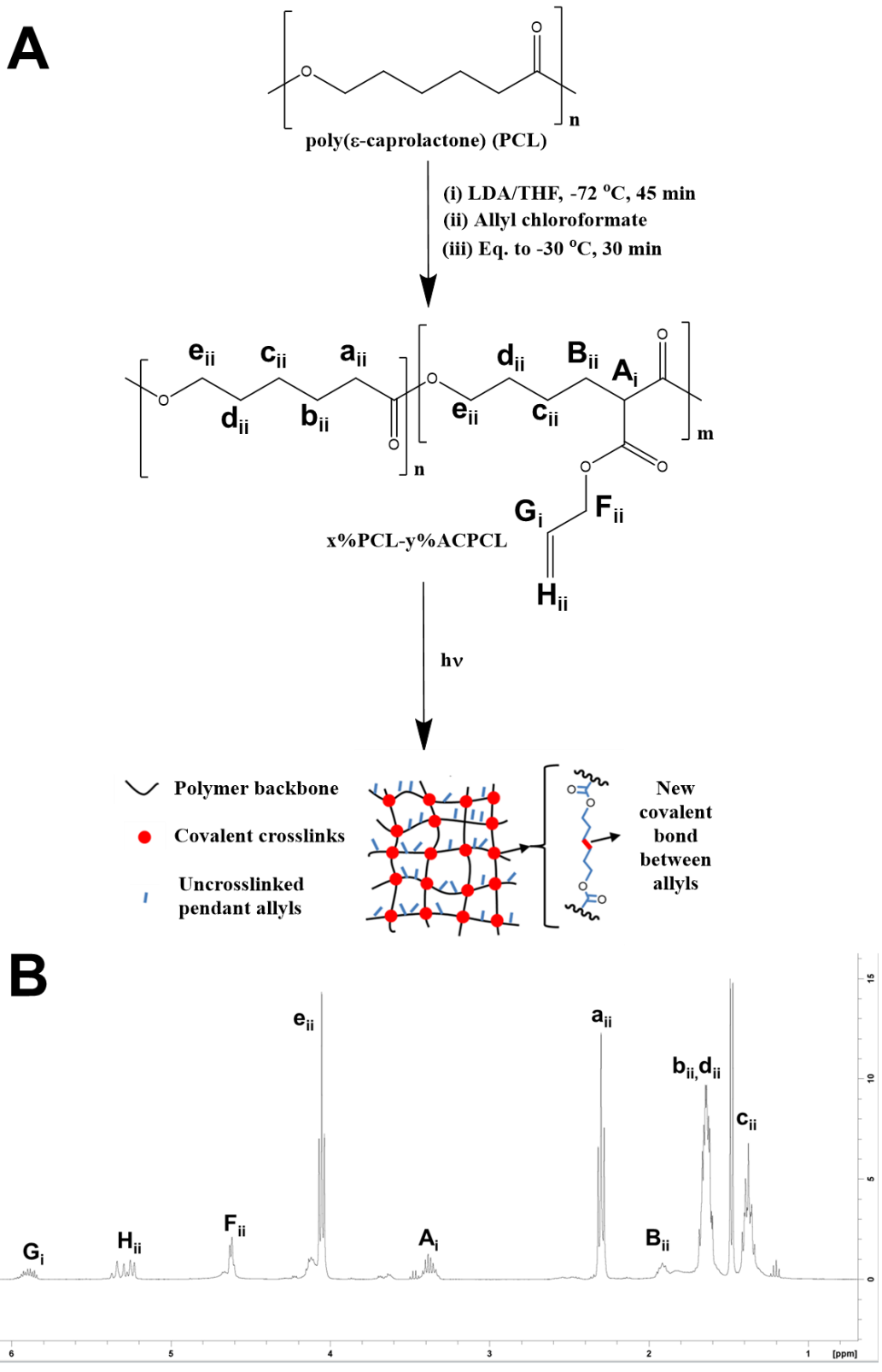


**Figure 4-3 Synthetic Scheme for x%PCL-y%ACPCL synthesis via direct LDA modification by LDA**

(A) PCL is mixed in dropwise to a solution containing LDA in THF at -72 °C before addition of allyl chloroformate, equilibration to -30 °C, and quenching with a saturated ammonium chloride solution. (B) $^{1}$H-NMR of 79.8%PCL-20.2%ACPCL synthesized by this reaction (400 MHz, $CDCl_3$, 25 °C, TMS): δ = 5.92 (m, 1H;, -C**H**=$CH_2$ (***G**$_i$*)), 5.31 (m, 2H; -CH=C**H**$_2$ (***H**$_{ii}$*)), 4.63 (m, 2H; -CH=C**H**$_2$O (***F**$_{ii}$*)), 4.15 (m, 2H; -OC**H**$_2$ (***e**$_{ii}$*)), 3.35 (m, 1H; -C**H**-$CH_2$ (***A**$_i$*)), 2.33 (t, $^{3}$J(H,H) = 7.5 Hz, 2H; -C**H**$_2$ (***a**$_{ii}$*)), 1.96 (m, 2H; -C**H**$_2$ (***B**$_{ii}$*)), 1.62 (m, 4H; -C**H**$_2$ (***b**$_{ii}$*,***d**$_{ii}$*)), 1.39 ppm (m, 2H; -C**H**$_2$ (***c**$_{ii}$*)).

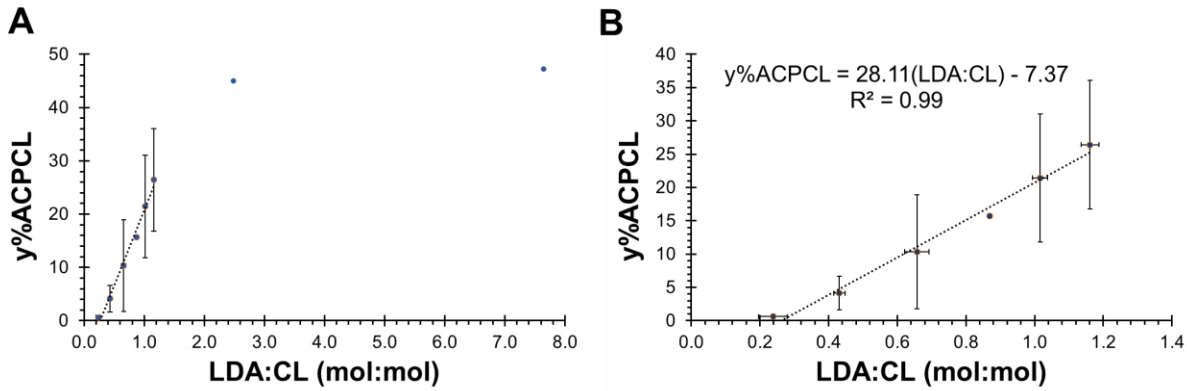


**Figure 4-4 Effect of LDA:CL feed ratio on y%ACPCL**
The degree of allyloxycarbonyl substitution, represented as y%ACPCL in the x%PCL-y%ACPCL copolymer, is dependent on the amount of LDA fed into the reaction with PCL. This relationship is linear beyond a 1.2:1 ratio and increases past a 2:1 ratio before apparently saturating at y = 45 – 50%. Where replicate reactions are combined, error bars indicate mean ± standard deviation.

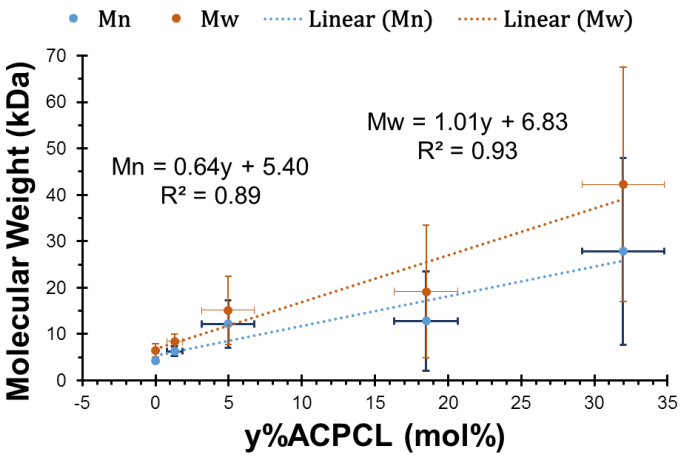


**Figure 4-5 Effect of y%ACPCL on molecular weight properties**
A moderate increase $M_w$ (less so in $M_n$) appears to accompany an increase in y%ACPCL as y is increased past 20%. The higher $M_w$ and polydispersity index (PDI, $M_w/M_n$) is consistent with previous studies and may be due to an increase in transesterification reactions at higher allyl compositions.

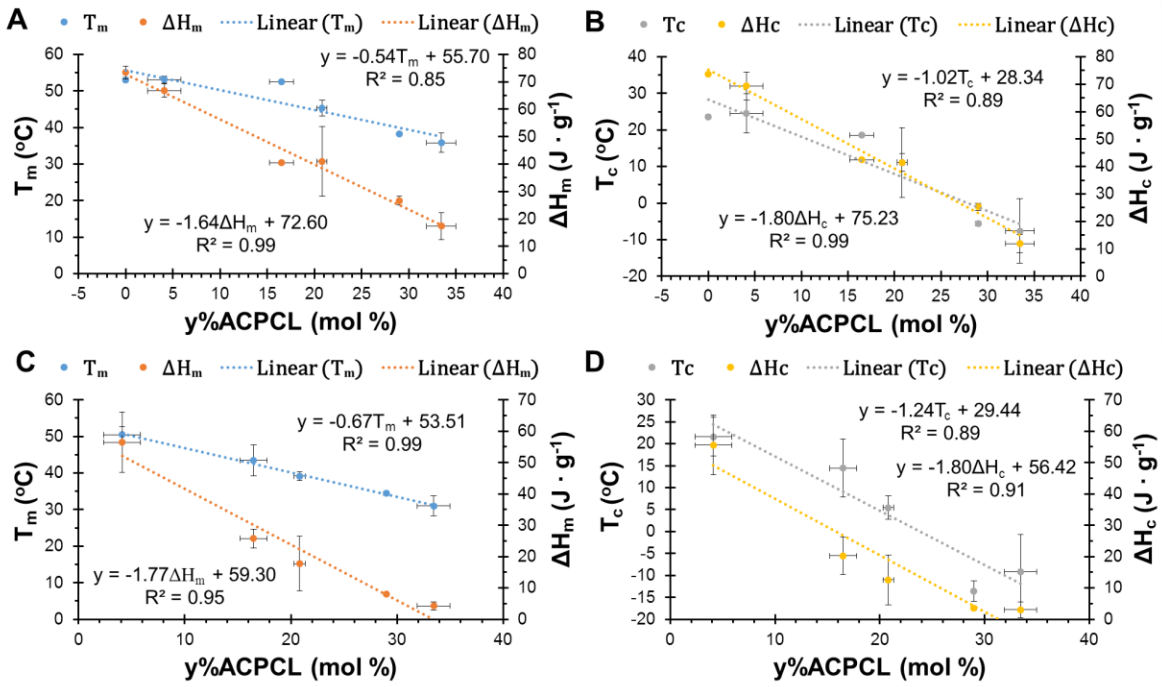


**Figure 4-6 Effect of y%ACPCL on Thermal Properties**
Increasing allyl content (y%ACPCL) results in a decrease in melting temperature ($T_m$), enthalpy of fusion ($\Delta H_m$), crystallization temperature ($T_c$), and enthalpy of crystallization ($\Delta H_c$) and indicates the strong dependence of thermal properties of this copolymer system on this molar ratio.

**Table 4-2 Thermal Properties of x%PCL-y%ACPCL Copolymers from LDA-based modification before crosslinking**

| y% in x%PCL-y%ACPCL | $T_m$ ($^oC$) | $\Delta H_m$ (J $g^{-1}$) | $X_C$ (%) | $T_c$ ($^9C$) | $\Delta H_c$ (J $g^{-1}$) | $T_g$ ($^oC$) |
|---|---|---|---|---|---|---|
| 0% (10 kD PCL) | 53.0 ± 0.6 | 73..3 ± 2.4 | 52.6 ± 1.7 | 23.6 ± 0.55 | 73.7 ± 0.49 | -66.5 ± 0.79 |
| 4.1 ± 1.8% | 53.1 ± 1.0 | 66.7 ± 2.5 | 47.8 ± 1.8 | 24.5 ± 5.4 | 69.3 ± 5.1 | -66.9 ± 0.35 |
| 16.5 ± 1.3% | 52.5 ± 2.1 | 41.2 ± 1.1 | 29.5 ± 0.75 | 19.3 ± 0.74 | 42.6 ± 0.11 | -56.4 ± 2.6 |
| 20.8 ± 0.52% | 45.3 ± 2.1 | 41.0 ± 12.8 | 29.4 ± 9.2 | 11.1 ± 2.4 | 41.4 ± 12.8 | -52.8 ± 4.1 |
| 29.0% | 38.2 ± 0.45 | 26.6 ± 1.6 | 19.0 ± 1.1 | -5.64 ± 0.58 | 25.3 ± 1.3 | -49.5 ± 1.9 |
| 33.5 ± 1.5% | 35.8 ± 2.7 | 17.3 ± 4.8 | 12.4 ± 3.5 | -7.62 ± 8.8 | 11.9 ± 3.3 | -53.7 ± 1.5 |

**Table 4-3 Thermal Properties of UV-crosslinked x%PCL-y%ACPCL Copolymer Films from LDA-based modification**

| y% in x%PCL-y%ACPCL | $T_m$ ($^oC$) | $\Delta H_m$ (J $g^{-1}$) | $X_C$ (%) | $T_c$ ($^9C$) | $\Delta H_c$ (J $g^{-1}$) | $T_g$ ($^oC$) |
|---|---|---|---|---|---|---|
| 0% (10 kD PCL) | 53.0 ± 0.6 | 73..3 ± 2.4 | 52.6 ± 1.7 | 23.6 ± 0.55 | 73.7 ± 0.49 | -66.5 ± 0.79 |
| 4.1 ± 1.8% | 53.1 ± 1.0 | 66.7 ± 2.5 | 47.8 ± 1.8 | 24.5 ± 5.4 | 69.3 ± 5.1 | -66.9 ± 0.35 |
| 16.5 ± 1.3% | 52.5 ± 2.1 | 41.2 ± 1.1 | 29.5 ± 0.75 | 19.3 ± 0.74 | 42.6 ± 0.11 | -56.4 ± 2.6 |
| 20.8 ± 0.52% | 45.3 ± 2.1 | 41.0 ± 12.8 | 29.4 ± 9.2 | 11.1 ± 2.4 | 41.4 ± 12.8 | -52.8 ± 4.1 |
| 29.0% | 38.2 ± 0.45 | 26.6 ± 1.6 | 19.0 ± 1.1 | -5.64 ± 0.58 | 25.3 ± 1.3 | -49.5 ± 1.9 |
| 33.5 ± 1.5% | 35.8 ± 2.7 | 17.3 ± 4.8 | 12.4 ± 3.5 | -7.62 ± 8.8 | 11.9 ± 3.3 | -53.7 ± 1.5 |

After generating consistent results using a 1:1:1 ratio of LDA:CL:allyl chloroformate, it was desired to scale up polymer synthesis to do extensive experiments including *in vivo* studies and external stent prototype fabrication, and make PCL-ACPCL copolymers more palatable for commercial applications. A cGMP contract manufacturer (Silar Laboratories, Scotia, New York) was hired to synthesize a 200 g batch of PCL-ACPCL utilizing the optimized LDA modification protocol. As it was its first time conducting this synthesis, Silar prudently decided to break up the reaction into two separate 100 g batches and verify whether allyloxycarbonyl substitution on PCL was successfully achieved. This substitution was verified by Silar by running FTIR on the resultant polymer after quenching the reaction with ammonium chloride solution and working up a small quantity of the reaction. FTIR spectra for the two 100 g batches were consistent with this substitution: the appearance of a C=C bond stretch (1649 $cm^{-1}$), an olefinic C-H stretch (3085 $cm^{-1}$), and a more pronounced carbonyl C=O peak (1728 $cm^{-1}$) (Figure 4-7). The quenched reaction solution was shipped to Vanderbilt University where it was extracted with ethyl acetate and water, dried on a rotary evaporator and under vacuum, washed several times with methanol solution, and precipitated with cold diethyl ether. After drying the solution under vacuum, allylic and CL peaks on $^{1}$H-NMR spectra (Figure 4-3) determined the composition of the synthesized polymer batch to be 67.6%PCL-32.4%ACPCL. (68%PCL-32%ACPCL). GPC run in DMF running buffer on an Agilent system equipped with refractive index and light scattering detectors determined its absolute molecular weight properties, indicating an $M_n$ = 9390 Da and polydispersity index (PDI, $M_w/M_n$) = 2.20. Thermal properties measured by DSC revealed this polymer composition to have a $T_m$ = 38.2 ± 0.13 $^oC$ and 32.8 ± 2.8 $^oC$ before and after cross-linking, respectively.

This melting temperature is ideal for biomedical engineering applications that rely on the ability of shape memory polymers to recover their device form (i.e. in the shape of a stent) from a minimally invasive surgical device at body temperature. It could also prove advantageous in the context of external stenting by potentially obviating the need for addition sutures to fit around venous anastomoses. A summary of the polymer's thermal properties before and after crosslinking are provided in Table 4-4below.

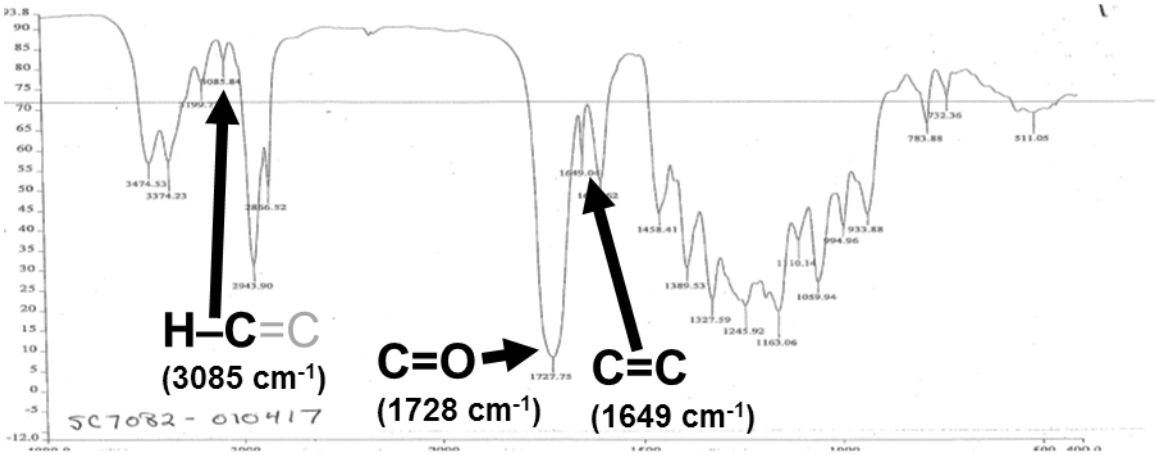


**Figure 4-7 FTIR Spectra from x%PCL-y%ACPCL Synthesis by Silar Laboratories**
FTIR spectra reveal the appearance of a C=C bond stretch (1649 $cm^{-1}$), an olefinic C-H stretch (3085 $cm^{-1}$), and a more pronounced carbonyl C=O stretch peak (1728 $cm^{-1}$). This provided evidence of the successful substitution of the allyl carboxylates, which was also confirmed by $^{1}$H-NMR.

**Table 4-4 Thermal properties of 68%PCL-32%ACPCL synthesized by Silar**

| y% in x%PCL-y%ACPCL | $T_m$ (°C) | $\Delta H_m$ (J $g^{-1}$) | $X_C$ (%) | $T_c$ (°C) | $\Delta H_c$ (J $g^{-1}$) | $T_g$ (°C) |
|---|---|---|---|---|---|---|
| Before crosslinking | 38.2 ± 0.13 | 15.8 ± 7.1 | 11.3 ± 5.1 | 0.40 ± 0.25 | 10.9 ± 4.4 | -52.8 ± 0.10 |
| After crosslinking | 32.8 ± 2.8 | 4.94 ± 1.6 | 3.54 ± 1.2 | -16.3 ± 5.1 | 4.31 ± 3.2 | -50.6 ± 4.0 |

### 4.3.2 External stent fabrication

An in-house method for external stent fabrication involving dip casting and laser ablation has also been realized in consultation with Medical Murray that is conducive to high volume prototyping and production manufacturing by a cGMP manufacturer (Fig. 4).

Viscosity, speed of withdrawal, and spinning while exposed to UV light have been optimized to enable fabrication of external stents with relatively uniform thickness. Consistent pores can be generated utilizing a KERN laser engraver affixed to a rotary motor.

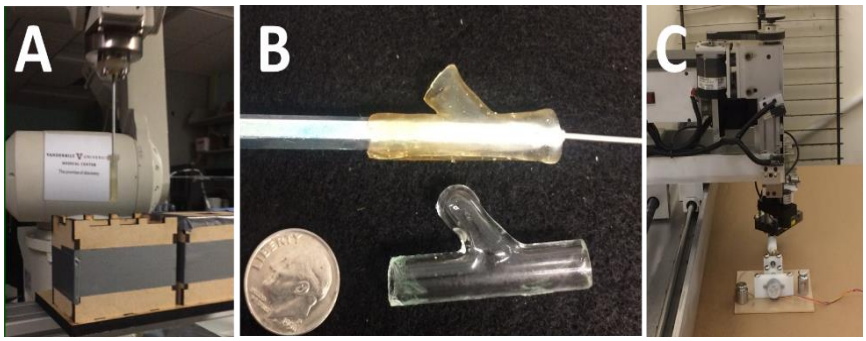


**Figure 4-8 External Stent Fabrication**
A) Dip-casting of stainless steel mandrels into polymer solutions while exposed to UV light enables crosslinking of y-shape external stents (B). C) KERN laser engraver affixed to a rotary motor enables line by line cutting of pores into prototypes.

### 4.3.3 Pilot animal study

All animal work was done in accordance with Vanderbilt University's Institutional Animal Care and Use Committee (IACUC). To provide some indication of which pore layout in terms of pore size (i.e. pore diameter) and spacing may elicit more neovascularization with more favorable inflammatory and fibrogenic responses, 6 different PCL-ACPCL pore arrays with varying pore sizes and spacings were first prepared for implantation. Numbers of the design denote pore diameter size (1 = 293 ± 41 μm, 2 = 665 μm ± 24 μm, 3 = 1067 ± 35 μm), whereas letters indicate spacing distance (A = 172 ± 55 μm, B = 224 ± 56 μm). Two weeks after implantation of the scaffolds in the subcutaneous pocket in the back of 4 mice, H&E-stained subcutaneous mouse tissue directly surrounding and embedded with the porous PCL-ACPCL scaffold designs revealed varying degrees of neovascularization, inflammation, and fibrogenesis (Figure 4-1). The semi-quantitative

histological scoring criterion adapted from elsewhere (Table 2-1)[140, 266] was applied to each sample for neovascularization, inflammation, and fibrogenesis by a board-certified veterinary pathologist, and a cumulative score was calculated by summing of each histological criterion (Figure 4-10). A nonparametric Kruskal-Wallis one-way ANOVA indicated that no significant differences in distribution were detected amongst the groups for the 4 categorical values that were tabulated (p-values of neovascularization = 0.3547, inflammation = 0.1207, fibrogenesis = 0.1547, cumulative score = 0.1013). Nonetheless, some interesting observations can be derived from this power-limited pilot study. For all of the groups tested except for Design 1A, neovessels bridged the implant in at least one focus (Neovascularization Score = 3, Table 4-1) on day 14 for at least one of the 3 – 4 samples tested. All of the designs tested except for 1B and 3B also had a sample with no observable neovessels by H&E staining (Neovascularization Score = 0). Extent of inflammation was assessed by the relative abundance of multinucleated giant cells, histiocytes (i.e. tissue macrophages or dendritic cells), lymphocytes, plasma cells, and neutrophils. Marked inflammation, as evidenced by a thick, circumferential cuff of inflammatory cells around the implant, was detected for at least one of the samples of Designs 1A and 3A. Inflammatory responses of other samples, including at least one of those from Designs 1A and 3A, were more moderate or mild in nature, with less aggressive aggregation of multinucleated giant cells, fewer neutrophils, and the area surrounding the implant less affected (Inflammation Score $\geq$ 1, with Inflammation Score = 3 being the mildest). Connective tissue bridges the implant at multiple foci for at least one sample of Designs 2A, 3A, and 1B (Fibrogenesis Score = 0) and at least bridges the implant focally for at least one sample of each design except for Design 1A. Designs 1A and 3B both had

at least one sample in which fibrosis was limited to the periphery of the implant (Fibrogenesis Score = 3). Cumulative scores for the designs ranged from 2 – 7, with the highest median and mean score (Cumulative Score = 6) achieved from Design 3B.

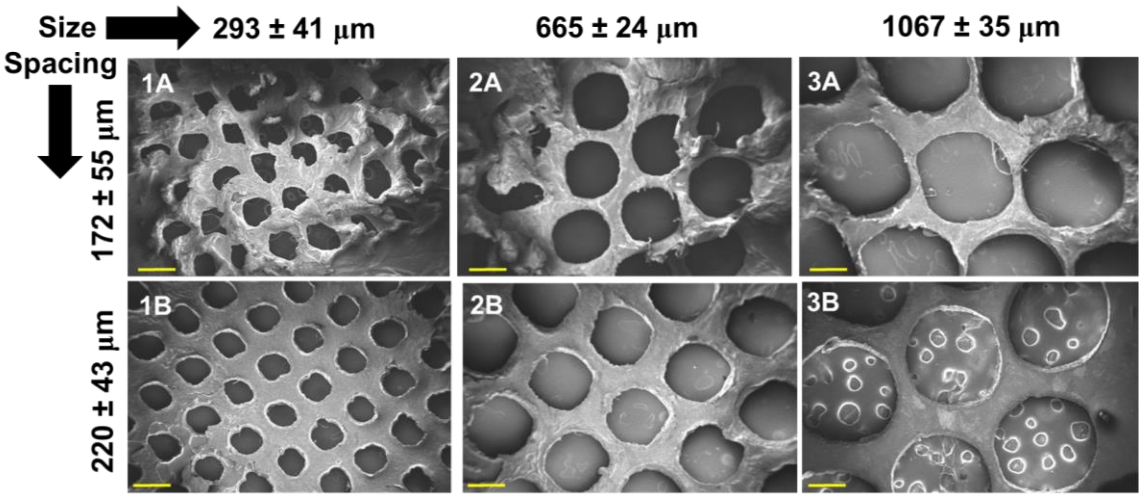


**Figure 4-9 PCL-ACPCL porous scaffold designs for pilot in vivo study**
SEM micrographs of porous scaffold designs are displayed with equivalent pore spacing in rows and pore sizes in columns (scalebar = 400 µm).

**Table 4-5 Pore parameter characterization for individual and grouped designs of pilot study**

| Design | Diameter (µm) | Spacing (µm) | Void Area ($mm^2$ x $10^3$) | Porosity (%) |
|---|---|---|---|---|
| 1A | 273 ± 42 | 198 ± 68 | ~117 | ~30 |
| 2A | 658 ± 26 | 152 ± 46 | ~680 | ~60 |
| 3A | 1040 ± 25 | 124 ± 29 | ~1700 | ~72 |
| 1B | 320 ± 17 | 220 ± 35 | ~160 | ~32 |
| 2B | 671 ± 20 | 225 ± 51 | ~710 | ~51 |
| 3B | 1100 ± 29 | 243 ± 89 | ~1900 | ~61 |
| A | 273, 658, 1040 | 172 ± 54 (198, 152, 124) | ~117, 680, 1700 | 30, 60, 72 |
| B | 320, 671, 1100 | 224 ± 56 (220, 225, 243) | ~160, 710, 1900 | 32, 51, 61 |
| 1 | 293 ± 41 (273, 320) | 198, 220 | ~117, 160 | 30, 32 |
| 2 | 665 ± 24 (658, 671) | 152, 225 | ~680, 710 | 60, 51 |
| 3 | 1067 ± 35 (1040, 1100) | 124, 243 | ~1700, 1900 | 72, 61 |

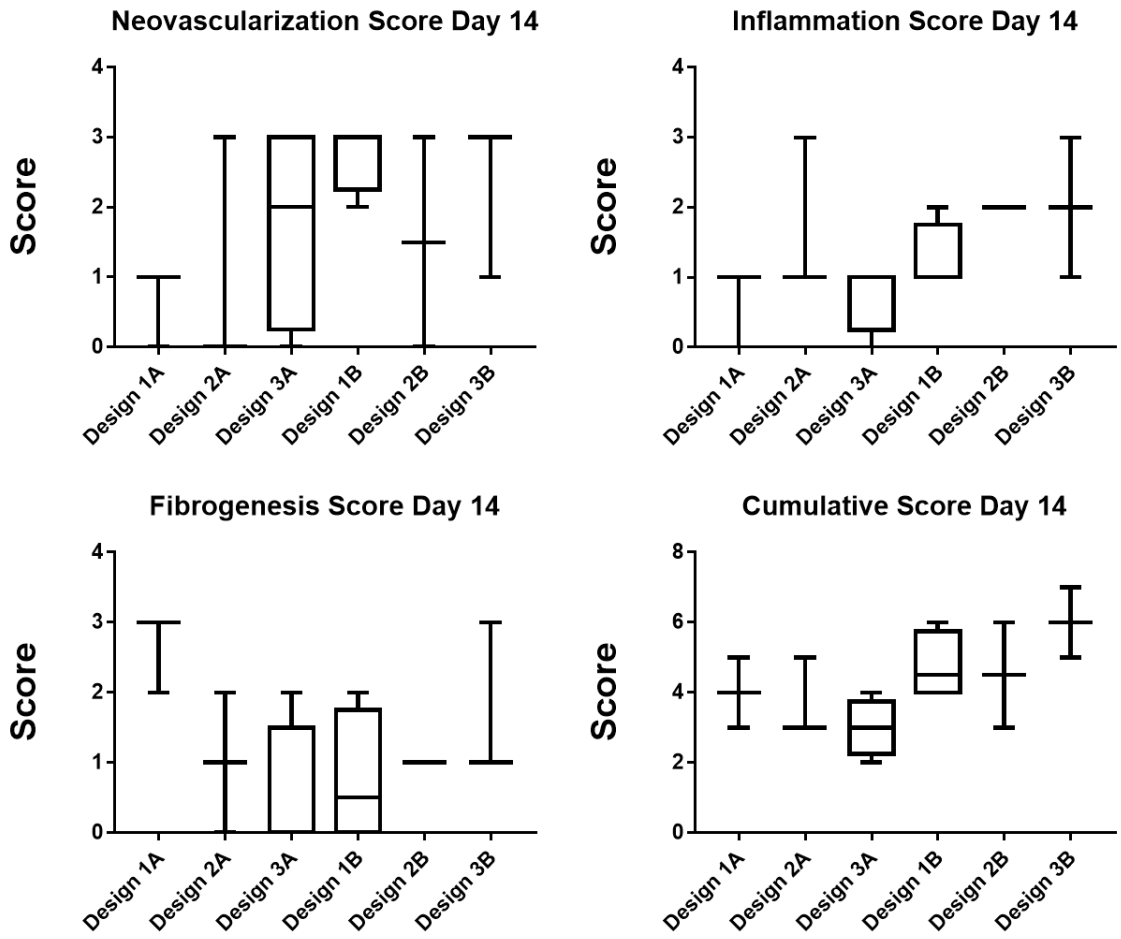


**Figure 4-10 Histological Scoring Results from pilot study**
Box & whiskers plots of histological data from pilot study (N = 3 – 4 mice), with large horizontal lines indicating median values, solid vertical lines indicating range, and boxes indicating standard deviation. A nonparametric Kruskal-Wallis one-way analysis of variance (ANOVA) of each output indicated no statistically different differences in distributions amongst the groups (p-values of neovascularization = 0.3547, inflammation = 0.1207, fibrogenesis = 0.1547, cumulative score = 0.1013).

The overall winning design of this study is unclear because no statistically significant differences were detected between the groups by Kruskal-Wallis ANOVAs and Dunn's post-hoc tests, and preferences of the desired responses depend on how these criterion are prioritized for the particular *in vivo* application. Based on previous external stent studies that have found a reduction in neointimal hyperplasia to vein grafts to be

correlated inversely with the degree of adventitial angiogenesis, it is hypothesized that prioritization should be placed on neovascular responses to implant designs. It may also be desirable to mitigate inflammation and fibrosis to promote constructive remodeling and avoid potential complications such as immune rejection which could compromise the safety and performance of the device. Therefore, although it is a highly-imperfect measure based only on semi-quantitative information, it is hypothesized that a higher Cumulative Score is also indicative of a more favorable and/or biocompatible outcome. Although no statistically significant differences were detected for these ordinal, semi-quantitative variables as previously discussed, combining the designs into groups of equivalent pore size (Groups 1, 2, and 3) and spacing (Groups A and B) (Table 4-5) did render some interesting results. A summary table of statistical comparisons is summarized in Table 3. Before making any conclusions from this analysis, statistical differences between pore sizes for the pore size groups (1, 2, and 3) and between pore spacing for the pore spacing groups (A and B) were confirmed through statistical testing, assuming that these parameters approximate a normal distribution with equivalent variances between groups. A one-way ANOVA analysis followed by Tukey's post-hoc indicated statistically significant differences in pore size between groups 1, 2, and 3 ($p < 0.0001$), and an unpaired student t-test comparing pore spacing of groups A and B also detected statistically significant differences in pore spacing between A and B ($p = 0.0031$). Grouping designs in this way provided a means to more meaningfully compare the effects of pore size and spacing on histological outcomes. While the Kruskal-Wallis test of Groups 1, 2, and 3 on histological outcomes did not detect any significant differences in distribution, a two-tailed Mann-Whitney test detected a statistically significant difference in Cumulative Score when

comparing pore spacing groups A and B (p = 0.0099) (Table 4-6). This suggests that semi-quantitative assessment of overall tissue responses from the established histological scoring criterion are likely to differ between groups A (pore spacing = 172 ± 55 μm) and B (pore spacing = 224 ± 56 μm). This statistical result and the observation of a higher median and mean Cumulative Score for Group B compared to Group A (Figure 4-11) suggests that it is possible PCL-ACPCL scaffolds with more spaced out pores elicit more favorable tissue responses by some combination of more neovascularization and/or less inflammation and fibrosis in comparison to closer-spaced pores.

**Table 4-6 Statistical Comparison Summary of Designs Grouped by Equivalent Pore Size and Spacing from Pilot Study**

| | | Histological Outcome Assessed | | | |
|---|---|---|---|---|---|
| **Parameter Compared** | **Statistical Test** | **Neovascularizataion** | **Inflammation** | **Fibrogenesis** | **Cumulative Score** |
| Pore size | Kruskal-Wallis | p = 0.5513, ns | p = 0.2733 | p = 0.6036 | p = 0.7959 |
| Pore spacing | Mann-Whitney | p = 0.0812, ns | p = 0.0516, ns | p = 0.827, ns | p = 0.0099** |

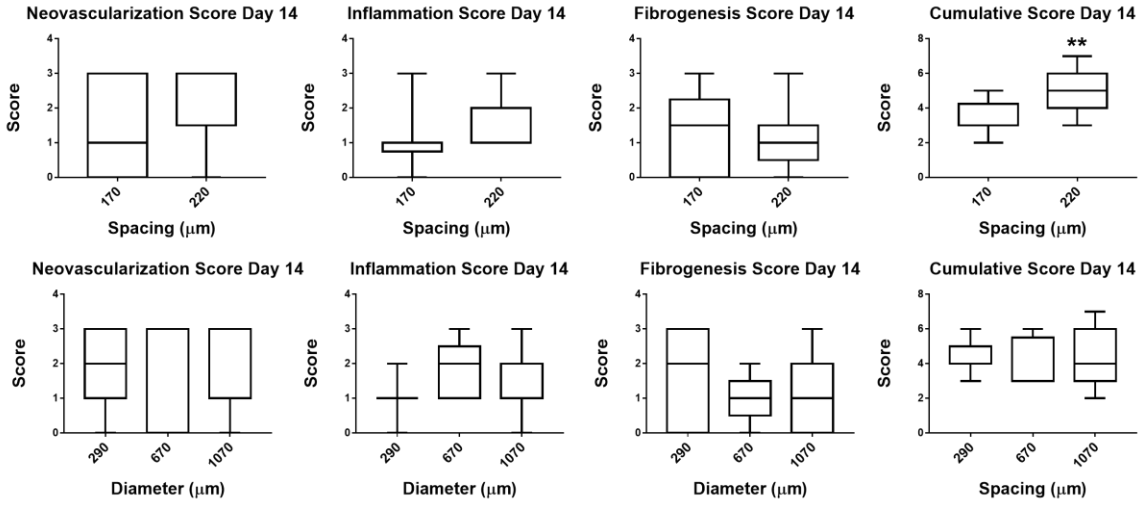


**Figure 4-11 Side-by-side Comparison of Pore Size and Spacing Effects on Histological Outcomes for Pilot Study**

Grouped designs in terms of pore size and pore spacing are plotting for each outcome from the pilot study. A statistically significant difference was detected from a Mann-Whitney test, which suggests that there is likely some difference in overall tissue responses for designs with different pore spacings.

### 4.3.4 Larger mouse cohort

#### 4.3.4.1 Pore Design Characterization

To further evaluate this hypothesis and see if a promising candidate design can be identified for external stenting applications, a larger mouse study was planned that, according to the proportional odds model,[268, 269] was to provide > 80% power to detect meaningful differences ($p < 0.05$) in Cumulative Score between high and low spacing groups on a logarithmic scale, assuming a similar distribution to the smaller study (Figure C-1). The scaffolds used for the in vivo study were 4 different candidate pore designs of 68%PCL-32%ACPCL (A – D) paired for pore size and spacing as well as two nonporous or microporous controls: non laser-ablated 68%PCL-32%ACPCL (E) and a ~6 mm x 8 mm x 0.64 mm piece of commercially-available Standard Wall GORETEX tubing comprised of expanded polytetrafluoroethylene (ePTFE) and reported to have micropores 10 – 30 μm in diameter (F) (Table 4-7). Prior to implantation, pore size and spacing were measured from SEM images of 4 – 8 different scaffolds for each porous design (Figure 4-12). Results were statistically analyzed with a one-way ANOVA followed by Tukey's post-hoc tests adjusted for multiple comparisons in order to evaluate how closely paired designs were in terms of size and spacing (Table 4-8). Designs intended to have different pore spacings (i.e. A,B vs. C,D) had a mean difference of 68.1 – 88.0 μm ($p < 0.0001$), whereas paired designs (i.e. A and B,C and D) had mean differences of 7.1 and 12.7 μm that were not statistically significant. Mean differences between designs with different pores sizes were > 500 μm ($p < 0.0001$) compared to just 13.4 and 41.0 μm for groups paired by pore size (A,C and B,D) that were not significant. The design library therefore possesses only two

unique pore spacings (151 ± 50 μm (A,B) and 229 ± 51 μm (C,D) paired) and two unique pore sizes (635 ± 51 μm (A,C) and 1160 ± 64 μm (B,D) paired), providing a convenient means to separately evaluate pore size and spacing effects on material properties and *in vivo* responses.

**Table 4-7 Pore properties for larger mouse cohort**

| Design | Polymer | Pore Diameter (μm) | Spacing (μm) | Estimated Void Area ($mm^2$ x $10^3$) | Estimated Porosity (%) | $E_{tn}$(37 °C) (MPa) | $\varepsilon_{max}$ (%) | $\sigma_{max}$ (MPa) |
|---|---|---|---|---|---|---|---|---|
| A | 68%PCL-32%ACPCL | 627 ± 50 | 148 ± 45 | ~620 | ~59 | 0.92 ± 0.26 | 60.0 ± 13 | 0.15 ± 0.03 |
| B | 68%PCL-32%ACPCL | 1180 ± 78 | 155 ± 52 | ~2200 | ~71 | 0.57 ± 0.25 | 106 ± 17 | 0.17 ± 0.02 |
| C | 68%PCL-32%ACPCL | 640 ± 71 | 223 ± 42 | ~640 | ~50 | 1.08 ± 0.50 | 78 ± 65 | 0.26 ± 0.06 |
| D | 68%PCL-32%ACPCL | 1140 ± 86 | 226 ± 58 | ~2000 | ~62 | 1.11 ± 0.12 | 76 ± 46 | 0.29 ± 0.08 |
| E | 68%PCL-32%ACPCL | Non/micro | N/A | N/A | N/A | 2.4 ± 0.86 | 52 ± 30 | 0.44 ± 0.09 |
| F | GORETEX (ePTFE) | 10 – 30 μm[1] | N/A | N/A | N/A | 15.5 ± 1.6[1] | 139 ± 11[1] | 24.3 ± 1.8[1] |
| 150 | 68%PCL-32%ACPCL | 635, 1160 | 151 ± 50 | ~620, 2200 | ~59, 71 | 0.9, 0.57 | 60, 110 | 0.16 |
| 230 | 68%PCL-32%ACPCL | 635, 1160 | 229 ± 51 | ~640, 2000 | ~50, 62 | 1.1 | 78, 72 | 0.26 |
| 640 | 68%PCL-32%ACPCL | 635 ± 63 | 151, 229 | ~ 630 | ~59, 50 | 0.92, 1.1 | 60, 78 | 0.15, 0.26 |
| 1160 | 68%PCL-32%ACPCL | 1160 ± 64 | 151, 229 | ~2100 | ~71, 62 | 0.57, 1.1 | 110, 72 | 0.17, 0.26 |
| 0 – 30 | PCL-ACPCL, ePTFE | 0 – 30 | N/A | N/A | N/A | 2.4, 15.5 | 52, 139 | 0.44, 24.3 |

[1]Values reported from Lai et al for 12 mm x 4 mm x 1 mm thick ePTFE specimens in a dog bone shaped-design strained at a rate of 0.1 mm/s from.[270] For the sake of comparison, displacement reported was converted to a % by dividing by the original length of 12 mm and multiplying by 100%.

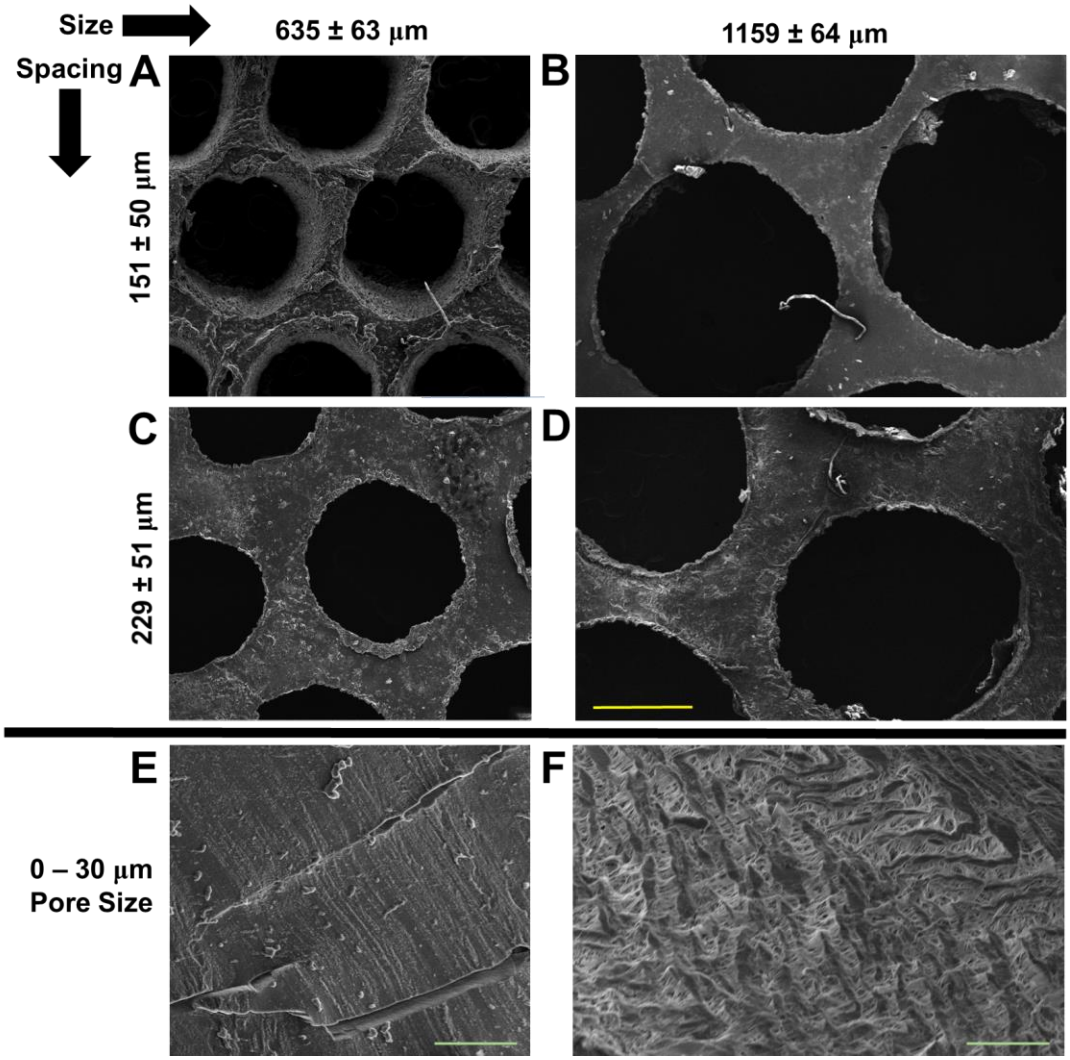


**Figure 4-12 Pore designs for larger mouse cohort**

SEM micrographs of the six scaffolds used as implants in the larger mouse cohort evaluating neovascularization, inflammation, and fibrogenesis over the course of 28 days. Macroporous Designs A - D are paired by equivalent size and spacing to evaluate the influence of these parameters on *in vivo* responses. Images are scaled to the same magnification for A - D (top yellow scale bar = 500 μm), while nonporous PCL-ACPCL (Design E) and microporous ePTFE (Design F) implants are shown at 10X of this magnification (bottom green scale bar = 50 μm).

**Table 4-8 Statistical Summary of Pore Parameter Comparisons for Scaffold Designs**

| | Pore Spacing | | | Pore Size | | |
|---|---|---|---|---|---|---|
| Design Compared | Mean Difference | Significant? | Adjusted P value | Mean Difference | Significant? | Adjusted P value |
| A vs. B | -7.172 | No | 0.2963 | -554.8 | Yes (****) | <0.0001 |
| A vs. C | -75.26 | Yes (****) | <0.0001 | -13.44 | No | 0.2759 |
| A vs. D | -87.99 | Yes (****) | <0.0001 | -513.9 | Yes (****) | <0.0001 |
| B vs. C | -68.09 | Yes (****) | <0.0001 | 541.4 | Yes (****) | <0.0001 |
| B vs. D | -80.82 | Yes (****) | <0.0001 | 40.95 | No | 0.0882 |
| C vs. D | -12.73 | No | 0.1027 | -500.4 | Yes (****) | <0.0001 |

Mechanical properties were evaluated for the pore designs as they are an important consideration for external stents and other implantable devices. Young's modulus at body temperature ($E_{tn}(37^oC)$, maximum stress ($\sigma_{max}$), and maximum strain ($\varepsilon_{max}$) were measured isothermally at 37 $^oC$ using a Dynamic Mechanical Analyzer in tensile Controlled Force mode with a stress ramp of 0.1 MPa $s^{-1}$ as was done in a previous study. Interestingly, the Young's modulus of both nonporous (2.4 ± 0.86) and porous (mean = 0.57 – 1.11 MPa) 68%PCL-32%ACPCL designs were very close to the average physiological modulus of healthy human coronary arteries (1.48 MPa),[240] suggesting suitability of the designs for vascular and soft tissue applications from a mechanical perspective. As expected, ablating pores in the crosslinked polymer designs resulted in significant decreases in $E_{tn}(37^oC)$ and $\sigma_{max}$ for all of the designs ($p < 0.003$). Decreasing the spacing of the pores from 229 ± 51 μm (C,D) to 151 ± 51 μm (A,B) further reduced both $E_{tn}(37^oC)$ and $\sigma_{max}$, but not in a statistically significant manner when evaluated as part of the 5 group cohort of mechanical data. However, pairwise comparisons of pore spacing and size revealed a statistically significant decrease in $\sigma_{ma}$ when spacing is reduced from 230 to 150 μm ($p = 0.0025$) but not when pore size is changed approximately two-fold ($p = 0.3662$). These results suggest that pore spacing is a better predictor of mechanical properties than pore size.

#### 4.3.4.2 Histological Scoring and Characterization of the Polymer-Tissue Interface

To evaluate the effect of pore size and spacing on neovascularization, inflammation, and fibrosis, 21 mice were implanted with the 6 different scaffolds (Table 4-7) separated by 6 small independent incisions in the back. Placement of all 6 designs in each mouse were randomized in terms of positioning in the subcutaneous pocket of the back. A total of 5, 8, and 8 mice were sacrificed on Days 4, 14, and 28, respectively, and evaluated using the histological scoring schematic (Figure 4-13, Figure 4-14, Table 4-9, Table 4-1). SEM microscopy was also performed on tissue explants of each design on Day 4 (Figure 4-15), 14 (Figure 4-16), and 28 (Figure 4-17) to provide a three-dimensional visualization of certain architectural features of the polymer-tissue interfaces such as deposition of sheets of extracellular matrix components, connective tissue, and cellular milieu on and surrounding scaffold surfaces, including within pores (Figure 4-15C). On day 4, histological analysis of H&E staining revealed that there was very little fibrosis (Fibrosis Score = 3) or neovascularization (Neovascularization Score = 0) detected for any of the samples, while inflammation was mostly mild with some multifocal aggregates of multinucleated giant cells, histiocytes, lymphocytes, and plasma cells present but no abundance of neutrophils. SEM micrographs of the polymer tissue interface on Day 4 corroborate this finding, as the surrounding tissue appears separated from the polymer surface prior to the formation of fibrovascular tissue (Figure 4-15). No statistically significant differences in distributions for the semi-quantitative measures were observed on Day 4. On Day 14, there was an increase in the presence of neovessels and connective tissue restricted primarily to the periphery of the implant (Neovascularization = 1, Fibrosis = 3) but beginning to invest interstices (Neovascularization = 2, Fibrosis = 2) and bridge the implant (Neovascularization = 3, Fibrogenesis = 1) for some of the samples. This is

reflected in the higher neovascularization scores and lower fibrogenesis scores for Day 14, which was detected as statistically significant from Day 4 to 14 for Neovascularization only ($p < 0.0001$) when applying a Kruskal-Wallis and Dunn's post hoc comparison of the combined Neovascularization Scores of all designs at the three different time points. SEM micrographs on Day 14 do not allow for evaluation of margins of all of the designs, but it appears that the tissue-implant interface begins to blur together multi-focally in porous designs (Figure 4-16A-D). This likely indicates some minor level of inflammation-mediated degradation and replacement by fibrovascular tissue, which is largely absent in the nonporous controls (Figure 4-16E-F). The only statistical differences detected between individual designs over time or between groups on Day 14 for the four histological criterion were Neovascularization from Day 4 to 14 for Design E ($p = 0.0082$) and a difference in Cumulative Scores between Designs A and F ($p = 0.0177$). Design E actually had the lowest mean Neovascularization Score ($0.875 \pm 0.356$) and same median Neovascularization Score (1.0) of all of the other designs on Day 14, but the Dunn's post hoc test comparing rank sums was able to detect this difference from Day 4 because it also had the lowest standard deviation (0.356). The difference in Cumulative Score detected between Designs A and F on Day 14 also corresponded with the greatest mean difference in this semi-quantitative measure. This result, combined with the observation that the mean Neovascularization Score of Design A was higher than F, implies that the significantly lower Cumulative Score for Design A is likely due to more aggressive inflammation and fibrogenesis on Day 14 (i.e. lower Inflammation and Fibrogenesis Scores). Pairing the cohort into groups of equivalent spacing (150 μm (A,B) vs. 230 μm (C,D) vs. non/microporous (E,F)) revealed that there was a significant difference in the Cumulative

Score of the 150 μm group (5.41 ± 0.71) compared to both the 230 μm (6.19 ± 0.85, p = 0.0178) and non/microporous controls (6.38 ± 0.53, p = 0.0022), but no difference between the 230 μm and non/microporous controls (p > 0.9999). In contrast, paring the cohort into groups of equivalent pore size (640 μm (A,C) vs. 1160 μm (B,D) vs. 0-30 μm (E,F)) revealed no significant difference between groups. Statistical analysis of Inflammation Scores followed the same pattern, with significant differences between 150 μm (1.81 ± 0.83) and 230 μm spacing groups (1.81 ± 0.83, p = 0.0369) as well as 150 μm group and non/microporous groups (2.50 ± 0.66, p = 0.0295), but no difference between 230 μm spacing and non/microporous groups (p > 0.9999) as well as no difference when comparing pore sizes. These results therefore suggest that there is more intense inflammation with lower spacing designs at 14 days, and pore sizes of the designs do not have as much of an influence on the inflammatory reaction.

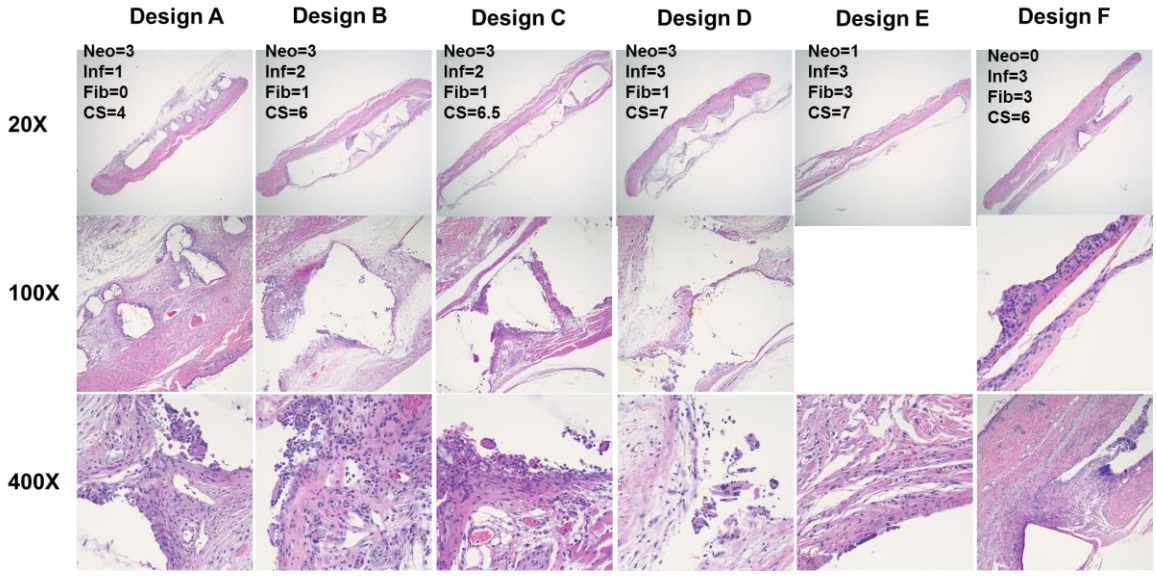


**Figure 4-13 Histological Scoring of Designs**
Representative H&E stained slides of designs and their corresponding scores for each of the metrics. Neo = Neovascularization, Inf = Inflammation, Fib = Fibrogenesis, CS = Cumulative Score.

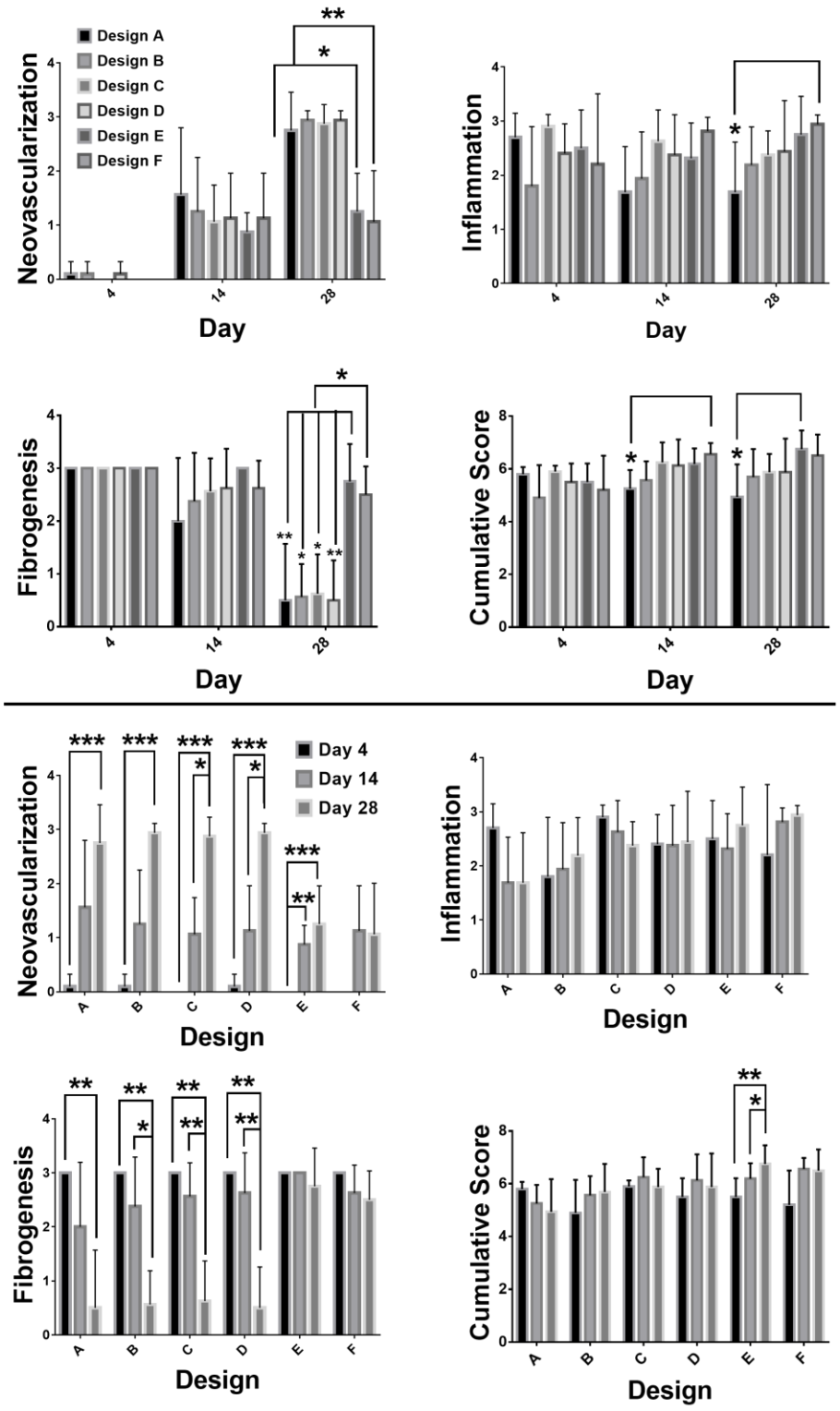


**Figure 4-14 Histological Scores from 28 Day Subcutaneous Implantation**
Side-by-side comparisons of neovascularization, inflammation, fibrogenesis, and cumulative score semi-quantitative assessments for Designs A – F (Top 4) and Days 4, 14, and 28 (Bottom 4). * = $p < 0.05$, ** = $p < 0.01$, *** = $p < 0.001$.

**Table 4-9 Descriptive Statistics from Histological Scoring**

| Design | Neovascularization Day 4 | | | | Neovascularization Day 14 | | | | Neovascularization Day 28 | | | |
|---|---|---|---|---|---|---|---|---|---|---|---|---|
| | $\ddot{x} \pm \sigma$ | $\tilde{x}$ | min | max | $\ddot{x} \pm \sigma$ | $\tilde{x}$ | min | max | $\ddot{x} \pm \sigma$ | $\tilde{x}$ | min | max |
| ***A*** | 0.1±0.22 | 0 | 0 | 0.5 | 1.56±1.2 | 1 | 0 | 3 | 2.75±0.71 | 3 | 1 | 3 |
| ***B*** | 0.1±0.22 | 0 | 0 | 0.5 | 1.25±1.0 | 1 | 0 | 3 | 2.94±0.18 | 3 | 2.5 | 3 |
| ***C*** | 0 | 0 | 0 | 0 | 1.06±0.68 | 1 | 0 | 3 | 2.88±0.36 | 3 | 2 | 3 |
| ***D*** | 0.1±0.22 | 0 | 0 | 0.5 | 1.13±0.83 | 1 | 0 | 3 | 2.94±0.18 | 3 | 2.5 | 3 |
| ***E*** | 0 | 0 | 0 | 0 | 0.88±0.36 | 1 | 0 | 1 | 1.25±0.71 | 1 | 1 | 3 |
| ***F*** | 0 | 0 | 0 | 0 | 1.13±0.83 | 1.25 | 0 | 2 | 1.06±0.94 | 1.25 | 0 | 2 |
| ***150*** | 0.1±0.21 | 0 | 0 | 0.5 | 1.41±1.1 | 1 | 0 | 3 | 2.84±0.51 | 3 | 1 | 3 |
| ***230*** | 0.05±0.16 | 0 | 0 | 0.5 | 1.09±0.74 | 1 | 0 | 3 | 2.91±0.27 | 3 | 2 | 3 |
| ***640*** | 0.05±0.16 | 0 | 0 | 0.5 | 1.31±1.0 | 1 | 0 | 3 | 2.81±0.54 | 3 | 1 | 3 |
| ***1160*** | 0.1±0.21 | 0 | 0 | 0.5 | 1.19±0.89 | 1 | 0 | 3 | 2.94±0.17 | 3 | 2.5 | 3 |
| ***0- 30*** | 0 | 0 | 0 | 0 | 1.0±0.63 | 1 | 0 | 2 | 1.16±0.81 | 1 | 0 | 3 |
| **Design** | **Inflammation Day 4** | | | | **Inflammation Day 14** | | | | **Inflammation Day 28** | | | |
| | $\ddot{x} \pm \sigma$ | $\tilde{x}$ | *min* | *max* | $\ddot{x} \pm \sigma$ | $\tilde{x}$ | *min* | *max* | $\ddot{x} \pm \sigma$ | $\tilde{x}$ | *min* | *max* |
| ***A*** | 2.7±0.45 | 3 | 2 | 3 | 1.69±0.84 | 1.75 | 0.5 | 3 | 1.69±0.92 | 1.5 | 0.5 | 3 |
| ***B*** | 1.8±2.9 | 1 | 1 | 3 | 1.94±0.86 | 1.75 | 0.5 | 3 | 2.19±0.70 | 2.25 | 1 | 3 |
| ***C*** | 2.9±0.22 | 3 | 2.5 | 3 | 2.63±0.58 | 3 | 1.5 | 3 | 2.38±0.44 | 2.25 | 2 | 3 |
| ***D*** | 2.4±0.54 | 2 | 2 | 3 | 2.38±0.74 | 2.5 | 1 | 3 | 2.44±0.94 | 3 | 0.5 | 3 |
| ***E*** | 2.5±0.70 | 3 | 1.5 | 3 | 2.31±0.65 | 2.5 | 1 | 1 | 2.75±0.71 | 3 | 1 | 3 |
| ***F*** | 2.2±1.3 | 3 | 0 | 3 | 2.81±0.26 | 3 | 2.5 | 2 | 2.94±0.18 | 3 | 2.5 | 3 |
| ***150*** | 2.25±0.92 | 2.75 | 1 | 3 | 1.81±0.83 | 1.75 | 0.5 | 3 | 1.94±0.83 | 2 | 0.5 | 3 |
| ***230*** | 2.65±0.47 | 3 | 2 | 3 | 2.50±0.66 | 3 | 1 | 3 | 2.41±0.71 | 2.5 | 0.5 | 3 |
| ***640*** | 2.8±0.35 | 3 | 2 | 3 | 2.16±0.85 | 2.25 | 0.5 | 3 | 2.03±0.78 | 2 | 0.5 | 3 |
| ***1160*** | 2.1±0.88 | 2 | 1 | 3 | 2.16±0.81 | 2 | 0.5 | 3 | 2.31±0.81 | 2.5 | 0.5 | 3 |
| ***0- 30*** | 2.35±1.0 | 3 | 0 | 3 | 2.56±0.54 | 2.5 | 1 | 2 | 2.84±0.51 | 3 | 1 | 3 |
| **Design** | **Fibrogenesis Day 4** | | | | **Fibrogenesis Day 14** | | | | **Fibrogenesis Day 28** | | | |
| | $\ddot{x} \pm \sigma$ | $\tilde{x}$ | *min* | *max* | $\ddot{x} \pm \sigma$ | $\tilde{x}$ | *min* | *max* | $\ddot{x} \pm \sigma$ | $\tilde{x}$ | *min* | *max* |
| ***A*** | 3±0 | 3 | 3 | 3 | 2.0±1.2 | 2.5 | 0 | 3 | 0.50±1.1 | 0 | 0 | 3 |
| ***B*** | 3±0 | 3 | 3 | 3 | 2.38±0.92 | 3 | 1 | 3 | 0.56±0.62 | 0.5 | 0 | 1.5 |
| ***C*** | 3±0 | 3 | 3 | 3 | 2.56±0.63 | 3 | 1.5 | 3 | 0.63±0.74 | 0.5 | 0 | 2 |
| ***D*** | 3±0 | 3 | 3 | 3 | 2.63±0.74 | 3 | 1 | 3 | 0.5±0.76 | 0 | 0 | 2 |
| ***E*** | 3±0 | 3 | 3 | 3 | 3±0 | 3 | 3 | 3 | 2.75±0.71 | 3 | 1 | 3 |
| ***F*** | 3±0 | 3 | 3 | 3 | 2.63±0.52 | 3 | 2 | 3 | 2.5±0.53 | 2.5 | 2 | 3 |
| ***150*** | 3±0 | 3 | 3 | 3 | 2.19±1.0 | 3 | 0 | 3 | 0.53±0.84 | 0 | 0 | 3 |
| ***230*** | 3±0 | 3 | 3 | 3 | 2.59±0.66 | 3 | 1 | 3 | 0.56±0.73 | 0 | 0 | 2 |
| ***640*** | 3±0 | 3 | 3 | 3 | 2.28±0.97 | 3 | 0 | 3 | 0.56±0.89 | 0 | 0 | 3 |
| ***1160*** | 3±0 | 3 | 3 | 3 | 2.5±0.82 | 3 | 1 | 3 | 0.53±0.67 | 0 | 0 | 2 |
| ***0- 30*** | 3±0 | 3 | 3 | 3 | 2.81±0.40 | 3 | 2 | 3 | 2.63±0.62 | 1 | 1 | 3 |
| **Design** | **Cumulative Score Day 4** | | | | **Cumulative Score Day 14** | | | | **Cumulative Score Day 28** | | | |
| | $\ddot{x} \pm \sigma$ | $\tilde{x}$ | *min* | *max* | $\ddot{x} \pm \sigma$ | $\tilde{x}$ | *min* | *max* | $\ddot{x} \pm \sigma$ | $\tilde{x}$ | *min* | *max* |
| ***A*** | 5.8±0.28 | 6 | 5.5 | 6 | 5.25±0.71 | 5.5 | 4 | 6 | 4.94±1.2 | 4.5 | 3.5 | 7 |
| ***B*** | 4.9±1.2 | 4 | 4 | 6.5 | 5.56±0.73 | 5.75 | 4.5 | 6.5 | 5.69±1.1 | 5.75 | 4 | 3 |
| ***C*** | 5.9±0.22 | 6 | 5.5 | 6 | 6.25±0.76 | 6.25 | 5 | 7 | 5.88±0.69 | 6 | 5 | 7 |
| ***D*** | 5.5±0.71 | 5 | 5 | 6.5 | 6.13±0.99 | 6.5 | 5 | 7 | 5.88±1.28 | 6 | 3.5 | 7 |
| ***E*** | 5.5±0.71 | 6 | 4.5 | 6 | 6.19±0.59 | 6.25 | 5 | 7 | 6.75±0.70 | 7 | 5 | 7 |
| ***F*** | 5.2±1.3 | 6 | 3 | 6 | 6.56±0.42 | 6.5 | 6 | 7 | 6.5±0.80 | 6.75 | 5 | 7.5 |
| ***150*** | 5.35±0.97 | 5.75 | 4 | 6.5 | 5.41±0.71 | 5.5 | 4 | 6.5 | 5.31±1.2 | 5.5 | 3.5 | 7 |
| ***230*** | 5.7±0.54 | 6 | 5 | 6.5 | 6.19±0.85 | 6.25 | 5 | 7 | 5.88±0.99 | 6 | 3.5 | 7 |
| ***640*** | 5.85±0.24 | 6 | 5.5 | 6 | 5.75±0.88 | 6.5 | 4 | 7 | 5.41±1.1 | 5.75 | 3.5 | 7 |
| ***1160*** | 5.2±1.0 | 5 | 4 | 6.5 | 5.84±0.89 | 6 | 4.5 | 7 | 5.78±1.1 | 6 | 3.5 | 7 |
| ***0- 30*** | 5.35±1.0 | 6 | 3 | 6 | 6.38±0.53 | 6.5 | 5 | 7 | 6.63±0.74 | 7 | 5 | 7.5 |

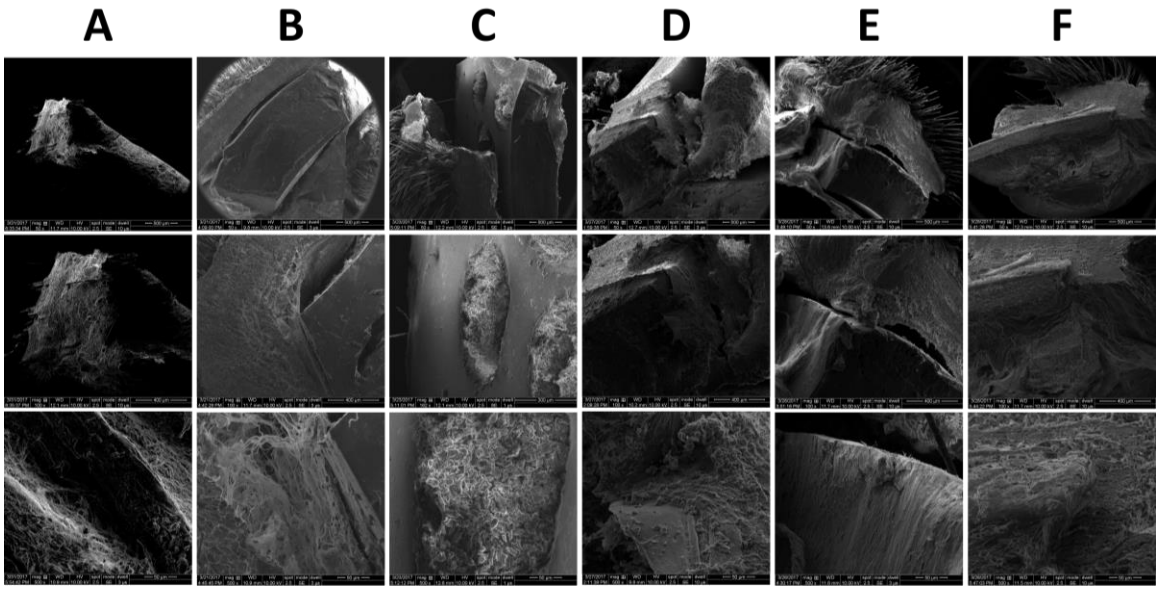


**Figure 4-15 Representative SEM images of polymer-tissue interfaces on Day 4**
SEM micrographs of the polymer-tissue interface on Day 4 reveal some of the three-dimensional tissue architecture in and around the polymer-tissue interface. Polymers appear dark and relatively uniform in structure, while the tissue appears more illuminated and finely structured. Architectural features in these images include threaded sheets of extracellular matrix deposition on the polymer surface (A, D, E) and cellular milieu within pores (C).

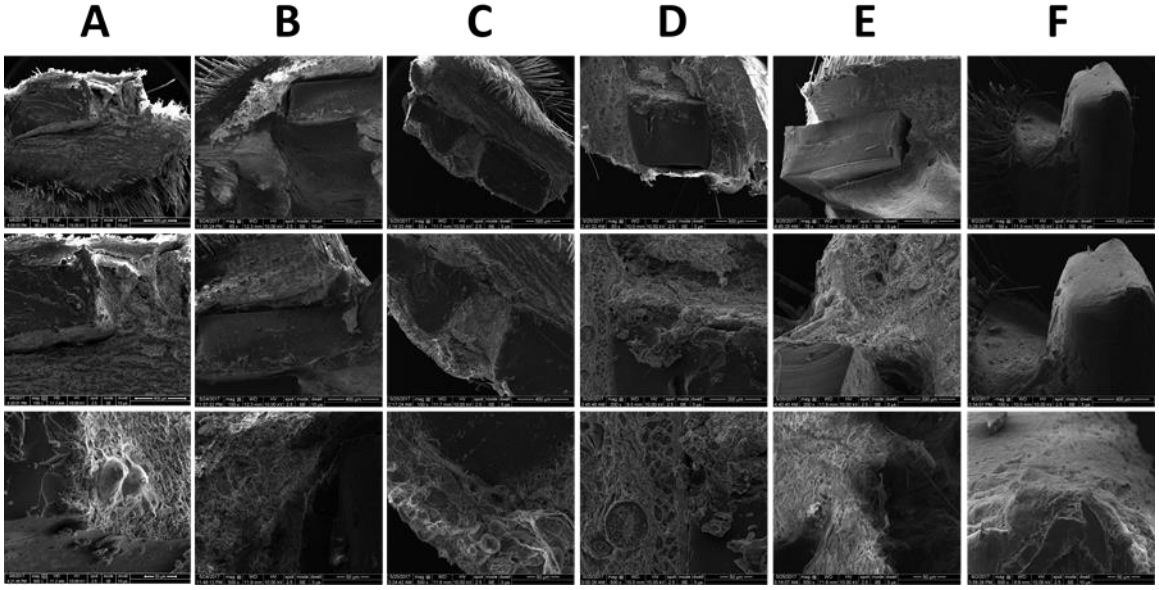


**Figure 4-16 Representative SEM images of polymer-tissue interfaces on Day 14**
SEM micrographs of the polymer-tissue interface on Day 14 reveal some of the three-dimensional tissue architecture in and around the polymer-tissue interface. Polymers appear dark and relatively uniform in structure, while the tissue appears more illuminated and finely structured. In general, fibrovascular connective tissue layers appear thicker with a more diverse array of cell shapes and sizes than on Day 14.

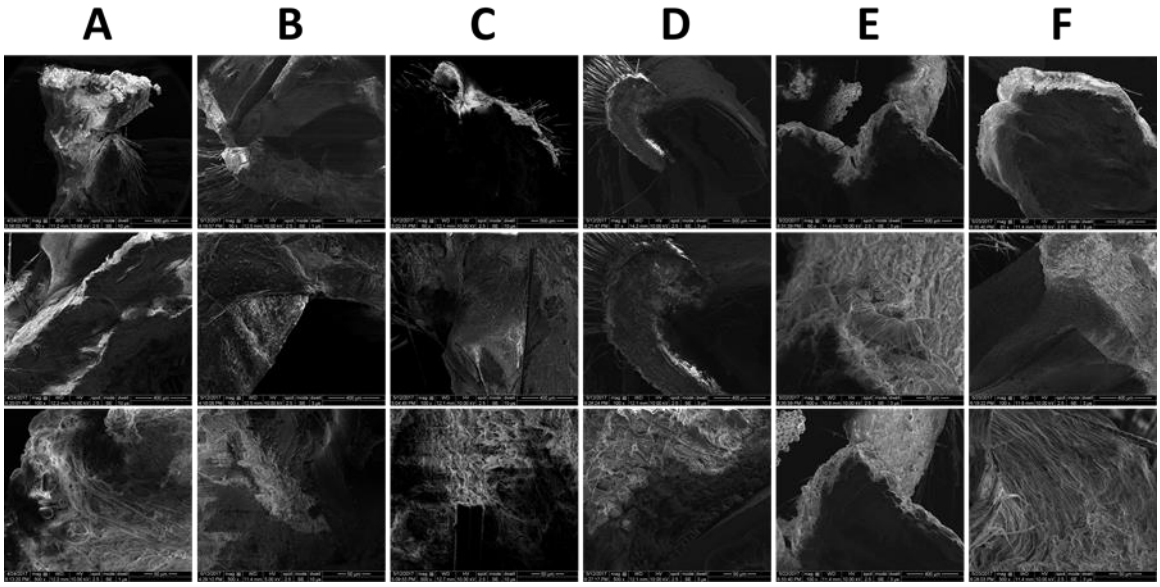


**Figure 4-17 Representative SEM images of polymer-tissue interfaces on Day 28**
SEM micrographs of the polymer-tissue interface on Day 28 reveal some of the three-dimensional tissue architecture in and around the polymer-tissue interface. Polymers appear dark and relatively uniform in structure, while the tissue appears more illuminated and finely structured. Similar features are detected for these designs in comparison to Day 14.

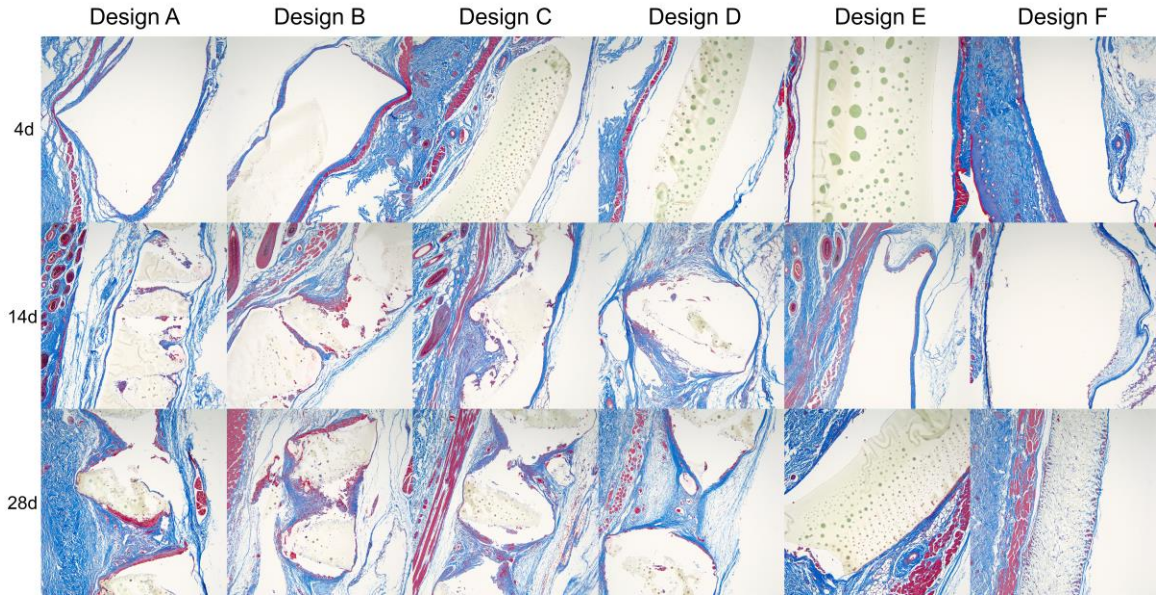


**Figure 4-18 Masson's Trichrome Staining of Designs A – F**

Masson's Trichrome staining of tissue explants from each design indicate the increase in fibrogenesis over time for porous designs. At 28 days, connective tissue bridges implants at multiple foci for most pore designs but not for nonporous ones.

Neovascularization and fibrogenesis continued to progress in the porous designs from Day 14 to Day 28, with vessels bridging implants in at least one focus (median Neovascularization Score of 3 for Designs A - D) and connective tissue bridging at multiple foci (median Fibrogenesis Score of 0 or 0.5 for A - D) for most of the porous samples. The increase in connective tissue bridging can be visualized by Masson's Trichrome staining on the designs at the three different timepoints (Figure 4-18). Nonporous controls E and F were the opposite, with minimal neovascularization (Neovascularization Score = $1.16 \pm 0.81$) and fibrogenesis (Fibrogenesis Score = $2.63 \pm 0.62$). All porous and nonporous designs were statistically significant from each other by Neovascularization and Fibrogenesis Scores. Inflammation remained mild (Inflammation Score = 2) to minimal for (Inflammation Score = 3) for all of the designs except for Design A, which was more moderate overall ($1.69 \pm 0.92$). As such, a statistically significant difference was detected between Design A and Design F for Inflammation Score ($p = 0.0318$) and this was also the only comparison that was significantly different by Cumulative Score ($p = 0.0182$). Comparing groups by pore spacing and size also revealed significant differences in Inflammation Scores and Cumulative Scores for small spacing vs. nonporous groups ($p \leq 0.001$) and small pore size vs. nonporous groups ($p \leq 0.0029$). Although no significant differences were detected in the semi-quantitative histological criterion between pore design groups on Day 28, these results intimate that a small pore spacing and size combination elicits a more moderate inflammatory response from x%PCL-y%ACPCL implants.

### 4.3.5 CD31 Quantification

To further assess and compare neovascularization responses of designs, a microvessel detection algorithm was run that quantified the total number of vessels, total and average vessel area, average vessel perimeter, and microvessel density by colorimetrically detecting DAB that was used to stain against CD31. Consistent with trends observed through the Neovascularization Score over time, there was a statistically significant increase in the number of blood vessels for all of the porous designs from Day 4 to Day 28 ($p \leq 0.0027$), with no difference detected over time for nonporous designs. A significant difference in the number of blood vessels was also detected for Design B from Day 4 to Day 14 ($p = 0.0101$). On Day 14, the total number of blood vessels from Design B were significantly different than non/microporous Designs E ($p = 0.0008$) and F ($p = 0.0136$) as well as smaller pore-sized Design A ($p = 0.0121$). Total vessel area was also different between Design B and nonporous controls on Day 14 ($p \leq 0.04$), but not between Designs B and A ($p = 0.0762$). Coupling the designs based on equivalent spacing revealed that both spacings were different from nonporous controls in terms of both total vessel number ($p \leq 0.0285$) and total vessel area ($p \leq 0.0226$). When comparing between groups coupled by pore size, only the 1160 μm group was statistically different from nonporous controls for both total vessel number ($p = 0.0003$) and total vessel area ($p = 0.0006$). A difference in total vessel number was detected between the 635 μm and 1160 μm diameter groups on Day 14 ($p = 0.0155$) that was not by total vessel area ($p = 0.0666$).

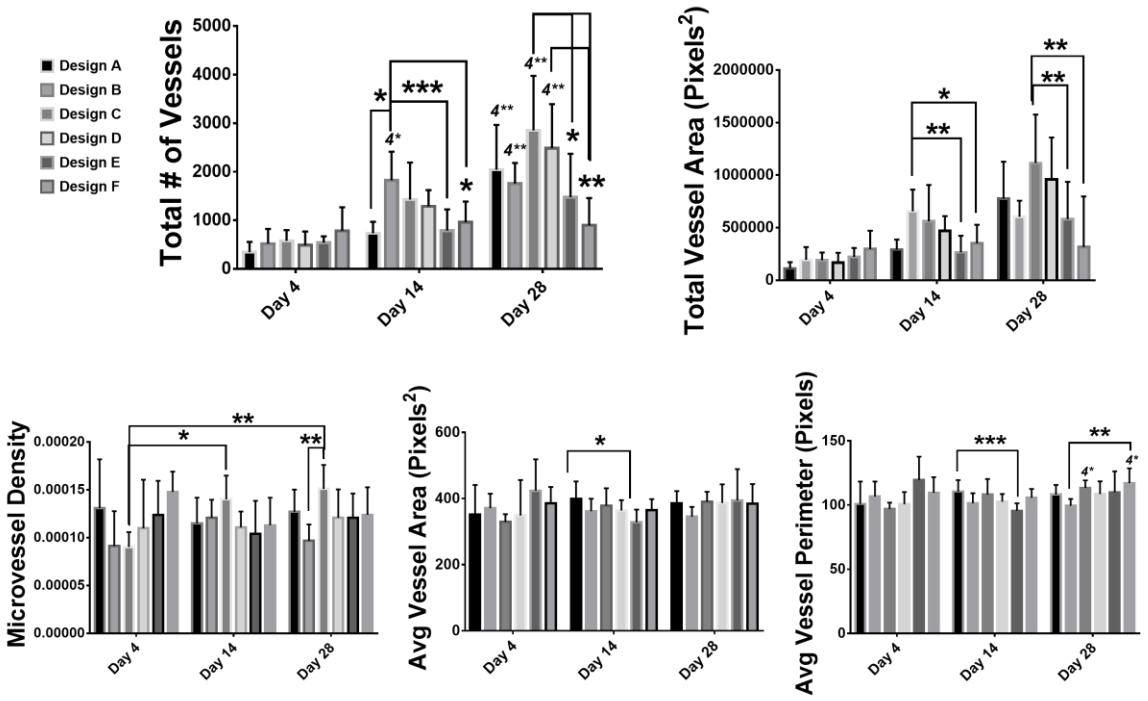


**Figure 4-19 CD31 Quantification of Neovascularization**
Colorimetric detection of DAB staining was used to quantify CD31 and detect the presence of newly formed vessels within a few hundred microns of the implants.

On Day 28, trends in total vessel number and area were virtually identical. All porous designs had greater vessel number and vessel area than nonporous designs as expected. Design C had the highest total number of vessels and area, followed by Design D. Both of these designs were significantly different from Design F ($p \leq 0.0037$) for both metrics. Design C was also significantly different than Design E in terms of total vessel number ($p = 0.0431$). In corroboration with this trend, microvessel density was highest for Design C at 28 days, which was statistically significant in comparison to the smaller spaced and larger sized Design B ($p = 0.0048$). Comparisons based on pore spacing and pore size groups revealed that all were different than nonporous controls for total vessel number and area on Day 28 as expected. The 230 μm group (C,D) was also different from the 150 μm

spaced group for both total vessel number ($p = 0.02111$) and area ($p = 0.0241$), which implied that the larger spacing is more conducive to neovascularization over the course of one month.

### 4.3.6 Macrophage Phenotype Characterization

Macrophages are phagocytic cells that are central to the inflammatory response as they are recruited to damaged or disrupted tissue sites through chemotaxis. They secrete a vast array of stimulating factors themselves to regulate the inflammatory response in a number of ways. Depending on their function as a pro-inflammatory or wound healing stimulator, they tend to classified into two broad categories, pro-inflammatory M1 and pro-wound healing M2, but also have several subset phenotypes and are quite fluid in nature. In general, it is understood that a shift from a "classically-activated", pro-inflammatory M1 macrophage phenotype to an "alternatively-activated", pro-tissue remodeling M2 macrophage phenotype indicative of constructive wound healing responses such as neovascularization.[271] Although macrophage phenotype characterization of external supports is currently underexplored and largely unknown, it is hypothesized that this shift from M1 to M2 over 28 days is desirable to fully resolve tissue and promote neovascular effects that are favorable towards reducing neointimal hyperplasia.[116, 272] For example, a recent study evaluating murine laser-induced choroidal neovascularization demonstrated that new blood vessel formation correlated with a transient upregulation in M1 phenotype followed by a sustained shift to M2.[273] However, macrophage phenotypes exist across a diverse spectrum and some recent studies have found that both M1 and M2 phenotypes are significantly upregulated in scaffolds such as glutaraldehyde-crosslinked ones that

exhibited an increase in new blood vessel formation after 10 days when implanted in subcutaneous mouse tissue.[274] Inflammation has been shown to be beneficial for neovascularization, such as when bone marrow mononuclear cells (BMCs) promoted early monocyte recruitment by secreting significant amounts of monocyte chemoattractant protein-1, which help tissue engineered vascular grafts (TEVGs) transform into functional neovessels.[275] In most contexts, ePTFE is a relatively inert polymer owing to its strong carbon-fluoride bond and non-degradability. In its microporous format, it exhibited minimal adhesion with a mean implantation lifetime of 420 days after laparoscopic ventral hernia repair in 65 repoerative patients, and it also reduced adhesions in a rabbit peritoneal model of laparoscopic ventral hernia repair relative to polypropylene and HA/polypropylene meshes.[276] It did not promote the substantial inflammatory and neovascularization response that Dacron external meshes did when applied to porcine vein grafts, and was ineffective in this context while Dacron meshes correspondingly reduced neointimal formation.[83, 117] Meanwhile, the specific roles that macrophages play in fibrogenesis are largely unknown, but fibrotic lesions are accompanied by a high degree of chronic inflammatory cell infiltration where monocytes and macrophages are present.[277] ePTFE also exhibited less neovascularization and fibrogenesis than the PCL-ACPCL scaffolds in this study, so it was anticipated that it would have less macrophages. The effect of the presence of pores as well as pore size and spacing parameters are explored for macrophage phenotypes to investigate their role in the tissue responses observed and elucidate any corresponding geometric relationships to this behavior.

A pan macrophage marker (F4/80), M1 macrophage marker (iNOS), and M2 macrophage marker (CD206) were utilized to characterize macrophage phenotypes of

histiocytes observed to be present within tissue constructs to varying degrees, from minimal and part of a foreign body cellular response affecting less than half of the implant circumference, to more marked and part of the formation of a thick cuff around the circumference. It was expected that designs eliciting more favorable and less marked inflammatory responses would also exhibit more of a switch to an M2 macrophage phenotype over time. To avoid Type I errors while aiming to detect significant differences between each design at a given timepoint as well as the given designs over time, two 2-way ANOVA analyses followed by post-hoc Tukey's tests were conducted to define the distinctiveness of interactions for each test case (i.e. same design over time or different designs at each time). It was anticipated that the relatively inert, microporous ePTFE control would have lower F4/80 and iNOS positivity than porous Designs A - D. On Days 14 and 28, Design F had the lowest positivity for F4/80 ($0.583 \pm 0.091$ and $0.546 \pm 0.15$, respectively) and was distinct from all other designs in this regard ($p < 0.0001$), which implied less macrophages present from ePTFE implantation as expected. iNOS was also significantly lower on Day 4 than porous Designs B and C, possibly due to a lack of M1-mediated angiogenesis. iNOS expression was also significantly lower on Day 28 than Designs A – C.

The iNOS positivity was significantly lower for Design A relative to Designs B and C, which implies that larger pore sizes and spacings may promote an M1 macrophage phenotype at early timepoints; this transient upregulation of an M1 phenotype at early stages has been shown to promote neovascularization. Conversely, scaffolds which promote an eventual switch toward an M2 macrophage phenotype are expected to fully resolve their wound healing process. On Day 28, Design D had significantly lower iNOS

positivity than Design B, which implies that the wider-spaced design (D) may better promote wound healing resolution. On Day 28, Design F exhibited a significantly higher CD206/iNOS ratio than all other designs. This may mean that the wound has been more fully resolved with the ePTFE microporous control, whereas inflammation-mediated neovascularization and fibrogenic processes may still be ongoing without full wound resolution in the other designs.

Combining staining data of groups based on equivalent pore size and spacing revealed some interesting insights with regards to this characterization of macrophage phenotype. On Day 14, smaller pores (A+C, 635 μm diameter) exhibited significantly greater CD206 positivity (mean difference = 0.0452, p = 0.141), lower iNOS positivity (mean difference = - 0.0655, p = 0.0017), and a higher CD206/iNOS ratio (mean difference = 0.463, p = 0.0004) than larger pores (B+D, 1160 μm diameter). On Day 28, smaller pores again were more positive for CD206 (mean difference = 0.0322, p = 0.0147), while larger spacings (C+D, 230 μm) had significantly lower iNOS positivity (mean difference = 0.0687, p = 0.0304). No differences were detected for F4/80 positivity. Taken together, this implies that the ~635 μm diameter, ~230 μm spacing group (Design C) elicits an inflammatory response characterized by more of the "tissue remodeling" M2 phenotype. This also coincides with the design exhibiting the greatest amount of neovascularization as measured by total blood vessel number, total vessel area, and microvessel density by the CD31 microvessel detection algorithm (Figure 4-19).

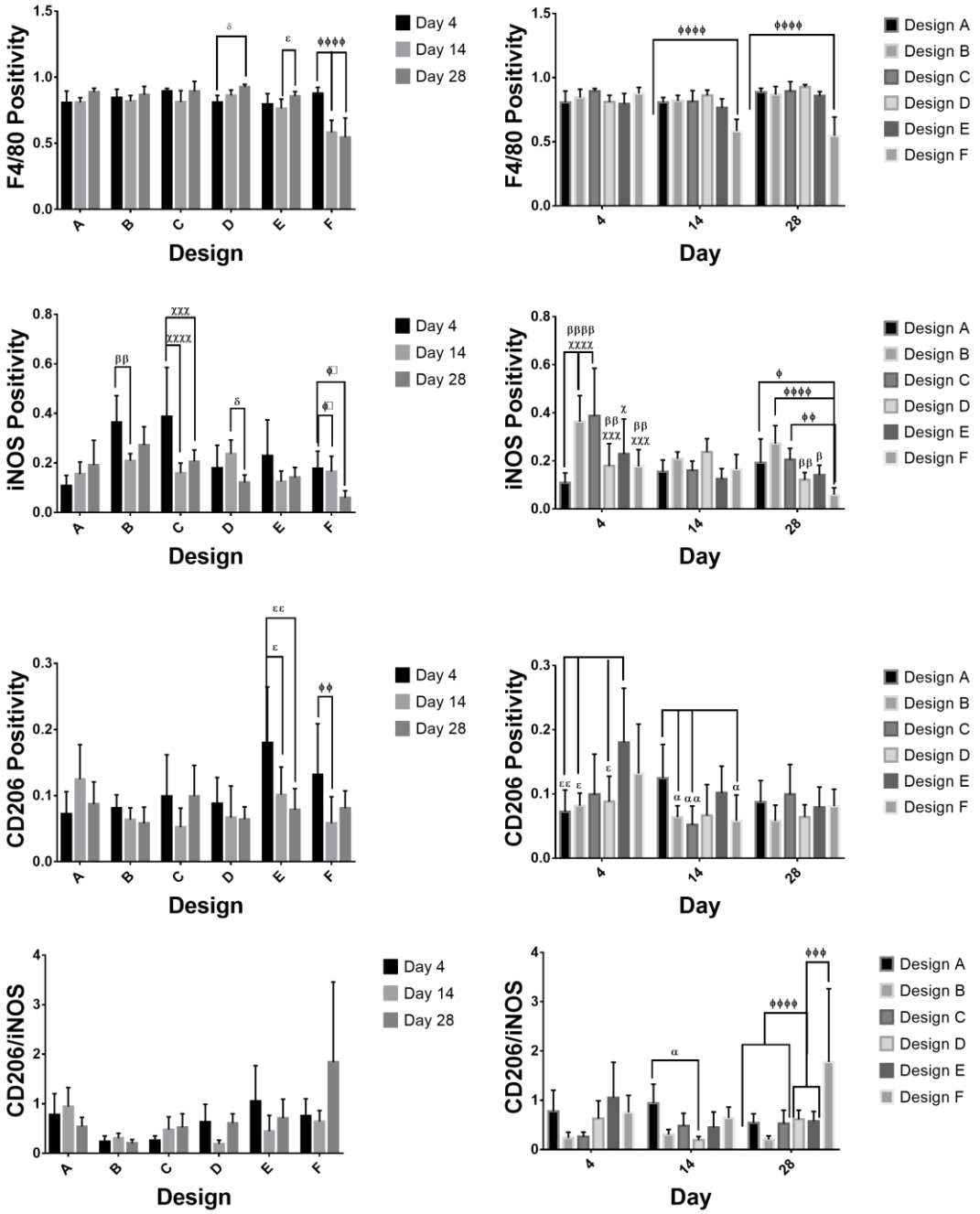


**Figure 4-20 Macrophage Phenotype Characterization**
Tissues were immunohistochemically stained to identify macrophage phenotype, with F4/80 as a pan macrophage marker, iNOS as an M1 marker, and CD206 as an M2 marker. Greek symbols correspond to statistically significant differences detected between test group and the English-equivalent of the Greek design: $\alpha = p < 0.05$ between Design A and test, $\beta = p < 0.05$ from Design B, $\gamma$ = diff. from C, $\delta$ = diff from D, $\varepsilon$ = diff from E, $\theta$ = diff. from F.

### 4.3.7 MMP Staining

Matrix metalloproteinases (MMPs) are a family of 25 endopeptidases that are known to play an important role in regulating wound healing processes, primarily by processing of bioactive molecules such as cytokines, chemokines, and growth factors located within or around extracellular matrix (ECM) proteins.[278] It was desired to determine whether the MMPs detected were indeed localized, at least in part, around the polymer-tissue interface, especially whether they co-localized with monocyte-macrophages, the primary orchestrators of the wound healing response. As differences in neovascularization were detected between designs grouped by spacing and non/microporous controls, and some modest yet insignificant differences were observed from a limited set of samples from each design type, it was also thought possible that perhaps some differences in the presence of MMPs could be detected between groups. MMP-3 and MMP-9 (along with MMP-1) are known to regulate the most widespread array of chemokine signals that are important drivers of the inflammatory response.[274] MMP-9 has notably been shown to be secreted in high levels by M2 macrophages known to promote angiogenesis, especially by the M2c subgroup.[274] While MMPs primarily function by impacting chemokines, growth factors, and their respective receptors, MMP-1, 3, 9, 13 and 14 all have also shown the ability to degrade collagen directly, an essential aspect of the final, resolution stage of wound healing.[279]

Tissue sections containing the polymer-tissue interface were immunohistochemically stained for MMPs 3 (Figure 4-21), 9 (Figure 4-22), 12 (Figure 4-23), 13 (Figure 4-24) and 14 (Figure 4-25), as all of these MMPs were detected from proteomics analysis of tissue extracts and are known to play a role in the wound healing

process. Cells labeled positively for MMPs are separated into those observed immediately adjacent to the implant (within approximately 100 µm distance) and the associated reactive neotissue ("peri-polymer localization"), and those observed at a greater distance, separated by a fascial plane ("other cells labeled") (Table 4-10). For each, cell types are listed from strongest/most intense staining to weakest/least intense staining. Granular, cytoplasmic staining for MMPs was observed in several cell types in the experimental tissue specimens, but notably co-localized with macrophages peripheral to the polymer-tissue implant the strongest of any other cell type. This implies that MMPs are secreted by macrophages that infiltrate the polymer-tissue interface. MMP-9 primarily digests gelatin and has been shown to be secreted in high levels by M2 macrophages known to promote angiogenesis, especially by the M2c subgroup.[274] MMP-3 and MMP-9, along with MMP-1, are known to regulate the most widespread array of chemokine signals that are important drivers of the inflammatory response.[274] IHC staining of MMP-9 co-localized with monocyte/macrophages and multinucleated giant cells, as did all of the MMPs.

**Table 4-10 Summary of observations from MMP IHC staining**

| | Peri-polymer localization | Other cells labeled |
|---|---|---|
| **MMP3** | Monocyte-macrophages<br>Multinucleated giant cells<br>Endothelium | Dermal monocyte-macrophages<br>Neutrophils<br>Epidermal sebocytes<br>Striated myocytes |
| **MMP9** | Monocyte-macrophages<br>Multinucleated giant cells | Dermal monocyte-macrophages<br>Neutrophils |
| **MMP12** | Monocyte-macrophages<br>Multinucleated giant cells<br>Endothelium<br>Fibroblasts | Striated myocyes<br>Apocrine epithelial cells<br>Epidermal sebocytes<br>Dermal macrophages<br>Neutrophils<br>Epidermal keratinocytes |
| **MMP13** | Monocyte-macrophages<br>Multinucleated giant cells | Dermal monocyte-macrophages<br>Neutrophils |
| **MMP14** | Monocyte-macrophages<br>Multinucleated giant cells<br>Endothelium | Dermal monocyte-macrophages<br>Neutrophils<br>Epidermal sebocytes<br>Striated myocytes<br>Epidermal keratinocytes |

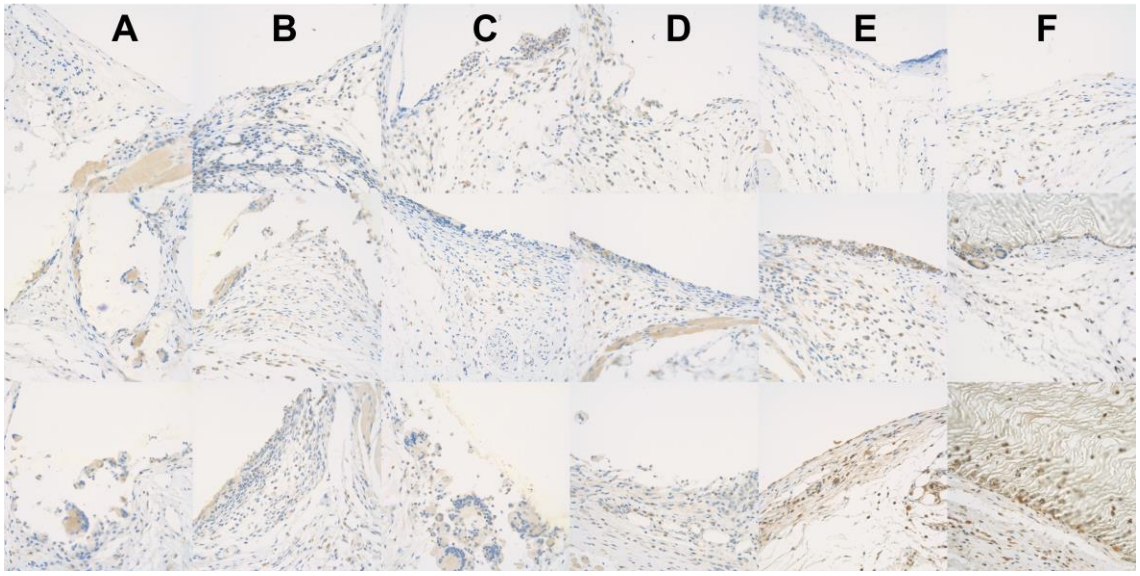


**Figure 4-21 MMP-3 IHC Labeling**

Immunohistochemical labeling for MMP-3 on the polymer-tissue interface of slides for Designs A – F on Days 4 (top), 14 (middle), and 28 (bottom). Monocyte-macrophages,

multinucleated giant cells, and endothelium stain positive (brown) at the peri-polymer localization. Other cells labeled are dermal monocyte-macrophages, neutrophils, epidermal sebocytes, and striated myocytes.

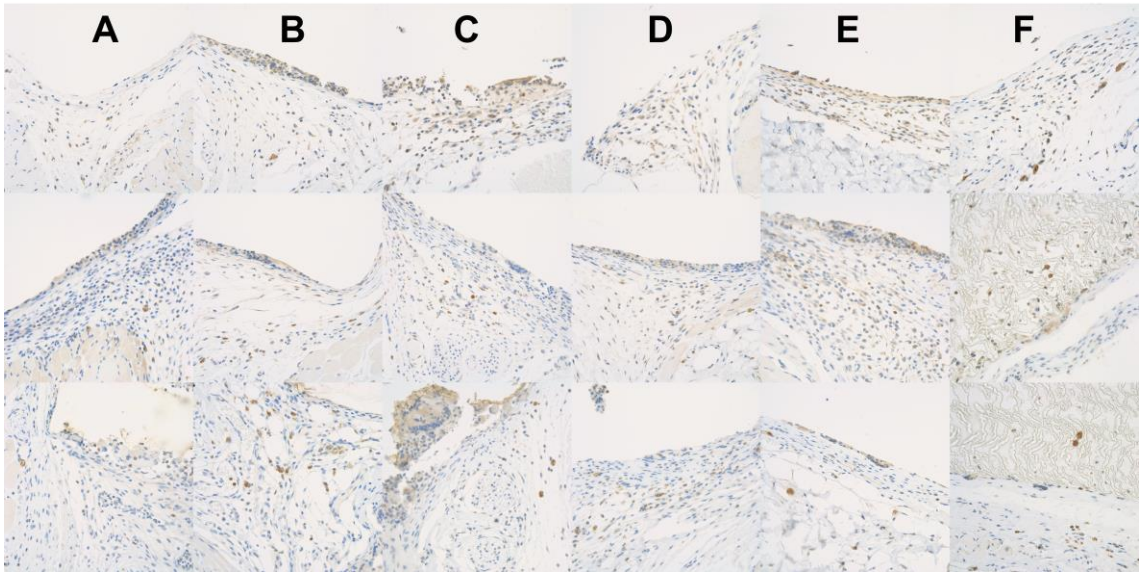


**Figure 4-22 MMP-9 IHC Labeling**
Immunohistochemical labeling for MMP-9 on the polymer-tissue interface of slides for Designs A – F on Days 4 (top), 14 (middle), and 28 (bottom). Monocyte-macrophages and multinucleated giant cells stain positive (brown) at the peri-polymer localization. Other cells labeled are dermal monocyte-macrophages and neutrophils.

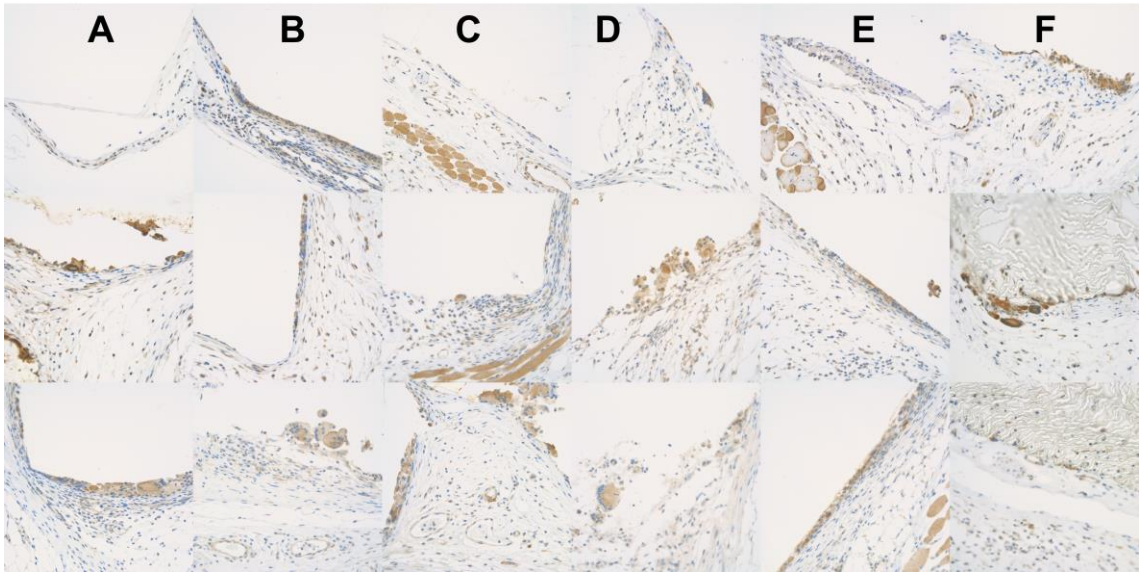


**Figure 4-23 MMP-12 IHC Labeling**
Immunohistochemical labeling for MMP-12 on the polymer-tissue interface of slides for Designs A – F on Days 4 (top), 14 (middle), and 28 (bottom). Monocyte-macrophages,

multinucleated giant cells, endothelium, and fibroblasts stain positive (brown) at the peri-polymer localization. Other cells labeled are striated myocytes, apocrine epithelial cells, epidermal sebocytes, dermal macrophages, neutrophils, and epidermal keratinocytes.

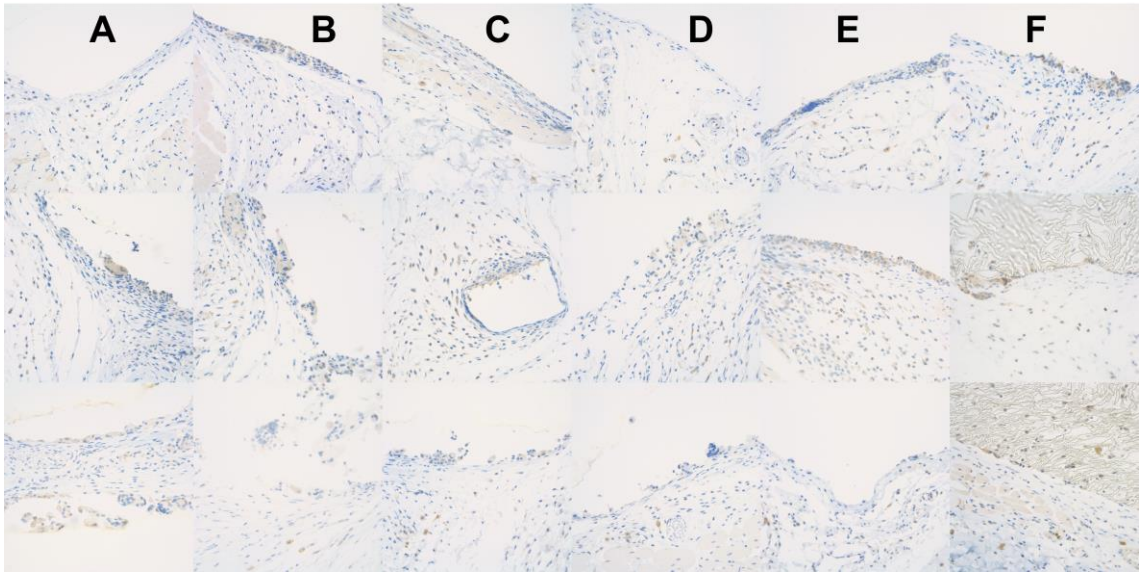


**Figure 4-24 MMP-13 IHC Labeling**
Immunohistochemical labeling for MMP-13 on the polymer-tissue interface of slides for Designs A – F on Days 4 (top), 14 (middle), and 28 (bottom). Monocyte-macrophages, and multinucleated giant cells stain positive (brown) at the peri-polymer localization. Other cells labeled are dermal monocyte-macrophages and neutrophils.

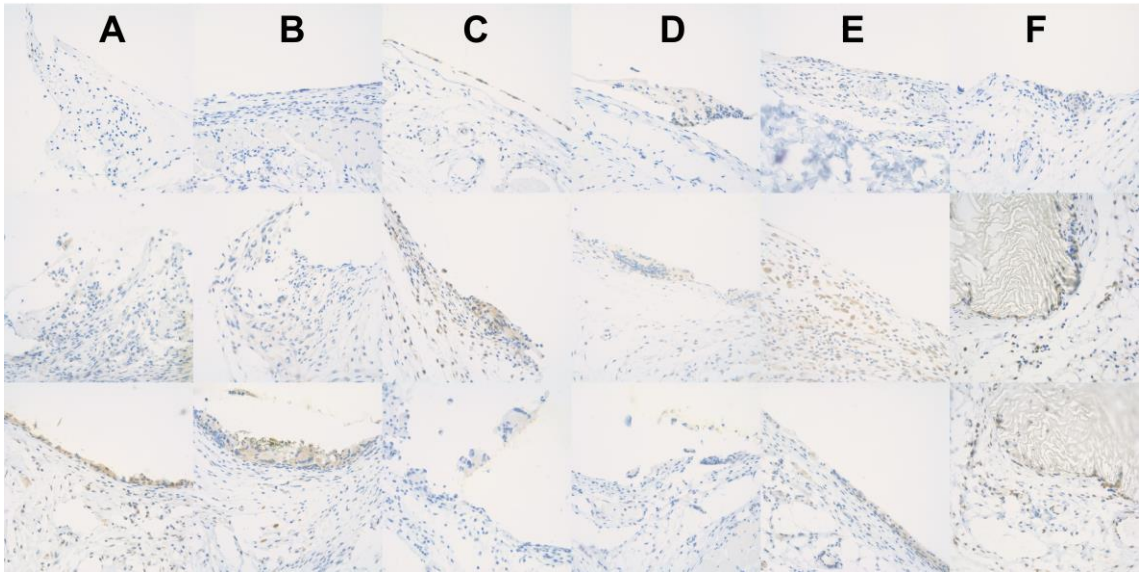


**Figure 4-25 MMP-14 IHC Labeling**
Immunohistochemical labeling for MMP-14 on the polymer-tissue interface of slides for Designs A – F on Days 4 (top), 14 (middle), and 28 (bottom). Monocyte-macrophages, multinucleated giant cells, and endothelium stain positive (brown) at the peri-polymer

localization. Other cells labeled are dermal monocyte-macrophages, neutrophils, epidermal sebocytes, striated myocytes, and epidermal keratinocytes.

## 4.4 Discussion

PCL-based SMPs were synthesized via direction PCL modification, a synthetic process that was able to be emulated by a contract manufacturer. A 1:1:1 ratio of LDA:CL:allyl chloroformate produced 68%PCL-32%ACPCL, which possessed a melting temperature below body temperature (32.8 ± 2.8 $^{o}$C), indicating that this material could be useful in biomedical applications where shape recovery and/or moldability at body temperature is beneficial. Such applications possibly include implementation in minimally-invasive surgical devices and constructs. Another potential utility of the material is in the form of an external stent to mitigate neointimal hyperplasia in vein grafts and hemodialysis access sites. As applying external stents in these applications has been shown in large animal models to correlate with a mitigation in neointimal hyperplasia, it was desired to test the ability of this material to promote this process in the format of a porous scaffold. In an initial pilot study, it appeared that a larger spaced design (~220 μm vs. 170 μm) could possibly result in a design with a higher Cumulative Score (semi-quantitative summation of Neovascularization (high score = more vascularization), Inflammation (high score = low inflammation), and Fibrogenesis (high score = low fibrogenesis). This suggested that wider-spaced pores may promote a more favorable response through promotion or downregulation of some combination of these factors.

To investigate this, 4 porous 68%PCL-32%ACPCL scaffolds paired by equivalent pore size (635 ± 63 μm, 1159 ± 64 μm) and spacing (151 ± 50 μm, 229 ± 51 μm) were implanted subcutaneously in mice along with nonporous 68%PCL-32%ACPCL and microporous ePTFE controls. Prior to implantation, porous designs (Designs A –D) and the nonporous PCL-ACPCL control (Design E) were evaluated in terms of their mechanical properties. Comparison of pore size and spacing effects revealed a statistically

significant decrease in maximum stress ($\sigma_{ma}$) when spacing is reduced from 230 to 150 μm ($p = 0.0025$), but not when pore size is changed approximately two-fold ($p = 0.3662$). These results suggest that pore spacing is a better predictor of mechanical properties than pore size. To evaluate the effects of pore size and spacing of these PCL-ACPCL constructs on tissue response, a total of 21 mice were implanted with Designs A – F and sacrificed on Days 4, 14, and 28. Semi-quantitative histological scoring of these samples by a board-certified veterinary pathologist revealed that porous designs promoted both neovascularization and fibrogenesis relative to non/microporous controls. All porous and nonporous designs were statistically significant from each other by Neovascularization and Fibrogenesis Scores. Inflammation remained mild (Inflammation Score = 2) to minimal for (Inflammation Score = 3) for all of the designs except for Design A, which was more moderate overall ($1.69 \pm 0.92$). As such, a statistically significant difference was detected between Design A and Design F for Inflammation Score ($p = 0.0318$) and this was also the only comparison that was significantly different by Cumulative Score ($p = 0.0182$). Comparing groups by pore spacing and size also revealed significant differences in Inflammation Scores and Cumulative Scores for small spacing vs. nonporous groups ($p \leq 0.001$) and small pore size vs. nonporous groups ($p \leq 0.0029$). Although no significant differences were detected in the semi-quantitative histological criterion between pore design groups on Day 28, these results intimate that a small pore spacing and size combination elicits a more upregulated inflammatory response from x%PCL-y%ACPCL implants.

Neovascularization was further characterized via a microvessel detection algorithm that quantified the total vessel number, total and average vessel area, average vessel

perimeter, and microvessel density of each design via colorimetric quantification of DAB staining against CD31. On Day 28, trends in total vessel number and area were virtually identical. All porous designs had greater vessel number and vessel area than nonporous designs as expected. Design C had the highest total number of vessels and area, followed by Design D. Both of these designs were significantly different from Design F ($p \leq 0.0037$) for both metrics. Design C was also significantly different than Design E in terms of total vessel number ($p = 0.0431$). In corroboration with this trend, microvessel density was highest for Design C at 28 days, which was statistically significant in comparison to the smaller spaced and larger sized Design B ($p = 0.0048$). Comparisons based on pore spacing and pore size groups revealed that all were different than nonporous controls for total vessel number and area on Day 28 as expected. The 230 μm group (C,D) was also different from the 150 μm spaced group for both total vessel number ($p = 0.02111$) and area ($p = 0.0241$), which implied that the larger spacing (Designs C and D) is more conducive to neovascularization over the course of one month.

Macrophage are known to be integral to the regulation of tissue responses and, although their phenotypic behavior exists across a spectrum, are classically characterized to either promote inflammation (M1) or wound healing (M2). Macrophage phenotypes were characterized in terms of their M1 and M2 phenotypes via immunohistochemical staining with F4/80 as a pan macrophage marker, iNOS as an M1 macrophage marker, and CD206 as an M2 marker. Designs B and C were shown to express more of a pro-inflammatory M1 phenotype on Day 4 compared to the low pore size, low pore spacing design (A). As transient upregulation of M1 phenotypes has been shown to stimulate pro-angiogenic processes, this result may help explain why the wider spaced 230 μm group

elicited more neovascularization as assessed by the CD31 microvessel detection algorithm. Conversely, iNOS positivity in Designs C and D was significantly reduced at 28 days for each group relative to Day 4, unlike the shorter-spaced Designs A and B. This suggests that Designs C and D may induce less chronic inflammation and undergo more of a wound healing response than shorter spaced designs, although it is unclear to what degree this occurs without longer-term studies. IHC staining for MMPs 3, 9, 12, 13, and 14 revealed some granular, co-localized staining of monocyte-macrophages peripheral to the implant, suggesting their possible role in the inflammatory, fibrotic, and neovascular processes observed.

Like any other implant, implantation of an external stent around the vein results in some degree of injury to the surrounding tissue that perturbs homeostasis and results in a complex wound healing response.[91] As alluded to earlier, the intensity and duration of this inflammatory response may play an important role in the function of the external stent and defines the biocompatibility of the device. Physicochemical and geometric properties of the external stent partially govern this response, which is characterized by the degree of acute inflammation, chronic inflammation, granulation tissue formation, foreign body reaction, and fibrosis.[91] The foreign body reaction, comprised of foreign body giant cells and granulation tissue (i.e. macrophages, fibroblasts, capillaries), is a critical step in the type of biological response elicited and is highly dependent upon the topology and surface chemistry of the implant. These properties mediate the type and quantity of proteins adsorbed on the surface of the substrate, which provide ligands for monocyte or macrophage attachment and may also signal the macrophage fusion process that generates foreign body giant cells.[91]

Comparison of neovascularization, inflammatory, and fibrotic tissue responses elicited by macroporous 68%PCL-32%ACPCL scaffolds and microporous ePTFE implants reveals that the PCL-ACPCL scaffolds are more pro-inflammatory, pro-neovascular, and pro-fibrotic than ePTFE. It is hypothesized that materials promoting more neovascularization will more effectively mitigate neointimal hyperplasia by helping the vein adapt more readily to the intense pressure and flow conditions experienced by the vein in the arteriovenous environment. The positive impact of neovascularization on the performance of tissue-engineered bypass grafts supports this notion.[275] It is unclear what degree of inflammation and foreign body reaction is ideal for external stenting, but it has been shown that complement and mast cells migrate onto NH-reducing macroporous polyester (Dacron) sheaths and deposit ECM proteins. Lymphocytes, neutrophils, giant cells, and T-cells were shown to be entrapped by these sheaths,[7] but not with the ineffective microporous ePTFE stents.[83, 117] Qualitatively, these scaffolds appear to promote a similar inflammatory and immune response to that described. A side-by-side comparison between PCL-ACPCL and Dacron meshes would more clearly answer how these scaffolds compare in terms of neovascularization, fibrosis, and inflammatory responses. Also, even if comparative subcutaneous mouse experiments such as these could be done, it is unclear whether more intense inflammatory and/or fibrotic processes are favorable for mitigation of intimal hyperplasia in a venous environment. Further studies more precisely evaluating the role that these processes play in neointimal hyperplasia would be instrumental to improving external stent function and patency outcomes for hemodialysis, coronary bypass, and peripheral bypass patients. Evaluation of subcutaneous mouse tissue response

to porous 68%PCL-32%ACPCL scaffold implantation appears to promote neovascularization processes that are desirable for vascular engineering applications.

## 4.5 Conclusions

In this Aim, x%PCL-y%ACPCL copolymers were synthesized through direct modification of PCL in a manner much quicker and more conducive to scale up. A contract manufacturer, Silar Laboratories, synthesized a large batch of 68%PCL-32%ACPCL, which was used in subsequent in vivo experiments to evaluate the role of pore size and spacing on neovascularization, inflammation, and fibrogenic processes. Characterization of mechanical properties of porous scaffolds revealed that the differences caused by an increase in spacing from 150 μm to 230 μm has a greater impact on mechanical properties such as maximum stress than an approximate two-fold increase in pore size. As polyester (Dacron) external stents have demonstrated an ability to mitigate neointimal hyperplasia, which also correlate with an increase in adventitial angiogenesis, it is hypothesized that external supports promoting neovascularization are beneficial for external stenting of venous tissue in hemodialysis and bypass grafting environments. Neovascularization, inflammation, and fibrogenesis were evaluated through semi-quantitative histological adapted from elsewhere. Results show that macroporous 68%PCL-32%ACPCL scaffolds upregulate neovascularization and fibrogenesis relative to ePTFE microporous grafts. It was desired to evaluate the ability of porous scaffolds to induce neovascularization, as it has been shown to be an indirect corollary to mitigating intimal hyperplasia in large animal studies. After 28 days, histological semi-quantitative measures as well as CD31 microvessel detection algorithms quantifying total vessel number, total vessel area, and microvessel density revealed that porous PCL-ACPCL scaffolds promoted neovascularization relative to microporous ePTFE. Fibrogenesis also appeared to be

upregulated, as assessed by the degree of connective tissue bridging of the implants after 28 days as well as Masson's trichrome staining. Immunohistochemistry-based macrophage phenotype characterization indicated that pro-inflammatory M1 macrophages were significantly upregulated in porous designs B (~1160 μm diameter, 150 μm spacing) and C (635 μm diameter, 230 μm spacing) relative to A (635 μm pore size, 150 μm spacing). iNOS positivity indicating the pro-inflammatory M1 macrophage phenotype was significantly reduced from Days 4 to 28 with the wider-spaced pore designs C and D, but not with smaller spaced ones. This may imply more a shift towards the M2 "wound-healing" macrophage phenotype with these designs relative to smaller spaced ones, although M2/M1 ratio was highest for microporous ePTFE at 28 days IHC staining of MMPs 3, 9, 12, 13, and 14 suggests co-localization of these important wound healing regulators with monocyte-macrophages at the polymer-tissue interface. Further studies are required to determine whether the neovascularization, inflammatory, and fibrotic processes are beneficial for external stenting applications, but this study warrants further investigation.

# CHAPTER 5: SUMMARY AND FUTURE DIRECTIONS

## 5.1 Summary

In Aim 1, a new class of PCL-based shape memory polymers were synthesized and characterized for their mechanical, shape memory, and endothelial cell compatibility effects. The polymer library exhibited tunable thermomechanical properties, good ductility, high shape fixity and shape recovery, and switch-like shape recovery around body temperatures for many compositions. *In vitro* endothelial cell compatibility was assessed via a resazurin viability assay and demonstrated >85% viability relative to TCPS. These SMPs appear to represent a promising new biomaterial for biomedical applications such as external stenting of vein grafts and hemodialysis vascular access sites as partially moldable, ductile, and slowly biodegradable material with apparent cytocompatiblity.

In Aim 2, the x%PCL-y%ACPCL synthetic scheme was simplified and standardized to enable scaled up synthesis by a contract manufacturer. Porous polymer scaffolds with wider spaced pores (230 μm vs. 150 μm) were resilient to higher stresses, and exhibited a tensile modulus close to that of healthy coronary arteries (0.57 – 1.11 MPa for porous scaffolds compared to 1.48 MPa). Semi-quantitative assessment of neovascularization, inflammation, and fibrogenesis was evaluated by a board-certified veterinary pathologist and revealed that macroporous scaffolds promoted more neovascularization and fibrogenesis than nonporous controls. CD31 quantification via a microvessel detection algorithm determined that the total number and area of vessels was upregulated in pores, especially those with wider spacing. Macrophage phenotype characterization by IHC indicated that some designs show higher positivity for M1 macrophages at early time points, and this is significantly downregulated at later timepoints, which indirectly implies

that more constructive tissue remodeling processes may be occurring in three of the four porous scaffolds. These results warrant further investigation into the application of this material in the form of an external stent, as other large animal studies have shown that promotion of neovascularization processes may help to mitigate neointimal hyperplasia.

## 5.2 Future Work

### 5.2.1 Evaluation of vein responses to external stents in relevant experimental models

In order to optimize external supports, models that are most relevant to the human physiology and most conducive to attaining mechanistic insights of external stents should be employed. No ideal model directly mimetic of NH and human disease conditions currently exists. However, models chosen should match the conduit caliber, hemodynamics, and thrombogenicity as closely as possible to that of the disease state in humans.[280, 281] Larger native vessel diameters should be chosen to best simulate the low shear stress conditions of the anastomoses encountered clinically. This means that large animals such as nonhuman primates, pigs, canines, and sheep are more appropriate selections than small animals for studying an external support's effects on NH. Nonhuman primates represent the closest approximation to humans in terms of blood compatibility, thrombosis, and endothelialization of devices, but may not always be an option due to high cost and low availability. Other factors that play a role in experimental relevance of external stent assessment are the type of artery and vein employed, length of implantation, and type of anastomosis used (i.e. end-to-side or end-to-end). An end-to-side anastomosis geometry should be employed whenever possible in order to better mimic clinical flow conditions.

A detailed assessment of variables to consider when selecting an animal model and differences between them can be found elsewhere.[280, 281]

*Ex vivo* and *in vitro* models are often more appropriate in terms of time, cost, and throughput to optimize and screen design parameters. For example, it may be more efficient to assess mechanical properties of external stents in an *ex vivo* flow-based model. Such *ex vivo* flow systems have emerged as a useful tool to study human venous tissue responses to treatments while under the duress of physiologically relevant flow and pressure conditions in the absence of blood components.[22, 282] In one study, Longchamp et al. demonstrated that a 4 mm Dacron mesh with 750 μm, diamond-shaped pores (Provena®, B. Braun Medical SA) could reduce distention and NH in an engineered perfusion system that exposed SVGs to physiological pressures (120/80 mmHg at 1 Hz) for 3 or 7 days. The mesh also reduced VSMC apoptosis and subsequent medial fibrosis, while preventing upregulation of matrix metalloproteinases (MMP-2, MMP-9) responsible for depositing the ECM that comprises the neointima. Endothelial function, as measured by gene expression of endothelial nitric oxide synthase (eNOS), was also improved with mesh treatments relative to the unstented veins. The meshes exhibited these effects significantly more while exposed to physiological pressures, indicating that the mechanical support provided by the mesh was important in mitigating NH (at least in a blood component-free system). While such findings ultimately need to be proven in a more physiologically-relevant model, this study provides a preliminary example of how *ex vivo* models can provide unique insights into external stent design parameters.

While a few approaches have evaluated the effects of external stents on human venous responses in *ex vivo* models with artery-mimetic pressure and flow,[22] very little, if

any, optimization of external stent designs has been done with these models, in part because they are still not very high-throughput. Moreover, despite the role that the end-to-side geometry of the anastomosis has been shown to play in WSSGs, turbulence, and NH,[111, 283, 284] few, if any, end-to-side *ex vivo* models exist to account for this. Likewise, hemodynamic effects that external supports elicit are thought to play an important role but are currently understudied, limited to a few small-scale clinical trials.[98, 128] In addition, comparative studies examining the role of design parameters on positive remodeling effects (e.g. vascularization) and inflammatory responses are essentially limited to hernia repair mesh evaluations.[90, 140]

Future work will attempt to overcome these critical knowledge gaps besetting prior external stents with a more appropriate, informed selection of material and device design. Parameters will be optimized via a high-throughput computational fluid dynamic (CFD) model recapitulating external stent application to the venous anastomosis. The CFD model will be tested, adjusted, and validated from human AVG responses to artery-mimetic pressure and flow in an end-to-side *ex vivo* flow chamber. Effects of external stent parameters can be iteratively evaluated and understood in this way to better ensure optimal device design early on in development. Evaluation of designs to promote neovascularization while minimizing inflammation and fibrosis will also aid in identifying the most promising design candidates.

An *ex vivo* flow chamber has been developed that can generate artery-mimetic pressure and flow (e.g. 120/80 mm Hg pressure at 1 Hz) (Figure 5-1). The precise geometry of the venous anastomosis can be captured and input into a CFD model using Computed Tomography (CT) (Figure 5-1and Figure 5-2). An initial experiment has been conducted

in the flow system evaluating flow through a y-shape tubular-mimetic of the venous anastomosis in Dr. Byram's Laboratory (Figure 5-1B). An ultrasound transducer was placed across pre-determined areas of the anastomosis[285] (Figure 5-3), and a sequence was used to extract cross-sectional fluid flow measurements. Hemodynamic parameters such as wall shear stress (WSS), wall shear stress gradients (WSSGs), oscillatory shear index (OSI), relative residence time (RRT), and turbulence intensity can now be computed using scripts developed by Dr. Luo's Laboratory. These experimental results demonstrate the feasibility of utilizing the methods described herein to characterize anastomosis hemodynamics.

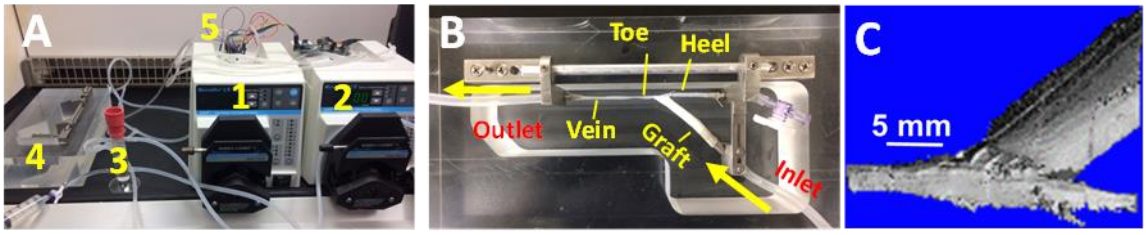


**Figure 5-1 Ex vivo flow System and CT Image of venous anastomosis**
A) Ex vivo flow system consisting of 1) gearing and 2) air pump in a circulating loop with 3) glass pressure column connected to 4) flow chamber with 5) pressure transducers. B) Flow Chamber and C) CT image of AVG anastomosis.

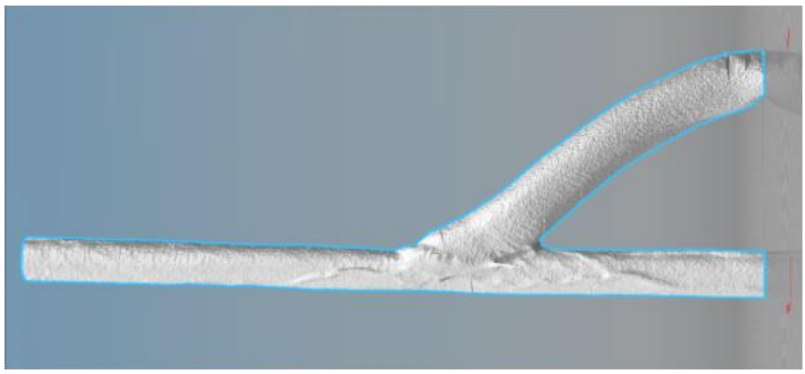

**Figure 5-2 CT Image of venous anastomosis using Syndaver Labs synthetic vein**
An arteriovenous anastomosis was constructed using a synthetic vein and CT scanned.

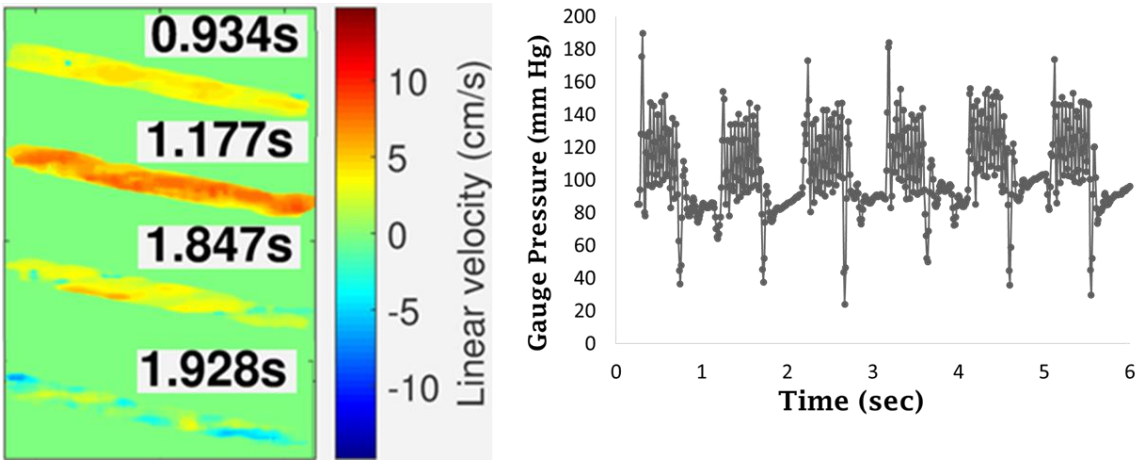


**Figure 5-3 Ultrasound Flow Experiment**
Ultrasound flow experiments show flow downstream of the tubular anastomosis toe. Flow rates are synchronized with pressure.

A CFD model of the venous anastomosis will be created in ANSYS and validated in an *ex vivo* flow chamber to robustly and expediently optimize biomechanical effects of stent parameters. *Ex vivo* experiments will first be conducted using phantom veins before transitioning to human veins.

5.2.1.1 CFD model creation for fluid-structure interaction (FSI)

The pulsatile flow and compliant vein wall together with the flexible external stent represents a coupled FSI problem that will be modeled by CFD using the commercial package, ANSYS. The CFD model will include transient solutions of vein wall deformation and transitional/turbulent flow. To simulate vein wall mechanics, a hyperelastic model[286, 287] will be adopted in order to incorporate nonlinear and large expansion of the vein under arterial pressure. Anisotropic effects will also be included to accommodate the difference between circumferential loading and axial loading;[288] for human veins, Young's modulus varies from 0.03 - 2.5 MPa (depending on loading) circumferentially and from 0.16 - 0.5 MPa axially. Young's modulus of the graft is ~ 80

MPa, with a Poisson's ratio of 0.5 assumed for both graft and vein.[289] Blood flow is assumed to be incompressible and Newtonian as non-Newtonian effects did not significantly alter flow patterns.[290] As the Reynolds number is moderate, direct numerical simulations will be used to capture flow separation and 3D vortices.[290] Outputs of the model include time-dependent expansion of the vein wall and tensile stress and strain in tissue; hemodynamic variables include WSS, WSSG, OSI, RRT, and turbulence intensity.

#### 5.2.1.2 Model validation with phantom veins

To mimic the physical experiment, the 3D geometry of the anastomosis from CT imaging (Figure 5-2) will be imported into ANSYS along with flow data from *ex vivo* experiments. To validate the model, vein wall expansion and flow velocity will be compared at several specified locations both within and downstream of the anastomosis Figure 5-4A). Both the centerline and near-wall locations at each cross section will be used for fluid velocity comparison and quantification.

Vein phantoms from Syndaver Labs (4 mm ID, up to 15 cm length) will initially be used for model validation to save time and conserve resources. Phantoms will be tied end-to-side at 45$^{o}$ to 6 mm GORE PTFE Standard Wall tubing in the *ex vivo* flow chamber using double-armed 6-0 prolene monofilament sutures. The constructed AVG will then be secured to the *ex vivo* flow chamber flush with Blood Mimicking Fluid (CIRS Inc.). As described in *Preliminary Experiments*, an ATL L12-5 ultrasound transducer will be placed across pre-determined areas around the anastomosis,[285] and a sequence will be used to extract cross-sectional fluid flow measurements spaced approximately 156 μm apart at a sampling frequency of 9 MHz. The matrix of flow data will be analyzed in Matlab to assess

maxima, minima, and average flow rates at each cross-section and project these flows onto contour and 3D maps (Figure 5-4B) in addition to hemodynamic outputs (WSS, etc.). A total of 20 AVGs (10 with/without external stent) will be evaluated in this manner.

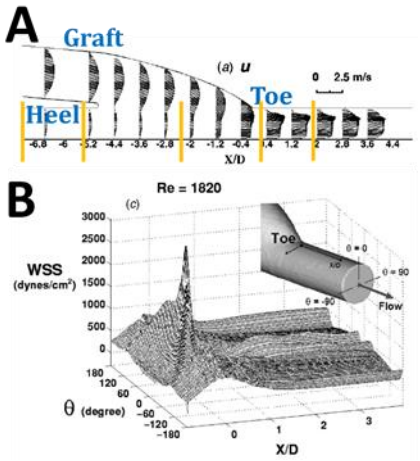


**Figure 5-4 Hemodynamic Characterization of Flow**
Depiction of cross-sectional velocity profiles (orange lines signify sectioning locations for paraffin embedding) and B) projection of time-averaged WSS (TAWSS) across the venous anastomosis (adapted from Loth et al).[285]

After model validation, batch CFD simulations will be run by systematically changing the following design parameters because they affect static and dynamic vein wall expansion under pulsatile flow conditions; as a result, they can alter flow separation patterns in the anastomosis and shear layer stability causing flow transition to turbulence.[154] *Scaffold stiffness* [E'(37°C) = 1, 5, 10 MPa] – These values are within the range measured for the compliant SMP library, accounting for a reduction in stiffness from pores.[15] *Diameter* [ID = 4, 6, 8 mm] – Looser-fitting, 8 mm diameter external supports better reduced NH than tighter-fitting ones,[8] presumably due to more neoadventitial angiogenesis. In contrast, more constrictive Nitinol external stents were better,[10, 11] although this may have caused buckling and patency issues in clinical trials.[134, 135] The range proposed acknowledges typical vein sizes of 3 – 4 mm. *Length* [L = 2, 4, 8 cm] – It

is unclear how long an external stent should extend beyond the anastomosis before the separated flow becomes reattached, as there has been no such investigation. This range is reasonable given that ~59% and 19% of AVG failures occur within 1 and 6 – 10 cm, respectively.[52] *Thickness* [T = 0.3, 0.5, or 1 mm] – Scaffolds should be thick enough for facile handling, bearing in mind that a thicker construct 1) could impede connectivity between vein and surrounding connective tissue, risking hypoxia-induced NH, and 2) require more material. *Pore size and spacing* [750, 1000, 1250 μm and 150, 250, 350 μm] – Based on preliminary data and diffusion limits beyond ~350 μm, parameters chosen reside medial to the design eliciting the highest cumulative score. Approximately 100 runs are expected to be required to perform the parametric study. In the end, 7 external stent designs (6 most promising, 1 less promising) will be applied to phantom AVGs (N = 10) in a 37 $^{o}$C, 5% $CO_2$ incubator. Videos will be taken of the external stent wrapping around the anastomosis to assess and improve ease of use. Flow measurements will be taken as described.

#### 5.2.1.3 Model validation with human AVGs

After study with vein phantoms, de-identified human cadaver veins will be used for flow experiments. Untreated control segments will be assessed for viability (stress > 0.025 x$10^5$ N/$m^2$) in muscle baths.[291] If viable, two ~10 cm segments will be used to construct a treated and control AVG. Both will be cultured at 37 $^{o}$C, measured by ultrasound, and CT scanned at 24 hours. This process will be repeated for 7 stent designs in order to refine the parametric CFD model for human veins. Using the updated model, the three most promising external stent designs elucidated from the simulations will then be evaluated

under standard flow conditions by quantitatively assessing flow and biomechanical response after 1, 3 and 7 days. Vein morphometry and proliferative densities will also be determined to test the overarching hypothesis that NH correlates with biomechanical observations. AVGs will be fixed in 10% formalin immediately following CT scans and sectioned into 6 segments prior to paraffin embedding (Fig. 8D). Each section will be stained with Mason's Trichrome and BrdU. Vein morphometry (intimal and medial area, recalculated lumen diameter, intimal/medial thickness) and proliferative densities in the intimal and medial layers will then be assessed according to Berceli et al.[292] Correlations of morphometric and proliferative measures to biomechanical outputs (WSS, etc.) predicted from the CFD model will be evaluated.

#### 5.2.1.4 Potential Problems and Alternative Approaches

Simulation results from the CFD model may not match the experimental results very well initially. To improve the model, lower flow speeds (and thus lower Reynolds numbers) can be utilized while keeping the pressure at the same level. This would make it easier to run flow simulations and afford focus on vein deformation only. Similarly, flow simulation can be validated separately by using a stiffer phantom with little wall deformation. After both vein mechanics and flow simulations are successfully achieved, we can then move to realistic, coupled FSI simulation.

It is expected that there will be some clear correlations between WSSGs, RRT, and OSI, and that reinforcement with the most promising external stent designs will result in a greater attenuation of these outputs than the least promising designs. These factors are also expected to correlate with a reduction in NH and proliferative densities within the intima.

If there are incongruences in these observations, the number of biological replicates will be increased and additional ultrasound measurements such as vein-wall vibration velocities corresponding to activation of mechanotransductive pathways (e.g. densitometric analysis of phosphorylated ERK1/2 Westerns) will be investigated.[285] In addition, underlying mechanisms related to switches in behavior of smooth muscle cells and myofibroblasts from contractile to synthetic phenotypes can be further explored on the immunostaining and/or genetic levels. For example, Berceli et al. evaluated phenotypic smooth muscle cell markers (e.g. tangelin, MYH11, α-actin) indicative of a switch from contractile to synthetic.

### 5.2.2 Incorporation of a therapeutic to further reduce neointimal hyperplasia

As previously discussed in Sections 2.3 and 2.5.2, localized, sustained release of therapeutic molecules to the adventitia is another promising approach to reduce neointimal hyperplasia. Combining the positive effects of an external support with therapeutics can, in theory, work synergistically to abrogate neointimal hyperplasia. As eluded to in Section 2.3.1, one promising therapeutic candidate is a peptide inhibitor targeted against Mitogen Activated Protein Kinase II (MK2i), as it has shown promise to reduce NH and exhibits anti-fibrotic and anti-inflammatory properties.[23, 24] However, serial ultrasound measurements in a murine inferior vena cava interposition model suggest that vein grafts progressively thicken following an initial NH reduction after 7 days.[25] This indicates the need for more localized, sustained release of MK2i to the vein, especially considering that the half-life of MK2i is only 3 days and the majority of VSMC proliferation and migration

occurs over the first 4 weeks.[4] It is hypothesized that sustained release of MK2i over 2 – 4 weeks may be desirable for internal and/or external stent applications.

#### 5.2.2.1 Gelatin hydrogels as a therapeutic depot

##### 5.2.2.1.1 Pro-angiogenic effects of a gelatin hydrogel

In situ crosslinkable, gelatin-derived hydrogels provide tunable mechanical properties to potentially control release of therapeutics and also promote vasculogenesis.[293, 294] Injectable hydrogels were developed by conjugating hydroxyphenyl propionic acid to gelatin (GHPA) that crosslinks in situ via a horseradish peroxidase (HRP)-mediated reaction (Figure 5-5A). This process enables rapid gelation of hydrogels with tunable mechanical strengths as determined by crosslinking density (Figure 5-5B and excellent long-term biocompatibility (up to 2 weeks) with murine mesenchymal stem cells (MSCs) when encapsulated in 3D culture.[294] Encapsulated MSCs began to form tubular networks with upregulation of CD31 and Flk1 in vitro (Figure 5-5C), suggesting that the gelatin-derived hydrogel has the potential to promote the differentiation of MSCs into an endothelial lineage. The angiogenic potential of these hydrogels was recently confirmed with encapsulated Flk1-LacZ MSCs implanted ventral subcutaneously on polyvinyl alcohol sponges in CL53/B16 mice after 2 weeks, with robust neovasculature and upregulation of EC markers (Figure 5-5D). These results indicate that adding in situ crosslinked gelatin hydrogel supports could promote neo-vasa vasorum formation in HSVs.

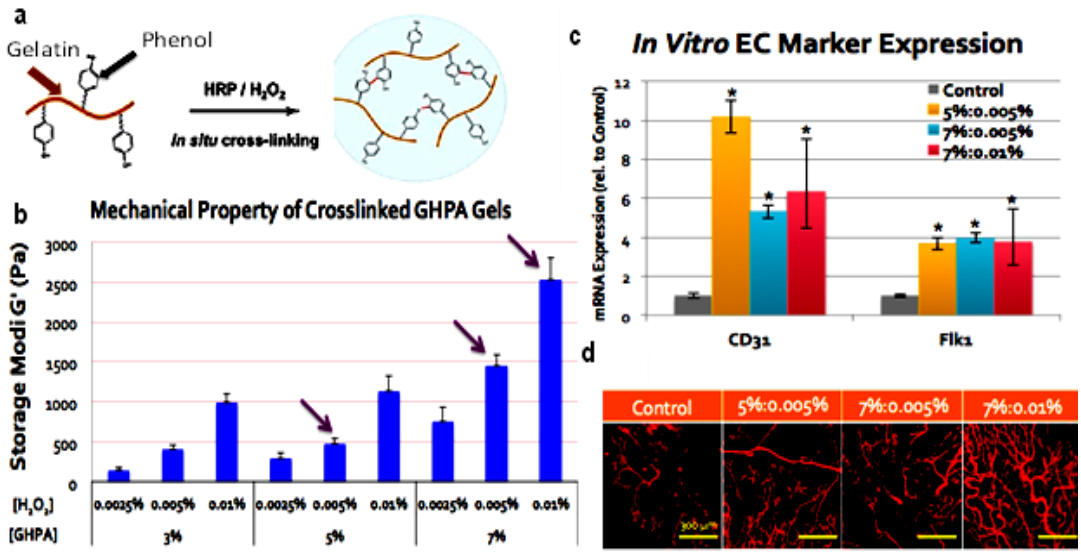


**Figure 5-5 Crosslinkable gelatin hydrogels**
A) Schematic of GHPA crosslinking. B) Storage moduli (G') of crosslinked GHPA hydrogels with varying GHPA (%w/v) and $H_2O_2$ (%w/v) concentrations (N = 3), with indicated compositions used for biological experiments. C) qRT-PCR MSC expression for endothelial cell markers CD31 and Flk-1 after 15 day culture in GHPA hydrogels compared to TCPS controls (N = 3, * = $p<0.05$). D) Fluorescent microangiography images of harvested scaffolds from subcutaneous mouse implantation 2 weeks post-implantation. Images adapted from Lee et al.[294] Copyright 2014, John Wiley & Sons.

5.2.2.1.2 Sustained release of MK2i from gelatin hydrogels

The tunable crosslinking densities of GHPA hydrogels offer a means to control the release therapeutic molecules such as MK2i. MK2i was conjugated to carboxylfluorescein (FAM) via standard NHS coupling[295] to enable facile release quantification by fluorescent measurement of the released supernatant. The conjugate was loaded into the three hydrogels (7.0 wt% GHPA; 0.5%, 0.05%, or 0.0025% H2O2) by incorporating it into PBS solution containing the gelatin prior to crosslinking. A total of 0.2 and 0.91 mg of MK2i can be loaded into the hydrogels as at least one of these amounts should allow ~14 µg/day of MK2i to be released (if zero-order kinetics can be achieved) over 28 days to achieve 100 µM/day in a volume equivalent to a typical cephalic vein anastomosis (3 mm diameter, 230

μm thickness, and 30 mm length equivalent to 60 μL). This dose (100 μM) effectively prevented intimal hyperplasia when used *ex vivo* during the time of explant in the mouse and rabbit venous interposition models and is the equivalent to the minimal effective dose delivered daily in a bleomycin mouse model of idiopathic pulmonary fibrosis.[25, 296]

Different amounts can be screened because the diffusion coefficients driving release of the MK2i from the gelatin hydrogels are unknown and should be determined to better control and predict MK2i release.[297-300] After crosslinking, hydrogels can be incubated in PBS for 28 days; fresh PBS is exchanged at each timepoint to mimic the "infinite sink" condition experienced *in vivo*. The collected supernatants will be read on a plate reader at an excitation/emission of 494/517 nm and compared to unloaded gelatin hydrogels and MK2i-FAM controls without gelatin from which a standard curve will be derived.

GHPA hydrogels (7% w/v) with 3 different $H_2O_2$ concentrations [0.5%, 0.05%, and 0.0025%] were crosslinked in a 24-well plate (n = 4) and incubated in 800 μL PBS at 37 $^oC$. At each time point, samples of the supernatant were transferred to a 96-well plate, and the remainder of the media was exchanged in an attempt to mimic the "infinite sink" condition experienced in the body. Initially, frequent timepoints were taken (15 minutes, 30 minutes, 2 hours), followed by every 12 hours and every 24 hours. As expected, release rates of MK2i are dependent on the crosslinking degree (e.g. $H_2O_2$ concentration) of the GHPA hydrogels (Figure 5-6). Notably, the lowest crosslinked GHPA hydrogel (7%;0.0025%) contains the largest pores and has the most burst release. Conversely, the highest crosslinked GHPA hydrogel (7%;0.5%) contains the smallest pores and allows the least amount of burst release.

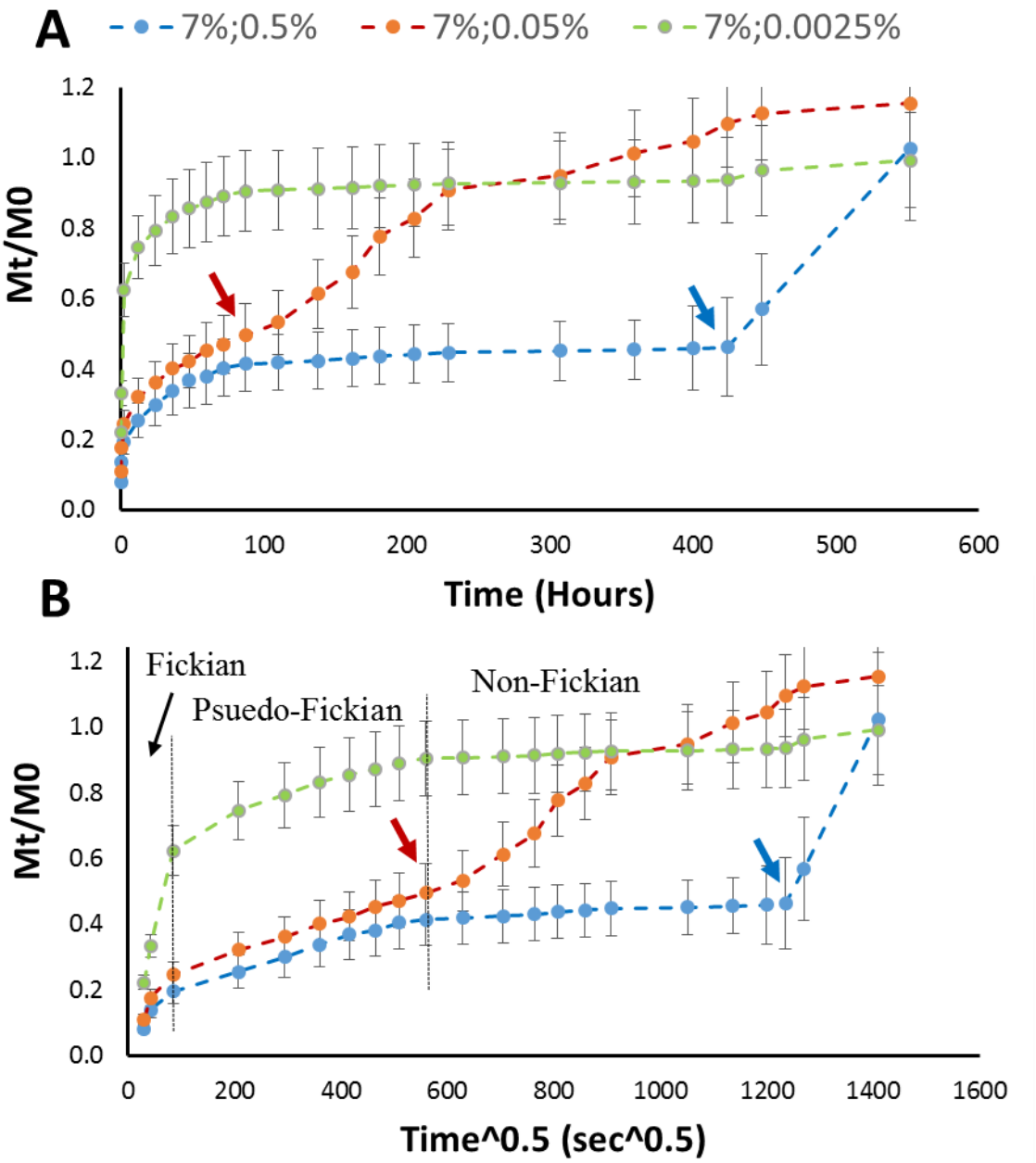


**Figure 5-6 Release of MK2i-FAM from GHPA hydrogels**
The A) Concentration vs. time. The GHPA hydrogel with the higher crosslinking density (more $H_2O_2$, i.e. 0.5%) releases MK2i (160 μg = 100 μM loading) at a slower rate than the less crosslinked GHPA hydrogels, as expected. Arrows indicate a shift towards zero-order release of MK2i-FAM for the two more highly crosslinked GHPA hydrogels (7%;0.5% and 7%;0.05%). B) Concentration vs. $t^{0.5}$ do demonstrate a fit to a Fick's second law of diffusion. Note the transition from a Fickian to non-Fickian release profile.

As expected,[301] there is an initial burst release of MK2i from the hydrogels within the first 2 hours (**Figure 18**). The high degree of initial burst release is due to i) peptide near the surface of the hydrogel-solvent interface and ii) peptide release that is more rapid through larger pores of the hydrogel matrix than through smaller ones[301]. The initial linear portion of the plot represents diffusion-controlled release of MK2i, which can be represented by the 1-D unsteady-state form of Fick's second law of diffusion for a hydrogel matrix containing dispersed peptide.[301-304] It states that for small values of time (t),

**Equation 5-1:**

$$\frac{M_t}{M_\infty} = \left(\frac{16 D_{app} * t}{\pi H^2}\right)^{0.5}$$

In this equation, $D_{app}$ is the apparent diffusivity, and $M_t$ and $M_\infty$ are the cumulative mass of MK2i release after time t and infinite time, respectively. H represents the thickness of the hydrogel.

Following this initial, rapid diffusion-controlled release phase (i.e. Fickian phase) is a pseudo-Fickian phase in which release is still relatively linear with respect to $t^{0.5}$ (Figure 18B), but it is slowed by smaller pore sizes and/or specific interactions between MK2i and the gelatin hydrogel.[301-304] Essentially all of the MK2i is released from the lowest crosslinked GHPA hydrogel (7%;0.0025%) within the first 3 – 4 days. However, at this point 7%;0.05% hydrogel exudes near zero-order release of MK2i through the next two weeks (16 days total), albeit with uneven release kinetics. Meanwhile, the 7%;0.5% hydrogels appears to reach an equilibrium state until around day 17 or 18, at which point it also experiences a near zero-order release profile. The shift in release towards zero-order kinetics for 7%;0.05% and 7%;0.0025% indicated by the arrows in Figure 18A is desirable to maintain high concentrations of MK2i in tissue and may be the result of hydrogel degradation. Follow up experiments can be conducted to quantify degradation over time

as well as to evaluate fluorescent changes over time from unloaded gelatin hydrogels to ensure that this shift in release detected is not the result of autofluorescence from GHPA degradation products.

It should be cautioned that release kinetics *in vivo* will deviate substantially from those observed from GHPA depots in this *in vitro* experiment. The presence of collagenases and the multitude of mechanical forces enacting upon the hydrogel in an *in vivo* setting could dramatically alter and would likely abbreviate release kinetics. This emphasizes the need to test this type of approach in an *in vivo* setting. Moreover, it is a significant challenge from a fabrication standpoint to reliably incorporate hydrogels into polymeric scaffolds. Unless and until these challenges can be overcome, it may be advisable to pursue another avenue for sustaining release of therapeutics such as MK2i to the adventitia.

#### 5.2.2.2 Immobilized heparin as a therapeutic depot

Electrostatic interactions can be leveraged to sustain release of cationic therapeutics such as MK2i. Such interactions can be established to control release by modifying the surface with an anionic polymer, or even altering positively- and negatively-charged polymers in a layer-by-layer assembly.[305-307] Heparin is a prime candidate to induce this type of effect as a highly-sulfated glycosaminoglycan with a strong negative charge. Its negative charge not only can limit burst release of positively charged molecules, but it also can prevent platelet adhesion and improve hemocompatibility of synthetic biomaterials due to its anti-fouling effects.[308-310]

One simple method for adhering heparin to the hydrophobic surface of PCL or PCL-ACPCL is to dip the polymer surface into 3,4-dihydroxy-L-phenylalanine (DOPA), a

highly-adhesive molecule that binds to a wide variety of surface chemistries and polymerizes fairly rapidly via oxidation under ambient conditions.[311, 312] DOPA is a catecholic amino acid and is an important component of muscle adhesive proteins (MAPs). Oxidation converts the catechol to *o*-quinone which, as an electrophilic Michael acceptor, reacts with catechol groups to stabilize itself and form crosslinks between DOPA molecules. Zhu et al. previously immobilized heparin to the surface of poly(vinylidene fluoride) (PVDF) microporous membranes by subsequent dipping in DOPA and heparin solutions.[313] Initial experiments were conducted aiming to replicate this work and to determine optimal conditions that maximize the amount of heparin bound to the surface.

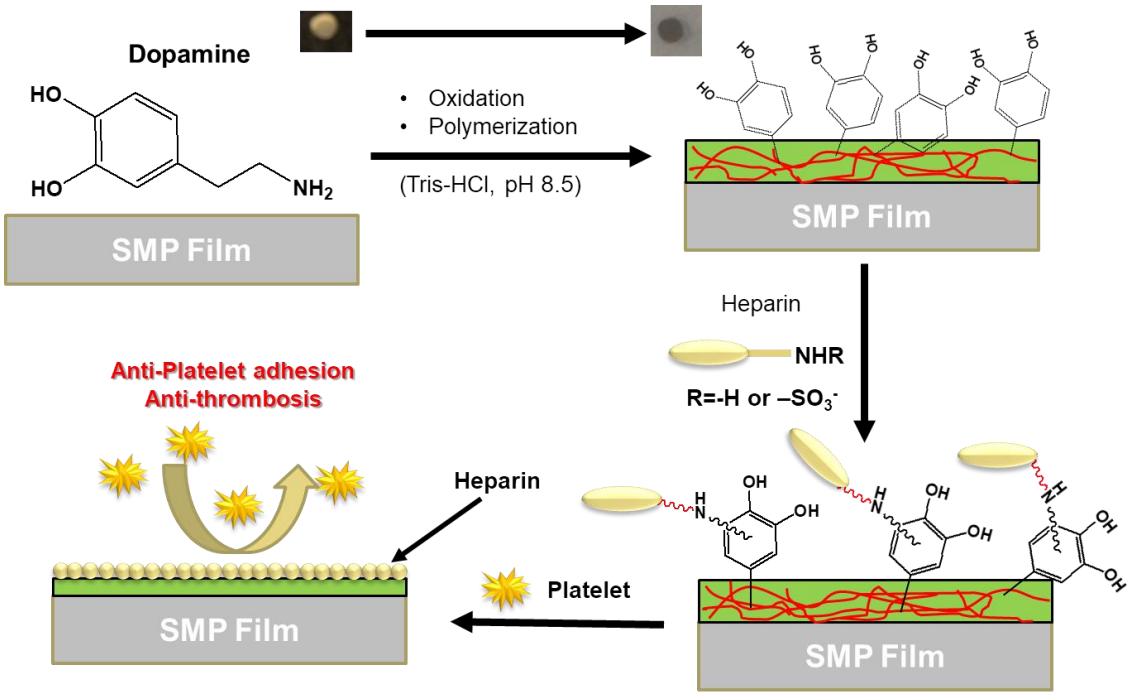


**Figure 5-7 Heparin binding to PCL-ACPCL surfaces via DOPA pre-treatment**
Crosslinked PCL-ACPCL films are dipped into DOPA solution and allowed to oxidize for more than 12 hours to enable polymerization and induce an adhesive DOPA surface coating. This coating is then dipped into a heparin solution to enable bonding between DOPA quinone species and amine groups of heparin. Adapted with permission from Zhu et al (Copyright 2009, Elsevier).[313]

Similar to Zhu et al., PCL-ACPCL films were incubated in 2.0 g/L DOPA with a 7:3 volumetric ratio of Tris (10 mM, pH 8.5): ethanol for 12 hours. After washing in a 45 $^{o}$C water bath for 24 hours, the films were immersed in aqueous heparin solutions at either 1, 10, or 50 mg/mL. The amount of heparin bound to the surface was quantified by a Toluidine Blue O stain. Films were incubated in 0.01 M HCL, 0.02 wt% NaCl, 0.04 wt% TBO, shaken at 37 $^{o}$C for 4 hours and rinsed twice with deionized water to form the heparin-TBO complex. This complex was solubilized with a 4:1 volumetric ratio of ethanol: 0.1 M NaOH and the absorbance at 530 nm was measured for all samples. The amount of immobilized heparin was quantified by a standard curve of varying heparin concentrations. A preliminary result indicated that increasing heparin concentration of the solution from 1 to 10 to 50 mg/mL resulted in an increase in $\mu g/cm^2$ immobilized heparin from 61.3 ± 11.0 to 85.7 ± 26.7 to 114 ± 14.0 (Figure 5-8). However, the 530 nm absorbance of DOPA-only dipped films was 78.2 $\mu g/cm^2$, which made this result a little bit difficult to interpret. Subsequent experiments quantified by the TBO assay followed similar trends, with higher absorbances observed from dipping into more concentrated heparin solutions, but significant absorbances read from DOPA-only coated films.

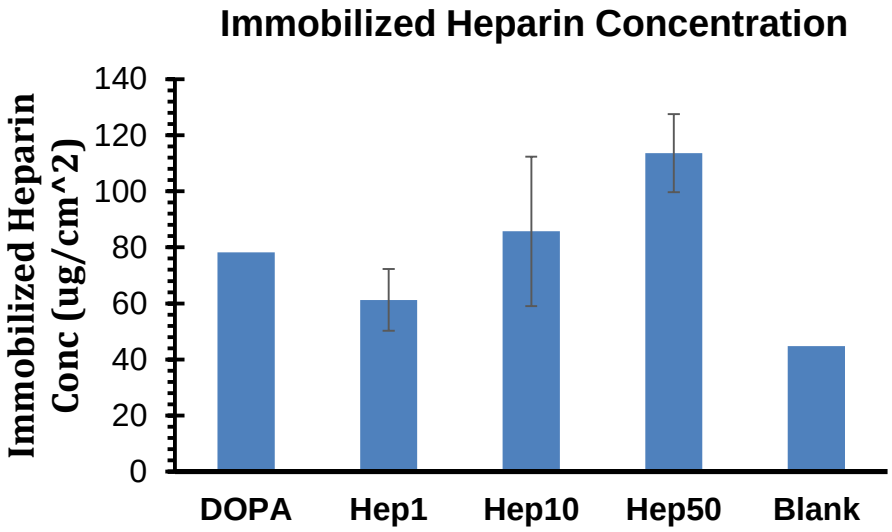


**Figure 5-8 Immobilized Heparin onto DOPA-coated PCL-ACPCL Films**
TBO staining results for polymer films dipped in heparin solutions of 0, 1, 10, and 50 mg/mL.

In an attempt to increase heparin bound to the surface, polymer surfaces were plasma-treated between DOPA and heparin dipping steps and 1-Ethyl-3-(3-dimethylaminopropyl)carbodiimide (EDC) was added to attempt to increase bonding of DOPA carboxyl groups with primary amines on heparin. The combination of mixing with the DOPA solution with EDC and plasma treating for 10 minutes before dipping into a saturated solution of heparin (200 mg/mL) resulted in the highest immobilized heparin concentration 21.9 $\mu g/cm^2$ (Figure 5-9), which was on par with the maximum immobilized heparin concentration from Zhu et al. It should be cautioned that further experiments utilizing complimentary assays should be conducted in order to verify that these conditions are indeed superior to others in immobilizing the maximum amount of heparin to the surface of PCL-ACPCL films.

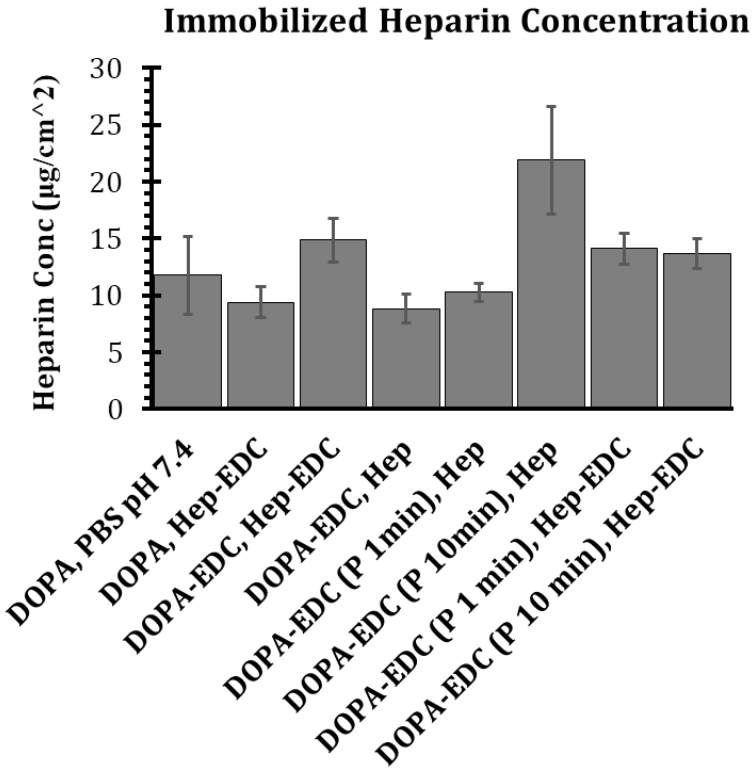


**Figure 5-9 Optimization of DOPA and heparin coating steps**
PCL-ACPCL films were dipped in 1) either DOPA or DOPA solution containing EDC (DOPA-EDC), followed by 2) either no plasma treatment, treatment for 1 min, or treatment for 10 minutes, and 3) dipped in either 200 mg/mL heparin solution or 200 mg/mL heparin solution containing EDC (Hep-EDC).

5.2.2.3 Co-immobilization of heparin-tyramine and MK2i to PCL surfaces

Prolonged exposure of DOPA to air reduces its adhesiveness and may result in inconsistencies in heparin grafting. Moreover, DOPA can take a considerable amount of time (> 12 hours) to be grafted to the surface. To improve reliability of this DOPA surface coating strategy and reduce processing time, heparin was functionalized with phenol groups that enable polymerization when oxidized and catalyzed with tyrosinase. Heparin density, wettability, and atomic composition of heparin-tyramine (i.e. HT, or heparin-DOPA) coatings immobilized to the surface of PCL substrates were characterized. The

non-fouling or anti-thrombogenic potential of these coatings were also evaluated *in vitro*. MK2i loading and release from these PCL-HT were evaluated over 28 days. The ability of this drug-release platform to inhibit VSMC migration and phosphorylation of target proteins involved with NH were also assessed *in vitro*. Fluorescence microscopy of human saphenous veins (HSV) wrapped with MK2i-loaded PCL-HT tubes over 6 hours and 3 days indicated that MK2i was penetrating HSV tissue. Methods and data described herein were courteously provided by Dr. Yunki Lee.

#### 5.2.2.3.1 Materials and Methods

##### 5.2.2.3.1.1 Materials

Heparin sodium (molecular weight = 12,000–15,000 g/mol) was supplied from Acros Organics (Geel, Belgium). Polycaprolactone (average molecular weight = 80,000 g/mol; PCL), tyramine hydrocholoride (TA), 1-ethyl-3-(3-dimethylamino-propyl)-carbodiimide (EDC), N-hydroxysuccinimide (NHS), toluidine blue O (TBO) and tyrosinase (from mushroom, 3610 units/mg solid) were obtained from Sigma-Aldrich (St. Louis, MO, USA). MK2i peptide (YARAAARQARAKALARQLGVAA) was supplied from EZBiolab (Carmel, IN, USA). Dulbecco's phosphate-buffered saline (DPBS) was purchased from Gibco BRL (Grand Island, NY, USA), and Tris-HCl buffer (10 mM, pH 8.5) was purchased from bioWORLD (Dublin, OH, USA).

For *in vitro* cell studies, rat vascular smooth muscle cells (VSMCs) were purchased from ATCC (Manassas, VA, USA), and were cultured at 37 °C and 5% CO2 in Dulbecco's modified Eagle medium (DMEM; Gibco, USA) supplemented with 10% fetal bovine serum (FBS) and 1% penicillin/streptomycin (PS). For western blot analysis, the specific

antibodies for total HSP27 and phosphor-HSP27 (serine 15) were obtained from Santa Cruz Biotechnology (Dallas, TX, USA) and Thermo Fisher Scientific (Waltham, MA, USA), respectively. The antibodies for CREB and phosphor-CREB were obtained from Cell signaling Technology (Danvers, MA, USA).

5.2.2.3.1.2 Synthesis of heparin-tyramine (HT) polymer

To synthesize tyrosinase-reactive HT polymer, tyramine (TA) was grafted to carboxylic groups of heparin using EDC/NHS coupling reaction. Briefly, heparin (1 g), EDC (1.53 g, 8 mmol) and NHS (0.58 g, 5 mmol) were dissolved in deionized water (DW, 100 mL), and the solution pH was then adjusted to 4.5–5 with HCl. After activation of carboxylic groups on heparin for 1 h, TA (0.55 g, 3 mmol) dissolved in DW was added to the heparin solution, and the reaction was carried out at room temperature for 24 h. The resulting solution was purified using a dialysis bag (molecular weight cut off = 3.5 kDa) for 3 d in DW. The purified solution was filtered using a bottle top filter with a pore size of 0.2 $\mu$m, and lyophilized for 3 d to obtain the HT polymer. The chemical structure of the HT conjugate was characterized by $^{1}$H NMR and UV spectrophotometry (V-750, Jasco, Japan). 1H NMR was performed on 5 wt% HT solution in D2O with a 300 MHz spectrometer (Bruker Instrument Inc., Billerica, MA, USA) to verify the corresponding peaks of phenol group in the HT polymer. For quantitative analysis on substitution degree of tyramine, the absorbance of HT polymer solution (1 mg/mL) was measured at 275 nm, and phenol content was determined against a calibration curve of tyramine hydrochloride solution.

5.2.2.3.1.3 Surface immobilization of HT via tyrosinase-triggered oxidative reaction

Prior to heparin-functionalization, PCL substrates were prepared by solvent casting.[314, 315] PCL solution (10 wt%) dissolved in 150 mL of THF was poured onto a glass Petri dish, and the solvent was evaporated slowly at room temperature. Round-shape PCL substrates (13 mm diameter) were collected by a hole puncher and washed three times with DW to remove residual THF.

HT-immobilized PCL substrates (PCL-HT) were prepared by simply dipping PCL into an HT polymer solution as previously described.[312] Briefly, the PCL substrates were immersed in a solution of HT polymer (1 wt%) dissolved in Tris-HCl buffer (10 mM, pH 8.5), and then 0.4 kU/mL of tyrosinase was added. After 3 h of incubation at room temperature, they were washed thoroughly with DW, and dried under vacuum.

5.2.2.3.1.4 Characterization of HT-immobilized PCL surfaces

After tyrosinase treatment, the immobilized heparin amount on the surface was quantified using a TBO assay.[316-318] Briefly, the bare PCL, PCL/HT (without tyrosinase) and PCL–HT samples were immersed in 1 mL of PBS (pH 7.4) solution containing 0.002 wt.% TBO, and were shaken for 30 min at room temperature. Then, 2 mL of hexane was added and vortexed for 5 min. The absorbance of aqueous phase was measured at 620 nm using a microplate reader (M1000, Tecan, Switzerland), and heparin amount was determined by a calibration curve of heparin solution.

To characterize HT-immobilized PCL substrates, changes in the surface wettability were analyzed by measuring static water contact angle using a contact angle analyzer (SEO, Phoenix 150, South Korea). A droplet of DW on the surface of pure PCL and PCL–

HT samples was visualized using an equipped camera. Changes in the surface atomic composition after HT immobilization on PCL surface were also analyzed by X-ray photoelectron spectroscopy (Thermo Electron, K-Alpha, USA) at the Center for Research Facilities, Kyunghee University, Korea.

5.2.2.3.1.5 In vitro protein/platelet adhesion tests on HT-immobilized PCL surfaces

Substrates (bare PCL and PCL–HT) were immersed and incubated in PBS medium containing fibrinogen (100 $\mu$g/mL) at 37 °C for in vitro protein absorption tests. After 3 h of incubation, the surface of each sample was gently rinsed three times with PBS, and then treated with 1% SDS to collect the absorbed protein. The amount of absorbed fibrinogen on the surface was quantified using a Micro BCA assay kit (Pierce, USA).

For *in vitro* platelet adhesion test, the platelet was obtained from fresh rat whole blood in accordance with the guidelines of Yonsei Laboratory Animal Research Center (YLARC; Seoul, Korea). Briefly, Sprague-Dawley (SD) rat (weights: 250–300 g) blood was collected using a syringe containing 0.1 M sodium citrate. By centrifuging the whole blood at 2,500 rpm for 10 min, platelet rich plasma (PRP) and platelet poor plasma (PPP) were separated from the red blood cells (RBC). After that, to isolate high concentration of platelet from the collected PRP, the samples were further centrifuged at 2,500 rpm for 10 min. The platelet pellets were diluted with buffer solution, and added to bare PCL and PCL–HT substrates (13 mm in diameter). Following incubation in platelet solution at 37 °C for 1 h, each sample was thoroughly washed three times, and fixed with 2% glutaraldehyde in PBS (0.1 M, pH 7.4) for 6 h. They were then fixed with 1% osmium tetroxide (OsO4) for 90 min, and dehydrated using a Critical Point Dryer (EM CPD300,

Leica, Austria). The adhered platelets on the surface were observed using the SEM (FE-SEM, Carl ZEISS, Germany) after platinum sputter coating (EM ACE600, Leica, Austria), and were quantified from the SEM images on random positions.

5.2.2.3.1.6 Characterization of MK2i-loaded PCL-HT substrates

To confirm the electrostatic interaction between MK2i and HT polymer, changes in zeta potential of HT/MK2i nanoparticles were analyzed by increasing MK2i feed amounts, as previously reported.[316] The nanoparticles formed with 1 mg/mL of HT (500 $\mu$L) and 0.1–50 mg/mL MK2i (500 $\mu$L) were prepared in PBS medium, and their zeta potential was measured using a DLS Zetasizer (Nano ZS, Malvern, USA). The concentration of HT polymer was fixed at 1 mg/mL, and mixing ratio (w/w) was varied from [MK2i]/[HT] = 0.1 to 50 to investigate the molecular interactions.

For *in vitro* MK2i release study, the MK2i peptides with different concentrations (100, 500 and 1000 $\mu$g/mL) were first loaded on the PCL–HT substrates by a simple dipping method. Briefly, 13 mm diameter substrates were immersed in 1 mL of Tris-HCl buffer (10 mM, pH 8.5) containing MK2i peptide, and the reaction was allowed at room temperature for 24 h. Then, the dehydrated PCL–HT/MK2i discs were placed in 24-well plate, and PBS (1 mL) was added to each well. The release experiment was carried out at 37 °C for 28 d. At predetermined time intervals, the supernatant was collected and replaced with the same volume of fresh buffer media for the next time point. The amounts of the released MK2i peptide in the collected media were measured at 562 nm using a Micro BCA assay kit (Pierce, USA), and the cumulative MK2i release kinetics were drawn as a function of time. As a negative control for heparin functionalization, the bare PCL incubated in MK2i solution was used. In addition, FITC-conjugated MK2i peptides (EZBiolab, USA;

100, 500 and 1000 $\mu$g/mL) were also loaded on the PCL–HT surfaces with the same protocol as described above, and the dried samples were visualized by fluorescence microscopy (Axio Observer, Zeiss, Germany) to confirm the distribution and loading amount of MK2i on the surface. In follow-up studies, 1 mg/mL of MK2i solution was used to prepare PCL–HT/MK2i substrates.

5.2.2.3.1.7 In vitro cytotoxicity of PCL-HT//MK2i substrates

To assess PCL-HT *in vitro* biocompatibility, cytotoxicity to mouse fibroblasts (NIH3T3) was investigated using both WST-1 assay (Sigma-Aldrich, USA) and live/dead staining assay (Invitrogen, USA). Bare PCL, PCL–HT and PCL–HT/MK2i samples were incubated in cell culture medium for 24 h, and then the extracted solution from each sample was collected. NIH3T3 cells were seeded onto 24-well plates (2 × 104 cells/well), and incubated for 24 h under standard culture condition (37 °C and 5% CO2) to allow for cell adhesion. Then, the adhered cells were treated with each extracted solution (1 mL) and incubated. As a control, the fresh medium without sample incubation was used. After 24 h, the WST-1 reagents (100 $\mu$L) were added to each well, and the plates were incubated for 2 h at 37 °C. Optical density (O.D.) was measured at 450 nm using a microplate reader (M1000, Tecan, Switzerland) to quantify the mitochondrial activity of the cells. The experiments were performed in triplicate.

Morphological change and cell viability of NIH3T3 cells cultured with each extracted solution were also observed using an optical and a fluorescence microscope (Axio Observer, Zeiss, Germany). For live/dead staining assay, cultured cells with extracts

were incubated for 30 min in a mixture solution containing both calcein AM and ethidium homodimer-1 (Invitrogen, USA), and then were imaged.

5.2.2.3.1.8 In vitro studies of VSMC migration and proliferation

To investigate the inhibitory effect of released MK2i on cellular migration, *in vitro* scratch-wound assays were performed using a Culture-Insert 2 well migration assay kit (Ibidi, USA) according to the manufacturer's instructions. VSMCs were seed within Insert 2 wells at a seeding density of 1 × 104 cells/well, and cultured to be reached at confluency (90–95%) for 1–2 d in DMEM-supplemented with 10% FBS and 1% PS, under standard culture condition. After gently removing the Culture-Insert 2 well to create the scratch wound, the culture medium was replaced with low serum growth medium containing 1% FBS to minimize cellular growth, and incubated overnight.[23, 291] Then, the cells were covered with samples (bare PCL, PCL–HT and PCL–HT/MK2i), and incubated in the medium containing 50 ng/mL of PDGF (R&D systems, USA). To prevent direct physical contact of sample discs with the adhered cells on the plate, a rubber O-ring with 13 mm in diameter (Parker, USA) was placed as a spacer between the bottom plate and disc-type sample. As a positive and negative control, the medium with and without 200 $\mu$g/mL of MK2i peptide was used, respectively. After 24 h of treatment with each sample, the wound areas were imaged under optical microscopy (Axio Observer, Zeiss, Germany), and quantified using an ImageJ software (NIH, USA). The wound closure rate (%) was determined by measuring the wound area ($W''$) at 24 h post sample treatment with respect to the initial scratch-wound area ($W\#$) using the following equation: $(W\# - W'') / W\# \times 100$. Each migration assay was repeated three times.

*In vitro* VSMC proliferation assay was also performed as a control for cell migration test. As described above, the same experiment condition with the scratch-wound assay was used. VSMCs were incubated with the culture medium containing 1% FBS in 24-well plate for 24 h, and then treated with 50 ng/mL of PDGF and samples (culture medium, bare PCL, PCL–HT, PCL–HT/MK2i and 200 $\mu$g/mL of MK2i). After 24 h of treatment, the WST-1 reagents (100 $\mu$L) were added to each well, and their optical density (O.D.) was measured at 450 nm to confirm VSMCs proliferation in each test condition.

5.2.2.3.1.9 Western blot analysis of target protein phosphorylation in VSMCs

VSMCs were grown to 90–95% confluence in a cell culture Petri dish (60 mm in diameter) with normal culture media (10% FBS and 1% PS). Separately, bare PCL and PCL–HT/MK2i were incubated in low serum growth medium (1% FBS), and the extracts were collected at predetermined time intervals (6 h, 1 d, 3 d and 7 d). Adhered cells were serum-starved for 24 h to minimize cell growth, and then treated with pre-extracted MK2i solutions for 2 h. As positive and negative control, the medium with and without 200 $\mu$g/mL of MK2i peptide were used, respectively. Following 2 h of treatment with the extracts, 30 $\mu$M lysophosphatidic acid (LPA; Tocris Bioscience, UK) was treated to each well. As a control for LPA treatment, the medium without LPA was also treated in the same condition. After 30 min of incubation with LPA at 37 °C, the cells were lysed, and then centrifuged at 14,000 rpm for 15 min at 4 °C. The total protein amount in the collected supernatant was measured using a Bio-Rad Protein assay kit. Equal amounts of protein (50 $\mu$g/lane) were loaded into 10% TGX Precast Gels (Bio-Rad, USA); the proteins were separated by electrophoresis, and they were transferred to a nitrocellulose membrane. For analysis of

heat shock protein 27 (HSP27) phosphorylation, the membrane was stained overnight at 4 °C with specific antibodies for total HSP27 (1:500 dilution) and phosphor-HSP27 (1:1000 dilution). For analysis of cAMP-response element binding protein (CREB) phosphorylation, the membrane was stained overnight at 4 °C with specific antibodies for total CREB (1:500 dilution) and phosphor-CREB (1:1000 dilution). After washing three times, the blots were treated with appropriate secondary antibodies for 1 h at room temperature, and imaged using Odyssey infrared scanner (Li-COR Bioscience, USA). Signal intensity of each band was quantified with Li-COR Odyssey software at 800 and 680 nm wavelengths. Each western blot experiment was repeated three times.

5.2.2.3.1.10Ex vivo MK2i delivery into human saphenous veins (HSVs)

For *ex vivo study using* MK2i-releasing PCL–HT sheath, the discarded human saphenous vein (HSV) was obtained from the patients undergoing peripheral or coronary vascular bypass surgery in accordance with approved IRB guidelines provided by Vanderbilt University Medical Center (VUMC). The HSV segment was cut into consecutive rings (2–3 mm in width), and PEG-based hydrogel was then filled inside HSV rings to prevent shrinkage. After that, the HSV rings were wrapped with each sample sheath (bare PCL or PCL–HT/Alexa 568–MK2i), and then they were incubated in RPMI 1640 medium containing 30% FBS, 1% L-glutamine and 1% PS under standard culture condition (37 °C and 5% CO2). To visualize the delivered MK2i in the HSV tissue, Alexa 568 (red fluorescence) was conjugated to MK2i peptide before loading on the surface of PCL–HT sheath (3/3.5 mm in internal/external diameter and 3 mm in width). After *ex vivo* organ culture for 6 h and 3 d, the HSV tissues were frozen in NEG-50 medium (Thermo

Scientific, USA), and sectioned (10 $\mu$m in thickness). The cross-sectioned tissues were stained with 4¢,6-diamidino-2-phenylindole (DAPI; Invitrogen, USA), and then imaged using a fluorescent digital scanner (Aperio VERSA 200, Leica, Germany).

5.2.2.3.2 Results and Discussion

5.2.2.3.2.1 Synthesis and characterization of HT polymers and PCL-HT substrates

To obviate challenges associated with heparin binding to DOPA-coated surfaces, a synthetic scheme was adopted from Park et al. that enables direct conjugation of DOPA to heparin for facile binding of heparin to polymeric surfaces.[319] Heparin was functionalized with conjugated phenol groups that enable conversion of monophenol groups to *o*-dihydroxyphenol (DOPA) and *o*-quinone under oxidative conditions in the presence of tyrosinase. Utilizing EDC/NHS coupling, tyramine (TA) was grafted to heparin to create the heparin-tyramine (HT) polymer (Figure 5-10A). The presence of phenol groups was confirmed by phenolic proton peaks in $^{1}$H-NMR spectra (Figure 5-10B) and quantified by absorbance at 275 nm to be 350 μmol/g of polymer (Figure 5-10C). The phenol-conjugated HT polymer was then immobilized to PCL surfaces by dipping 13 mm diameter PCL disks into 1 wt% HT solution under oxidative conditions (10 mM Tris, pH 8.5) in the presence of tyrosinase catalyst (Figure 5-11A). The darkening of solution after 90 minutes indicated successful conversion of phenol groups to DOPA (Figure 5-11B), but the reaction was carried out for 3 hours to better ensure efficient conversion. The amount of heparin immobilized to the surface was quantified by the TBO assay, and appeared saturated around 17 μg/cm$^2$ (Figure 5-12A). Immobilized heparin content was minimal (approximately 1 μg/cm$^2$) in the absence of tyrosinase treatment and was absent on the bare

PCL substrates (Figure 5-12B). Coating of heparin onto PCL substrates changed the water contact angle of the surface from 80$^{o}$ to 20$^{o}$, indicating a shift from a hydrophobic to a hydrophilic surface that may resist protein adsorption and platelet adhesion. X-ray photoelectron spectroscopy (XPS) revealed the an increase in amine (1.61% to 8.65%) and sulfur groups (0% to 3.19%) on PCL-HT compared to bare PCL surfaces, confirming successful immobilization of heparin onto PCL surfaces (Figure 5-12D-E, Table 5-1).

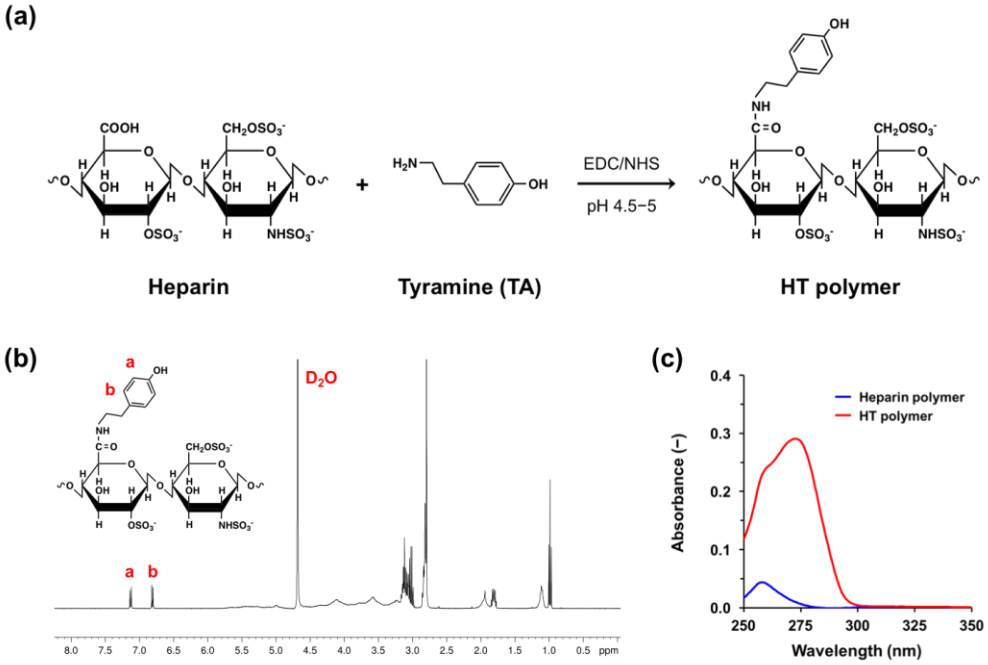


**Figure 5-10 Synthesis and characterization of phenol-conjugated heparin (HT) derivatives**
A) Synthetic route of HT polymer by an EDC/NHS coupling reaction, B) $^{1}$H NMR spectrum of HT polymer dissolved in $D_2O$, and C) UV absorbance spectra of heparin and HT polymers.

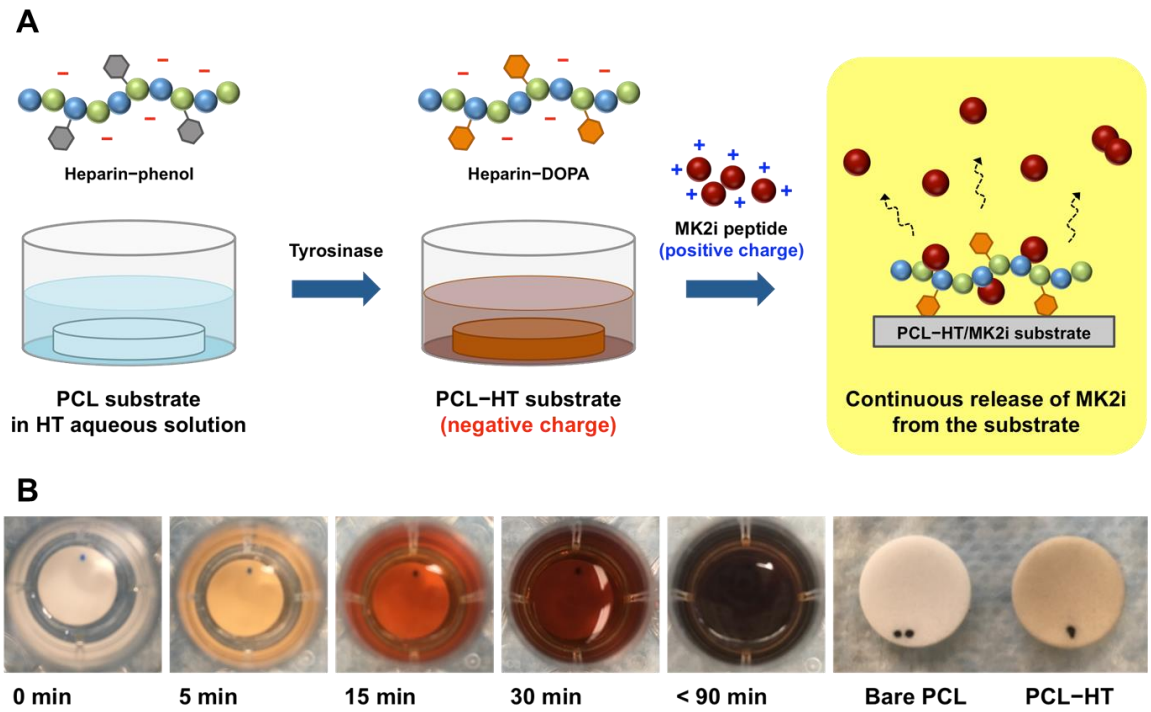


**Figure 5-11 Schematic illustration of tyrosinase-catalyzed heparin immobilization and MK2i loading and release**

A) PCL substrates (13 mm in diameter) were immersed in aqueous polymer solution containing heparin-tyramine (HT; 1 wt.%), and heparin was then immobilized on the PCL surface by the tyrosinase-triggered oxidative reaction. MK2i was then loaded on the heparinized PCL layer through electrostatic interactions between the MK2i peptide and HT polymer. (b) Photographs of the HT solution, and PCL–HT substrate after the 3 hour tyrosinase (0.4 kU/mL) treatment.

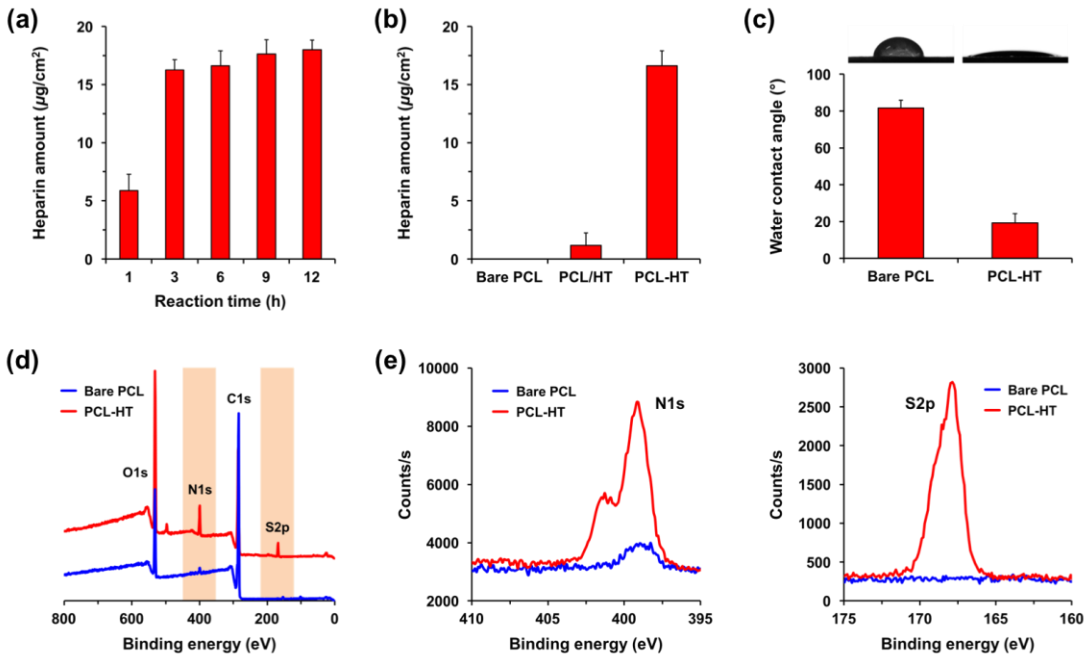


**Figure 5-12 Characterization of PCL-HT substrates**
Surface density of heparin: A) PCL–HT substrates with different tyrosinase-reaction times (1–12 h), and B) bare PCL, PCL/HT (without tyrosinase treatment) and PCL–HT (with tyrosinase treatment) for 3 h. C) Surface wettability and water contract angles before and after HT functionalization. XPS analysis: D) wide scan and E) narrow scan spectra for S2p/N1s in bare PCL and PCL–HT surfaces. Results in A)–C) are shown as mean ± S.D. (n = 3).

**Table 5-1 XPS elemental composition of bare PCL and PCL-HT surfaces**

| Sample | C (%) | O (%) | N (%) | S (%) |
|---|---|---|---|---|
| Bare PCL | 81.92 | 16.47 | 1.61 | - |
| PCL-HT | 58.91 | 29.25 | 8.65 | 3.19 |

5.2.2.3.2.2 Hemocompatibility of PCL and PCL-HT surfaces

Protein adsorption and number of platelets adhering to PCL and PCL-HT surfaces were determined to assess the non-fouling potential of these substrates. Protein adsorption, as measured by fibrinogen adhering to the surface of polymer disks after 3 hours via BCA assay, was significantly reduced on PCL-HT surfaces. Platelets isolated from rat blood

were incubated on polymer surfaces for 1 hour, and the number of platelets quantified by SEM were also significantly reduced on PCL-HT compared to PCL substrates according to these measurements. These results correlate with the reduction in water contact angle observed on PCL-HT, implying that the increased hydrophilicity of these surfaces may be responsible for the decrease in protein adsorption and platelet adhesion observed.

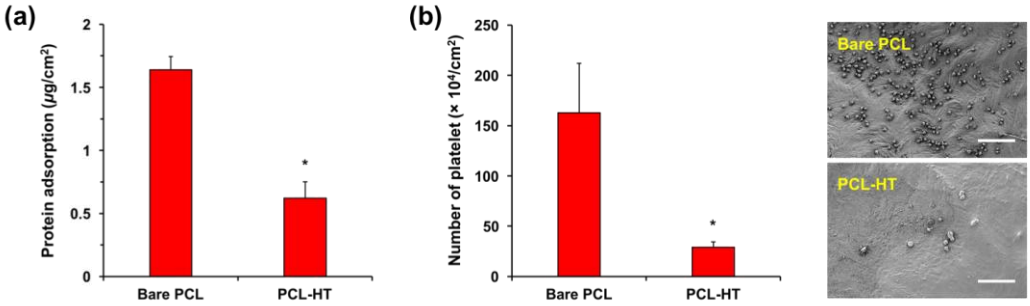


**Figure 5-13 In vitro hemocompatibility of PCL-HT substrates**
A) Absorbed fibrinogen amounts on bare PCL and PCL–HT surfaces. The substrates were incubated in protein solution (100 $\mu$g/mL), and then the absorbed fibrinogen amount was measured by a Micro BCA assay. B) Adhered platelet amounts on bare PCL and PCL–HT surfaces (left). The platelet isolated from rat whole blood was treated to the substrates for 1 h, and then the number of adhered platelet was determined from the images observed by SEM (right). Scale bars indicate 20 $\mu$m. All results are shown as mean ± S.D. (n = 3; *$P$ < 0.05 compared to bare PCL).

5.2.2.3.2.3 Characterization of MK2i-loaded PCL-HT substrates

PCL-HT substrates were dipped into MK2i solutions of varying concentrations. First, electrostatic interactions between HT polymers and MK2i were assessed. Zeta potential measurements of MK21/HT solutions revealed the near neutralization of charge as the MK2i/HT ratio increased from 0.1 to 50, implying that significant electrostatic interactions occur between MK2i and HT and that MK2i loading amounts may increase with increased MK2i concentrations (at least within the range tested) as expected. Loading of MK2i onto PCL-HT substrates showed sustained release over the course of 28 days for all three concentrations tested (100, 500 and 1000 μg/mL), compared to minimal sustained

release and low loading efficiency (< 5%) when bare PCL is simply mixed with 1000 μg/mL MK2i. Cumulative release of MK2i was highest for the highest concentration of MK2i tested (1 mg/mL) and was also most sustained. Fluorescence microscopy showed an increase in loading of FITC-MK2i as MK2i loading concentration increased. These results indicate that the 1 mg/mL MK2i coating has the most sustained release profile (97 – 272 μg/mL), with the 272 μg/mL representing a 100 μM concentration that was shown to be an effective MK2i concentration for limiting NH in other studies.[23, 291] This 1 mg/mL MK2i loading concentration was used to prepare substrates for all subsequent experiments.

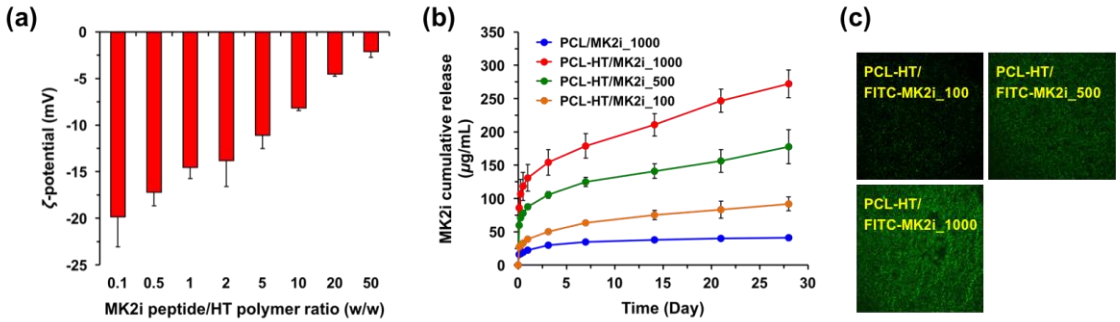


**Figure 5-14 Characterization of MK2i-loaded PCL-HT substrates**
A) Zeta potential values of HT/MK2i complex by varying the MK2i feed amount at fixed concentration of HT polymer (1 mg/mL). The mixing ratio (w/w) was varied from [MK2i]/[HT] = 0.1 to 50. B) *In vitro* release kinetics of MK2i peptide loaded on bare PCL and PCL–HT substrates. The MK2i peptides (100, 500 and 1000 $\mu$g/mL) were treated to the PCL–HT surfaces, and then the released MK2i amounts in the collected media were measured over 28 d. The cumulative MK2i release kinetics were drawn as a function of time. C) Fluorescence images on the surfaces of PCL–HT after treating FITC–MK2i peptides (100, 500 and 1000 $\mu$g/mL). Results in A) and B) are shown as mean ± S.D. (n = 3).

5.2.2.3.2.4 Effect of PCL-HT/MK2i on VSMC migration and proliferation

Migration and proliferation of VSMCs were assessed *in vitro* for PCL-HT/MK2i substrates as an initial assessment of its ability to inhibit factors associated with NH. Migration was evaluated by the scratch wound assay in which cells were placed in close

proximity with substrates and incubated in media containing PDGF to induce wound closure. PCL-HT/MK2i mitigated wound closure and VSMC migration significantly more so than both PCL-HT and bare PCL, indicating that drug elution limited VSMC migration (Figure 5-15A and B). The MK2i drug alone also reduced VSMC migration and wound closure, but not by as dramatic of an amount. VSMC proliferation, on the other hand, was not affected by MK2i or any substrate conditions as measured by optical density at 450 nm (Figure 5-15C). This lack of effect of substrates on VSMC proliferation could be related to the ability of extracts from these substrates to maintain high cell viability; > 90% viability of NIH3T3 fibroblasts relative to TCPS was maintained on all substrates over the course of 24 hours (Figure 5-16).

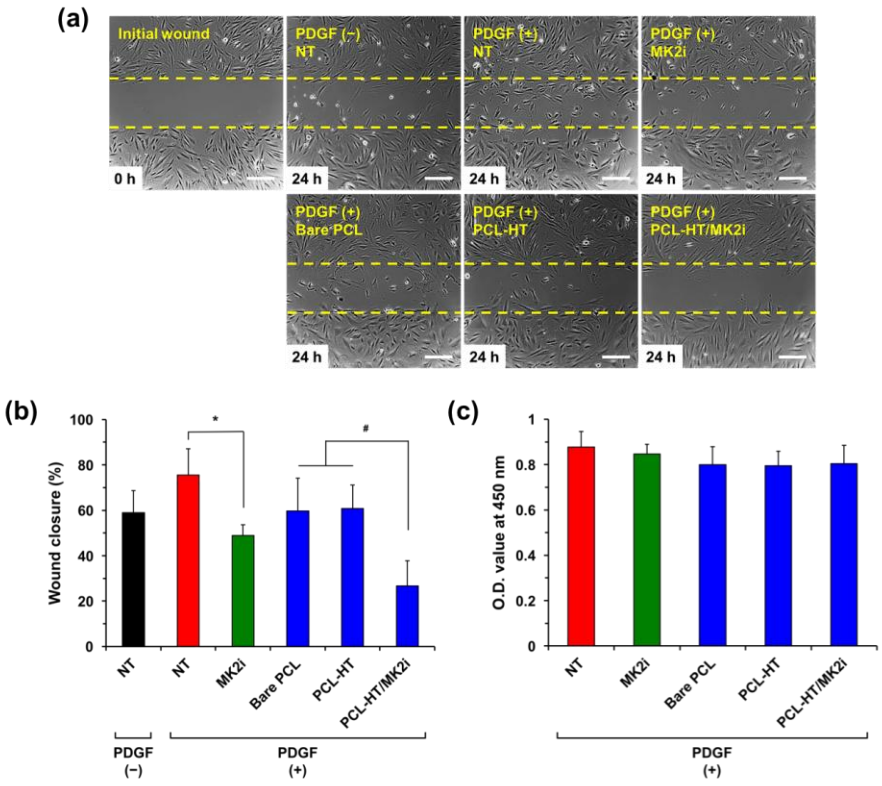


**Figure 5-15 In vitro migration and proliferation of VSMCs**
A) Representative images and B) quantified wound closure of the migrated VSMCs treated with MK2i-loaded PCL–HT. The cells were incubated in the medium containing PDGF (50 ng/mL) for 24 h. The wound closure (%) was determined by measuring the wound area at 24 h compared to the initial scratch wound area. As positive and negative controls, the

medium with or without 200 $\mu$g/mL of MK2i were used, respectively. Scale bars represent 200 $\mu$m. C) Effect of the released MK2i on proliferation of VSMCs. To prove that wound closure is not affected by cell proliferation, the proliferation assay was performed in the same experimental condition via the scratch wound assay. Results in B) and C) are shown as the mean ± S.D. (n = 3; *$P$ < 0.05 compared to NT, #$P$ < 0.05 compared to bare PCL and PCL–HT).

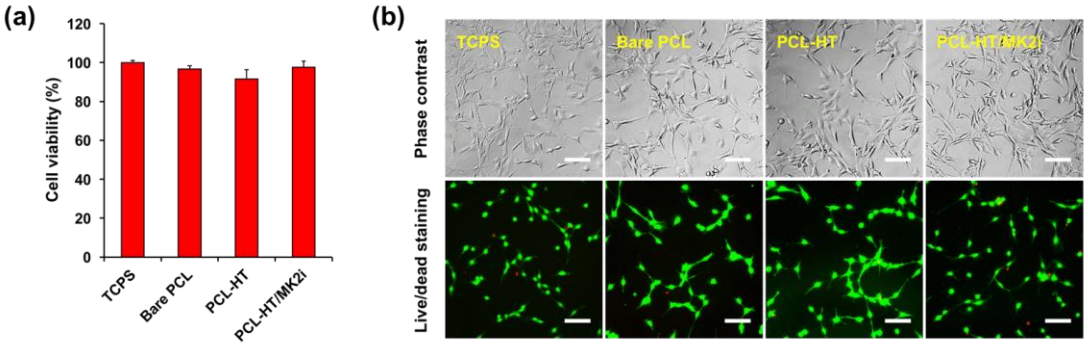


**Figure 5-16 Cytotoxicity of substrate extracts**
Cell viability of extracts from substrates was assessed by the A) WST-1 assay, and no significant differences were detected between test conditions. B) No differences in cell viability or cell morphology were detected by calcein/ethidium-1 homodimer live/dead staining either.

To determine the mechanism of action behind the observed inhibition in VSMC migration for MK2i and PCL-HT/MK2i, Western blots of known downstream MK2 targets that play a role in VSMC migration were performed from these *in vitro* experiments.[23, 291] One-time pre-treatment of VSMCs with 200 μg/mL of MK2i significantly reduced activation of both HSP27 and CREB (Figure 5-17). PCL-HT/MK2i also inhibited both of these targets in a similar fashion over the course of 7 days. Given that the half-life of MK2i is approximately 4 days, this result suggests that extended elution of MK2i from the PCL-HT substrates may continue and sustain this inhibitory effect of VSMC migration. Delivery of MK2i-Alexa 568 to HSVs *ex vivo* over the course of 6 hours and 3 days revealed the increased dispersion of the MK2i target through the HSV. This result suggests that MK2i can effectively penetrate and potentially accumulate in the HSV over time, possibly providing better long-term effects than the drug alone (Figure 2-5).

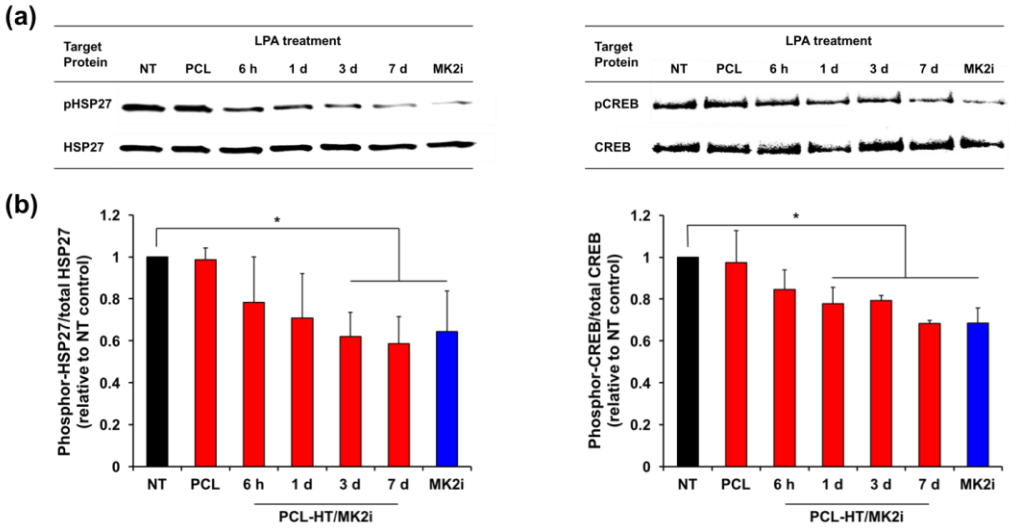


**Figure 5-17 Effect of released MK2i from PCL-HT/MK2i on phosphorylation of HSP27 and CREB in VSMCs**

A) Representative images of western blots showing the phosphorylation of target proteins (pHSP27 and pCREB) in VSMCs treated with the released MK2i. The PCL–HT/MK2i samples were incubated in low serum growth medium (1% FBS), and the extract solutions were collected after 6 h, 1 d, 3 d and 7 d. Following treatment of each extract to VSMCs for 2 h, LPA (30 $\mu$M) was exposed for 30 min. As a positive and negative control, the medium with or without 200 $\mu$g/mL of MK2i was used. B) Quantification of the relative ratios (phosphor-HSP27/total HSP27 and phosphor-CREB/total CREB). Results are shown as the average values ± S.D. (n = 3; *$P$ < 0.05 compared to NT).

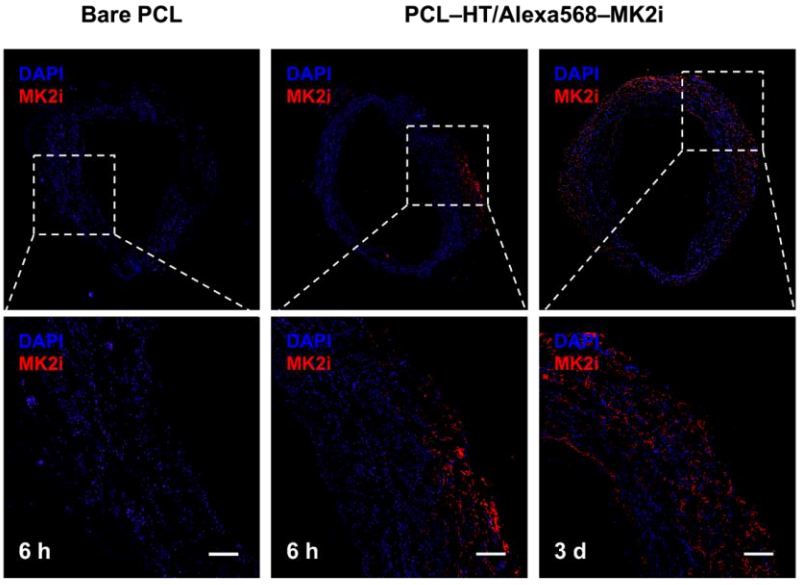


**Figure 5-18 MK2i delivery of PCL-HT/Mk2i to human saphenous veins (HSVs)**

Representative fluorescence images of the HSVs wrapped with bare PCL and PCL–HT/MK2i sheaths for 6 h and 3 d. MK2i peptide was labeled with Alexa 568 (red) before

loading on the surface of PCL–HT sheath. The cross-sectioned HSVs were stained with DAPI (blue). Scale bars indicate 200 $\mu$m.

#### 5.2.2.3.3 Conclusions

Heparin was effectively immobilized to the surface of PCL by simply dipping method employing a tyrosinase-mediated oxidation reaction, providing a convenient means to sustain localized release of cationic therapeutics such as MK2i. Subsequent dipping into a 1 mg/mL solution of MK2i resulted in 92 – 272 μg/mL of cumulative MK2i release, and this significantly inhibited VSMC migration but not proliferation over the course of 7 days *in vitro*. This anti-migratory of effect of the PCL-HT/MK2i substrates correlated with a decrease in phosphorylation of target proteins associated with neointimal hyperplasia, HSP27 and CREB. This may lead to a more sustained reduction in intimal thickness over time, which was not sustained well in a previous study evaluating one-time MK2i effects on murine vein graft wall thickness. It is unclear how the combination of MK2i with a PCL-ACPCL shape memory polymer substrate might work together in the form of an external without evaluating PCL-ACPCL external stent effects in a relevant model such as a porcine arteriovenous graft study. This approach, however, provides one fairly convenient method for sustaining release of MK2i, which may prove useful if additional *in vivo* experiments determine that a reduction in VSMC migration, as it relates inflammation and fibrosis, is desirable.

## 5.3 Future Perspectives in External Stenting

### 5.3.1 Modular Iteration of External Supports

While several promising studies have been conducted that clearly demonstrate the ability of external stents to reduce NH, there is still no external stent available for patients. More controlled, comparative studies will need to be conducted to isolate variable effects and garner more mechanistic insights on how external stents function. A variety of materials and copolymers should be explored for these purposes. These materials should be biodegradable so as to avoid infection risks from long-term implantation, macroporous to promote neoadventitial growth, and provide some level of mechanical support to reduce tangential wall stresses, either directly or indirectly, through adventitial angiogenesis. Copolymers are useful tools to examine phenomena such as how degradation profiles influence patency,[320] as numerous systems can be devised with tunable degradability by simple alterations in molar composition or molecular weight,[92, 93] and their effects on NH and graft patency can be observed over time. In the same way, copolymer systems can be used to tune mechanical properties and elucidate the level and timeline of support that is most beneficial towards minimizing NH.[15] The extent and timeframe of support-induced angiogenesis most beneficial for reducing NH should also be studied, perhaps by implanting external supports that have angiogenic and/or inflammatory agonists/antagonists incorporated in them.[321]

### 5.3.2 Advances in Active Approaches

Further mechanistic insights into passive external design parameter effects on NH reduction can also inform active design approaches. For example, a sustained inflammatory responses from degradation products of an external support could prove to at first be

beneficial in reducing NH, but have the opposite effect at later time points due to fibrosis and/or promotion of a synthetic, proliferative VSMC phenotype. In this case, a drug delivery platform can be incorporated that delays release until a later timepoint. Conversely, iterative modulation of active design approaches can inform the passive external support design. For example, a pro-angiogenic drug eluted from an external support may at first have a positive impact, before leading to an increase in NH later on. In this case, a more biocompatible and/or more slowly degrading polymer may be a more appropriate material selection to couple with this drug to mitigate the negative effects that were observed from an overly active angiogenesis.

In a classical scaffold design where the passive external support also serves as the depot for therapeutic agents, it may be difficult to decouple parameter interdependencies in the design such as amount of drug loaded and stent stiffness. The multi-layer polymer wrap or hydrogel systems previously discussed[163-172] may help to isolate these parameters in the design. Another means to accomplish this besides circumscribing polymer or hydrogel layers is to coat the surface with bioactive compounds. For example, heparin coatings can serve a dual purpose of imparting antithrombotic effects while also serving as a drug depot to deliver cationic therapeutics.[322] A common way to render such a surface is to co-employ highly adhesive polymers such as poly(dopamine)[313] or plasma treat the surface.[323] Although not definitively known in the external stenting context, it may also prove beneficial to improve endothelialization of the device, which could be done by coating or modifying the surface with cell-adhesive proteins or peptides such as fibronectin, collagen, gelatin, laminin, or Arg-Gly-Asp (RGD).[322] The topography of the material

surface could also be altered via techniques such as electron beam lithography to influence cell behavior and adhesion.[324, 325]

Advanced drug delivery approaches can also be applied to further improve the localization, specificity, and activity of drugs eluted from external supports, thereby reducing NH. For example, PLGA 90/10 microneedles loaded with paclitaxel were recently demonstrated to reduce NH more than free paclitaxel with two orders of magnitude more efficient delivery to the tunica media and adventitia in a rabbit balloon injury model.[168] In another study, Evans et al. demonstrated that pH-responsive nanopolyplexes enable dramatically more efficient intracellular uptake and activity of a mitogen-activated protein kinase (MAPK)-activated protein (MAPKAP) kinase 2 inhibitory peptide (MK2i), significantly reducing NH in human SVGs *ex vivo* and in an *in vivo* rabbit vein graft interposition model.[291] While significant regulatory hurdles remain with such approaches, active external stents designs may evolve in the coming years to incorporate more sophisticated and efficient drug delivery systems such as these.

### 5.3.3 Improving or Replacing Grafts

Many other approaches to reducing vein graft and hemodialysis access failure are currently being pursued. One area of intensive research has been to improve the performance of the graft itself by either modifying it or replacing it with an alternative material source. Modifications of ePTFE include approaches such as cross-helical yarn coverings to improve flow dynamics, tapering of size to gradually transition from vein to artery, and surrounding the ePTFE with a cuff to reduce regional turbulence, which can be reviewed elsewhere.[51] Alternative graft materials to replace ePTFE or SVGs include other

synthetic polymers,[326-330] combinations of synthetic and natural polymers,[331-339] and tissue-engineered vascular grafts (TEVGs) containing either cellularized synthetic/natural polymers[340-347] or decellularized natural materials.[348-354] While none of these alternative grafts have achieved significant adoption, Niklason et al. recently demonstrated safety and functionality of a decellularized TEVG (HUMACYL®, Humacyte Inc.) for hemodialysis patients.[350] HUMACYL is a human acellular vessel (HAV) derived from decellularized human tissue. In the 60-person cohort, secondary patency was 89% at one year and Humacyte is now recruiting patients for a Phase III trial. However, despite this promising development, NH will likely remain an issue with these grafts given that primary patency was only 38% for the 60 patients at one year, which compares closer to the 18 month patency rate (33%) than the 6 month patency rate (45%) from Huber et al.[1] Ultimately, a combination of complimentary approaches serve as hope for improving the quality and length of life of CAD, PAD, and ESRD patients.

In a classical scaffold design where the passive external support also serves as the depot for therapeutic agents, it may be difficult to decouple parameter interdependencies in the design such as amount of drug loaded and stent stiffness. The multi-layer polymer wrap or hydrogel systems previously discussed[163-172] may help to isolate these parameters in the design. Another means to accomplish this besides circumscribing polymer or hydrogel layers is to coat the surface with bioactive compounds. For example, heparin coatings can serve a dual purpose of imparting antithrombotic effects while also serving as a drug depot to deliver cationic therapeutics.[322] A common way to render such a surface is to co-employ highly adhesive polymers such as poly(dopamine)[313] or plasma treat the surface.[323] Although not definitively known in the external stenting context, it may also

prove beneficial to improve endothelialization of the device, which could be done by coating or modifying the surface with cell-adhesive proteins or peptides such as fibronectin, collagen, gelatin, laminin, or Arg-Gly-Asp (RGD).[322] The topography of the material surface could also be altered via techniques such as electron beam lithography to influence cell behavior and adhesion.[324, 325]

Advanced drug delivery approaches can also be applied to further improve the localization, specificity, and activity of drugs eluted from external supports, thereby reducing NH. For example, PLGA 90/10 microneedles loaded with paclitaxel were recently demonstrated to reduce NH more than free paclitaxel with two orders of magnitude more efficient delivery to the tunica media and adventitia in a rabbit balloon injury model.[168] In another study, Evans et al. demonstrated that pH-responsive nanopolyplexes enable dramatically more efficient intracellular uptake and activity of a mitogen-activated protein kinase (MAPK)-activated protein (MAPKAP) kinase 2 inhibitory peptide (MK2i), significantly reducing NH in human SVGs *ex vivo* and in an *in vivo* rabbit vein graft interposition model.[291] While significant regulatory hurdles remain with such approaches, active external stents designs may evolve in the coming years to incorporate more sophisticated and efficient drug delivery systems such as these.

Appendix A: Synthesis and Characterization of 100%PCL-DMA Control

## A.1 100%PCL-DMA

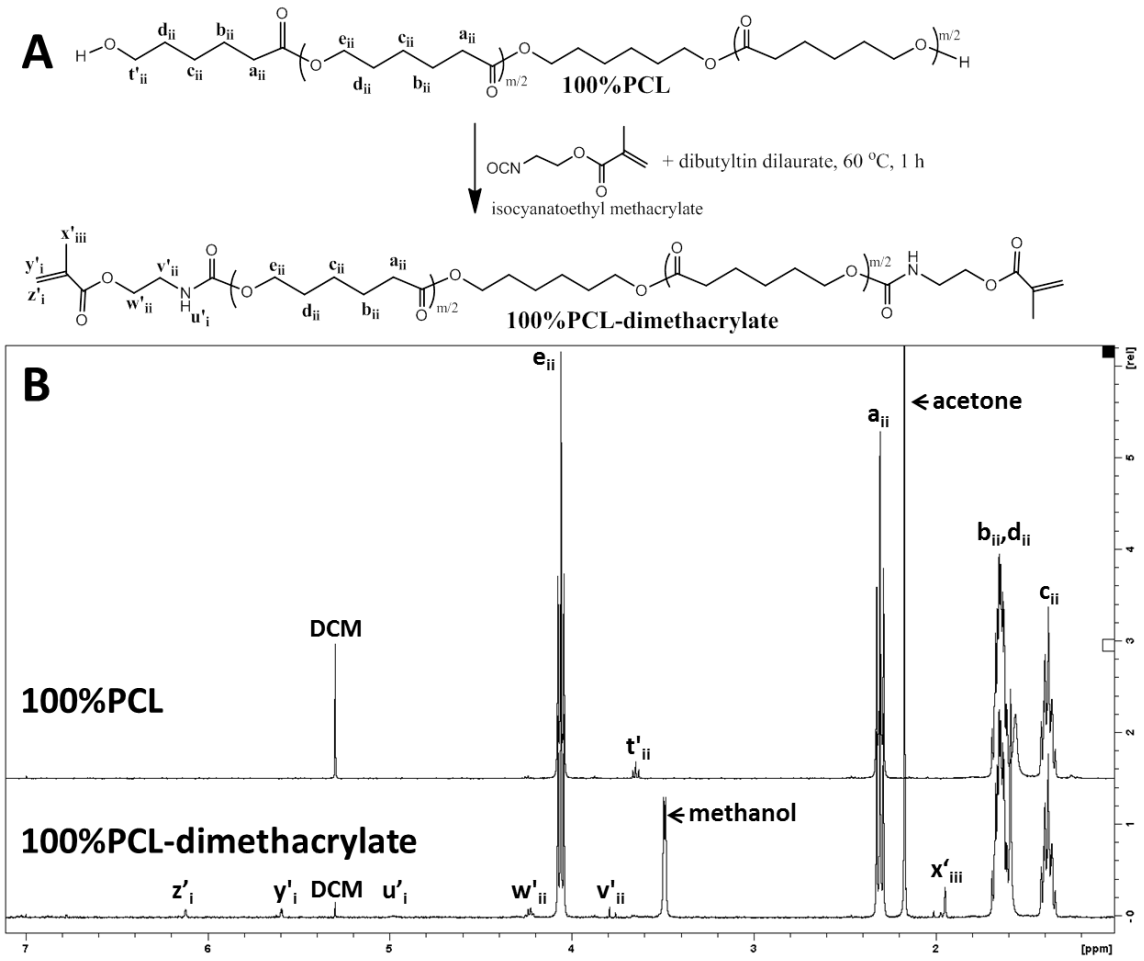


**Figure A-1 Synthesis of 100%PCL-DMA**

A) Synthetic scheme for 100%PCL-dimethacrylate control. B) $^{1}$H-NMR spectra of 100%PCL (top) and 100%PCL-dimethacrylate (bottom). 100%PCL $^{1}$H NMR (400 MHz, $CDCl_3$, 25 °C, TMS): δ = 4.06 (m, 2H; -OC**H**$_2$ (***e$_{ii}$***)), 3.66 (m, 2H; -C**H**$_2$ (***t'$_{ii}$***)), 2.33 (t, $^{3}$J(H,H) = 7.5 Hz, 2H; -C**H**$_2$ (***a$_{ii}$***)), 1.65 (m, 4H; -C**H**$_2$ (***b$_{ii}$,d$_{ii}$***)), 1.38 ppm (m, 2H; -C**H**$_2$ (***c$_{ii}$***)). 100%PCL-dimethacrylate $^{1}$H NMR (400 MHz, $CDCl_3$, 25 °C, TMS): δ = 6.12 (m, 1H, C**H**$_2$=C (***z'$_{ii}$***)), 5.61 (m, 1H, C**H**$_2$=C (***y'$_{ii}$***)), 5.00 (m, 1H, -$CH_2$N**H** (***u'$_i$***)), 4.24 (m, 2H, -OC**H**$_2$$CH_2$N (***w'$_{ii}$***)), 4.06 (m, 2H; -OC**H**$_2$ (***e$_{ii}$***)), 3.78 (m, 2H, -C**H**$_2$N (***v'$_{ii}$***)), 2.33 (t, $^{3}$J(H,H) = 7.5 Hz, 2H; -C**H**$_2$ (***a$_{ii}$***)), 1.97 (m, 3H, -C**H**$_3$ (***x'$_{iii}$***)), 1.65 (m, 4H; -C**H**$_2$ (***b$_{ii}$,d$_{ii}$***)), 1.38 ppm (m, 2H; -C**H**$_2$ (***c$_{ii}$***)).

Similar to Lendlein et al,[355] the terminal hydroxyl-to-methacrylate conversion rate, or degree of methacrylation ($D_M$), is calculated by summing the normalized methacrylate proton integrals from 6.12 ($I_{6.12}$) and 5.61 ppm ($I_{5.61}$) peaks for 100%PCL-dimethacrylate,

and then dividing by the normalized integral from the $CH_2$ protons adjacent to the terminal hydroxyls for unmodified 100%PCL at 3.66 ppm ($I_{3.66,notfunc}$):

**Equation A-1:**

$$D_M = (I_{6.12} + I_{5.61})/I_{3.66,notfunc} \times 100\%$$

## A.2 HCAEC Viability

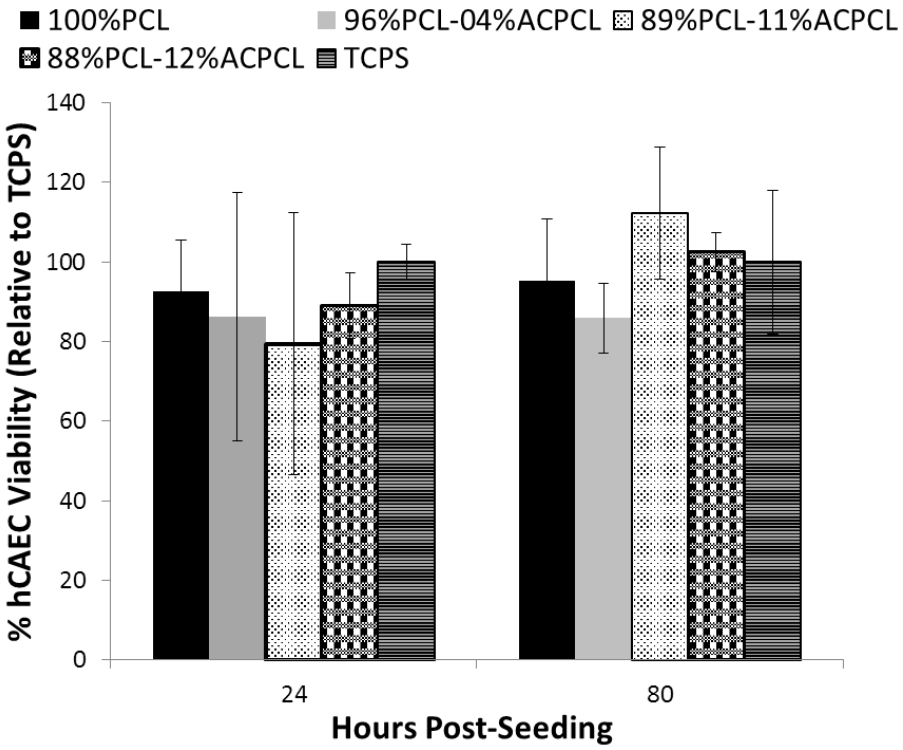


**Figure A-2 HCAEC Viability**
Viability of hCAECs co-incubated with polymer films at specified timepoints. No statistically significant differences were observed between test substrates (n = 4).

Appendix B: Further details of x%PCL-y%ACPCL

## B.1 Effect of Allyl Chloroformate:CL (A:CL) on y%ACPCL

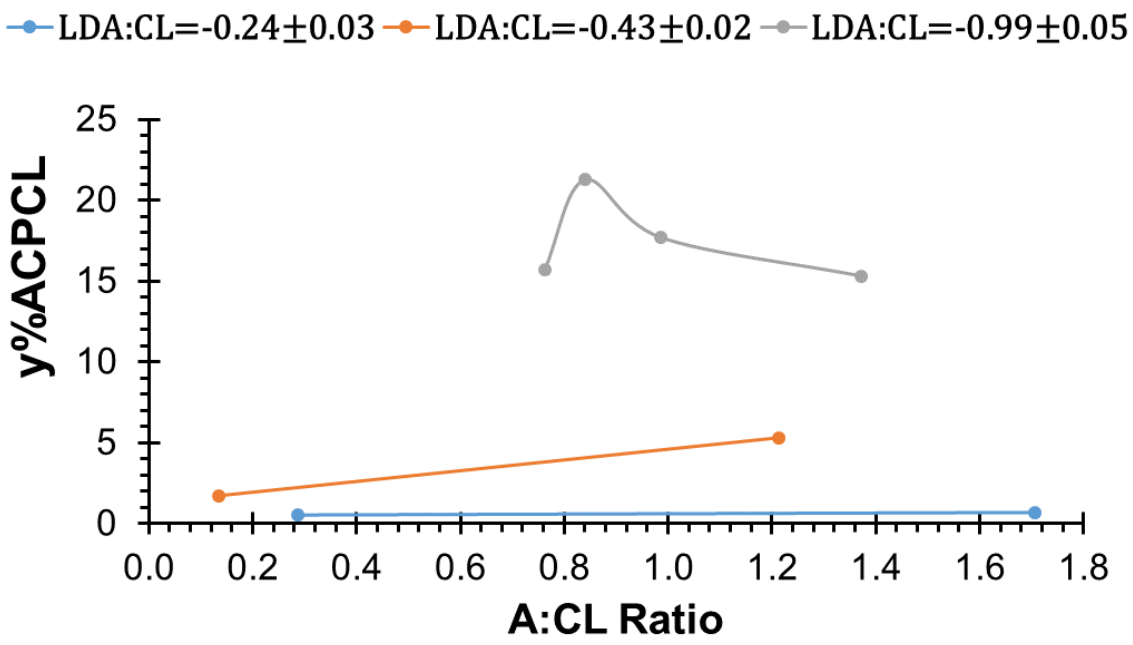


**Figure B-1 Effect of A:CL on y%ACPCL**

For most reactions tested, varying A:CL at fixed LDA:CL ratios within ± 0.05 did not appear to have much of an impact on the extent of allyloxycarbonyl substitution within the ranges tested. This further implicated the carbanion formation step via LDA addition as the rate limiting step. Based on these results, a 1:1:1 A:CL:LDA ratio represents an excess amount of allyl chloroformate to more definitively ensure complete reaction of allyloxycarbonyl groups with carbanion intermediates. An approximate 1:1 A:CL ratio was used for all subsequent reactions.

Appendix C: Immunohistochemistry Protocols

## C.1 Antibody Table

**Table C-1: Antibody Table with Dilutions for IHC**

| Antibody | Manufacturer | Species | Dilution | Clonality | Cat. number |
|---|---|---|---|---|---|
| CD31 | Dianova | Rat | 1:100 | Monoclonal | DIA-310 |
| F4/80 | Novus Biologicals | Rat | 1:900 | Monoclonal | NB600-404 |
| CD206 | Bioss | Rabbit | 1:100 | Polyclonal | bs-4727R |
| iNOS | Bioss | Rabbit | 1:100 | Polyclonal | bs-2072R |
| MMP3 | Bioss | Rabbit | 1:400 | Polyclonal | bs-0413R |
| MMP9 | Bioss | Rabbit | 1:100 | Polyclonal | bs-4593R |
| MMP12 | Cloud-Clone Corp | Rabbit | 1:1000 | Polyclonal | PAC056Hu01 |
| MMP13 | Abcam | Rabbit | 1:750 | Polyclonal | ab39012 |
| MMP14 | Cloud-Clone Corp. | Rabbit | 1:250 | Polyclonal | PAC056Mu01 |

## C.2 IHC Staining Protocol Details

### C.2.1 CD31

Slides were placed on the Leica Bond Max IHC stainer. All steps besides dehydration, clearing and cover slipping are performed on the Bond Max. Slides are deparaffinized. Heat induced antigen retrieval was performed on the Bond Max using their Epitope Retrieval 2 solution for 20 minutes. Slides were incubated with anti-CD31 (Cat.# DIA-310, Dianova, Hamburg, Germany) for one hour at a 1:100 dilution and followed by a biotinylated anti-rat secondary antibody (Cat.# BA-4000, Vector Laboratories, Inc., Burlingame, CA) for 15 minutes at a 1:200 dilution. The Bond Polymer Refine detection system was used for visualization. Slides were then dehydrated, cleared and cover slipped.

### C.2.2 F4/80

Slides were placed on the Leica Bond Max IHC stainer. All steps besides dehydration, clearing and cover slipping are performed on the Bond Max. Slides are deparaffinized. Enzymatic induced antigen retrieval was performed on the Bond Max using Proteinase K (Dako, North America, Inc) for 5 minutes. Slides were incubated with anti-F4/80 (NB600-404, Novus Biologicals) for one hour at a 1:900 dilution and then incubated in a rabbit anti-rat secondary antibody (BA-4001, Vector Laboratories, Inc.) for 15mins at a 1:200 dilution. The Bond Polymer Refine detection system was used for visualization. Slides were the dehydrated, cleared and cover slipped.

### C.2.3 NOS-2/iNOS

Slides were placed on the Leica Bond Max IHC stainer. All steps besides dehydration, clearing and cover slipping are performed on the Bond Max. Slides are deparaffinized.

Heat induced antigen retrieval was performed on the Bond Max using their Epitope Retrieval 2 solution for 20 minutes. Slides were incubated with anti-iNOS/NOS-2 (Cat# bs-2072R, Bioss Antibodies, Woburn, Massachusetts) for one hour at a 1:00 dilution. The Bond Polymer Refine detection system was used for visualization. Slides were then dehydrated, cleared and cover slipped.

### C.2.4 CD206

Slides were placed on the Leica Bond Max IHC stainer. All steps besides dehydration, clearing and cover slipping are performed on the Bond Max. Slides are deparaffinized. Heat induced antigen retrieval was performed on the Bond Max using their Epitope Retrieval 2 solution for 20 minutes. Slides were incubated with anti-MRC1/CD206 (Cat# bs-4727R, Bioss Antibodies, Woburn, Massachusetts) for one hour at a 1:00 dilution. The Bond Polymer Refine detection system was used for visualization. Slides were then dehydrated, cleared and cover slipped.

### C.2.5 MMP3

Slides were placed on the Leica Bond Max IHC stainer. All steps besides dehydration, clearing and cover slipping are performed on the Bond Max. Slides are deparaffinized. Heat induced antigen retrieval was performed on the Bond Max using their Epitope Retrieval 1 solution for 20 minutes. Slides were incubated with anti-MMP3 (Cat# bs-0413R, Bioss Antibodies, Woburn, Massachusetts) for one hour at a 1:400 dilution. The Bond Polymer Refine detection system was used for visualization. Slides were then dehydrated, cleared and cover slipped.

### C.2.6 MMP9

Slides were placed on the Leica Bond Max IHC stainer. All steps besides dehydration, clearing and cover slipping are performed on the Bond Max. Slides are deparaffinized. Heat induced antigen retrieval was performed on the Bond Max using their Epitope Retrieval 1 solution for 20 minutes. Slides were incubated with anti-MMP9 (Cat# bs-4593R, Bioss Antibodies, Woburn, Massachusetts) for one hour at a 1:100 dilution. The Bond Polymer Refine detection system was used for visualization. Slides were then dehydrated, cleared and cover slipped.

### C.2.7 MMP12

Slides were placed on the Leica Bond Max IHC stainer. All steps besides dehydration, clearing and cover slipping are performed on the Bond Max. Slides are deparaffinized. Heat induced antigen retrieval was performed on the Bond Max using their Epitope Retrieval 1 solution for 20 minutes. Slides were incubated with anti-MMP12 (Cat# PAA402Mu01, Cloud-Clone Corp., Katy, TX) for one hour at a 1:1000 dilution. The Bond

Polymer Refine detection system was used for visualization. Slides were then dehydrated, cleared and cover slipped.

### C.2.8 MMP13

Slides were placed on the Leica Bond Max IHC stainer. All steps besides dehydration, clearing and cover slipping are performed on the Bond Max. Slides are deparaffinized. Heat induced antigen retrieval was performed on the Bond Max using their Epitope Retrieval 2 solution for 10 minutes. Slides were incubated with anti-MMP13 (Cat# Ab39012, Abcam, Cambridge, MA) for one hour at a 1:750 dilution. The Bond Polymer Refine detection system was used for visualization. Slides were then dehydrated, cleared and cover slipped.

### C.2.9 MMP14

Slides were placed on the Leica Bond Max IHC stainer. All steps besides dehydration, clearing and cover slipping are performed on the Bond Max. Slides are deparaffinized. Heat induced antigen retrieval was performed on the Bond Max using their Epitope Retrieval 1 solution for 20 minutes. Slides were incubated with anti-MMP14 (Cat# PAC056Mu0, Cloud-Clone Corp., Katy, TX) for one hour at a 1:250 dilution. The Bond Polymer Refine detection system was used for visualization. Slides were then dehydrated, cleared and cover slipped.

## C.3 Quantification of protein expression by IHC Staining Detection Algorithms

**Table C-2 CD31**

| *** Algorithm Inputs *** | *** Algorithm Inputs *** |
|---|---|
| Algorithm | Microvessel Detection |
| Segmented Tissue from Background by Intensity | 210 |
| Segment vessels from tissue | 175 |
| Eliminate vessels with area less than this value | 60 |
| Eliminate vessels with area greater than this value | 5000 |
| Eliminate vessels with aspect ratio greater than this value = max(length/width)*100 | 1000 |
| 0 = Do not separate, 1 = Separate | 0 |
| Number of dilation/erosion iterations | 6 |
| Color Definition File | “My Own DAB”, very similar to “Default DAB” |

**“My Own DAB” Color Definition File Script:**

```
99 66 66 132 99 66 99 55 55 55 22 0 132 88 66 55 33 22 55 33 33 55
22 22 55 22 33 33 22 22 88 55 22 33 22 33 88 55 33 88 66 66 121 99
```

66 88 55 55 121 88 55 121 88 66 121 99 88 88 66 55 66 33 0 66 22 0
66 33 22 66 33 33 88 33 22 99 66 33 66 22 22 99 55 33 99 66 55 44 22
33 88 33 11 99 44 33 66 33 11 121 77 44 55 11 0 44 22 0 77 55 44 55
22 11 77 33 11 66 44 33 77 44 22 110 88 77 143 110 77 121 88 77 44
11 0 66 55 44 132 99 77 110 66 44 77 44 33 55 44 33 110 77 77 44 33
22 66 33 44 88 44 11 88 44 22 88 44 44 55 33 44 121 77 55 88 44 33
99 55 44 99 66 44 77 66 55 77 33 22 143 110 88 110 66 66 77 44 11 44
22 11 121 77 66 55 44 44 55 33 11 44 22 22 44 33 44 77 44 44 110 77
44 99 77 55 88 55 44 143 99 77 77 55 55 132 77 55 66 44 22 110 66 33
66 44 44 110 77 55 0 0 0 77 55 66 66 44 55 77 33 33 44 33 33

**Table C-3 F4/80 Detection Algorithm**

| *** Algorithm Inputs *** | *** Algorithm Inputs *** |
|---|---|
| Algorithm | Positive Pixel Count v9 |
| Version | 9.1 |
| View Width | 1000 |
| View Height | 1000 |
| Overlap Size | 0 |
| Image Zoom | 1. |
| Classifier | None |
| Class List | |
| Classifier Neighborhood | 0 |
| Pixel Area (millimeter-squared) | 1.51282e-007 |
| Hue Value (Center) | 0.1 |
| Hue Width | 0.5 |
| Color Saturation Threshold | 4.e-002 |
| Intensity Threshold WEAK (Upper Limit) | 190 |
| Intensity Threshold WEAK (Lower Limit) | 175 |
| Intensity Threshold MEDIUM (Upper Limit) | 175 |
| Intensity Threshold MEDIUM (Lower Limit) | 100 |
| Intensity Threshold STRONG (Upper Limit) | 100 |
| Intensity Threshold STRONG (Lower Limit) | 0 |
| Intensity Threshold Negative Pixels | -1 |

**Table C-4 CD206 Detection Algorithm**

| *** Algorithm Inputs *** | *** Algorithm Inputs *** |
|---|---|
| Algorithm | Positive Pixel Count v9 |
| Version | 9.1 |
| View Width | 1000 |
| View Height | 1000 |

| | |
|---|---|
| Overlap Size | 0 |
| Image Zoom | 1. |
| Classifier | None |
| Class List | |
| Classifier Neighborhood | 0 |
| Pixel Area (millimeter-squared) | 1.51282e-007 |
| Hue Value (Center) | 0.1 |
| Hue Width | 0.5 |
| Color Saturation Threshold | 4.e-002 |
| Intensity Threshold WEAK (Upper Limit) | 175 |
| Intensity Threshold WEAK (Lower Limit) | 150 |
| Intensity Threshold MEDIUM (Upper Limit) | 150 |
| Intensity Threshold MEDIUM (Lower Limit) | 120 |
| Intensity Threshold STRONG (Upper Limit) | 120 |
| Intensity Threshold STRONG (Lower Limit) | 0 |
| Intensity Threshold Negative Pixels | -1 |

**Table C-5 iNOS Detection Algorithm**

| *** Algorithm Inputs *** | *** Algorithm Inputs *** |
|---|---|
| Algorithm | Positive Pixel Count v9 |
| Version | 9.1 |
| View Width | 1000 |
| View Height | 1000 |
| Overlap Size | 0 |
| Image Zoom | 1. |
| Classifier | None |
| Class List | |
| Classifier Neighborhood | 0 |
| Pixel Area (millimeter-squared) | 1.51282e-007 |
| Hue Value (Center) | 0.1 |
| Hue Width | 0.5 |
| Color Saturation Threshold | 4.e-002 |
| Intensity Threshold WEAK (Upper Limit) | 220 |
| Intensity Threshold WEAK (Lower Limit) | 150 |
| Intensity Threshold MEDIUM (Upper Limit) | 150 |
| Intensity Threshold MEDIUM (Lower Limit) | 100 |
| Intensity Threshold STRONG (Upper Limit) | 100 |
| Intensity Threshold STRONG (Lower Limit) | 0 |
| Intensity Threshold Negative Pixels | -1 |

C.4 Power analysis to justify sample size calculations for planning the larger mouse cohort

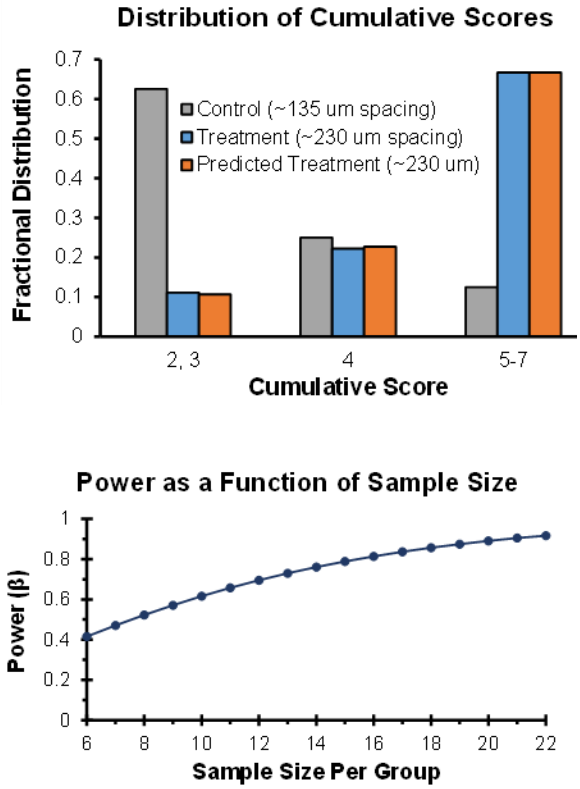


**Figure C-1 Power analysis**

Distribution of cumulative scores (top) reveals a significant shift in distribution between treatment (high spacing) and control (low spacing) groups on a logarithmic scale. There is a close match between the treatment group in the preliminary data to that predicted by the proportional odds model. Plotting power as a function of sample size (bottom) shows that N = 8 has 52% power and an N of 15 is required for ~80% power, assuming data from preliminary experiments represents those of the larger study planned.

# REFERENCES


1. Huber TS, Carter JW, Carter RL, Seeger JM. Patency of autogenous and polytetrafluoroethylene upper extremity arteriovenous hemodialysis accesses: A systematic review. *Journal of Vascular Surgery*. 2003;38:1005-1011

2. Al-Jaishi AA, Oliver MJ, Thomas SM, Lok CE, Zhang JC, Garg AX, Kosa SD, Quinn RR, Moist LM. Patency rates of the arteriovenous fistula for hemodialysis: A systematic review and meta-analysis. *American Journal of Kidney Diseases*. 2014;63:464-478

3. Shemesh D, Goldin I, Verstandig A, Berelowitz D, Zaghal I, Olsha O. Upper limb grafts for hemodialysis access. *The journal of vascular access*. 2015;16:34-39

4. Zwolak RM, Adams MC, Clowes AW. Kinetics of vein graft hyperplasia: Association with tangential stress. *Journal of vascular surgery*. 1987;5:126-136

5. Angelini GD, Izzat MB, Bryan AJ, Newby AC. External stenting reduces early medial and neointimal thickening in a pig model of arteriovenous bypass grafting. *The Journal of Thoracic and Cardiovascular Surgery*. 1996;112:79-84

6. Angelini GD, Lloyd C, Bush R, Johnson J, Newby AC. An external, oversized, porous polyester stent reduces vein graft neointima formation, cholesterol concentration, and vascular cell adhesion molecule 1 expression in cholesterol-fed pigs. *The Journal of Thoracic and Cardiovascular Surgery*. 2002;124:950-956

7. George SJ, Izzat MB, Gadsdon P, Johnson JL, Yim APC, Wan S, Newby AC, Angelini GD, Jeremy JY. Macro-porosity is necessary for the reduction of neointimal and medial thickening by external stenting of porcine saphenous vein bypass grafts. *Atherosclerosis*. 2001;155:329-336

8. Izzat MB, Mehta D, Bryan AJ, Reeves B, Newby AC, Angelini GD. Influence of external stent size on early medial and neointimal thickening in a pig model of saphenous vein bypass grafting. *Circulation*. 1996;94:1741-1745

9. Mehta D, George SJ, Jeremy JY, Izzat MB, Southgate KM, Bryan AJ, Newby AC, Angelini GD. External stenting reduces long-term medial and neointimal thickening and platelet derived growth factor expression in a pig model of arteriovenous bypass grafting. *Nat Med*. 1998;4:235-239

10. Zilla P, Human P, Wolf M, Lichtenberg W, Rafiee N, Bezuidenhout D, Samodien N, Schmidt C, Franz T. Constrictive external nitinol meshes inhibit vein graft intimal hyperplasia in nonhuman primates. *The Journal of Thoracic and Cardiovascular Surgery*. 2008;136:717-725

11. Zilla P, Wolf M, Rafiee N, Moodley L, Bezuidenhout D, Black M, Human P, Franz T. Utilization of shape memory in external vein-graft meshes allows extreme diameter constriction for suppressing intimal hyperplasia: A non-human primate study. *Journal of Vascular Surgery*. 2009;49:1532-1542

12. Emery RW, Solien E, Puskas JD. Implantation of the esvs mesh: Modification of recommended technique. *Innovations:Technology and Techniques in Cardiothoracic and Vascular Surgery*. 2015;10:146-149

13. Inderbitzin DT, Bremerich J, Matt P, Grapow MT, Eckstein FS, Reuthebuch O. One-year patency control and risk analysis of esvs®-mesh-supported coronary saphenous vein grafts. *Journal of Cardiothoracic Surgery*. 2015;10:108

14. Murphy GJ, Newby AC, Jeremy JY, Baumbach A, Angelini GD. A randomized trial of an external dacron sheath for the prevention of vein graft disease: The extent study. *The Journal of Thoracic and Cardiovascular Surgery*. 2007;134:504-505

15. Boire TC, Gupta MK, Zachman AL, Lee SH, Balikov DA, Kim K, Bellan LM, Sung H-J. Pendant allyl crosslinking as a tunable shape memory actuator for vascular applications. *Acta Biomaterialia*. 2015;24:53-63

16. Caro C, Jeremy J, Watkins N, Bulbulia R, Angelini G, Smith F, Wan S, Yim A, Sherwin S, Peiró J. The geometry of unstented and stented pig common carotid artery bypass grafts. *Biorheology*. 2002;39:507-512

17. Roy-Chaudhury P, Kelly BS, Miller MA, Reaves A, Armstrong J, Nanayakkara N, Heffelfinger SC. Venous neointimal hyperplasia in polytetrafluoroethylene dialysis grafts. *Kidney international*. 2001;59:2325-2334

18. Bassiouny HS, White S, Glagov S, Choi E, Giddens DP, Zarins CK. Anastomotic intimal hyperplasia: Mechanical injury or flow induced. *Journal of Vascular Surgery*. 1992;15:708-717

19. Swedberg SH, Brown B, Sigley R, Wight TN, Gordon D, Nicholls S. Intimal fibromuscular hyperplasia at the venous anastomosis of ptfe grafts in hemodialysis patients. Clinical, immunocytochemical, light and electron microscopic assessment. *Circulation*. 1989;80:1726-1736

20. Paulson WD, Kipshidze N, Kipiani K, Beridze N, DeVita MV, Shenoy S, Iyer SS. Safety and efficacy of local periadventitial delivery of sirolimus for improving hemodialysis graft patency: First human experience with a sirolimus-eluting collagen membrane (coll-r). *Nephrology Dialysis Transplantation*. 2012;27:1219-1224

21. Brown BN, Ratner BD, Goodman SB, Amar S, Badylak SF. Macrophage polarization: An opportunity for improved outcomes in biomaterials and regenerative medicine. *Biomaterials*. 2012;33:3792-3802

22. Longchamp A, Alonso F, Dubuis C, Allagnat F, Berard X, Meda P, Saucy F, Corpataux J-M, Déglise S, Haefliger J-A. The use of external mesh reinforcement to reduce intimal hyperplasia and preserve the structure of human saphenous veins. *Biomaterials*. 2014

23. Lopes LB, Brophy CM, Flynn CR, Yi Z, Bowen BP, Smoke C, Seal B, Panitch A, Komalavilas P. A novel cell permeant peptide inhibitor of mapkap kinase ii inhibits intimal hyperplasia in a human saphenous vein organ culture model. *J Vasc Surg*. 2010;52:1596-1607

24. Lopes LB, Flynn C, Komalavilas P, Panitch A, Brophy CM, Seal BL. Inhibition of hsp27 phosphorylation by a cell-permeant mapkap kinase 2 inhibitor. *Biochemical and biophysical research communications*. 2009;382:535-539

25. Muto A, Panitch A, Kim N, Park K, Komalavilas P, Brophy CM, Dardik A. Inhibition of mitogen activated protein kinase activated protein kinase ii with mmi-0100 reduces intimal hyperplasia ex vivo and in vivo. *Vascular pharmacology*. 2012;56:47-55

26. Bhasin M, Huang Z, Pradhan-Nabzdyk L, Malek JY, LoGerfo PJ, Contreras M, Guthrie P, Csizmadia E, Andersen N, Kocher O, Ferran C, LoGerfo FW. Temporal network based analysis of cell specific vein graft transcriptome defines key pathways and hub genes in implantation injury. *Plos One*. 2012;7:e39123

27. Owens CD, Gasper WJ, Rahman AS, Conte MS. Vein graft failure. *Journal of Vascular Surgery*. 2015;61:203-216

28. Taggart DP. Best practices in coronary revascularization procedures: Are we where we should be? *Current Opinion in Cardiology*. 2014;29:528-533

29. Zeller T, Rastan A, Macharzina R, Tepe G, Kaspar M, Chavarria J, Beschorner U, Schwarzwälder U, Schwarz T, Noory E. Drug-coated balloons vs. Drug-eluting stents for treatment of long femoropopliteal lesions. *Journal of Endovascular Therapy*. 2014;21:359-368

30. Saran R, Li Y, Robinson B. Us renal data system 2014 annual data report: Epidemiology of kidney disease in the united states. *Am J Kidney Dis*. 2015;66:(suppl 1): S1-S306

31. Bourassa M, Fisher L, Campeau L, Gillespie M, McConney M, Lesperance J. Long-term fate of bypass grafts: The coronary artery surgery study (cass) and montreal heart institute experiences. *Circulation*. 1985;72:V71-78

32. Chesebro JH, Fuster V, Elveback LR, Clements IP, Smith HC, Holmes DRJ, Bardsley WT, Pluth JR, Wallace RB, Puga FJ, Orszulak TA, Piehler JM, Danielson GK, Schaff HV, Frye RL. Effect of dipyridamole and aspirin on late vein-graft patency after coronary bypass operations. *New England Journal of Medicine*. 1984;310:209-214

33. Fitzgibbon GM, Kafka HP, Leach AJ, Keon WJ, Hooper GD, Burton JR. Coronary bypass graft fate and patient outcome: Angiographic follow-up of 5,065 grafts related to survival and reoperation in 1,388 patients during 25 years. *Journal of the American College of Cardiology*. 1996;28:616-626

34. Sabik Iii JF, Lytle BW, Blackstone EH, Houghtaling PL, Cosgrove DM. Comparison of saphenous vein and internal thoracic artery graft patency by coronary system. *The Annals of Thoracic Surgery*. 2005;79:544-551

35. Sabik JF. Understanding saphenous vein graft patency. *Circulation*. 2011;124:273-275

36. Conte MS. Molecular engineering of vein bypass grafts. *Journal of Vascular Surgery*. 2007;45:A74-A81

37. Harskamp RE, Lopes RD, Baisden CE, de Winter RJ, Alexander JH. Saphenous vein graft failure after coronary artery bypass surgery: Pathophysiology, management, and future directions. *Annals of Surgery*. 2013;257:824-833

38. Huijbregts HJT, Bots ML, Wittens CHA, Schrama YC, Moll FL, Blankestijn PJ, on behalf of the Csg. Hemodialysis arteriovenous fistula patency revisited: Results of a prospective, multicenter initiative. *Clinical Journal of the American Society of Nephrology : CJASN*. 2008;3:714-719

39. Goldman S, Zadina K, Moritz T, Ovitt T, Sethi G, Copeland JG, Thottapurathu L, Krasnicka B, Ellis N, Anderson RJ, Henderson W. Long-term patency of saphenous vein and left internal mammary artery grafts after coronary artery bypass surgeryresults from a department of veterans affairs cooperative study. *Journal of the American College of Cardiology*. 2004;44:2149-2156

40. Cheung AK, Sarnak MJ, Yan G, Dwyer JT, Heyka RJ, Rocco MV, Teehan BP, Levey AS. Atherosclerotic cardiovascular disease risks in chronic hemodialysis patients. *Kidney international*. 2000;58:353-362

41. Gray RJ, Horton KM, Dolmatch BL, Rundback JH, Anaise D, Aquino AO, Currier CB, Light JA, Sasaki TM. Use of wallstents for hemodialysis access-related venous stenoses and occlusions untreatable with balloon angioplasty. *Radiology*. 1995;195:479-484

42. White RA, Hollier LH. *Vascular surgery: Basic science and clinical correlations*. John Wiley & Sons; 2008.

43. Newby AC, Zaltsman AB. Molecular mechanisms in intimal hyperplasia. *The Journal of Pathology*. 2000;190:300-309

44. Mitra AK, Gangahar DM, Agrawal DK. Cellular, molecular and immunological mechanisms in the pathophysiology of vein graft intimal hyperplasia. *Immunol Cell Biol*. 2006;84

45. Lee T, Roy-Chaudhury P. Advances and new frontiers in the pathophysiology of venous neointimal hyperplasia and dialysis access stenosis. *Advances in chronic kidney disease*. 2009;16:329-338

46. Shi Y, O'Brien JE, Fard A, Mannion JD, Wang D, Zalewski A. Adventitial myofibroblasts contribute to neointimal formation in injured porcine coronary arteries. *Circulation*. 1996;94:1655-1664

47. Berguer R, Higgins RF, Reddy DJ. Intimal hyperplasia: An experimental study. *Archives of Surgery*. 1980;115:332-335

48. Sharony R, Pintucci G, Saunders PC, Grossi EA, Baumann FG, Galloway AC, Mignatti P. Matrix metalloproteinase expression in vein grafts: Role of inflammatory mediators and extracellular signal-regulated kinases-1 and -2. *American Journal of Physiology - Heart and Circulatory Physiology*. 2006;290:H1651-H1659

49. Cox JL, Chiasson DA, Gotlieb AI. Monophasic action potential symposium. Iistranger in a strange land: The pathogenesis of saphenous vein graft stenosis with emphasis on structural and functional differences between veins and arteries. *Progress in Cardiovascular Diseases*. 1991;34:45-68

50. Vijayan V, Smith F, Angelini G, Bulbulia R, Jeremy J. External supports and the prevention of neointima formation in vein grafts. *European journal of vascular and endovascular surgery: the official journal of the European Society for Vascular Surgery*. 2002;24:13-22

51. Li L, Terry CM, Shiu Y-TE, Cheung AK. Neointimal hyperplasia associated with synthetic hemodialysis grafts. *Kidney international*. 2008;74:1247-1261

52. Roy-Chaudhury P, Sukhatme VP, Cheung AK. Hemodialysis vascular access dysfunction: A cellular and molecular viewpoint. *Journal of the American Society of Nephrology*. 2006;17:1112-1127

53. Terry CM, Dember LM. Novel therapies for hemodialysis vascular access dysfunction: Myth or reality? *Clinical Journal of the American Society of Nephrology*. 2013;8:2202-2212

54. Thatte HS, Khuri SF. The coronary artery bypass conduit: I. Intraoperative endothelial injury and its implication on graft patency. *The Annals of Thoracic Surgery*. 2001;72:S2245-S2252

55. McGeachie J, Meagher S, Prendergast F. Vein-to-artery grafts: The long-term development of neo-intimal hyperplasia and its relationship to vasa vasorum and sympathetic innervation. *Australian and New Zealand Journal of Surgery*. 1989;59:59-65

56. Chanakira A, Dutta R, Charboneau R, Barke R, Santilli SM, Roy S. Hypoxia differentially regulates arterial and venous smooth muscle cell proliferation via pdgfr-β and vegfr-2 expression. *American Journal of Physiology - Heart and Circulatory Physiology*. 2012;302:H1173-H1184

57. Misra S, Fu AA, Misra KD, Shergill UM, Leof EB, Mukhopadhyay D. Hypoxia induces a phenotypic switch of fibroblasts to myofibroblasts through a mmp-2/timp mediated pathway: Implications for venous neointimal hyperplasia in hemodialysis access. *Journal of vascular and interventional radiology : JVIR*. 2010;21:896-902

58. Desai M, Mirzay-Razzaz J, von Delft D, Sarkar S, Hamilton G, Seifalian AM. Inhibition of neointimal formation and hyperplasia in vein grafts by external stent/sheath. *Vascular Medicine*. 2010;15:287-297

59. Motwani JG, Topol EJ. Aortocoronary saphenous vein graft disease: Pathogenesis, predisposition, and prevention. *Circulation*. 1998;97:916-931

60. Allaire MDE, Clowes MDAW. Endothelial cell injury in cardiovascular surgery: The intimal hyperplastic response1. *The Annals of Thoracic Surgery*. 1997;63:582-591

61. Haruguchi H, Teraoka S. Intimal hyperplasia and hemodynamic factors in arterial bypass and arteriovenous grafts: A review. *Journal of Artificial Organs*. 2003;6:227-235

62. Dobrin P, Littooy F, Endean E. Mechanical factors predisposing to intimal hyperplasia and medial thickening in autogenous vein grafts. *Surgery*. 1989;105:393-400

63. Maiellaro K, Taylor WR. The role of the adventitia in vascular inflammation. *Cardiovascular Research*. 2007;75:640-648

64. Whittemore AD, Donaldson MC, Polak JF, Mannick JA. Limitations of balloon angioplasty for vein graft stenosis. *Journal of Vascular Surgery*. 1991;14:340-345

65. Bizarro P, Coentrão L, Ribeiro C, Neto R, Pestana M. Endovascular treatment of thrombosed dialysis fistulae. *Catheterization and Cardiovascular Interventions*. 2011;77:1065-1070

66. Lok CE, Sontrop JM, Tomlinson G, Rajan D, Cattral M, Oreopoulos G, Harris J, Moist L. Cumulative patency of contemporary fistulas versus grafts (2000–2010). *Clinical Journal of the American Society of Nephrology*. 2013;8:810-818

67. Roy-Chaudhury P, Kruska L. Future directions for vascular access for hemodialysis. *Seminars in Dialysis*. 2015;28:107-113

68. Dixon BS, Beck GJ, Vazquez MA, Greenberg A, Delmez JA, Allon M, Dember LM, Himmelfarb J, Gassman JJ, Greene T. Effect of dipyridamole plus aspirin on hemodialysis graft patency. *New England Journal of Medicine*. 2009;360:2191-2201

69. Goldman S, Copeland J, Moritz T, Henderson W, Zadina K, Ovitt T, Kern KB, Sethi G, Sharma GV, Khuri S. Long-term graft patency (3 years) after coronary artery surgery. Effects of aspirin: Results of a va cooperative study. *Circulation*. 1994;89:1138-1143

70. Kohler T, Kaufman J, Kacoyanis G, Clowes A, Donaldson M, Kelly E, Skillman J, Couch N, Whittemore A, Mannick J. Effect of aspirin and dipyridamole on the patency of lower extremity bypass grafts. *Surgery*. 1984;96:462-466

71. Geraghty A, Welch K. Antithrombotic agents for preventing thrombosis after infrainguinal arterial bypass surgery (review). *Cochrane Database Syst Rev*. 2011:CD000536

72. Knatterud GL, Rosenberg Y, Campeau L, Geller NL, Hunninghake DB, Forman SA, Forrester JS, Gobel FL, Herd JA, Hickey A, Hoogwerf BJ, Terrin ML, White C. Long-term effects on clinical outcomes of aggressive lowering of low-density lipoprotein cholesterol levels and low-dose anticoagulation in the post coronary artery bypass graft trial. *Circulation*. 2000;102:157-165

73. Abbruzzese TA, Havens J, Belkin M, Donaldson MC, Whittemore AD, Liao JK, Conte MS. Statin therapy is associated with improved patency of autogenous infrainguinal bypass grafts. *Journal of Vascular Surgery*. 2004;39:1178-1185

74. Pisoni R, Barker-Finkel J, Allo M. Statin therapy is not associated with improved vascular access outcomes. *Clinical Journal of the American Society of Nephrology*. 2010;5:1447-1450

75. Kulik A, Ruel M, Jneid H, Ferguson TB, Hiratzka LF, Ikonomidis JS, Lopez-Jimenez F, McNallan SM, Patel M, Roger VL, Sellke FW, Sica DA, Zimmerman L. Secondary prevention after coronary artery bypass graft surgery: A scientific statement from the american heart association. *Circulation*. 2015;131:927-964

76. Alexander JH, Hafley G, Harrington RA, Peterson ED, Ferguson TB, Jr., Lorenz TJ, Goyal A, Gibson M, Mack MJ, Gennevois D, Califf RM, Kouchoukos NT. Efficacy and safety of edifoligide, an e2f transcription factor decoy, for prevention of vein graft failure following coronary artery bypass graft surgery: Prevent iv: A randomized controlled trial. *JAMA*. 2005;294:2446-2454

77. Conte MS, Bandyk DF, Clowes AW, Moneta GL, Seely L, Lorenz TJ, Namini H, Hamdan AD, Roddy SP, Belkin M, Berceli SA, DeMasi RJ, Samson RH, Berman SS. Results of prevent iii: A multicenter, randomized trial of edifoligide for the prevention of vein graft failure in lower extremity bypass surgery. *J Vasc Surg*. 2006;43:742-751; discussion 751

78. Dwivedi AJ, Roy-Chaudhury P, Peden EK, Browne BJ, Ladenheim ED, Scavo VA, Gustafson PN, Wong MD, Magill M, Lindow F. Application of human type i pancreatic elastase (prt-201) to the venous anastomosis of arteriovenous grafts in patients with chronic kidney disease. *The journal of vascular access*. 2014;15:376-384

79. Hye RJ, Peden EK, O'Connor TP, Browne BJ, Dixon BS, Schanzer AS, Jensik SC, Dember LM, Jaff MR, Burke SK. Human type i pancreatic elastase treatment of arteriovenous fistulas in patients with chronic kidney disease. *Journal of Vascular Surgery*. 2014;60:454-461.e451

80. Muto A, Model L, Ziegler K, Eghbalieh SD, Dardik A. Mechanisms of vein graft adaptation to the arterial circulation: Insights into the neointimal algorithm and management strategies. *Circulation journal: official journal of the Japanese Circulation Society*. 2010;74:1501

81. Ward B, Seal BL, Brophy CM, Panitch A. Design of a bioactive cell-penetrating peptide: When a transduction domain does more than transduce. *J Pept Sci*. 2009;15:668-674

82. Parsonnet V, Lari A, Shah IH. New stent for support of veins in arterial grafts. *Archives of Surgery*. 1963;87:696-702

83. Karayannacos PE, Hostetler JR, Bond MG, Kakos GS, Williams RA, Kilman JW, Vasko JS. Late failure in vein grafts: Mediating factors in subendothelial fibromuscular hyperplasia. *Annals of Surgery*. 1978;187:183-188

84. Barra J, Volant A, Leroy J, Braesco J, Airiau J, Boschat J, Blanc J, Penther P. Constrictive perivenous mesh prosthesis for preservation of vein integrity.

Experimental results and application for coronary bypass grafting. *The Journal of Thoracic and Cardiovascular Surgery*. 1986;92:330-336

85. Kohler TR, Kirkman TR, Clowes AW. The effect of rigid external support on vein graft adaptation to the arterial circulation. *Journal of Vascular Surgery*. 1989;9:277-285

86. Violaris AG, Newby AC, Angelini GD. Effects of external stenting on wall thickening in arteriovenous bypass grafts. *The Annals of Thoracic Surgery*. 1993;55:667-671

87. Ross R, Raines EW, Bowen-Pope DF. The biology of platelet-derived growth factor. *Cell*.46:155-169

88. George S, Izzat M, Gadsdon P, Johnson J, Yim A, Wan S, Newby A, Angelini G, Jeremy J. Macro-porosity is necessary for the reduction of neointimal and medial thickening by external stenting of porcine saphenous vein bypass grafts. *Atherosclerosis*. 2001;155:329-336

89. Carella GS, Stilo F, Benedetto F, David A, Risitano DC, Buemi M, Spinelli F. Femoro-distal bypass with varicose veins covered by prosthetic mesh. *Journal of Surgical Research*. 2011;168:e189-e194

90. Zhu L-M, Schuster P, Klinge U. Mesh implants: An overview of crucial mesh parameters. *World Journal of Gastrointestinal Surgery*. 2015;7:226-236

91. Anderson JM. Biological responses to materials. *Annual Review of Materials Research*. 2001;31:81-110

92. Maurus PB, Kaeding CC. Bioabsorbable implant material review. *Operative Techniques in Sports Medicine*. 2004;12:158-160

93. Nair LS, Laurencin CT. Biodegradable polymers as biomaterials. *Progress in Polymer Science*. 2007;32:762-798

94. Zilla P, Moodley L, Wolf MF, Bezuidenhout D, Sirry MS, Rafiee N, Lichtenberg W, Black M, Franz T. Knitted nitinol represents a new generation of constrictive external vein graft meshes. *Journal of Vascular Surgery*. 2011;54:1439-1450

95. Ben-Gal Y, Taggart DP, Williams MR, Orion E, Uretzky G, Shofti R, Banai S, Yosef L, Bolotin G. Expandable external support device to improve saphenous vein graft patency after cabg. *Journal of Cardiothoracic Surgery*. 2013;8

96. Zurbrügg HR, Wied M, Angelini GD, Hetzer R. Reduction of intimal and medial thickening in sheathed vein grafts. *The Annals of Thoracic Surgery*. 1999;68:79-83

97. Webb CM, Orion E, Taggart DP, Channon KM, Di Mario C. Oct imaging of aorto-coronary vein graft pathology modified by external stenting: 1-year post-surgery. *European Heart Journal - Cardiovascular Imaging*. 2015

98. Meirson T, Orion E, Di Mario C, Webb C, Patel N, Channon KM, Ben Gal Y, Taggart DP. Flow patterns in externally stented saphenous vein grafts and development of intimal hyperplasia. *The Journal of Thoracic and Cardiovascular Surgery*. 2015;150:871-879

99. Batellier J, Tedgui A. Reduction of atherogenesis in an arterialized venous graft by using an external sleeve. *Chirurgie; memoires de l'Academie de chirurgie*. 1992;118:659

100. Batellier J, Wassef M, Merval R, Duriez M, Tedgui A. Protection from atherosclerosis in vein grafts by a rigid external support. *Arteriosclerosis, Thrombosis, and Vascular Biology*. 1993;13:379-384

101. Liu SQ, Moore MM, Yap C. Prevention of mechanical stretch-induced endothelial and smooth muscle cell injury in experimental vein grafts. *Journal of Biomechanical Engineering*. 1999;122:31-38

102. Stooker W, Niessen HWM, Baidoshvili A, Wildevuur WR, Van Hinsbergh VWM, Fritz J, Wildevuur CRH, Eijsman L. Perivenous support reduces early changes in human vein grafts: Studies in whole blood perfused human vein segments. *The Journal of Thoracic and Cardiovascular Surgery*. 2001;121:290-297

103. Zou R-J, Zou L-J, Huang S-D, Wang Y, Han L, Ji G-Y, Xu Z-y. Effect of external stents on prevention of intimal hyperplasia in a canine vein graft model. *Chinese medical journal*. 2007;120:2264-2267

104. Edwards WH, Martin RS, Jenkins JM, Mulherin JL. Primary graft infections. *Journal of Vascular Surgery*. 1987;6:235-239

105. Bunt T. Vascular graft infections: An update. *Cardiovascular Surgery*. 2001;9:225-233

106. Jeremy JY, Bulbulia R, Johnson JL, Gadsdon P, Vijayan V, Shukla N, Smith FC, Angelini GD. A bioabsorbable (polyglactin), nonrestrictive, external sheath inhibits porcine saphenous vein graft thickening. *The Journal of thoracic and cardiovascular surgery*. 2004;127:1766-1772

107. Vijayan V, Shukla N, Johnson JL, Gadsdon P, Angelini GD, Smith FCT, Baird R, Jeremy JY. Long-term reduction of medial and intimal thickening in porcine saphenous vein grafts with a polyglactin biodegradable external sheath. *J Vasc Surg*. 2004;40

108. Abbott WM, Megerman J, Hasson JE, L'Italien G, Warnock DF. Effect of compliance mismatch on vascular graft patency. *Journal of Vascular Surgery*. 1987;5:376-382

109. Okuhn SP, Connelly DP, Calakos N, Ferrell L, Man-Xiang P, Goldstone J. Does compliance mismatch alone cause neointimal hyperplasia? *J Vasc Surg*. 1989;9

110. Trubel W, Schima H, Moritz A, Raderer F, Windisch A, Ullrich R, Windberger U, Losert U, Polterauer P. Compliance mismatch and formation of distal anastomotic intimal hyperplasia in externally stiffened and lumen-adapted venous grafts. *European Journal of Vascular and Endovascular Surgery*. 1995;10:415-423

111. Ballyk PD, Walsh C, Butany J, Ojha M. Compliance mismatch may promote graft–artery intimal hyperplasia by altering suture-line stresses. *Journal of Biomechanics*. 1997;31:229-237

112. Mori N, Takano K, Miyake T, Nishio T, Muto S, Koshizuka K, Nakagomi H, Kubo M, Tada Y. A comparison of prosthetic materials used to repair abdominal wall defects. *Pediatric Surgery International*. 1998;13:487-490

113. Dasdia T, Bazzaco S, Bottero L, Buffa R, Ferrero S, Campanelli G, Dolfini E. Organ culture in 3-dimensional matrix: In vitro model for evaluating biological compliance of synthetic meshes for abdominal wall repair. *Journal of Biomedical Materials Research*. 1998;43:204-209

114. Allon M, Litovsky S, Young CJ, Deierhoi MH, Goodman J, Hanaway M, Lockhart ME, Robbin ML. Medial fibrosis, vascular calcification, intimal hyperplasia, and arteriovenous fistula maturation. *American Journal of Kidney Diseases*. 2011;58:437-443

115. Jiang Z, Tao M, Omalley KA, Wang D, Ozaki CK, Berceli SA. Established neointimal hyperplasia in vein grafts expands via tgf-β-mediated progressive fibrosis. *American Journal of Physiology - Heart and Circulatory Physiology*. 2009;297:H1200-H1207

116. Jeremy JY, Gadsdon P, Shukla N, Vijayan V, Wyatt M, Newby AC, Angelini GD. On the biology of saphenous vein grafts fitted with external synthetic sheaths and stents. *Biomaterials*. 2007;28:895-908

117. Moritz A, Grabenwöger F, Raderer F, et al. Mesh tube—constricted varicose veins used as bypass grafts for infrainguinal arterial reconstruction. *Archives of Surgery*. 1992;127:416-420

118. Cosson M, Debodinance P, Boukerrou M, Chauvet MP, Lobry P, Crépin G, Ego A. Mechanical properties of synthetic implants used in the repair of prolapse and

urinary incontinence in women: Which is the ideal material? *International Urogynecology Journal*. 2003;14:169-178

119. Orenstein SB, Saberski ER, Kreutzer DL, Novitsky YW. Comparative analysis of histopathologic effects of synthetic meshes based on material, weight, and pore size in mice. *Journal of Surgical Research*. 2012;176:423-429

120. Pereira-lucena CG, Artigiani Neto R, de Rezende DT, Lopes-Filho dGJ, Matos D, Linhares MM. Early and late postoperative inflammatory and collagen deposition responses in three different meshes: An experimental study in rats. *Hernia*. 2014;18:563-570

121. Woodruff MA, Hutmacher DW. The return of a forgotten polymer—polycaprolactone in the 21st century. *Progress in Polymer Science*. 2010;35:1217-1256

122. You Q, Wang F, Duan L, Du X, Xiao M, Shen Z. Construction of small-caliber, polydiaxanone cyclohexanone vascular stents. *Cell Biochemistry and Biophysics*. 2010;57:35-43

123. Steinbuchel A, Tomihata K, Suzuki M, Oka T, Ikada Y. Biodegradable polymers and macromoleculesa new resorbable monofilament suture. *Polymer Degradation and Stability*. 1998;59:13-18

124. You Q, Duan L, Wang F, Du X, Xiao M. Characterization of the inhibition of vein graft intimal hyperplasia by a biodegradable vascular stent. *Cell Biochemistry and Biophysics*. 2011;59:99-107

125. Liao SW, Lu X, Putnam AJ, Kassab GS. A novel time-varying poly lactic-co glycolic acid external sheath for vein grafts designed under physiological loading. *Tissue engineering*. 2007;13:2855-2862

126. Sato A, Kawamoto S, Watanabe M, Suzuki Y, Takahashi G, Masaki N, Kumagai K, Saijo Y, Tabayashi K, Saiki Y. A novel biodegradable external mesh stent improved long-term patency of vein grafts by inhibiting intimal–medial hyperplasia in an experimental canine model. *General Thoracic and Cardiovascular Surgery*. 2016;64:1-9

127. Ben-Gal Y, Taggart DP, Williams MR, Orion E, Uretzky G, Shofti R, Banai S, Yosef L, Bolotin G. Expandable external support device to improve saphenous vein graft patency after cabg. *Journal of Cardiothoracic Surgery*. 2013;8:122-122

128. Meirson T, Orion E, Avrahami I. Numerical analysis of venous external scaffolding technology for saphenous vein grafts. *Journal of Biomechanics*.48:2090-2095

129. Taggart DP, Ben Gal Y, Lees B, Patel N, Webb C, Rehman SM, Desouza A, Yadav R, De Robertis F, Dalby M, Banning A, Channon KM, Di Mario C, Orion E. A randomized trial of external stenting for saphenous vein grafts in coronary artery bypass grafting. *The Annals of Thoracic Surgery*. 2015;99:2039-2045

130. Franz T, Human P, Dobner S, Reddy BD, Black M, Ilsley H, Wolf MF, Bezuidenhout D, Moodley L, Zilla P. Tailored sizes of constrictive external vein meshes for coronary artery bypass surgery. *Biomaterials*. 2010;31:9301-9309

131. Franz T, Reddy BD, Human P, Zilla P. A mathematical method for constraint-based cluster analysis towards optimized constrictive diameter smoothing of saphenous vein grafts. *Medical & Biological Engineering & Computing*. 2010;48:519-529

132. Moodley L, Franz T, Human P, Wolf MF, Bezuidenhout D, Scherman J, Zilla P. Protective constriction of coronary vein grafts with knitted nitinol. *European Journal of Cardio-Thoracic Surgery*. 2013;44:64-71

133. Chemla E, Velazquez CC, D'Abate F, Ramachandran V, Maytham G. Arteriovenous fistula construction with the vasq™ external support device: A pilot study. *Journal of Vascular Access*. 2016;17:243-248

134. Emery RW, Solien E, Klima U. Clinical evaluation of the esvs mesh: First-in-man trial outcomes. *ASAIO Journal*. 2015;61:178-183

135. Rescigno G, Aratari C, Matteucci SM, Parisi R, Gironi G, Schicchi N, D'Alfonso A, Cola V, Torracca L. Saphenous vein graft wrapping by nitinol mesh: A word of caution. *The Thoracic and cardiovascular surgeon*. 2015;63:292-297

136. Etave F, Finet G, Boivin M, Boyer J-C, Rioufol G, Thollet G. Mechanical properties of coronary stents determined by using finite element analysis. *Journal of Biomechanics*. 2001;34:1065-1075

137. Migliavacca F, Petrini L, Colombo M, Auricchio F, Pietrabissa R. Mechanical behavior of coronary stents investigated through the finite element method. *Journal of Biomechanics*. 2002;35:803-811

138. Shimko DA, Shimko VF, Sander EA, Dickson KF, Nauman EA. Effect of porosity on the fluid flow characteristics and mechanical properties of tantalum scaffolds. *Journal of Biomedical Materials Research Part B: Applied Biomaterials*. 2005;73B:315-324

139. Xu HHK, Quinn JB, Takagi S, Chow LC, Eichmiller FC. Strong and macroporous calcium phosphate cement: Effects of porosity and fiber reinforcement on mechanical properties. *Journal of Biomedical Materials Research*. 2001;57:457-466

140. Lake SP, Ray S, Zihni AM, Thompson Jr DM, Gluckstein J, Deeken CR. Pore size and pore shape – but not mesh density – alter the mechanical strength of tissue ingrowth and host tissue response to synthetic mesh materials in a porcine model of ventral hernia repair. *Journal of the Mechanical Behavior of Biomedical Materials*. 2015;42:186-197

141. Hollister SJ. Porous scaffold design for tissue engineering. *Nat Mater*. 2005;4:518-524

142. Zhang Z, Wang Z, Liu S, Kodama M. Pore size, tissue ingrowth, and endothelialization of small-diameter microporous polyurethane vascular prostheses. *Biomaterials*. 2004;25:177-187

143. Desai M, Mirzay-Razzaz J, Von Delft D, Sarkar S, Hamilton G, Seifalian AM. Inhibition of neointimal formation and hyperplasia in vein grafts by external stent/sheath. *Vasc Med*. 2010;15

144. LU JX, FLAUTRE B, ANSELME K, HARDOUIN P, GALLUR A, DESCAMPS M, THIERRY B. Role of interconnections in porous bioceramics on bone recolonization in vitro and in vivo. *J Mater Sci: Mater Med*. 1999;10:111-120

145. Bai F, Zhang J, Wang Z, Lu J, Chang J, Liu J, Meng G, Dong X. The effect of pore size on tissue ingrowth and neovascularization in porous bioceramics of controlled architecture in vivo. *Biomedical Materials*. 2011;6:015007

146. Klosterhalfen B, Klinge U. Retrieval study at 623 human mesh explants made of polypropylene – impact of mesh class and indication for mesh removal on tissue reaction. *Journal of Biomedical Materials Research Part B: Applied Biomaterials*. 2013:n/a-n/a

147. Greca FH, Souza-Filho ZA, Giovanini A, Rubin MR, Kuenzer RF, Reese FB, Araujo LM. The influence of porosity on the integration histology of two polypropylene meshes for the treatment of abdominal wall defects in dogs. *Hernia*. 2008;12:45-49

148. Klinge U, Klosterhalfen B. Modified classification of surgical meshes for hernia repair based on the analyses of 1,000 explanted meshes. *Hernia*. 2012;16:251-258

149. Karageorgiou V, Kaplan D. Porosity of 3d biomaterial scaffolds and osteogenesis. *Biomaterials*. 2005;26:5474-5491

150. Roosa SMM, Kemppainen JM, Moffitt EN, Krebsbach PH, Hollister SJ. The pore size of polycaprolactone scaffolds has limited influence on bone regeneration in an in vivo model. *Journal of Biomedical Materials Research Part A*. 2010;92A:359-368

151. Li XM, Rittgers SE. Hemodynamic factors at the distal end-to-side anastomosis of a bypass graft with different pos:Dos flow ratios. *J Biomech Eng*. 2001;123

152. Li L, Terry CM, Blumenthal DK, Kuji T, Masaki T, Kwan BCH, Zhuplatov I, Leypoldt JK, Cheung AK. Cellular and morphological changes during neointimal hyperplasia development in a porcine arteriovenous graft model. *Nephrology Dialysis Transplantation*. 2007;22:3139-3146

153. Ku DN, Giddens DP, Zarins CK, Glagov S. Pulsatile flow and atherosclerosis in the human carotid bifurcation. Positive correlation between plaque location and low and oscillating shear stress. *Arteriosclerosis*. 1985;5

154. Loth F, Fischer PF, Bassiouny HS. Blood flow in end-to-side anastomoses. *Annu Rev Fluid Mech*. 2008;40

155. Trubel W, Moritz A, Schima H, Raderer F, Scherer R, Ullrich R, Losert U, Polterauer P. Compliance and formation of distal anastomotic intimal hyperplasia in dacron mesh tube constricted veins used as arterial bypass grafts. *ASAIO Journal*. 1994;40:M273-M278

156. Schoettler J, Jussli-Melchers J, Grothusen C, Stracke L, Schoeneich F, Stohn S, Hoffmann G, Cremer J. Highly flexible nitinol mesh to encase aortocoronary saphenous vein grafts: First clinical experiences and angiographic results nine months postoperatively. *Interactive CardioVascular and Thoracic Surgery*. 2011;13:396-400

157. Fuster V, Charlton P, Boyd A. Clinical protocol. A phase iib, randomized, multicenter, double-blind study of the efficacy and safety of trinam (eg004) in stenosis prevention at the graft-vein anastomosis site in dialysis patients. *Human gene therapy*. 2001;12:2025-2027

158. Conte MS, Nugent HM, Gaccione P, Guleria I, Roy-Chaudhury P, Lawson JH. Multicenter phase i/ii trial of the safety of allogeneic endothelial cell implants after the creation of arteriovenous access for hemodialysis use: The v-health study. *Journal of vascular surgery*. 2009;50:1359-1368.e1351

159. Mátyás L, Berry M, Menyhei G, Tamás L, Acsády G, Cuypers P, Halmos F, de Vries AC, Forgacs V, Ingenito G, Avelar R. The safety and efficacy of a paclitaxel-eluting wrap for preventing peripheral bypass graft stenosis: A 2-year controlled randomized prospective clinical study. *European Journal of Vascular and Endovascular Surgery*. 2008;35:715-722

160. Paulson W, Kipiani K, Beridze N, DeVita M, Shenoy S, Iyer S. Safety and efficacy of locally eluted sirolimus for prolonging av graft patency (ptfe graft plus coll-r)—first in man experience. *J Am Soc Nephrol*. 2008;19:252A

161. Dean PG, Lund WJ, Larson TS, Prieto M, Nyberg SL, Ishitani MB, Kremers WK, Stegall MD. Wound-healing complications after kidney transplantation: A prospective, randomized comparison of sirolimus and tacrolimus1. *Transplantation*. 2004;77:1555-1561

162. Troppmann C, Pierce JL, Gandhi MM, Gallay BJ, McVicar JP, Perez RV. Higher surgical wound complication rates with sirolimus immunosuppression after kidney transplantation: A matched-pair pilot study. *Transplantation*. 2003;76:426-429

163. Wu B, Mottola G, Chatterjee A, Lance KD, Chen M, Siguenza IO, Desai TA, Conte MS. Perivascular delivery of resolvin d1 inhibits neointimal hyperplasia in a rat model of arterial injury. *Journal of Vascular Surgery*.

164. Abbasi K, Shalileh K, Anvari MS, Rabbani S, Mahdanian A, Ahmadi SH, Moshtaghi N, Movahedi N, Karimi A. Perivascular nitric oxide delivery to saphenous vein grafts prevents graft stenosis after coronary artery bypass grafting: A novel sheep model. *Cardiology*. 2011;118:8-15

165. Filova E, Parizek M, Olsovska J, Kamenik Z, Brynda E, Riedel T, Vandrovcova M, Lisa V, Machova L, Skalsky I, Szarszoi O, Suchy T, Bacakova L. Perivascular sirolimus-delivery system. *International Journal of Pharmaceutics*. 2011;404:94-101

166. Sanders WG, Hogrebe PC, Grainger DW, Cheung AK, Terry CM. A biodegradable perivascular wrap for controlled, local and directed drug delivery. *Journal of Controlled Release*. 2012;161:81-89

167. Liu Z, Guo Z, Si Y, Zhang X, Shi Z, Chen F, Fu W. The research and preparation of a bi-layer biodegradable external sheath with directional drug release profiles for vein graft. *Applied Surface Science*. 2013;284:819-825

168. Lee KJ, Park SH, Lee JY, Joo HC, Jang EH, Youn Y-N, Ryu W. Perivascular biodegradable microneedle cuff for reduction of neointima formation after vascular injury. *Journal of Controlled Release*. 2014;192:174-181

169. Yu X, Takayama T, Goel SA, Shi X, Zhou Y, Kent KC, Murphy WL, Guo L-W. A rapamycin-releasing perivascular polymeric sheath produces highly effective inhibition of intimal hyperplasia. *Journal of Controlled Release*. 2014;191:47-53

170. Xie P, Shi E, Gu T, Zhang Y, Mao N. Inhibition of intimal hyperplasia of the vein graft with degradable poly lactic-co-glycolic acid vascular external sheaths carrying slow-release bosentan. *European Journal of Cardio-Thoracic Surgery*. 2015;48:842-849

171. Chaudhary MA, Guo L-W, Shi X, Chen G, Gong S, Liu B, Kent KC. Periadventitial drug delivery for the prevention of intimal hyperplasia following open surgery. *Journal of Controlled Release*. 2016;233:174-180

172. Skalský I, Szárszoi O, Filová E, Pařízek M, Lytvynets A, Malušková J, Lodererová A, Brynda E, Lisá V, Burdíková Z, Čapek M, Pirk J, Bačáková L. A perivascular system releasing sirolimus prevented intimal hyperplasia in a rabbit model in a medium-term study. *International Journal of Pharmaceutics*. 2012;427:311-319

173. Gregory EK, Webb AR, Vercammen JM, Flynn ME, Ameer GA, Kibbe MR. Periadventitial atra citrate-based polyester membranes reduce neointimal hyperplasia and restenosis after carotid injury in rats. *American Journal of Physiology - Heart and Circulatory Physiology*. 2014;307:H1419-H1429

174. Lendlein A, Kelch S. Shape-memory polymers. *Angewandte Chemie International Edition*. 2002;41:2034-2057

175. Lendlein A, Jiang H, Jünger O, Langer R. Light-induced shape-memory polymers. *Nature*. 2005;434:879-882

176. Schmidt AM. Electromagnetic activation of shape memory polymer networks containing magnetic nanoparticles. *Macromolecular Rapid Communications*. 2006;27:1168-1172

177. Sahoo NG, Jung YC, Cho JW. Electroactive shape memory effect of polyurethane composites filled with carbon nanotubes and conducting polymer. *Materials and Manufacturing Processes*. 2007;22:419-423

178. Mendez J, Annamalai PK, Eichhorn SJ, Rusli R, Rowan SJ, Foster EJ, Weder C. Bioinspired mechanically adaptive polymer nanocomposites with water-activated shape-memory effect. *Macromolecules*. 2011;44:6827-6835

179. Han XJ, Dong ZQ, Fan MM, Liu Y, Wang YF, Yuan QJ, Li BJ, Zhang S. Ph - induced shape - memory polymers. *Macromolecular Rapid Communications*. 2012;33:1055-1060

180. Sun L, Huang WM, Ding Z, Zhao Y, Wang CC, Purnawali H, Tang C. Stimulus-responsive shape memory materials: A review. *Materials & Design*. 2012;33:577-640

181. Hu J, Zhu Y, Huang H, Lu J. Recent advances in shape–memory polymers: Structure, mechanism, functionality, modeling and applications. *Progress in Polymer Science*. 2012;37:1720-1763

182. Berg GJ, McBride MK, Wang C, Bowman CN. New directions in the chemistry of shape memory polymers. *Polymer*. 2014;55:5849-5872

183. Julich-Gruner KK, Löwenberg C, Neffe AT, Behl M, Lendlein A. Recent trends in the chemistry of shape-memory polymers. *Macromolecular Chemistry and Physics*. 2013;214:527-536

184. Liu C, Qin H, Mather P. Review of progress in shape-memory polymers. *Journal of materials chemistry*. 2007;17:1543-1558

185. Pretsch T. Review on the functional determinants and durability of shape memory polymers. *Polymers*. 2010;2:120-158

186. Small W, Singhal P, Wilson TS, Maitland DJ. Biomedical applications of thermally activated shape memory polymers. *Journal of materials chemistry*. 2010;20:3356-3366

187. Serrano MC, Ameer GA. Recent insights into the biomedical applications of shape - memory polymers. *Macromolecular bioscience*. 2012;12:1156-1171

188. Lendlein A, Behl M, Hiebl B, Wischke C. Shape-memory polymers as a technology platform for biomedical applications. *Expert Review of Medical Devices*. 2010;7:357-379

189. Xue L, Dai S, Li Z. Biodegradable shape-memory block co-polymers for fast self-expandable stents. *Biomaterials*. 2010;31:8132-8140

190. Yakacki CM, Shandas R, Lanning C, Rech B, Eckstein A, Gall K. Unconstrained recovery characterization of shape-memory polymer networks for cardiovascular applications. *Biomaterials*. 2007;28:2255-2263

191. Ortega J, Maitland D, Wilson T, Tsai W, Savaş Ö, Saloner D. Vascular dynamics of a shape memory polymer foam aneurysm treatment technique. *Annals of biomedical engineering*. 2007;35:1870-1884

192. Maitland DJ, Small W, Ortega JM, Buckley PR, Rodriguez J, Hartman J, Wilson TS. Prototype laser-activated shape memory polymer foam device for embolic treatment of aneurysms. *Journal of biomedical optics*. 2007;12:030504-030504-030503

193. Small W, Buckley PR, Wilson TS, Benett WJ, Hartman J, Saloner D, Maitland DJ. Shape memory polymer stent with expandable foam: A new concept for endovascular embolization of fusiform aneurysms. *Biomedical Engineering, IEEE Transactions on*. 2007;54:1157-1160

194. McGinn JT, Usman S, Lapierre H, Pothula VR, Mesana TG, Ruel M. Minimally invasive coronary artery bypass grafting: Dual-center experience in 450 consecutive patients. *Circulation*. 2009;120:S78-S84

195. Small IV W, Wilson T, Benett W, Loge J, Maitland D. Laser-activated shape memory polymer intravascular thrombectomy device. *Optics Express*. 2005;13:8204-8213

196. Maitland DJ, Metzger MF, Schumann D, Lee A, Wilson TS. Photothermal properties of shape memory polymer micro - actuators for treating stroke*. *Lasers in Surgery and Medicine*. 2002;30:1-11

197. Metzger MF, Wilson TS, Schumann D, Matthews DL, Maitland DJ. Mechanical properties of mechanical actuator for treating ischemic stroke. *Biomedical Microdevices*. 2002;4:89-96

198. Rachev A, Felden L, Ku DN. Design and fabrication of a mechanically matched vascular graft. *Journal of biomechanical engineering*. 2011;133:091004

199. Safranski DL, Smith KE, Gall K. Mechanical requirements of shape-memory polymers in biomedical devices. *Polymer Reviews*. 2013;53:76-91

200. Paterson-Brown S, Cheslyn-Curtis S, Biglin J, Dye J, Easmon CS, Dudley HA. Suture materials in contaminated wounds: A detailed comparison of a new suture with those currently in use. *The British journal of surgery*. 1987;74:734-735

201. Bunt T, Haynes J. Synthetic vascular graft infection. The continuing headache. *Am Surg*. 1984;50:43

202. Xue L, Dai S, Li Z. Synthesis and characterization of elastic star shape-memory polymers as self-expandable drug-eluting stents. *Journal of materials chemistry*. 2012;22:7403-7411

203. Ebara M, Uto K, Idota N, Hoffman JM, Aoyagi T. Shape - memory surface with dynamically tunable nano - geometry activated by body heat. *Advanced Materials*. 2012;24:273-278

204. Shih CC, Lin SJ, Chen YL, Su YY, Lai ST, Wu GJ, Kwok CF, Chung KH. The cytotoxicity of corrosion products of nitinol stent wire on cultured smooth muscle cells. *Journal of biomedical materials research*. 2000;52:395-403

205. Serrano M, Pagani R, Vallet-Regı M, Pena J, Ramila A, Izquierdo I, Portoles M. In vitro biocompatibility assessment of poly (< i> ε</i>-caprolactone) films using l929 mouse fibroblasts. *Biomaterials*. 2004;25:5603-5611

206. Filion TM, Xu J, Prasad ML, Song J. In vivo tissue responses to thermal-responsive shape memory polymer nanocomposites. *Biomaterials*. 2011;32:985-991

207. Ratna D, Karger-Kocsis J. Recent advances in shape memory polymers and composites: A review. *Journal of Materials Science*. 2008;43:254-269

208. Lendlein A, Schmidt AM, Schroeter M, Langer R. Shape - memory polymer networks from oligo (ϵ - caprolactone) dimethacrylates. *Journal of Polymer Science Part A: Polymer Chemistry*. 2005;43:1369-1381

209. Rousseau IA. Challenges of shape memory polymers: A review of the progress toward overcoming smp's limitations. *Polymer Engineering & Science*. 2008;48:2075-2089

210. Lendlein A, Langer R. Biodegradable, elastic shape-memory polymers for potential biomedical applications. *Science*. 2002;296:1673-1676

211. Garle A, Kong S, Ojha U, Budhlall BM. Thermoresponsive semicrystalline poly (ε-caprolactone) networks: Exploiting cross-linking with cinnamoyl moieties to design polymers with tunable shape memory. *ACS applied materials & interfaces*. 2012;4:645-657

212. Nair DP, Cramer NB, Scott TF, Bowman CN, Shandas R. Photopolymerized thiol-ene systems as shape memory polymers. *Polymer*. 2010;51:4383-4389

213. Nair DP, Cramer NB, McBride MK, Gaipa JC, Shandas R, Bowman CN. Enhanced two-stage reactive polymer network forming systems. *Polymer*. 2012;53:2429-2434

214. Uygun M, Tasdelen MA, Yagci Y. Influence of type of initiation on thiol–ene "click" chemistry. *Macromolecular Chemistry and Physics*. 2010;211:103-110

215. Nair DP, Podgórski M, Chatani S, Gong T, Xi W, Fenoli CR, Bowman CN. The thiol-michael addition click reaction: A powerful and widely used tool in materials chemistry. *Chemistry of Materials*. 2013;26:724-744

216. Xu X, Davis KA, Yang P, Gu X, Henderson JH, Mather PT. Shape memory rgd - containing networks: Synthesis, characterization, and application in cell culture. *Macromolecular Symposia*. 2011;309:162-172

217. Wang X, Boire TC, Bronikowski C, Zachman AL, Crowder SW, Sung H-J. Decoupling polymer properties to elucidate mechanisms governing cell behavior. *Tissue Engineering Part B: Reviews*. 2012;18:396-404

218. Jeong H, Kim B, Choi Y. Synthesis and properties of thermotropic liquid crystalline polyurethane elastomers. *Polymer*. 2000;41:1849-1855

219. Bothe M, Mya KY, Lin EMJ, Yeo CC, Lu X, He C, Pretsch T. Triple-shape properties of star-shaped poss-polycaprolactone polyurethane networks. *Soft Matter*. 2012;8:965-972

220. Luo H, Liu Y, Yu Z, Zhang S, Li B. Novel biodegradable shape memory material based on partial inclusion complex formation between α-cyclodextrin and poly(ϵ-caprolactone). *Biomacromolecules*. 2008;9:2573-2577

221. Messori M, Degli Esposti M, Paderni K, Pandini S, Passera S, Riccò T, Toselli M. Chemical and thermomechanical tailoring of the shape memory effect in poly(ε-caprolactone)-based systems. *Journal of Materials Science*. 2013;48:424-440

222. Mya KY, Gose HB, Pretsch T, Bothe M, He C. Star-shaped poss-polycaprolactone polyurethanes and their shape memory performance. *Journal of materials chemistry*. 2011;21:4827-4836

223. Neuss S, Blomenkamp I, Stainforth R, Boltersdorf D, Jansen M, Butz N, Perez-Bouza A, Knüchel R. The use of a shape-memory poly(ε-caprolactone)dimethacrylate network as a tissue engineering scaffold. *Biomaterials*. 2009;30:1697-1705

224. Mani G, Feldman MD, Patel D, Agrawal C. Coronary stents: A materials perspective. *Biomaterials*. 2007;28:1689-1710

225. Parrish B, Quansah JK, Emrick T. Functional polyesters prepared by polymerization of $\alpha$ - allyl (valerolactone) and its copolymerization with $\varepsilon$ - caprolactone and $\delta$ - valerolactone. *Journal of Polymer Science Part A: Polymer Chemistry*. 2002;40:1983-1990

226. Mahmud A, Xiong X-B, Lavasanifar A. Novel self-associating poly (ethylene oxide)-b lock-poly (ε-caprolactone) block copolymers with functional side groups on the polyester block for drug delivery. *Macromolecules*. 2006;39:9419-9428

227. Molander GA, Harris CR. Sequenced reactions with samarium (ii) iodide. Tandem intramolecular nucleophilic acyl substitution/intramolecular barbier cyclizations. *Journal of the American Chemical Society*. 1995;117:3705-3716

228. Darcos V, Antoniacomi S, Paniagua C, Coudane J. Cationic polyesters bearing pendent amino groups prepared by thiol–ene chemistry. *Polymer Chemistry*. 2012;3:362-368

229. Pitt CG, Chasalow F, Hibionada Y, Klimas D, Schindler A. Aliphatic polyesters. I. The degradation of poly (ϵ - caprolactone) in vivo. *Journal of Applied Polymer Science*. 1981;26:3779-3787

230. Guo B, Chen Y, Lei Y, Zhang L, Zhou WY, Rabie ABM, Zhao J. Biobased poly (propylene sebacate) as shape memory polymer with tunable switching temperature for potential biomedical applications. *Biomacromolecules*. 2011;12:1312-1321

231. Defize T, Riva R, Raquez J-M, Dubois P, Jérôme C, Alexandre M. Thermoreversibly crosslinked poly(ε-caprolactone) as recyclable shape-memory polymer network. *Macromolecular Rapid Communications*. 2011;32:1264-1269

232. Wagermaier W, Kratz K, Heuchel M, Lendlein A. Characterization methods for shape-memory polymers. In: Lendlein A, ed. *Shape-memory polymers*. Springer Berlin Heidelberg; 2010:97-145.

233. Lancaster MV, Fields RD. Microbiocides and conversion of resazurin to resorfurin. 1996

234. Hu X, Chen X, Liu S, Shi Q, Jing X. Novel aliphatic poly (ester - carbonate) with pendant allyl ester groups and its folic acid functionalization. *Journal of Polymer Science Part A: Polymer Chemistry*. 2008;46:1852-1861

235. Karikari AS, Edwards WF, Mecham JB, Long TE. Influence of peripheral hydrogen bonding on the mechanical properties of photo-cross-linked star-shaped poly (d, l-lactide) networks. *Biomacromolecules*. 2005;6:2866-2874

236. Xue L, Dai S, Li Z. Synthesis and characterization of three-arm poly (ε-caprolactone)-based poly (ester− urethanes) with shape-memory effect at body temperature. *Macromolecules*. 2009;42:964-972

237. Yakacki CM, Shandas R, Lanning C, Rech B, Eckstein A, Gall K. Unconstrained recovery characterization of shape-memory polymer networks for cardiovascular applications. *Biomaterials*. 2007;28:2255-2263

238. Zhu G, Liang G, Xu Q, Yu Q. Shape - memory effects of radiation crosslinked poly (ϵ - caprolactone). *Journal of Applied Polymer Science*. 2003;90:1589-1595

239. Li F, Zhu W, Zhang X, Zhao C, Xu M. Shape memory effect of ethylene–vinyl acetate copolymers. *Journal of Applied Polymer Science*. 1999;71:1063-1070

240. Karimi A, Navidbakhsh M, Shojaei A, Faghihi S. Measurement of the uniaxial mechanical properties of healthy and atherosclerotic human coronary arteries. *Materials Science and Engineering: C*. 2013;33:2550-2554

241. Ota S. Current status of irradiated heat-shrinkable tubing in japan. *Radiation Physics and Chemistry (1977)*. 1981;18:81-87

242. Kleinheins G, Starkl W, Nuffer K. Special features of quality assurance measures for radiation-cured, heat-shrunk products. 1984

243. Kleinhans G, Heidenhain F. Actively moving polymers. *Kunststoffe*. 1986;76:1069-1073

244. Feldkamp DM, Rousseau IA. Effect of the deformation temperature on the shape - memory behavior of epoxy networks. *Macromolecular Materials and Engineering*. 2010;295:726-734

245. Gall K, Yakacki CM, Liu Y, Shandas R, Willett N, Anseth KS. Thermomechanics of the shape memory effect in polymers for biomedical applications. *Journal of Biomedical Materials Research Part A*. 2005;73:339-348

246. McClung AJ, Tandon GP, Baur JW. Deformation rate-, hold time-, and cycle-dependent shape-memory performance of veriflex-e resin. *Mechanics of Time-Dependent Materials*. 2013;17:39-52

247. Lam CX, Hutmacher DW, Schantz JT, Woodruff MA, Teoh SH. Evaluation of polycaprolactone scaffold degradation for 6 months in vitro and in vivo. *Journal of Biomedical Materials Research Part A*. 2009;90:906-919

248. Maciaq T KJ, Wilkins L, Stemerman MB, Weinstein R. Organizational behavior of human umbilical vein endothelial cells. *The Journal of cell biology*. 1982;94:511-520

249. Yang C-S, Wu H-C, Sun J-S, Hsiao H-M, Wang T-W. Thermo-induced shape-memory peg-pcl copolymer as a dual-drug-eluting biodegradable stent. *ACS applied materials & interfaces*. 2013;5:10985-10994

250. Kratz K, Voigt U, Lendlein A. Temperature-memory effect of copolyesterurethanes and their application potential in minimally invasive medical technologies. *Advanced Functional Materials*. 2012;22:3057-3065

251. Li G, Fei G, Xia H, Han J, Zhao Y. Spatial and temporal control of shape memory polymers and simultaneous drug release using high intensity focused ultrasound. *Journal of materials chemistry*. 2012;22:7692-7696

252. Yang D, Huang W, He X, Xie M. Electromagnetic activation of a shape memory copolymer matrix incorporating ferromagnetic nanoparticles. *Polymer International*. 2012;61:38-42

253. Fei G, Tuinea-Bobe C, Li D, Li G, Whiteside B, Coates P, Xia H. Electro-activated surface micropattern tuning for microinjection molded electrically conductive shape memory polyurethane composites. *RSC Advances*. 2013;3:24132-24139

254. Hribar KC, Metter RB, Ifkovits JL, Troxler T, Burdick JA. Light-induced temperature transitions in biodegradable polymer and nanorod composites. *Small*. 2009;5:1830-1834

255. Liu Y, Boyles JK, Genzer J, Dickey MD. Self-folding of polymer sheets using local light absorption. *Soft Matter*. 2012;8:1764-1769

256. Liu Y, Miskiewicz M, Escuti MJ, Genzer J, Dickey MD. Three-dimensional folding of pre-strained polymer sheets via absorption of laser light. *Journal of Applied Physics*. 2014;115:204911

257. Zhang H, Zhang J, Tong X, Ma D, Zhao Y. Light polarization-controlled shape-memory polymer/gold nanorod composite. *Macromolecular Rapid Communications*. 2013;34:1575-1579

258. Zhang H, Zhao Y. Polymers with dual light-triggered functions of shape memory and healing using gold nanoparticles. *ACS applied materials & interfaces*. 2013;5:13069-13075

259. Palder SB, Kirkman RL, Whittemore AD, Hakim RM, Lazarus JM, Tilney NL. Vascular access for hemodialysis. Patency rates and results of revision. *Annals of Surgery*. 1985;202:235-239

260. Allon M, Lockhart ME, Lilly RZ, Gallichio MH, Young CJ, Barker J, Deierhoi MH, Robbin ML. Effect of preoperative sonographic mapping on vascular access outcomes in hemodialysis patients. *Kidney international*. 2001;60:2013-2020

261. Asif A, Cherla G, Merrill D, Cipleu CD, Briones P, Pennell P. Conversion of tunneled hemodialysis catheter–consigned patients to arteriovenous fistula. *Kidney international*. 2005;67:2399-2406

262. Asif A, Roy-Chaudhury P, Beathard GA. Early arteriovenous fistula failure: A logical proposal for when and how to intervene. *Clinical Journal of the American Society of Nephrology*. 2006;1:332-339

263. Boire TC, Balikov DA, Lee Y, Guth CM, Cheung-Flynn J, Sung H-J. Biomaterial-based approaches to address vein graft and hemodialysis access failures. *Macromolecular Rapid Communications*. 2016;37:1860-1880

264. Brown BN, Londono R, Tottey S, Zhang L, Kukla KA, Wolf MT, Daly KA, Reing JE, Badylak SF. Macrophage phenotype as a predictor of constructive remodeling following the implantation of biologically derived surgical mesh materials. *Acta Biomaterialia*. 2012;8:978-987

265. Vijayan V, Shukla N, Johnson JL, Gadsdon P, Angelini GD, Smith FC, Baird R, Jeremy JY. Long-term reduction of medial and intimal thickening in porcine

saphenous vein grafts with a polyglactin biodegradable external sheath. *Journal of vascular surgery*. 2004;40:1011-1019

266. Deeken CR, Melman L, Jenkins ED, Greco SC, Frisella MM, Matthews BD. Histologic and biomechanical evaluation of crosslinked and non-crosslinked biologic meshes in a porcine model of ventral incisional hernia repair. *Journal of the American College of Surgeons*. 2011;212:880-888

267. Labet M, Thielemans W. Synthesis of polycaprolactone: A review. *Chemical Society Reviews*. 2009;38:3484-3504

268. Whitehead J. Sample size calculations for ordered categorical data. *Statistics in Medicine*. 1993;12:2257-2271

269. Walters SJ. Sample size and power estimation for studies with health related quality of life outcomes: A comparison of four methods using the sf-36. *Health and Quality of Life Outcomes*. 2004;2:26

270. Heydorn WH, Zajtchuk R, Miller J, Schuchmann GF. Gore-tex grafts for replacement of the superior vena cava. *The Annals of Thoracic Surgery*. 1977;23:539-544

271. Badylak SF, Valentin JE, Ravindra AK, McCabe GP, Stewart-Akers AM. Macrophage phenotype as a determinant of biologic scaffold remodeling. *Tissue Engineering Part A*. 2008;14:1835-1842

272. Boire TC, Balikov DA, Lee Y, Guth CM, Cheung - Flynn J, Sung HJ. Biomaterial - based approaches to address vein graft and hemodialysis access failures. *Macromolecular Rapid Communications*. 2016

273. Yang Y, Liu F, Tang M, Yuan M, Hu A, Zhan Z, Li Z, Li J, Ding X, Lu L. Macrophage polarization in experimental and clinical choroidal neovascularization. *Scientific Reports*. 2016;6:30933

274. Spiller KL, Anfang R, Spiller KJ, Ng J, Nakazawa KR, Daulton JW, Vunjak-Novakovic G. The role of macrophage phenotype in vascularization of tissue engineering scaffolds. *Biomaterials*. 2014;35:4477-4488

275. Roh JD, Sawh-Martinez R, Brennan MP, Jay SM, Devine L, Rao DA, Yi T, Mirensky TL, Nalbandian A, Udelsman B, Hibino N, Shinoka T, Saltzman WM, Snyder E, Kyriakides TR, Pober JS, Breuer CK. Tissue-engineered vascular grafts transform into mature blood vessels via an inflammation-mediated process of vascular remodeling. *Proceedings of the National Academy of Sciences*. 2010;107:4669-4674

276. Koehler RH, Begos D, Berger D, Carey S, LeBlanc K, Park A, Ramshaw B, Smoot R, Voeller G. Minimal adhesions to eptfe mesh after laparoscopic ventral incisional hernia repair: Reoperative findings in 65 cases. *Zentralblatt für Chirurgie*. 2003;128:625-630

277. Wermuth PJ, Jimenez SA. The significance of macrophage polarization subtypes for animal models of tissue fibrosis and human fibrotic diseases. *Clinical and Translational Medicine*. 2015;4:2

278. Gill SE, Parks WC. Metalloproteinases and their inhibitors: Regulators of wound healing. *The International Journal of Biochemistry & Cell Biology*. 2008;40:1334-1347

279. Parks WC, Wilson CL, Lopez-Boado YS. Matrix metalloproteinases as modulators of inflammation and innate immunity. *Nat Rev Immunol*. 2004;4:617-629

280. Kónya A, Wright KC, Gounis M, Kandarpa K. Animal models for atherosclerosis, restenosis, and endovascular aneurysm repair. In: Conn PM, ed. *Sourcebook of models for biomedical research*. Totowa, NJ: Humana Press; 2008:369-384.

281. Byrom MJ, Bannon PG, White GH, Ng MKC. Animal models for the assessment of novel vascular conduits. *Journal of Vascular Surgery*. 2010;52:176-195

282. Piola M, Soncini M, Pesce M, Fiore GB. A lumped-parameter approach for designing a novel pulsatile bioreactor for ex-vivo studies of human saphenous vein remodeling. *2015 37th Annual International Conference of the IEEE Engineering in Medicine and Biology Society (EMBC)*. 2015:2588-2591

283. White SS, Zarins CK, Giddens DP, Bassiouny H, Loth F, Jones SA, Glagov S. Hemodynamic patterns in two models of end-to-side vascular graft anastomoses: Effects of pulsatility, flow division, reynolds number, and hood length. *Journal of Biomechanical Engineering*. 1993;115:104-111

284. Frauenfelder T, Boutsianis E, Schertler T, Husmann L, Leschka S, Poulikakos D, Marincek B, Alkadhi H. Flow and wall shear stress in end-to-side and side-to-side anastomosis of venous coronary artery bypass grafts. *BioMedical Engineering OnLine*. 2007;6:35

285. Loth F, Fischer PF, Arslan N, Bertram CD, Lee SE, Royston TJ, Shaalan WE, Bassiouny HS. Transitional flow at the venous anastomosis of an arteriovenous graft: Potential activation of the erk1/2 mechanotransduction pathway. *Journal of Biomechanical Engineering*. 2003;125:49-61

286. Karimi A, Navidbakhsh M, Alizadeh M, Shojaei A. A comparative study on the mechanical properties of the umbilical vein and umbilical artery under uniaxial loading. *Artery Research*. 2014;8:51-56

287. Wesly RL, Vaishnav RN, Fuchs JC, Patel DJ, Greenfield JC. Static linear and nonlinear elastic properties of normal and arterialized venous tissue in dog and man. *Circulation Research*. 1975;37:509-520

288. Rezakhaniha R, Stergiopulos N. A structural model of the venous wall considering elastin anisotropy. *Journal of Biomechanical Engineering*. 2008;130:031017-031017

289. Zervides C, Narracott AJ, Lawford PV, Hose DR. The role of venous valves in pressure shielding. *BioMedical Engineering OnLine*. 2008;7:8

290. Loth F, Fischer PF, Bassiouny HS. Blood flow in end-to-side anastomoses. *Annual Review of Fluid Mechanics*. 2008;40:367-393

291. Evans BC, Hocking KM, Osgood MJ, Voskresensky I, Dmowska J, Kilchrist KV, Brophy CM, Duvall CL. Mk2 inhibitory peptide delivered in nanopolyplexes prevents vascular graft intimal hyperplasia. *Science translational medicine*. 2015;7:291ra295-291ra295

292. Klein B, Destephens A, Dumeny L, Hu Q, He Y, O'Malley K, Jiang Z, Tran-Son-Tay R, Berceli S. Hemodynamic influence on smooth muscle cell kinetics and phenotype during early vein graft adaptation. *Annals of Biomedical Engineering*. 2016:1-12

293. Lee Y, Bae JW, Oh DH, Park KM, Chun YW, Sung HJ, Park KD. In situ forming gelatin-based tissue adhesives and their phenolic content-driven properties. *Journal of Materials Chemistry B*. 2013;1:2407-2414

294. Lee SH, Lee Y, Chun YW, Crowder SW, Young PP, Park KD, Sung H-J. In situ crosslinkable gelatin hydrogels for vasculogenic induction and delivery of mesenchymal stem cells. *Advanced Functional Materials*. 2014:n/a-n/a

295. Roberts M, Bentley M, Harris J. Chemistry for peptide and protein pegylation. *Advanced Drug Delivery Reviews*. 2002;54:459-476

296. Vittal R, Fisher A, Gu H, Mickler EA, Panitch A, Lander C, Cummings OW, Sandusky GE, Wilkes DS. Peptide-mediated inhibition of mitogen-activated protein kinase-activated protein kinase-2 ameliorates bleomycin-induced pulmonary fibrosis. *American journal of respiratory cell and molecular biology*. 2013;49:47-57

297. Biondi M, Ungaro F, Quaglia F, Netti PA. Controlled drug delivery in tissue engineering. *Advanced Drug Delivery Reviews*. 2008;60:229-242

298. Hoare TR, Kohane DS. Hydrogels in drug delivery: Progress and challenges. *Polymer*. 2008;49:1993-2007

299. DiTizio V, Karlgard C, Lilge L, Khoury AE, Mittelman MW, DiCosmo F. Localized drug delivery using crosslinked gelatin gels containing liposomes: Factors influencing liposome stability and drug release. *Journal of biomedical materials research*. 2000;51:96-106

300. Lee PI. Kinetics of drug release from hydrogel matrices. *Journal of Controlled Release*. 1985;2:277-288

301. Koutsopoulos S, Unsworth LD, Nagai Y, Zhang S. Controlled release of functional proteins through designer self-assembling peptide nanofiber hydrogel scaffold. *Proceedings of the National Academy of Sciences*. 2009;106:4623-4628

302. Nagai Y, Unsworth LD, Koutsopoulos S, Zhang S. Slow release of molecules in self-assembling peptide nanofiber scaffold. *Journal of Controlled Release*. 2006;115:18-25

303. Park GS, Crank J. Diffusion in polymers. 1968

304. Higuchi T. Mechanism of sustained - action medication. Theoretical analysis of rate of release of solid drugs dispersed in solid matrices. *Journal of pharmaceutical sciences*. 1963;52:1145-1149

305. Lee SW, Kim B-S, Chen S, Shao-Horn Y, Hammond PT. Layer-by-layer assembly of all carbon nanotube ultrathin films for electrochemical applications. *Journal of the American Chemical Society*. 2009;131:671-679

306. Decher G. Fuzzy nanoassemblies: Toward layered polymeric multicomposites. *Science*. 1997;277:1232-1237

307. Choi D, Hong J. Layer-by-layer assembly of multilayer films for controlled drug release. *Archives of Pharmacal Research*. 2014;37:79-87

308. Capila I, Linhardt RJ. Heparin–protein interactions. *Angewandte Chemie International Edition*. 2002;41:390-412

309. Sarkar S, Sales KM, Hamilton G, Seifalian AM. Addressing thrombogenicity in vascular graft construction. *Journal of Biomedical Materials Research Part B: Applied Biomaterials*. 2007;82B:100-108

310. Liang Y, Kiick KL. Heparin-functionalized polymeric biomaterials in tissue engineering and drug delivery applications. *Acta Biomaterialia*. 2014;10:1588-1600

311. Ye Q, Zhou F, Liu W. Bioinspired catecholic chemistry for surface modification. *Chemical Society Reviews*. 2011;40:4244-4258

312. Lee H, Dellatore SM, Miller WM, Messersmith PB. Mussel-inspired surface chemistry for multifunctional coatings. *Science*. 2007;318:426-430

313. Zhu L-P, Yu J-Z, Xu Y-Y, Xi Z-Y, Zhu B-K. Surface modification of pvdf porous membranes via poly(dopa) coating and heparin immobilization. *Colloids and Surfaces B: Biointerfaces*. 2009;69:152-155

314. Li S, Garreau H, Pauvert B, McGrath J, Toniolo A, Vert M. Enzymatic degradation of block copolymers prepared from ε-caprolactone and poly(ethylene glycol). *Biomacromolecules*. 2002;3:525-530

315. Tang ZG, Black RA, Curran JM, Hunt JA, Rhodes NP, Williams DF. Surface properties and biocompatibility of solvent-cast poly[ε-caprolactone] films. *Biomaterials*. 2004;25:4741-4748

316. Liu T, Liu Y, Chen Y, Liu S, Maitz MF, Wang X, Zhang K, Wang J, Wang Y, Chen J, Huang N. Immobilization of heparin/poly-l-lysine nanoparticles on dopamine-coated surface to create a heparin density gradient for selective direction of platelet and vascular cells behavior. *Acta Biomaterialia*. 2014;10:1940-1954

317. Kim SE, Song S-H, Yun YP, Choi B-J, Kwon IK, Bae MS, Moon H-J, Kwon Y-D. The effect of immobilization of heparin and bone morphogenic protein-2 (bmp-2) to titanium surfaces on inflammation and osteoblast function. *Biomaterials*. 2011;32:366-373

318. Kim SE, Yun Y-P, Shim K-S, Park K, Choi S-W, Shin DH, Suh DH. Fabrication of a bmp-2-immobilized porous microsphere modified by heparin for bone tissue engineering. *Colloids and Surfaces B: Biointerfaces*. 2015;134:453-460

319. Park KM, Park KD. Facile surface immobilization of cell adhesive peptide onto tio2 substrate via tyrosinase-catalyzed oxidative reaction. *Journal of Materials Chemistry*. 2011;21:15906-15908

320. Wang X, Boire TC, Bronikowski C, Zachman AL, Crowder SW, Sung HJ. Decoupling polymer properties to elucidate mechanisms governing cell behavior. *Tissue engineering. Part B, Reviews*. 2012;18:396-404

321. Zachman AL, Wang X, Tucker-Schwartz JM, Fitzpatrick ST, Lee SH, Guelcher SA, Skala MC, Sung HJ. Uncoupling angiogenesis and inflammation in peripheral artery disease with therapeutic peptide-loaded microgels. *Biomaterials*. 2014

322. Choi WS, Joung YK, Lee Y, Bae JW, Park HK, Park YH, Park J-C, Park KD. Enhanced patency and endothelialization of small-caliber vascular grafts fabricated

by coimmobilization of heparin and cell-adhesive peptides. *ACS Applied Materials & Interfaces*. 2016;8:4336-4346

323. Wan Y, Yang J, Yang J, Bei J, Wang S. Cell adhesion on gaseous plasma modified poly-(l-lactide) surface under shear stress field. *Biomaterials*. 2003;24:3757-3764

324. Curtis A, Wilkinson C. Topographical control of cells. *Biomaterials*. 1997;18:1573-1583

325. Yim EKF, Darling EM, Kulangara K, Guilak F, Leong KW. Nanotopography-induced changes in focal adhesions, cytoskeletal organization, and mechanical properties of human mesenchymal stem cells. *Biomaterials*. 2010;31:1299-1306

326. Hahn MS, McHale MK, Wang E, Schmedlen RH, West JL. Physiologic pulsatile flow bioreactor conditioning of poly(ethylene glycol)-based tissue engineered vascular grafts. *Annals of Biomedical Engineering*. 2007;35:190-200

327. Jing X, Mi H-Y, Salick MR, Cordie TM, Peng X-F, Turng L-S. Electrospinning thermoplastic polyurethane/graphene oxide scaffolds for small diameter vascular graft applications. *Materials Science and Engineering: C*. 2015;49:40-50

328. Mercado-Pagán ÁE, Kang Y, Findlay MW, Yang Y. Development and evaluation of elastomeric hollow fiber membranes as small diameter vascular graft substitutes. *Materials Science and Engineering: C*. 2015;49:541-548

329. Nezarati RM, Eifert MB, Dempsey DK, Cosgriff-Hernandez E. Electrospun vascular grafts with improved compliance matching to native vessels. *Journal of Biomedical Materials Research Part B: Applied Biomaterials*. 2015;103:313-323

330. Pavia FC, La Carrubba V, Mannella GA, Ghersi G, Brucato V. Poly lactic acid based scaffolds for vascular tissue engineering. *Chem Eng Trans*. 2012;27

331. Fu W, Liu Z, Feng B, Hu R, He X, Wang H, Yin M, Huang H, Zhang H, Wang W. Electrospun gelatin/pcl and collagen/plcl scaffolds for vascular tissue engineering. *Int J Nanomedicine*. 2014;9:2335-2344

332. Han J, Lazarovici P, Pomerantz C, Chen X, Wei Y, Lelkes PI. Co-electrospun blends of plga, gelatin, and elastin as potential nonthrombogenic scaffolds for vascular tissue engineering. *Biomacromolecules*. 2011;12:399-408

333. He W, Yong T, Teo WE, Ma Z, Ramakrishna S. Fabrication and endothelialization of collagen-blended biodegradable polymer nanofibers: Potential vascular graft for blood vessel tissue engineering. *Tissue engineering*. 2005;11:1574-1588

334. Shi C, Yuan W, Khan M, Li Q, Feng Y, Yao F, Zhang W. Hydrophilic pcu scaffolds prepared by grafting pegma and immobilizing gelatin to enhance cell adhesion and proliferation. *Materials Science and Engineering: C*. 2015;50:201-209

335. TIWARI A, SALACINSKI HJ, PUNSHON G, HAMILTON G, SEIFALIAN AM. Development of a hybrid cardiovascular graft using a tissue engineering approach. *The FASEB Journal*. 2002;16:791-796

336. Vatankhah E, Prabhakaran MP, Semnani D, Razavi S, Morshed M, Ramakrishna S. Electrospun tecophilic/gelatin nanofibers with potential for small diameter blood vessel tissue engineering. *Biopolymers*. 2014;101:1165-1180

337. Wang W, Hu J, He C, Nie W, Feng W, Qiu K, Zhou X, Gao Y, Wang G. Heparinized plla/plcl nanofibrous scaffold for potential engineering of small-diameter blood vessel: Tunable elasticity and anticoagulation property. *Journal of Biomedical Materials Research Part A*. 2015;103:1784-1797

338. Zhu G-C, Gu Y-Q, Geng X, Feng Z-G, Zhang S-W, Ye L, Wang Z-G. Experimental study on the construction of small three-dimensional tissue engineered grafts of electrospun poly-ε-caprolactone. *J Mater Sci: Mater Med*. 2015;26:1-16

339. Zhu Y, Gao C, He T, Shen J. Endothelium regeneration on luminal surface of polyurethane vascular scaffold modified with diamine and covalently grafted with gelatin. *Biomaterials*. 2004;25:423-430

340. Buttafoco L, Engbers-Buijtenhuijs P, Poot AA, Dijkstra PJ, Vermes I, Feijen J. Physical characterization of vascular grafts cultured in a bioreactor. *Biomaterials*. 2006;27:2380-2389

341. Daamen WF, van Moerkerk HTB, Hafmans T, Buttafoco L, Poot AA, Veerkamp JH, van Kuppevelt TH. Preparation and evaluation of molecularly-defined collagen–elastin–glycosaminoglycan scaffolds for tissue engineering. *Biomaterials*. 2003;24:4001-4009

342. Lamprou D, Zhdan P, Labeed F, Lekakou C. Gelatine and gelatine/elastin nanocomposites for vascular grafts: Processing and characterization. *Journal of Biomaterials Applications*. 2011;26:209-226

343. Lekakou C, Lamprou D, Vidyarthi U, Karopoulou E, Zhdan P. Structural hierarchy of biomimetic materials for tissue engineered vascular and orthopedic grafts. *Journal of Biomedical Materials Research Part B: Applied Biomaterials*. 2008;85B:461-468

344. Patterson JT, Gilliland T, Maxfield MW, Church S, Naito Y, Shinoka T, Breuer CK. Tissue-engineered vascular grafts for use in the treatment of congenital heart

disease: From the bench to the clinic and back again. *Regenerative Medicine*. 2012;7:409-419

345. Salifu AA, Nury BD, Lekakou C. Electrospinning of nanocomposite fibrillar tubular and flat scaffolds with controlled fiber orientation. *Annals of Biomedical Engineering*. 2011;39:2510-2520

346. Elsayed Y, Lekakou C, Labeed F, Tomlins P. Fabrication and characterisation of biomimetic, electrospun gelatin fibre scaffolds for tunica media-equivalent, tissue engineered vascular grafts. *Materials Science and Engineering: C*. 2016;61:473-483

347. Hibino N, McGillicuddy E, Matsumura G, Ichihara Y, Naito Y, Breuer C, Shinoka T. Late-term results of tissue-engineered vascular grafts in humans. *The Journal of Thoracic and Cardiovascular Surgery*. 2010;139:431-436.e432

348. Rosenberg N, Martinez A, Sawyer PN, Wesolowski SA, Postlethwait RW, Dillon ML. Tanned collagen arterial prosthesis of bovine carotid origin in man. Preliminary studies of enzyme-treated heterografts. *Annals of Surgery*. 1966;164:247-256

349. Quint C, Arief M, Muto A, Dardik A, Niklason LE. Allogeneic human tissue-engineered blood vessel. *Journal of Vascular Surgery*. 2012;55:790-798

350. Lawson JH, Glickman MH, Ilzecki M, Jakimowicz T, Jaroszynski A, Peden EK, Pilgrim AJ, Prichard HL, Guziewicz M, Przywara S, Szmidt J, Turek J, Witkiewicz W, Zapotoczny N, Zubilewicz T, Niklason LE. Bioengineered human acellular vessels for dialysis access in patients with end-stage renal disease: Two phase 2 single-arm trials. *The Lancet*.387:2026-2034

351. Sarkar S, Schmitz-Rixen T, Hamilton G, Seifalian AM. Achieving the ideal properties for vascular bypass grafts using a tissue engineered approach: A review. *Med Biol Eng Comput*. 2007;45

352. Chan-Park MB, Shen JY, Cao Y, Xiong Y, Liu Y, Rayatpisheh S, Kang GC-W, Greisler HP. Biomimetic control of vascular smooth muscle cell morphology and phenotype for functional tissue-engineered small-diameter blood vessels. *Journal of Biomedical Materials Research Part A*. 2009;88A:1104-1121

353. Sell SA, McClure MJ, Garg K, Wolfe PS, Bowlin GL. Electrospinning of collagen/biopolymers for regenerative medicine and cardiovascular tissue engineering. *Advanced Drug Delivery Reviews*. 2009;61:1007-1019

354. Pashneh-Tala S, MacNeil S, Claeyssens F. The tissue-engineered vascular graft—past, present, and future. *Tissue Engineering. Part B, Reviews*. 2016;22:68-100

355. Lendlein A, Schmidt AM, Schroeter M, Langer R. Shape-memory polymer networks from oligo(ϵ-caprolactone)dimethacrylates. *Journal of Polymer Science Part A: Polymer Chemistry*. 2005;43:1369-1381